UNIVERSITÀ DEGLI STUDI DI PALERMO

Progetto: DELIAS – "Ricercatori ed Esperti Di Alta Tecnologia e Innovazione Tecnologica Applicata al Settore dei Beni Culturali" a valere sull'Avviso n. 713/Ric. del 29 ottobre 2010
TITOLO III
"CREAZIONE DI NUOVI DISTRETTI E/O NUOVE AGGREGAZIONI PUBBLICO–PRIVATE"

Codice identificativo progetto: PON03PE_00214_2/F9

UNIONE EUROPEA
Fondo Europeo di Sviluppo Regionale

Ministero dell'Istruzione, dell'Università e della Ricerca

Ministero dello Sviluppo Economico

Ministro per la Coesione Territoriale

Dottorato in Information and Communication Technologies
Dipartimento di Energia, Ingegneria dell'Informazione e Modelli Matematici
Settore Scientifico Disciplinare ING-IND/23, ING-INF/01

ELECTROCHEMICALLY PREPARED HIGH-*K* THIN FILMS FOR RESISTIVE SWITCHING DEVICES

IL DOTTORE
ANDREA ZAFFORA

LA COORDINATRICE
PROF.SSA ILENIA TINNIRELLO

IL TUTOR
PROF. ROBERTO MACALUSO

CO TUTOR
PROF.SSA MONICA SANTAMARIA
PROF. VINCENZO LA CARRUBBA

CICLO XXX
ANNO 2018

Contents

1 Introduction

The success of the semiconductors industry relies on the continuous improvement of integrated circuits performances. The cost of a single transistor on a silicon chip during the last 40 years has decreased more than a millionfold, as the number of devices on a single chip increased more than a millionfold, following the exponential dependence commonly known as Moore's law.[1] Numerous challenges arise from both device physics and manufacturing capabilities perspectives for further devices scaling. Traditional scaling based on reduction of physical dimensions of Metal–Oxide–Semiconductor Field Effect Transistors (MOSFETs), with simultaneous reduction of supply voltages and dissipated power, is reaching its limits. In particular physical limits of SiO_2 (that has been used as gate dielectric for more than 40 years because of its manufacturability and ability to deliver continued transistor performance improvements) have been reached, leading to a huge increase in the gate leakage current due to direct tunnelling of electrons, resulting in energy waste and a build-up of heat.

The solution to the tunnelling problem is to replace SiO_2 with a physically thicker layer of new materials with higher dielectric constant, thus keeping the same capacitance but decreasing the tunnelling current. In this frame, the dielectrics science is crucial in providing the dominant technology in integrated capacitors or gate insulators. Among the high-*k* materials, oxides such as HfO_2, Nb_2O_5, Ta_2O_5, ZrO_2, TiO_2 have been extensively studied to be used both in electronic passive elements (e.g. electrolytic capacitors, with oxides used in a Metal-Insulating-Metal, MIM, junction), in active elements (e.g. MOSFETs) as well as in emerging resistive switching memories (ReRAMs).

Since Hf, Nb, Ta, Zr, Ti are "valve metals", electrochemical oxidation, namely anodizing, could be an alternative way to produce high-quality metal oxides because it is a non-vacuum, low-temperature, low-cost process in contrast to the typical techniques largely used in electronic industry that usually require expensive high/ultrahigh vacuum conditions. This electrochemical technique allows to grow oxides with well-defined characteristics such as thickness, composition, structure and morphology by easily controlling operating parameters

such as formation potential, growth rate, electrolyte and metal substrate compositions.

It is important to mention that technology advancement of Complementary Metal Oxide Semiconductor (CMOS) applications has started gradually to shift its focus from single metal oxides to doped or mixed oxides.[2–5] The idea behind this choice is that by mixing high-*k* dielectrics or by their doping with appropriate elements it would be possible to engineer the electrical properties of the materials, combining the favourable properties of the starting dielectrics while suppressing their individual disadvantages. In this frame, the electrochemical oxidation of metallic alloys results in the growth of mixed oxides leading to tailored and controlled optical and dielectric properties of the grown layers.

This Ph.D. work is focused on the electrochemical preparation of several high-*k* oxide thin films that can be used in different fields of electronics, memories world included. Section 2 will be devoted: i) to the fundamentals of the electrochemical anodizing process, exploring how the oxide features (e.g. thickness, structure, composition) are linked to the process parameters; ii) to the fundamentals about the response under irradiation of a metal/semiconductor/electrolyte junction that will be used to interpret the results of the photoelectrochemical characterization of the anodic oxides; iii) to the fundamentals underlying the working operation of the so-called Redox-based Resistive Switching Memories, ReRAM, that are among the most interesting in the field of emerging nonvolatile memories.

Section 3 will be devoted to the experimental part of the research activity, explaining which techniques were used to prepare the metal substrates, the anodic oxides and what kind of characterizations were carried out to study the solid state properties of the anodic layers and their performances in ReRAM devices.

Sections 4, 5 and 6 will be devoted to understand how the process parameters of anodizing process can influence the solid state properties of the anodic oxides. In particular, the influence of the anodizing electrolyte composition, of the anodizing conditions (e.g. sweep rate etc.) and of the metallic substrate composition on the solid state properties of the anodic layers will be studied. To this aim, different systems have been chosen: Al-Ta and Hf-Nb

alloys were anodized in different conditions and the resulting anodic oxides have been studied. Ta_2O_5 is one of the most promising candidates for storage capacitors due to its high dielectric constant (~ 30) and low leakage current. One of the main drawback of this oxide is its band gap which is reported to be low with respect to the value necessary to assure good devices performances. A promising oxide partner for Ta_2O_5 is Al_2O_3, not only due to its very high band gap, but also due its glass former character which reduces the possibility of crystallization. Moreover, Al can be incorporated as substitutional atoms into Ta_2O_5, acting as acceptor and compensating oxygen vacancies with consequent minimization of leakage current. Anodizing magnetron-sputtered Al-Ta alloys allowed to prepare mixed Al-Ta oxides trying to exploit the advantages of pure partner oxides. Regarding Hf-Nb alloys, Hafnium oxide (HfO_2) is probably one of the most studied materials since it replaced SiO_2 as gate dielectric in CMOS-based and logic devices because it combines a large band-gap (5.1 - 6.1 eV), a dielectric constant (~ 20) significantly higher than that of SiO_2 (3.9), high thermal stability and high thermodynamic stability in contact with Silicon. Since Nb_2O_5 has a higher dielectric constant (40 - 50) with respect to HfO_2, anodizing Hf-Nb alloys could be a promising strategy to further increase the dielectric constant and, thus, prepare high-*k* oxides.
Section 7 will be devoted to the idea to apply the anodizing process in preparing in a simple and reliable way high-quality oxides as solid electrolytes for ReRAM devices. Since two of the most studied and used oxides in resistive switching memories are Ta_2O_5 and HfO_2, Ta/Ta_2O_5 and Hf/HfO_2 junctions were prepared by electrochemical anodizing and the properties of the anodic oxides as solid electrolytes for ReRAMs were studied by completing the devices with Pt top electrode. In addition, Nb/Nb_2O_5 and several metal alloy/anodic mixed oxide systems were studied as junctions for resistive switching memories.

2 Fundamentals

A brief recall about some fundamental concepts regarding anodic oxides growth is given in the following Section 2.1. This is necessary to better understand how the process parameters can influence electronic, dielectric, morphological and structural properties of anodic oxides that are studied in this work. In particular, barrier-type anodic oxides growth will be discussed, leaving to the specialized literature further details about the fabrication of porous or nanostructured anodic layers.[6–10] Then, some basic concepts about the response under illumination of semiconducting or insulating materials will be discussed in Section 2.2, highlighting how it is possible to get information about solid state properties of the oxides by using Photocurrent Spectroscopy. Finally, an overview of resistive switching memories will be given in Section 2.3, trying to describe what are the physical processes underlying the operation of these devices and what materials can be used to improve memories performances.

2.1 Anodizing

Anodizing is a low-temperature, low-cost electrochemical process which allows to grow oxides of tuneable composition and properties on the surface of valve metals (Nb, Ta, Al, Zr, Ti, Hf, W, Bi, Sb, etc.) and valve metals alloys.[11] The anodic oxides are produced by the reaction of metal cations, coming from the oxidation of metal substrate, and oxygen anions, coming from the electrolyte (as shown in Figure 2.1), so that it is possible to grow high-quality oxides by applying an anodic polarization to the metal substrate in a suitable liquid electrolyte. Such anodic oxide layers are widely employed in several technological fields, for instance as coating against corrosion,[12] as dielectric for electrolytic capacitor,[13] or recently also as gate oxide in thin film field effect transistors (TFFT).[14–17]

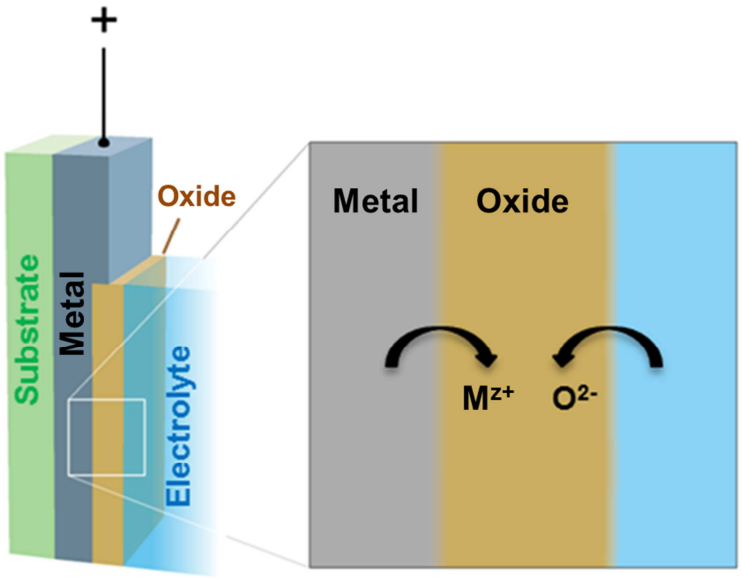

Figure 2.1 Anodizing process: the oxide thickens thanks to the reaction between metal cations (coming from the oxidation of the metal substrate) and oxygen anions (coming from the electrolyte).

The overall reaction that well describes the anodic oxide (MO_x) layer growth from a metallic substrate M is the following:

$$M + xH_2O \rightarrow MO_x + xH_2 \qquad 2.1$$

The current associated to the growth is ionic due to the ions movement, sustained by a high electric field in the order of 10^6 – 10^7 V cm^{-1} that contribute to the de-protonation of water molecules at the oxide/electrolyte interface to produce O^{2-} and OH^- anions.[18,19]

The choice of the anodizing conditions has a direct influence on film thickness and on its crystalline or amorphous nature, while the electrochemical bath and the base alloy affect the composition of the oxides. This point is very important because metastable alloys of various compositions can be easily prepared by several techniques, like magnetron sputtering. Concerning the electrochemical bath, apart the effect related to the possible incorporation into the oxide of species coming from the electrolyte, it is important to consider the role of pH and aggressive ions in determining the morphology of the growing layer from barrier to porous

films.[20]

2.1.1 Barrier-type Anodic Oxides and their Growth Kinetics: *High Field Model*

Barrier-type oxide film is a "nonporous, thin oxide layer possessing electronic and ionic conductivity at high electric field strength".[21 and refs. therein] Usually these oxides, grown on valve metals or valve metals alloys, display ionic current only if the electrode potential exceeds the formation potential (or almost 75% of it) thus leading to the thickening of the oxide with very low electronic current. The latter can be due to oxygen evolution reaction in condition of anodic polarization or to hydrogen evolution reaction under cathodic polarization when the electrode potential reaches values where these processes become thermodynamically possible. It is worth to say that the presence or not of electronic, i.e. leakage, current strongly depends on the solid state properties of the oxides.

Despite a homogeneity in thickness and structure, barrier-type oxide layers can also show heterogeneity due to the differences in composition related to impurities (from the substrate and/or electrolyte), and/or to intermetallic compounds and precipitates present in the substrate.[22]

First researchers that studied the ions mobility during the anodizing process were Güntherschulze and Betz in 1934.[23] Studying the growth of Al and Ta anodic oxides, they found an exponential dependence of the ionic current density on electric field strength according to the following equation:

$$i = i_0 \exp(\beta E) \qquad 2.2$$

that generally identifies the *high field model*. In Equation 2.2, i is the ionic current involved in the oxide growth, i_0 and β are material-dependent constants, and E is the electric field strength across the oxide. Usually, E is calculated as the ratio between the potential drop, ΔU, across the oxide and the film thickness, d_{ox}, as follows:

$$E = \frac{\Delta U}{d_{ox}} = \frac{U_F - U_0}{d_{ox}} \qquad 2.3$$

where U_F is the formation potential and U_0 can be either the flat band potential, U_{FB}, in case the metal is covered by an air-formed oxide, or the equilibrium potential, U_{eq}, in case of bare metal. Most of the time, flat band potential is considered in evaluating the electric field across the oxide since valve metals, due to their low thermodynamic nobility, are usually covered by an air-formed passive oxide layer.

The model is based on the hopping migration of the ions during the growth that move from regular sites or interstitial positions to vacancies or other interstitial positions in their neighbourhoods. Ions hopping requires an activation energy W that increases with the jump distance a,[21,24] that is constant in crystalline as well as in amorphous materials, guaranteed from the short range order. These concepts are better shown in Figure 2.2.

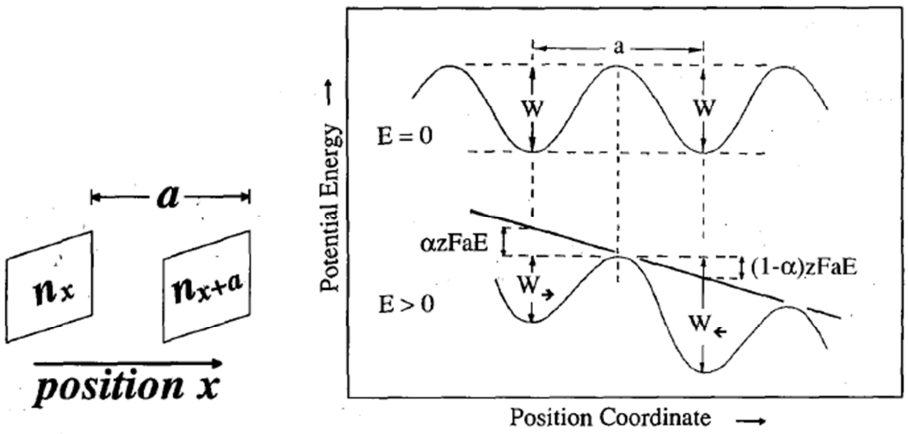

Figure 2.2 (Left) Two adjacent lattice planes in the oxide layer and (right) the influence of the electric field strength on the activation energy of hopping ions.[21]

Therefore, the ionic current expressed by Equation 2.2 is determined by the height of the potential energy barrier corresponding to the rate-determining step of the overall process, that can be lowered by the imposed electric field strength. During the oxide growth, two possible

rate-determining steps can be considered:

i. ionic transport across the metal/oxide interface (Mott-Cabrera model);[25,26]
ii. ionic transport across the oxide (Verwey model);[27]

Mott and Cabrera[25,26] studied the mechanism of growth of thin oxides by anodizing. In their model, the authors considered the transfer of ions across the metal/oxide interface as rate-determining step, assuming fast the transfer of ions through the bulk oxide. The authors rearranged Equation 2.2 considering the role played by ions which vibrate in simple harmonic motion in one dimension and, in presence of a strong electric field strength, they acquire a sufficient energy to surmount the potential energy barrier. The ionic current is then given by the following equation:

$$i = qn\nu \, exp\frac{-(W - q\alpha aE)}{k_B T} \qquad 2.4$$

where n is the number of ions of charge q at the metal/oxide interface per unit area, ν is the frequency of atomic vibrations, W is the height of the potential barrier for injection of a cation into the oxide, a is the jump distance, α is the symmetry coefficient of the activation barrier, T is the temperature, and k_B is Boltzmann's constant.

Verwey[27] proposed a high field model in which the rate determining step was the ion movement through the bulk of the oxide, thus the most important difference between the Verwey and the Mott and Cabrera models is the meaning of i_0 and β. In Mott-Cabrera model these parameters contain the activation distance and the height of potential barrier existing at the metal/oxide interface whilst, in the second case, a and W are referred to the bulk of the oxide.

Despite the high field model is accepted by many authors, many papers were published with results about deviations from this model. Further details about these deviations can be found

in specialized literature.[20,21 and refs. therein]

It is important to say that, during the anodizing process, the total circulating current is the sum of different contributions:

$$i_{tot} = i_{ion} + i_{diss} + i_{el} \quad (2.5)$$

where i_{ion} is the ionic current that sustains the anodic film growth according to the high field model, i_{diss} is the dissolution current due to possible anodic film dissolution in specific conditions according to Pourbaix's diagrams and i_{el} is the electronic current that flows through the oxides and allows faradaic process such as oxygen evolution. Therefore, it is possible to define a growth efficiency of the anodizing process, expressed as:

$$\eta = \frac{i_{ion}}{i_{tot}} = \frac{i_{ion}}{i_{ion} + i_{diss} + i_{el}} \quad (2.6)$$

Through the growth efficiency, it is also possible to estimate the anodic oxide thickness according to the Faraday's law, as follows:

$$d_{ox} = \eta \frac{Q\ MW}{z\ F\ \rho\ A} \quad (2.7)$$

where Q is the circulated charge during the anodic oxide growth, MW is the molecular weight of the oxide, z is the number of moles of electrons necessary to form a mole of oxide, F is the Faraday's constant, ρ is the oxide density and A is the surface exposed during anodizing process.

2.1.2 Ionic Transport during Anodic Oxides Growth

In order to have information about the composition of the anodic oxides, it is important to understand how much of the ionic current involved in the anodizing process is carried from every ion that participates to the oxide thickening. This issue arises when the metallic substrate is an alloy, so that more cations are involved in the anodic oxide growth, or when foreign species are incorporated from the electrolyte besides O^{2-} anions, so that the composition of the oxide can be different and a layered structure can form.

Starting from the seminal papers of Pringle and coworkers,[28–32] other groups, such as the group of University of Manchester headed by Prof. G.C. Wood and Prof. G.E. Thompson and the group of Hokkaido University headed by Prof. H. Habazaki, devoted many papers to studying how the anodizing parameters can influence the oxides properties and composition.

In the anodic oxidation system, the two reactants metal and oxygen are separated by a layer of their product. As the product layer becomes thicker, either metal or oxygen or both must be transported across existing film, as metal cations M^{z+} and oxygen anions O^{2-}, according to the high field mechanism discussed in Section 2.1.1. Therefore, there are five possibilities for the reaction to form the anodic oxide:[29]

i. The metal cations alone migrate, and the reaction to form new oxide occurs only at the oxide/electrolyte interface;
ii. The oxygen anions alone migrate, so that the new oxide is formed only at the metal/oxide interface;
iii. When both metal cations and oxygen anions migrate, two mechanisms i. and ii. could occur together, so that new oxide would be formed at both interfaces;
iv. When both metal cations and oxygen anions migrate, however, the new oxide could be formed within the existing oxide through the transport of material from each side;
v. Since mechanisms iii and iv are not mutually exclusive, the new oxide could be formed both within the existing oxide and at the interfaces.

To define a measure for the relative migration of metal cations and oxygen anions, let consider a reference plane in the oxide, parallel to the two interfaces.[29] The formation of new oxide between this plane and the oxide/electrolyte interface can only occur if metal cations are transported outward across the plane; similarly, oxygen anions must cross in the opposite direction to form new oxide between the plane and the metal surface (see Figure 2.3).

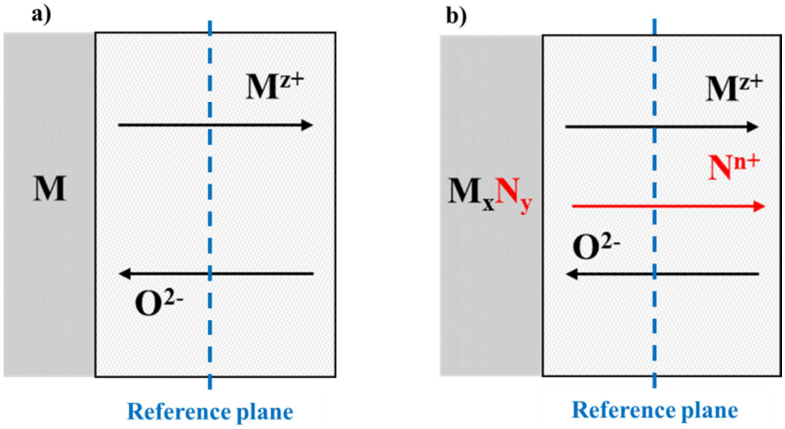

Figure 2.3 Movement of metallic cations and oxygen anions during anodic oxide growth on (a) pure metal and on (b) metal alloy.[20]

If the total amount of new oxide is proportional to the charge passed during anodizing, the amount of new oxide formed on each side of the reference plane is proportional to the fraction of the charge carried by the metal cations and the oxygen anions. The fraction of the new oxide formed on either side of the reference plane is proportional to the transport numbers of the metal $t_{M^{z+}}$ and oxygen $t_{O^{2-}}$ across it, expressed as:

$$t_{M^{z+}} = \frac{i_{M^{z+}}}{i_{form}} = \frac{i_{M^{z+}}}{i_{M^{z+}} + i_{O^{2-}}} \qquad 2.8$$

$$t_{O^{2-}} = \frac{i_{O^{2-}}}{i_{form}} = \frac{i_{O^{2-}}}{i_{M^{z+}} + i_{O^{2-}}} \qquad 2.9$$

The five mechanisms discussed earlier can be recast in terms of transport numbers:

i. The oxide thickens thanks only to the metal cations migration: $t_{M^{z+}} = 1$, $t_{O^{2-}} = 0$;
ii. The oxide thickens thanks only to the oxygen anions migration: $t_{M^{z+}} = 0$, $t_{O^{2-}} = 1$;
iii. The oxide thickens thanks to both migrations being formed only at the interfaces, only within oxide, and at both the interfaces and within oxide: $t_{M^{z+}} < 1$, $t_{O^{2-}} < 1$.

It is noteworthy to mention that the ions transport numbers depend on the their transport properties in a specific oxide matrix. For this reason, they are related with the physico-chemical properties of the ions (radius, charge, mass) and with the solid-state properties of the growing oxide (crystalline or amorphous nature, lattice parameters, concentrations of defects). In the case of anodizing of metallic alloys, the resulting oxide will be a mixed oxide; the presence of two or more cations, M^{z+} and N^{y+}, should be taken into account considering two or more separate transport numbers, $t_{M^{z+}}$ and $t_{N^{y+}}$. The possible differences in cations transport numbers can lead to a mixed oxide where the atomic ratio between the partner metals is different with respect to the underlying alloy. It is possible to distinguish three main cases:

i. $t_{M^{z+}} < 1$, $t_{N^{y+}} = 0$: formation of an oxide that includes only one cation;[33]
ii. $t_{M^{z+}} > t_{N^{y+}}$: an anodic film richer in M is expected to be formed. In such cases the anodic film can also show a bilayered structure with an outer layer rich in the faster migrating metal;[34,35]
iii. $t_{M^{z+}} \sim t_{N^{y+}}$: formation of a mixed oxide with a M/N ratio in the mixed oxide comparable to that of the underlying alloy.

Typical cations transport numbers are in the range 0.20 – 0.40 for amorphous materials (e.g. oxides grown on Al, Ta, Nb etc.),[28,34] whilst they are close to 0 for crystalline anodic oxides (such as that grown on Zr or Hf).[28] It is important to note that, even if a cation is immobile when a pure metal is anodized, same cation can migrate during the anodic oxidation of metallic alloys because it moves in a completely different oxide matrix.[36]

2.2 Photoelectrochemical Behaviour of Semiconductor/Electrolyte Interface

In order to better understand how a semiconductor (SC)/electrolyte (El) interface responses to a light stimulus, it is useful to describe the density of states (DOS) distribution in a crystalline as well as in an amorphous material.

Typically, amorphous materials maintain the same short-range order than their crystalline counterparts and the main differences come out from the absence of the long-range order, typical of crystalline phases.[37–40] Therefore, the density of electron states remains a valid concept for non-crystalline as for crystalline materials since the long-range disorder perturbs but does not annihilate the band structure. The effect on the DOS distribution in the crystalline and amorphous materials can be seen in Figure 2.4.

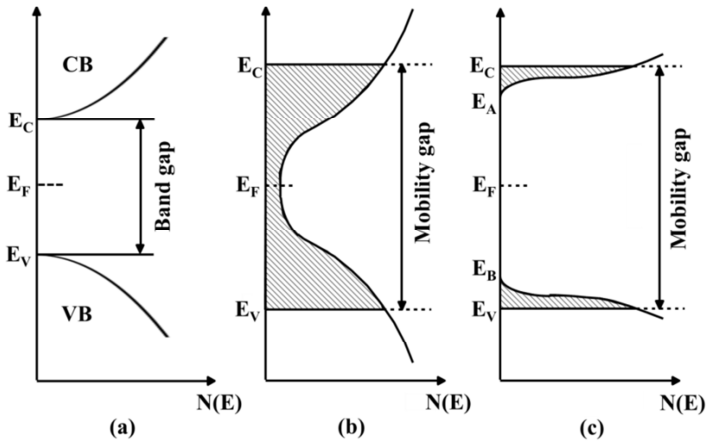

Figure 2.4 Model of the electronic structure for a crystalline semiconductor (a), amorphous semiconductor following the Cohen-Fritzsche-Ovshinsky (CFO) model (b), and amorphous semiconductor following the Mott-Davis model (c).

In Figure 2.4(a), crystalline material band structure is reported with the "classical" band gap, E_g, without any DOS distribution inside it. The absence of long-range order in amorphous materials leads to the presence of a finite DOS within the so-called mobility gap, E_g^m. In the case of Cohen-Fritzsche-Ovshinsky (CFO) model, the non-crystalline structure would lead to overlapping band tails of localized states as in Figure 2.4(b). Those derived from the conduction band would be neutral when empty and those from the valence band neutral when full. The proposal of overlapping tails is considered unlikely to apply to amorphous semiconductors and insulators that are transparent in the visible or infrared.[40] Mott-Davis model considers only the long-range lattice disorder, leading to the DOS distribution shown in Figure 2.4(c). These differences between the distributions of electronic states in crystalline and disordered materials have noticeable influence on the photoelectrochemical, as well as on the impedance, behaviour of the amorphous SC/El junction.

The absorption process of incident light in the bulk of a SC is sketched in Figure 2.5(a): Φ_0 (in cm^{-2} s^{-1}) is the photon flux entering the semiconductor (corrected for the reflections losses at the SC/El interface), which is absorbed following the Lambert–Beer law. The number of electron–hole pairs generated per second and unit of volume at any distance from the SC surface, $g(x)$, is given by:

$$g(x) = \phi_0 \alpha \exp(-\alpha x) \qquad 2.10$$

where α (in cm^{-1}), the light absorption coefficient of the semiconductor, is a function of the impinging irradiation wavelength. It is assumed that each absorbed photon, having energy $h\nu \geq E_g$ originates a free electron–hole couple. Optical transitions at energies near the band gap of a crystalline material may be direct or indirect. In the first case no intervention of other particles is required, apart the incident photon and the electron of the VB (see Figure 2.5(c)); in the second case the optical transition is assisted by the intervention of lattice vibrations (see Figure 2.5(d)).

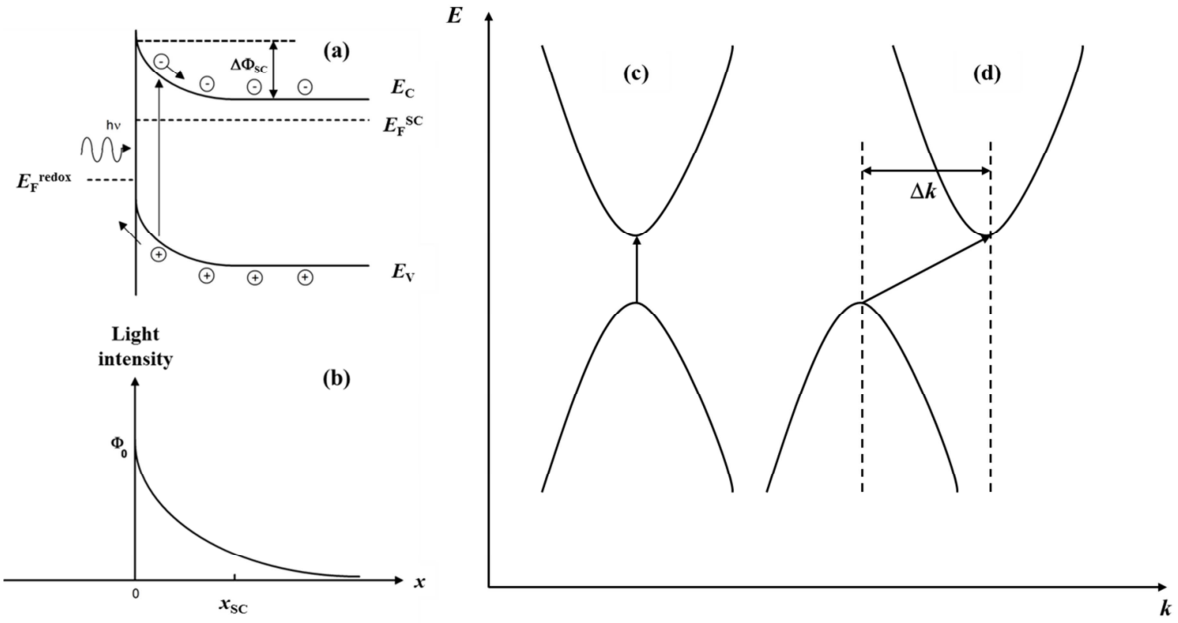

Figure 2.5 Schematic representation of a irradiated crystalline n-type SC/El interface under anodic polarization, showing the electron–hole pair generation (a) and the change of light intensity due to the absorption process within the semiconductor (b). Band-to-band direct transitions (c) and band-to-band indirect transitions (d).

Considering a polarization $\Delta\Phi_{SC}$ inside the SC, the width of the space-charge region, x_{SC}, changes with $\Delta\Phi_{SC}$ according to the following equation:

$$x_{SC} = x_{SC}^{0}\left(|\Delta\Phi_{SC}| - \frac{k_B T}{e}\right)^{0.5} \qquad 2.11$$

where x_{SC}^{0} represents the space-charge width into the SC electrode at 1 V of band bending and its value depends on the concentration of mobile carriers into the SC. In terms of electrode potential, U_E, for not heavily doped SC and in an absence of an appreciable density of electronic surface states (SS), it is possible to write:

$$\Delta\Phi_{SC} = U_E - U_{FB}(ref.) \qquad 2.12$$

where U_{FB}(ref.) represents the flat band potential measured with respect to a reference electrode in the electrochemical scale.

With these premises, it is possible to describe the response of the SC/El interface starting from the seminal paper of Gärtner of 1959 on the behaviour of illuminated solid-state Schottky barrier,[41] integrated by the paper of Butler published in 1977 about the semiconducting properties of WO_2.[42]

In the Gärtner-Butler model, the total photocurrent, I_{ph}, collected in the external circuit is calculated as sum of two terms: a migration term, I_{drift}, and a diffusion term, I_{diff}. The first one takes into account the contribution of the minority carriers generated into the space-charge region; the second one accounts for the minority carriers entering the edge of the space-charge region from the bulk field-free region ($x > x_{SC}$) of SC. No light reflection at the rear interface is assumed, so that all the entering light is absorbed within the SC. Moreover, it is assumed that minority carriers generated in the space-charge region of the SC do not recombine at all, owing to the presence of an electric field which separates efficiently the photogenerated carriers. The same assumption is made for the minority carriers arriving at the depletion edge from the bulk region of the SC.[43] Therefore, the total photocurrent in a n-type semiconductor can be expressed as follows:

$$I_{ph} = I_{drift} + I_{diff} = e\Phi_0\left[1 - \frac{e^{-\alpha x_{SC}}}{1 + \alpha L_p}\right] + e\, p_0 \frac{D_p}{L_p} \qquad 2.13$$

where D_p and L_p are the hole diffusion coefficient and diffusion length respectively and p_0 is the equilibrium concentration of holes in the bulk of the (not illuminated) SC. The same equation holds for p-type SCs, with D_n and L_n (electron diffusion coefficient and diffusion length) instead of D_p and L_p and n_0 (electrons equilibrium concentration) instead of p_0.

For wide band gap materials ($E_g > 2$ eV) where the bulk concentration of minority carriers is

very small, Equation 2.13 can be further simplified by neglecting the last term. In this case, if $\alpha x_{SC} << 1$ (slightly absorbed light) and $\alpha L_p << 1$ (small diffusion length for minority carriers), the photocurrent crossing the n-type SC/El interface can be rewritten as:

$$I_{ph} = e\Phi_0 \alpha x_{SC}^0 \left(U_E - U_{FB} - \frac{k_B T}{e}\right)^{0.5} \qquad 2.14$$

Equation 2.14 foresees a quadratic dependence of the photocurrent on the electrode potential, which can be used for getting out the flat band potential of the junction. The measurement of the photocurrent as a function of U_E is called photocharacteristic. In fact, by neglecting the term $k_B T/e$, a plot of $(I_{ph})^2$ vs. U_E should intercepts the voltage axis at the flat band potential, U_{FB}, regardless the employed irradiating wavelength, λ, as long as $\alpha x_{SC} << 1$ condition is obeyed. It is important to remark that all previous equations pertain to the steady-state values of the d.c. photocurrent. The equations derived for steady-state remain valid also for chopped conditions provided that the lock-in measured signal remains proportional to the steady-state chopped value.[44,45]

It is noteworthy to mention that, according to Equation 2.14, the measured photocurrent is directly proportional to the light absorption coefficient. By considering that in the vicinity of the optical absorption threshold of the SC,[46] the relationship between the absorption coefficient and optical band gap of material, E_g^{opt}, can be written as:

$$\alpha = A\frac{\left(h\upsilon - E_g^{opt}\right)^{n/2}}{h\upsilon} \qquad 2.15$$

so that it is possible to derive the following expression:

$$Q\ h\upsilon\ \propto \left(h\upsilon - E_g^{opt}\right)^{n/2} \qquad 2.16$$

where $Q = (I_{ph})/e\Phi_0$ represents the photocurrent collection efficiency and E_g^{opt} the optical threshold for the onset of photocurrent at the illuminated electrode. Equation 2.16 shows that, at constant electrode potential, it is possible to get the optical band gap of the material from the dependence of the photocurrent on the irradiating wavelength (shortly referred as the photocurrent spectrum of the junction) of incident light at constant photon flux. In fact by plotting $(Q\ h\nu)^{2/n}$ vs. $h\nu$ at constant electrode potential it is possible to get a characteristic photon energy $h\nu_0 = E_g^{opt}$. For an ideal SC/El junction E_g^{opt} coincides with the minimum distance in energy between the filled states of the valence band (VB) and the empty states of the conduction band (CB) (band gap, E_g) as shown in Figure 2.4(a). By assuming a parabolic electronic density of states distribution, DOS, ($N(E) \propto E^{1/2}$) near the band edges, in the case of direct transitions (see Figure 2.5(c)) n assumes values equal to 1 or 3, depending on whether the optical transitions are allowed or forbidden in the quantum mechanical sense.[46] In the case of indirect optical transitions (see Figure 2.5(d)), the n value in Equation 2.16 is equal to 4.

In the case of amorphous materials, as many anodic oxides, the following relationship holds:[39]

$$\alpha\ h\upsilon\ \propto \left(h\upsilon - E_g^{m}\right)^2 \qquad 2.17$$

where $E_g^m = E_C - E_V$ is now the mobility gap of the a-SC (see Figure 2.4(b) and Figure 2.4(c)). The exponent 2 is reminiscent of the indirect optical transitions in crystalline materials but now photons interact with the solid as a whole: this type of transition in amorphous materials is termed non direct. Because some tailing of states is theoretically foreseen for a-SC by any proposed model of DOS, E_g^m represents an extrapolated rather than a real zero in the density of states.

In agreement with a general statement reported in literature,[40] it has been suggested[43,44,47] that, in absence of appreciable differences in short-range order of amorphous and crystalline counterparts, the mobility gap of amorphous films should be equal or larger than the band gap of the crystalline counterpart. Such a difference can be assumed as a measure of the influence of lattice disorder on optical gap of the films. The difference $\Delta E_{am} = E_g^{m} - E_g^{cryst}$ in the range of 0.1 – 0.35 eV, is in agreement with the expected extension of the localized states regions near the band edges due to the lattice disorder.[40] A different short-range order can imply the formation of a defective structure, with a high density of localized states within the mobility gap as well as changes in the density of the oxide layer, which is known to affect also the value of the optical gap in amorphous materials.

Due to the low mobility of carriers in amorphous materials, it is reasonable to assume that a negligible contribution to the measured photocurrent arises from the field-free region of the semiconductor. In this case, it is possible to assume a free carrier generation efficiency, η_g, position independent under irradiation with light having energy higher than the SC mobility gap. Under steady-state conditions, the photocurrent can be expressed as:

$$I_{ph} = \eta_g e\Phi_0 \frac{\alpha L_d}{1+\alpha L_d}\left[1 - exp\left(-x_{SC}\frac{1+\alpha L_d}{L_d}\right)\right] \qquad 2.18$$

where $L_d = \mu\tau E$, μ and τ being the drift mobility and the lifetime of the photocarriers respectively and E is the mean electric field in the space-charge region of the a-SC. The efficiency of free carriers generation in presence of geminate recombination effects, η_g, is a function of the thermalization distance, r_0, and E. An expression for $\eta_g(r_0, E)$ for amorphous materials was given by Pai and Enck.[48]

As done for crystalline semiconductors, it is still possible to assume for amorphous SCs a direct proportionality between the photocurrent yield, $Q = I_{ph}/e\Phi_0$, and the light absorption coefficient, α, in the vicinity of the absorption edge under constant electrode potential, allowing to replace α with the photocurrent yield in deriving the optical band gap of

amorphous semiconducting films from the photocurrent spectra. In the case of amorphous insulator/electrolyte junction, the entire oxide thickness d_{ox} has to be substituted to the space-charge width x_{SC} in Equation 2.18.

In presence of thin oxide layers, it is possible that under illumination a large fraction of photons impinging the film/solution interface arrive at the metal/film interface, by exciting metal electrons to higher energy levels and leaving vacant states below the Fermi level of the metal. In the case of very thin passive films ($d_{ox} \leq 2$ nm) external (into the electrolytic solution) photoemission processes become possible by tunnelling of excited electrons or holes at the metal surface throughout the film. The photoemission of electrons directly from the metal to the ground state of liquid water has been observed more frequently through very thin oxide films covering metals.[49,50]

When such an external photoemission process occurs, in absence of diffuse double layer effects or large adsorbed molecules, it is possible to write for the emission photocurrent the so-called *five half (5/2) power law*, which gives the dependence of photocurrent from photon energy and electrode potential as:[51]

$$I_{ph} = const.\,(h\upsilon - h\upsilon_0 - |e|U_E)^{5/2} \qquad 2.19$$

where U_E is the electrode potential measured with respect to a reference electrode, $h\nu_0$ is the photoelectric threshold at zero electrode potential (changing with reference electrode) and $h\nu$ is the photon energy in eV. At constant potential the photocurrent yield can be expressed as:

$$Q^{0.4} = const.\,(h\upsilon - E_{th}) \qquad 2.20$$

where $E_{th} = h\nu_0 + |e|U_E$ is the measured photoemission threshold, dependent on the imposed electrode potential. It follows that a change in the photoemission threshold vs potential of 1 eV/V is expected.

In the case of thicker films ($d_{ox} \geq 5$ nm), where the external photoemission processes are forbidden, the possibility of an internal photoemission process due to the injection of photoexcited electrons (or holes) from the metal into the CB (or VB) of the oxide layer must be considered. In such a case the internal emission photocurrent varies with the photon energy according to the so-called Fowler photoemission law:[51]

$$Q = const.(h\upsilon - E_{th})^2 \qquad 2.21$$

where E_{th} is the internal photoemission threshold energy, which can be obtained from a plot of $Q^{0.5}$ vs. the photon energy, $h\nu$, at constant photon flux. This threshold is a measure of the distance in energy between the Fermi level of the metal and the CB (electrons photoemission) or VB (holes photoemission) edge of the film. The occurrence of electrons or holes internal photoemission in the case of insulating films is established by the direction of the electric field, and in turn by the electrode potential value with respect to the photocurrent sign inversion potential. In absence of trapping effects, the inversion photocurrent potential can be used to determine the flat band potential of insulating oxides.

In the case of insulating anodic films on valve metals electrons internal photoemission processes are usually observed under cathodic polarization and under illumination with photons having energy lower than the optical band gap of the film. For semiconducting films no evidence of internal photoemission process is expected, owing to the absence of any electric field at the metal/film interface, as long as the space charge region of the SC is less than the film thickness. The knowledge of the internal photoemission threshold allows to locate the energy level of the conduction band of the oxide films with respect to the Fermi level of the underlying metal, once the work function of the metal is known.

2.3 Redox-based Resistive Switching Memories

Information is coded in languages that are formed by characters. The binary code, or Boolean

code, consists of only two characters, “0” and “1”, and, for this reason, it is the most elementary language to represent any information. This makes it most suitable for carriers with bi-stable states, frequently used in digital electronics which is the basis of the Information and Communication Technologies (ICT). The smallest binary information systems consist of a binary switch with some basic operations, as the WRITE operation that sets a dedicated state in the binary switch, the READ operation that detects the state of the switch and the TALK operation that transfers the state from/to the switch (without detecting the state). These basic operation can be used to cover the three areas of information technology: information storage by writing and reading the memory, information processing by logic operation, and information transfer by communicating the information.[52] In the information storage world, Dynamic Random Access Memories (DRAM) and Flash memories are the most common devices used today.

DRAMs are among the most used memories in computer systems today, from smartphones and tablets to servers and super computers.[52] The storage element is a MIM capacitor and the direction of charging (one plate positively charged and the other one negatively, and vice versa) represents the binary state, “0” and “1”. In order to keep the charge on the MIM_{cap} plates, the capacitor is connected to an access transistor that isolates the storage capacitor unless there is a READ or WRITE operation. These combinations of transistors and capacitors are called 1T-1C. In these devices, the retention time is less than 1 s and the information is lost when the supply voltage of the circuit is turned off. For this reason, DRAM are volatile memories.

Flash memories are based on MOSFETs technology with an additional floating gate, invented by Sze and Kahng in 1967.[53] They are surely the most used non volatile memories in electronics world. The working principle based on trapping excess electrons in the floating gate, makes the information can be retained in the device for more than 10 years. For a fast WRITE operation (ms to μs), the applied voltages have to be higher than 12 - 15 V.[52] The relationship between the write speed and the write voltage represents the voltage-time dilemma, which is a fundamental property of non volatile memories: the lower is the

operating voltage, the lower is the operation speed.

In the attempt to exploit the advantages of both memory systems, i.e. RAM organized with access transistors being non volatile, 2-terminal elements based on electrically switchable resistance have attracted considerable attention, often called with the term Resistive Switching Random Access Memories (RRAM).

In the field of RRAM devices, particular interest is devoted to Redox-based Resistive Switching Random Access Memories, namely ReRAM, in which redox reactions at interfaces and nano-ionic transport processes play a key role. A resistive switching memory cell in a RRAM is generally built by a capacitor-like MIM structure, composed by an insulating or resistive material (e.g. oxides or chalcogenides) sandwiched between two electron conductors. These MIM cells can be electrically switched between at least two different resistance states, after an initial electroFORMING cycle which is usually required to activate the switching property. By applying appropriate programming or write voltage pulses V_{wr}, a cell in its high-resistance (OFF or HRS) state can be SET to a low-resistance (ON or LRS) state or RESET back into the OFF state. ON and OFF states represent the Boolean “1” and “0” respectively, and are used for digital information storage and operations.[54,55]

Most ReRAM systems reported in the literature operate in the bipolar resistive switching (see Figure 2.6(a)). Starting in the HRS, a SET process can be triggered by a voltage V_{SET} higher than a characteristic threshold voltage V_{th1}, which leads to the LRS. Often, a current compliance (I_{CC}) is used for the SET operation in order to avoid damage to the cell and to optimize the operation. A READ operation is performed at a much smaller voltage magnitude V_{READ} to detect the current and avoiding any change in the resistance state. A voltage signal V_{RESET} of opposite polarity is used for the RESET process to switch the cell back into the HRS.[56]

On the contrary, unipolar resistive switching (see Figure 2.6(b)) is characterized by the fact that all WRITE and READ operations can be performed with voltage of only one polarity. Starting in the HRS, the SET process takes place at a voltage $V_{SET} > V_{th1}$, with a LRS current limited by a I_{CC}. It is important that the current compliance is released in the RESET process,

so that the current can exceed the compliance value, which leads to changing back into the HRS. The read operation is performed at a small voltage V_{READ} as in the bipolar operation.[56]

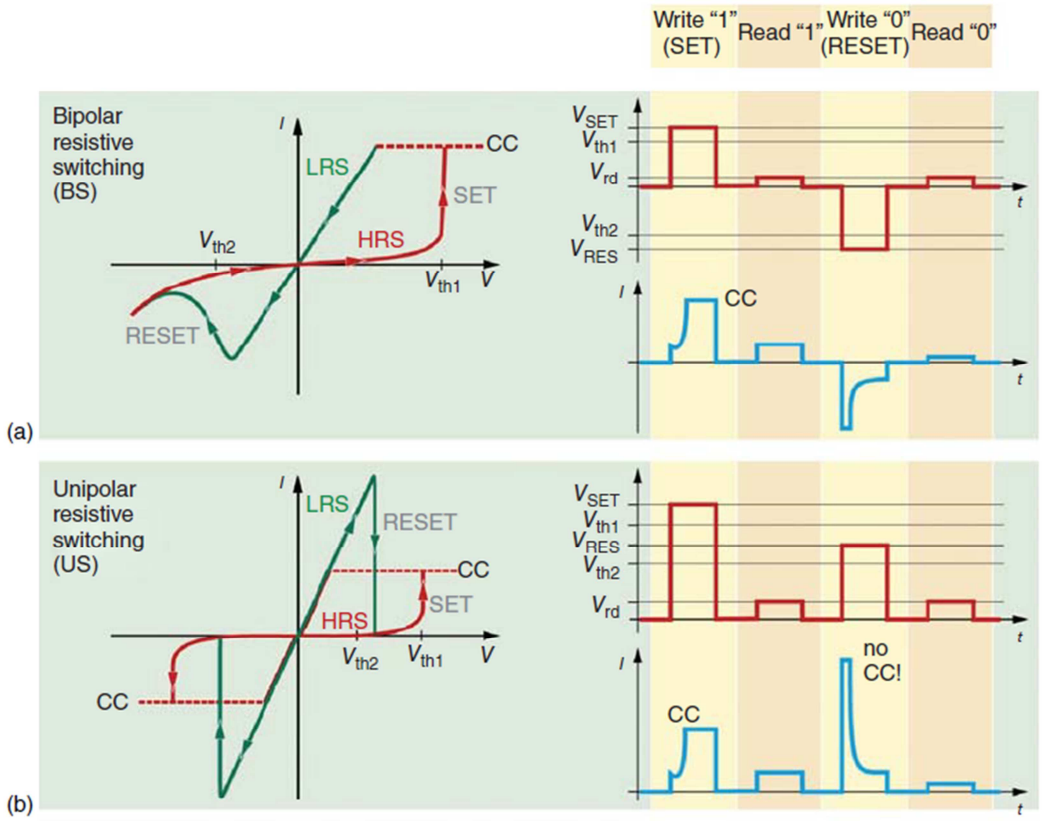

Figure 2.6 (a) Bipolar resistive switching and (b) Unipolar resistive switching.[56]

Generally speaking, two types of resistive switching can be distinguished, i.e. filamentary switching and area-dependent switching. In the former case the electrical switching of the solid electrolyte is due to the formation/disruption of conducting filament/filaments, that can be both metallic or formed by reduced oxide, depending on the material used in the device. In the latter case resistance change is supposed to take place uniformly at the interface between the electrolyte and a reactive metal electrode. Uniform resistance switching can be recognized by area-dependent LRS resistance and programming current, in contrast to area-independent switching in filamentary-type devices.[57]

Depending on the working principle of the ReRAM cells, three different types are

distinguished: Electrochemical Metallization Memories (ECM), Valence Change Memories (VCM) and Thermochemical Memories (TCM). Section 2.3.1 and Section 2.3.2 will be devoted to a deeper description of ECM and VCM memories. TCM memories use symmetric electrodes and are characterized from the formation and dissolution of the filaments due to thermal energy (Joule heating) generated by the high current flowing in the device. Among the three types of ReRAM, TCM memories have the lowest prospects for industrial realization. The reason why is that their operation principle implies higher power consumption and, in addition, the involved switching is unipolar so that their practical application is complicated.

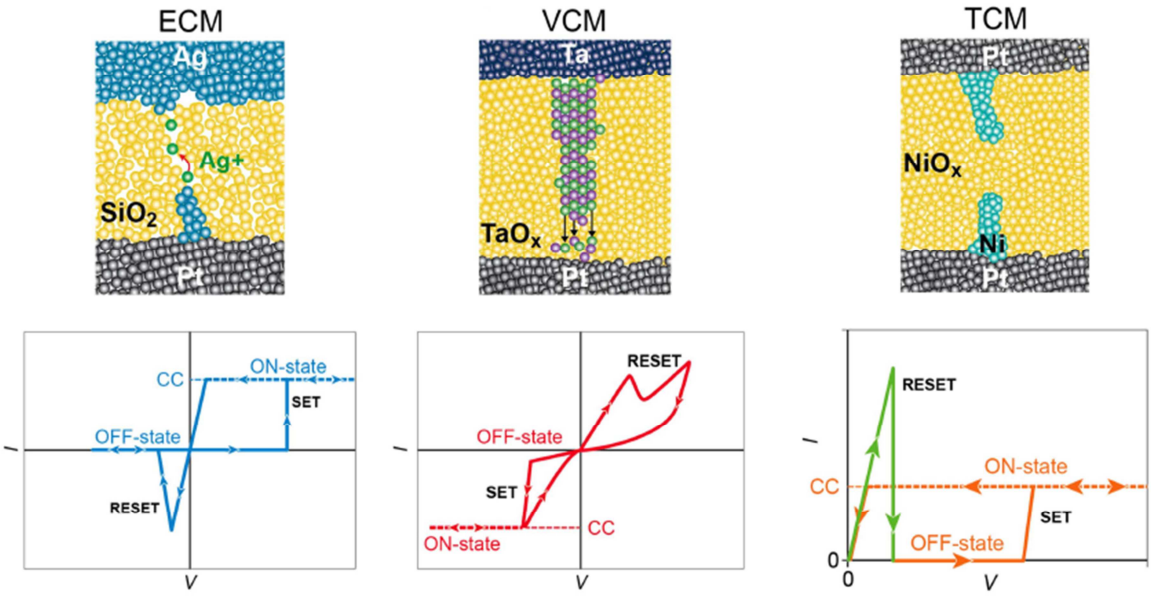

Figure 2.7 Devices structure and current–voltage (*I–V*) characteristics for ECM, VCM and TCM cells. Current compliance is typically used to limit the current in order to prevent irreversible damage.[58]

In order to be competitive with the DRAM and Flash memories, the performances of ReRAM devices that have to be addressed are:[55] WRITE voltages in the range of a few hundred of mV and WRITE pulses time < 100 ns; endurance > 10^7 cycles; resistance ratio > 10; retention time > 10 years.

2.3.1 Electrochemical Metallization Memories (ECM)

Electrochemical Metallization Memories (ECM) are devices composed by a simple metal/solid electrolyte/metal junction with some peculiarities: they consist of an active electrode (AE) (typically Ag or Cu, but other electrodes can be used), an electrochemically inert counter electrode (CE) (typically Pt, It or W but also some electronically conductive materials such as ITO or TiN can be used since it is supposed they are unable to exchange mobile ions with the electrolyte) and a thin solid electrolyte able to conduct ions sandwiched between both electrodes.[59,60] A schematic presentation of a ECM cell with Cu AE and Pt CE with a typical *I-V* sweep, and the related physical processes within the cell are presented in Figure 2.8.

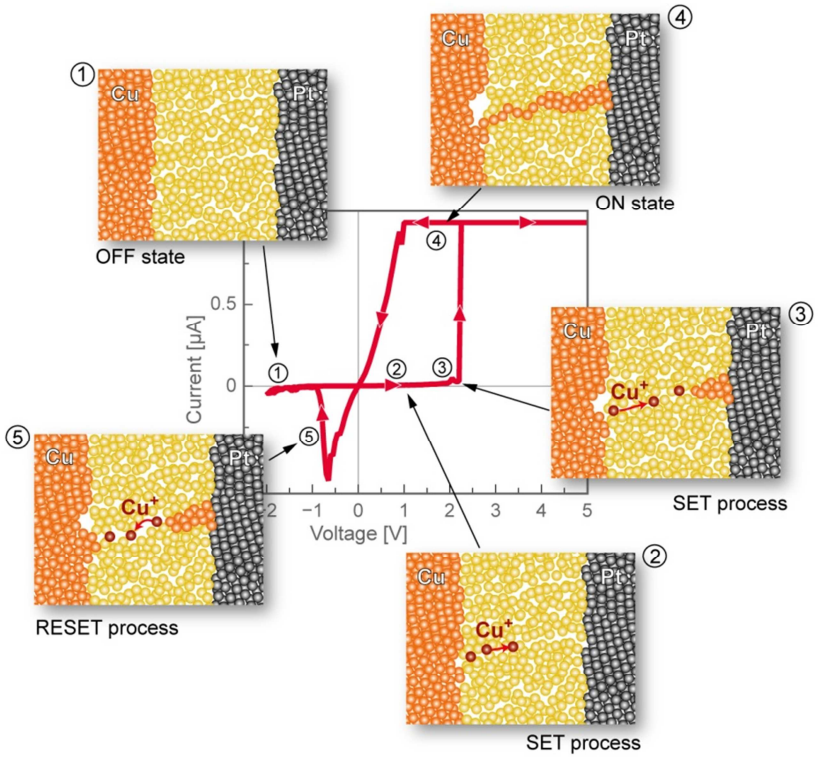

Figure 2.8 Schematic presentation of the processes during *I–V* sweep, including formation and dissolution of a Cu filament, in a ECM cell.[61]

If a sufficient voltage is applied to the Cu active electrode, it is possible to electrochemically oxidize it generating $Cu^{+/++}$ ions that enter in the solid electrolyte (step 1 and 2). After the migration of the Cu ions into the electrolyte sustained by the presence of high electric field strengths across the thin film, $Cu^{+/++}$ reach Pt inert electrode and start to be reduced. This leads to the electro-crystallization of Cu at the Pt surface (step 3). Because of the high current densities (~ MA cm^{-2}) and electric field strengths (~ 10^8 V m^{-1}) the deposit forms as a conducting Cu filament with a diameter typically varying between 5 and 10 nm. After the metal filament has grown sufficiently far to make an (electronic, e.g. galvanic) contact to the opposite Cu electrode, the cell has switched to the ON state (step 4) that is indicated by a rapid current increase in the *I-V* characteristic. The cell retains the ON state unless a sufficient voltage of opposite polarity is applied and the electrochemical dissolution of the metal filament leads to the RESET process (step 5), with the decreasing of the current to its initial OFF state (state 1).

This switching mechanism is universally accepted since the observation of the formation of metallic filament in different ECM cells by *in-situ* TEM observation.[62–65] Many parameters can influence the cell performances, such as the nature of both electrodes,[66,67] moisture (that can affect the migration of metal ions across the electrolyte[68,69] or can contribute in originating an electromotive force inside the cell[70]), temperature and chemical composition of the electrolyte matrix.[71,72]

Major performances of ECM cells are low SET voltages (in the range between 0.2 V and 1 V), low SET/RESET currents (down to pA range) with low power consumption and large (typically 10^6) OFF to ON resistance ratio.[72,73] Unfortunately, these systems suffer of instability of the filament that leads to insufficient retention of the ON states, especially for resistances above ~ 15 kΩ.[73]

2.3.2 Valence Change Memories (VCM)

When the redox processes at the oxide/electrode interfaces lead to a change in the valence state of the metal ion, the cells are called Valence Change Memories (VCM). These systems

are two-electrode devices as ECM cells and typically the metal electrodes are chosen so that to have two Schottky barriers at the electrode/electrolyte interfaces with different height. Low work function metals (and also easily oxidable), such as W, Ti, Ta, Hf, are usually used for the lower Schottky contact that becomes ohmic (OE) during the device operation[74] whilst Pt, or other high work function metals (e.g. Ir, Au etc.), can be selected for the higher Schottky contact.[56] In some cases, symmetric cells with Schottky electrodes are used e.g. Pt/Oxide/Pt and the FORMING process (reduction) is believed to ensure an ohmic contact at one of the interfaces.[75]

The resistive switching mechanism relies on the motion of mobile ionic defects under the applied electric field across the electrolyte. The most widely accepted model is based on (double) positively charged oxygen vacancy defects $V_O^{\bullet\bullet}$, but motion of metal cations has been evidenced and their role cannot be excluded.[76] A schematic presentation of a VCM cell, with ZrO_x sandwiched between Zr as ohmic contact and Pt as Schottky contact, with a typical *I-V* sweep, and the related physical processes within the cell are presented in Figure 2.9.

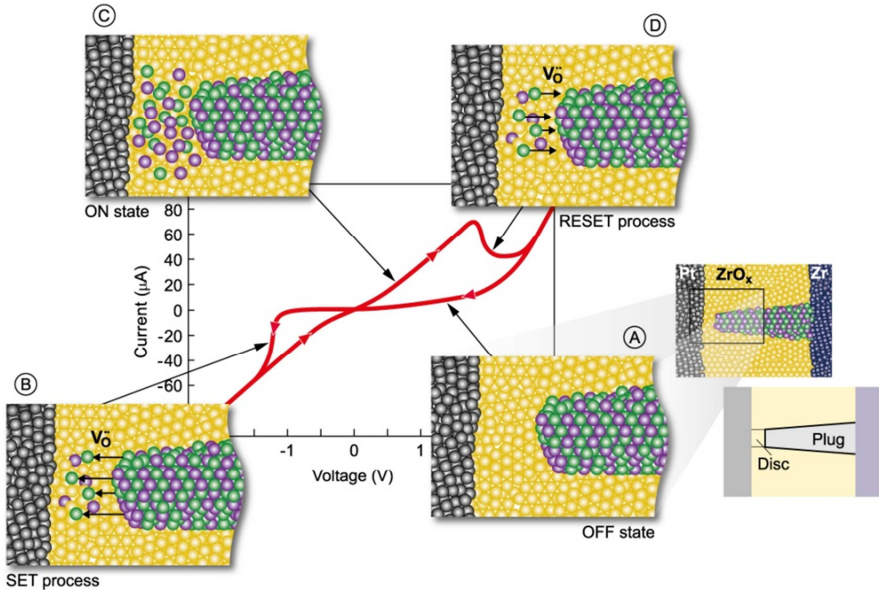

Figure 2.9 *I-V* sweep of a VCM cell. Green spheres: oxygen vacancies. Violet spheres: reduced metallic ions.[60]

The oxygen vacancies are introduced in the switching layer during the initial FORMING step,

which results in the formation of a filamentary region with a high concentration of oxygen vacancies between the two electrodes. However, during the RESET process the conducting filament is only partially dissolved (on the contrary of the complete dissolution of the metallic filament in ECM cells). Between the tip of the filament and the Schottky electrode a thin disc is formed that is less conductive than the filament (plug), but a bit more conductive from the surrounding oxide matrix. Thus, the Schottky barrier at that interface with Pt electrode determines the overall resistance. During SET process, the disc is reduced and becomes as conductive as the other part of the filament (ON state) whilst during RESET process it is oxidized and/or may also increase in thickness, defining the high resistive (OFF) state.[60]

An improvement in the devices performance has been recently achieved by adding another metallic layer to the simple MIM structure.[74,77] This metal layer is called oxygen exchange layer (OEL) or oxygen scavenger which is believed to induce a distributed reservoir of defects at the metal/insulating oxide interface, thus providing an unlimited availability of defects which are the building blocks for the conducting filament. More detailing, the chemical reaction between the OEL (metal) and the oxide layer results in the transport of oxygen anions from the dielectric into the metal by creating $V_O^{\cdot\cdot}$ or cations into the oxide. This intermediate layer directly influences the kinetic barriers for the defect mobility in the VCM cell, thus defining among others the switching speed and dissipated power. This oxygen vacancies reservoir layer was also detected in MIM structure without an additional metallic film, such as Ta/Ta_2O_5 and Hf/HfO_2 junctions, and it has a different short range structure and stoichiometry from that of the solid electrolyte bulk[76,78] and was suggested to play an essential role in the resistive switching by allowing easier transport of anions, cations, and electrons.[76,79,80]

From the devices performances point of view, VCM cells demonstrated much better retention than ECM cells. They are also able to provide intermediate resistance states (but not so finely distinctive) and show fast switching times. Disadvantages are the higher switching voltages and currents (i.e. higher power consumption) and the lower OFF/ON ratio which varies typically between 10 and 1000.[60]

3 Experimental

3.1 Samples Preparation

In order to study how the anodizing process parameters can influence the structural and the electronic properties of the high-*k* oxide thin films, different metal substrates, in composition and in shape, were used. In particular, metallic rods as well as magnetron sputtering-deposited metal substrates have been anodized in different process conditions. The following sections describe the experimental conditions adopted to prepare the metal substrates and ReRAMs devices.

3.1.1 Preparation of Hafnium rod

This metallic sample was used to check if the growth of Hf anodic oxides is well described by the high field mechanism (as discussed in Section 2.1.1). To this aim, a rod-shaped electrode is very useful since it is very easy to clean and prepare for the anodizing. This is an important characteristic since a high number of anodic growths is necessary for this type of study.
A Hafnium rod, provided by Goodfellow (97.0% in purity), of 0.5 cm in diameter was embedded in a Teflon cylinder and sealed by a two components epoxy resin (Torr Seal Varian Ass.). This procedure ensures that the same area is exposed during all the anodic growths and the following characterizations. Rod surface was additionally abraded with P800 and P1200 papers and then rinsed with distilled water. This mechanical polishing leads to a roughness factor *r* (i.e the ratio between the real and the geometrical surfaces) of ~ 1.2.

3.1.2 Preparation of magnetron sputtering-deposited metal substrates

Magnetron sputtering was used as technique to prepare metallic substrates because it enables to deposit layers that are flat at nm scale and uniform in thickness. This part of Ph.D. work has been carried out in the Laboratory of Interfacial Electrochemistry, Hokkaido University (Sapporo, Japan) supervised by Prof. Hiroki Habazaki.
In order to deposit flat, defects-free and reliable metallic samples, also the substrates must be

flat and uniform. Therefore, glass and alumina were chosen as substrates for the metals magnetron sputtering deposition.

Glass substrates (9 × 6 cm^2) of 1 mm thickness were degreased in an aqueous solution containing 30 g l^{-1} of surfactant (Okuno Chemical, Top Alclean 30) at 200 °C for 15 min. Afterwards, glasses were rinsed with abundant tap water and distilled water and dried just before sputtering procedure.

Alumina substrates were prepared starting from high purity (99.999 %) aluminum foils (1.5 × 5 cm^2). After rinsing with acetone, aluminum foils were electropolished to provide a smooth and bright surface. Electropolishing was performed under potentiostatic conditions (constant voltage of 20 V for 4 min) in an ethanol/perchloric acid (4:1 (v/v)) mixture.[81] Al foil was the anode during the procedure whilst another Al sheet, with a very high surface, was used as cathode. The electrolyte was kept between 0 and 5 °C (using a bath containing water and ice) and continuously stirred. Afterwards, Al foils were rinsed with ethanol and distilled water to remove all the residues of the electropolishing electrolyte. This step results in mirror-like surface for aluminum foils. Electropolished foils were then anodized up to 200 V at ~ 3 mA cm^{-2} in a 0.1 M ammonium pentaborate solution to provide flat and mechanically consistent substrates for magnetron sputtering procedure.

Pure metals and metallic alloys were then deposited through magnetron sputtering on the glass and alumina substrates. The deposition was carried out in a Shimadzu, SP-2C system that comprises a vacuum chamber, just one gun and three housings for the substrates. The presence of just one gun is not limiting in preparing metallic alloys: a target of 10 cm in diameter is used and, in order to prepare metal alloys, smaller targets (2 cm in diameter) of alloying element are placed symmetrically on the erosion zone of the underlying target. The number of targets determines the composition of the alloy: the higher is the number of small targets, the richer in alloying element will be the metal alloy. In order to get the deposited alloy films of uniform composition and thickness, the substrate holders were rotated around the central axis of the chamber as well as their own axes. The entire magnetron sputtering setup is sketched in Figure 3.1.

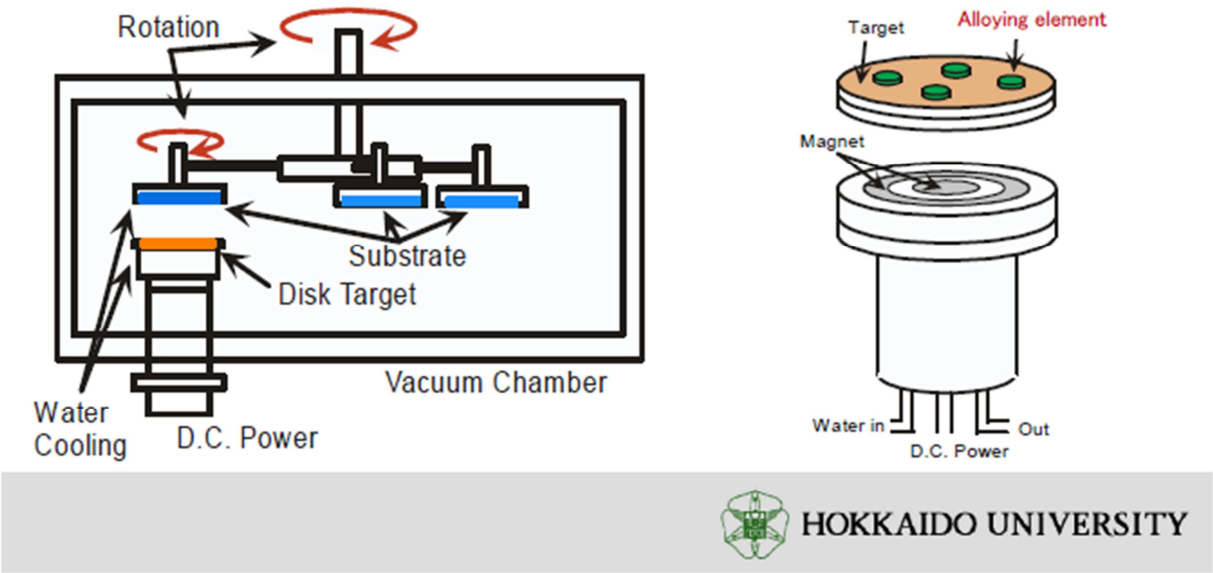

Figure 3.1 Magnetron sputtering setup used in the Laboratory of Interfacial Electrochemistry, Hokkaido University (Sapporo, Japan).

After installing the substrates and targets, the chamber was evacuated to less than 5×10^{-5} Pa, and then metals deposition was conducted in Argon atmosphere at ~ 0.3 - 0.4 Pa at 0.5 A for all the samples. The longer is the sputtering procedure, the thicker will be the metal layer on the substrates. Alloys composition was *a posteriori* determined by Field Emission-Electron Probe Micro-Analysis (FE-EPMA) (JEOL JXA-8530F).

3.1.3 Fabrication of ReRAM devices

In order to investigate the resistive switching properties of the metal/anodic oxide systems, Pt was deposited as top electrode onto all the samples. Through photolithography and lift-off procedures, Pt was defined in different pads shapes, as shown in Figure 3.2.

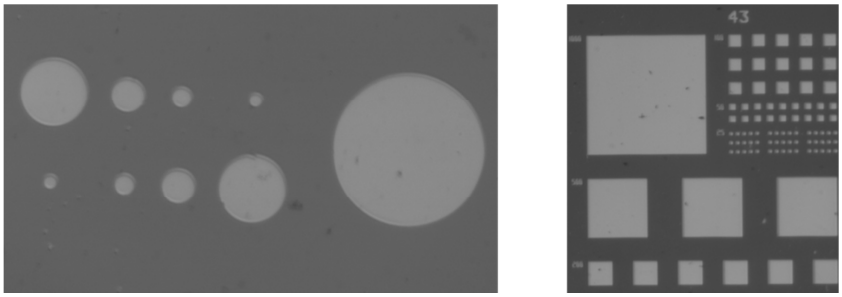

Figure 3.2 Pt pads in Metal/Anodic Oxide Metal/Pt ReRAM devices.

In the case of circular shape, pads diameters were 100, 150, 250, 500 and 1130 μm. In the case of squared shape, pads areas were 25×25, 50×50, 100×100, 200×200, 500×500 and 1000×1000 μm^2.

3.2 Electrochemical Growth of High-*k* Thin Films

As described in Section 2.1, the electrochemical technique used in this Ph.D. work to fabricate high-*k* thin films is the anodizing. This process is carried out by forcing the current to flow from the cathode to the anode using an external power source, e.g. a potentiostat. Therefore, anodizing can be performed by applying a constant potential difference between anode and cathode (potentiostatic mode), by imposing a constant current through the cell (galvanostatic mode) or by sweeping the electrode potential at fixed rate (potentiodynamic mode).[20]

In particular, for formation potentials up to 20 V vs. reference electrode, potentiodynamic mode was used. A three-electrode configuration was employed, comprising the working electrode (i.e. the metal substrate that will be converted in oxide), a counter electrode (i.e. the cell cathode that in all the case was a DSA (Dimensionally Stable Anode) electrode) and a reference electrode. The latter was a silver/silver chloride electrode (0 V vs Ag/AgCl = 0.197 V vs SHE) in almost all the measurements. When the oxide to be grown or characterized was Al_2O_3 or contain aluminum in a mixed oxide, the reference electrode was a mercury/mercury oxide electrode (0 V vs Hg/HgO = 0.098 V vs SHE) to avoid any problem of pitting by chlorides.[82] Two different potentiostats were used for this kind of measurements: Parstat 2263

and Biologic Multi-channel Potentiostat VMP2.
For thicker anodic oxides, i.e. for formation voltage $U_F \geq 50$ V, galvanostatic mode was employed with a two-electrode configuration, also called anode-cathode for the absence of a reference electrode. Two different current sources were used: Keithley 227 and Keithley 2410.

3.3 Characterization Techniques

In order to get information about the structural, morfological as well as electronic and optical properties of the anodic oxides, different *in-situ* and *ex-situ* techniques were used. The anodic layers characterization is surely crucial to better understand how the anodizing process parameters influence the final properties of the oxides and, consequently, the devices performances. Among different *in-situ* techniques, Photocurrent Spectroscopy, Differential Capacitance Measurements and Electrochemical Impedance Spectroscopy have been chosen for the study of the solid state and electronic properties of the anodic oxides, and will be described in the following Sections 3.3.1 and 3.3.2. Instead, as *ex-situ* techniques, Grazing Incidence X-Ray Diffraction, Glow Discharge Optical Emission Spectroscopy and Transmission Electron Microscopy has been used to get information about the structure and the composition of the anodic oxides, as described in the next Sections 3.3.3, 3.3.4 and 3.3.5. This *ex-situ* characterization was carried out in the Laboratory of Interfacial Electrochemistry of Hokkaido University. Finally, to test whether anodic oxides are suitable for ReRAM devices and to determine what are the performances of devices described in Section 3.1.3, Electrical Measurements were carried out at the Institut für Werkstoffe der Elektrotechnik 2 of the RWTH Aachen University, under the supervision of Dr. Ilia Valov.

3.3.1 Photocurrent Spectroscopy

Photocurrent Spectroscopy (PCS) is currently employed for the characterization of solid state properties of semiconducting and insulating materials, since the knowledge of their band gap is a prerequisite to any possible application in different fields such as solar energy conversion (photoelectrochemical and photovoltaic solar cells, photocatalysis) and microelectronics

(high-*k*, high band-gap materials).[83,84] As other optical techniques, PCS is a non-destructive technique based on the analysis of the electrochemical response (photocurrent or photo-potential) of the metal/oxide/electrolyte interface under irradiation with photons of suitable energy and intensity. At difference of other optical methods, PCS offers the further advantage that the photocurrent response of the anodic oxide or, more generally, semiconducting/insulating material is directly related to the amount of absorbed photons. This means that the technique is not demanding in terms of surface so that it can be also used on rough surfaces (e.g for monitoring long-lasting corrosion processes where changes of surface reflectivity are expected owing to possible roughening of metal surfaces covered by corrosion products).[43]

PCS is very useful, since it is able to provide information about some aspects already discussed in Section 2.2, and that are necessary to understand how the anodic oxides work in operation:

i. the energetics at the metal/oxide/electrolyte interface (oxide flat band potential determination, conduction and valence band edges location, internal photoemission threshold);
ii. the oxides electronic structure and indirectly (through the optical band gap/mobility gap values) chemical composition of the oxides *in situ*.[85,86]

Nevertheless, PCS presents also some limitations owing to the following aspects:

i. the technique is able to scrutinize only photoactive layers;
ii. the investigation of surface layers having optical band gap lower than 1 eV or larger than 5.5 eV requires special setup or they are experimentally not accessible in aqueous solutions;
iii. structural information and chemical composition of the layers are not accessible directly and complementary investigation based on other techniques can be required.

The first two limitations are rather apparent than real. With the exception of noble metals (Ir, Ru, etc.) which are covered by conducting oxides only at high electrode potentials, most of metals are thermodynamically unstable by immersion in aqueous solution and they become covered by oxide or hydroxide films having often insulating or semiconducting properties. Moreover, with the exception of very few oxides grown on metals of lower electronegativity, the most common oxides have band gap values largely lying within the optical window experimentally accessible by PCS.[44,47] The third limitation is the major one but it has been shown by different authors in the last years that PCS can provide indirectly compositional information once interpretative model of the photoelectrochemical behaviour of passive film/electrolyte interface is introduced, which accounts also for the complex electronic structure of amorphous materials.[83,87–90] Many papers and book chapters from Prof. Di Quarto's group can be read to have more details about this technique and which information are possible to get from PCS.[43–45,47,85,86]

PCS setup used for all the photoelectrochemical measurements in this Ph.D. work is shown in Figure 3.3. It is composed by a 450W UV-VIS xenon lamp coupled with a Kratos monochromator, which allows a monochromatic irradiation of the specimen that is filtered through a quartz window present in the cell. A two phase lock-in amplifier is coupled with a mechanical chopper (working at a frequency of 13 Hz).

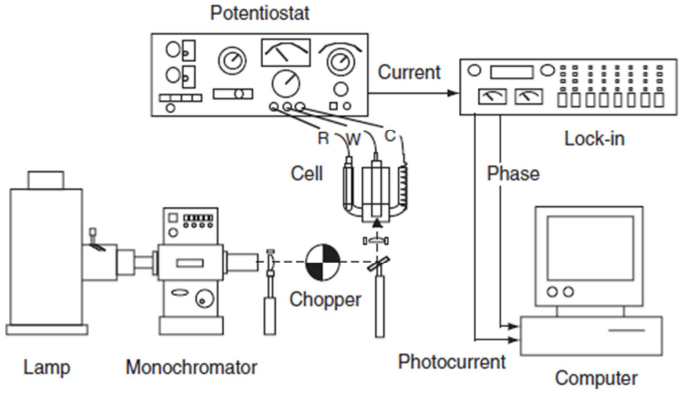

Figure 3.3 Schematic experimental setup employed for PCS studies.[47]

The use of a chopper together with a lock-in amplifier is necessary to extract weak photocurrent signals in presence of large dark current. When the photocurrent is measured by means of the lock-in technique, there is a periodically chopped photon flux. In this case, the lock-in measures a signal whose intensity depends on the ratio between the chopping angular frequency, ω_c, and the time constant of the electrical equivalent circuit of the junction, τ, including also the electrolyte resistance ($\tau = R_t C_t$, with R_t and C_t representing the total resistance and capacitance of the junction).[47]

All the photoelectrochemical measurements were carried out in 0.1 M ammonium biborate tetrahydrate electrolyte (ABE, $(NH_4)_2B_4O_7 \cdot 4H_2O$) (pH ~ 9) at room temperature. Photocurrent spectra were conducted at fixed U_E by recording I_{ph} every 15 s (i.e. every 5 nm according the rate with which the monochromator scans the wavelength) whilst photocharacteristics were recorded at fixed irradiating wavelength by scanning U_E toward cathodic direction at 10 mV s^{-1}. Current transients (OFF: dark, ON: light in the figures) were also recorded at fixed U_E and by chopping manually the irradiation of the samples.

3.3.2 Differential Capacitance Measurements and Electrochemical Impedance Spectroscopy

Differential Capacitance measurements and Electrochemical Impedance Spectroscopy (EIS) are very popular techniques for the characterization of semiconductor/electrolyte interfaces as well as in studying the electronic properties of semiconducting or insulating oxide thin films.[91,92] These methods involve the application of a small perturbation that can be of applied potential or of applied current but typically a potential perturbation of 10 mV is used. Electrochemical systems are usually strongly nonlinear systems thus, if a small perturbation is applied to the system, the cell response will be pseudo-linear. In this way, the current response to a sinusoidal potential will be a sinusoid at the same frequency but shifted in phase allowing application of a linear model for interpretation of spectra. The correct potential amplitude

represents a trade-off between the need to minimize nonlinear response (by using a small amplitude) and the need to minimize noise in the impedance response (by using a large amplitude). The amplitude depends surely on the system under investigation. For systems exhibiting a linear current-voltage curve, a very large amplitude can be used whilst for systems exhibiting very nonlinear current-voltage curves, a much smaller amplitude is needed.[93]

In Differential Capacitance measurements, the d.c. potential is swept typically (for a n-type semiconductor) from a strong anodic polarization (with respect to the flat band potential of the oxide film) to a polarization approaching the flat band potential, or even more cathodic when the oxide layer is so insulating that the current maintain low values also for cathodic polarization (blocking character to the hydrogen evolution reaction). The a.c signal frequency is fixed during the measurement. Typically the measurement is repeated for different a.c. signal frequencies in order to get reliable information on the electronic properties of the films, even though in many cases the study of the electronic properties is performed by using the Mott-Schottky analysis at only one frequency.[92,94,95]

EIS spectra are recorded by keeping constant the electrode potential and spanning the a.c. signal frequency in a range that is chosen to meet the dynamic response of the system under study. The challenge in the EIS data analysis is the choice of the electrical equivalent circuit to be employed in fitting the experimental data as well as on the physical meaning to attribute to the different passive elements of the electrical equivalent circuit. The physical understanding of the current paths and potential drops in the system serves to guide the structure of the corresponding electrical circuit. Most of the circuit elements in the model are common electrical elements such as resistors, capacitors, and inductors. The impedance response can be described as having real and imaginary components:

$$Z = Z_r + Z_j \qquad 3.1$$

When the input and output are in phase, the imaginary part of the impedance has a value of zero and the impedance has only a real contribution, Z_r. When the input and output are out of phase the real part of the impedance has a value of zero and the impedance has only imaginary contribution, Z_j. The relationship between the complex impedance and the phase angle is shown more clearly in the use of phasor diagrams and relationships, so that the impedance can be expressed as:

$$Z = |Z| \exp(j\Phi) \qquad 3.2$$

where |Z| represents the magnitude of the impedance vector and Φ represents the phase angle. The representation of impedance in terms of magnitude and phase angle as functions of frequency on a logarithmic scale are called Bode plots.[93]

The impedance of a resistor is independent of frequency and has no imaginary component. With only a real impedance component, the current through a resistor stays in phase with the voltage across the resistor. The impedance of an inductor increases as frequency increases. Inductors have only an imaginary impedance component and, as a result, the current through an inductor is phase-shifted 90 degrees with respect to the voltage. The impedance versus frequency behaviour of a capacitor is opposite to that of an inductor, so that impedance decreases as the frequency is raised. Capacitors also have only an imaginary impedance component so that the current through an capacitor is phase-shifted -90 degrees with respect to the voltage.

Another circuit element, the Constant Phase Element (CPE), Q, is often used in modelling the EIS spectra, most of the time to model the behaviour of a non-ideal capacitance. Generally speaking, when the assumption of a uniformly active electrode is not valid, a time-constant dispersion can be observed due to variation along the electrode surface of reactivity or of current and potential. The presence of time-constant (or frequency) distribution is frequently modeled by use of CPE element. The impedance of this element can be expressed as:[93]

$$Z_{CPE} = \frac{1}{(j\omega)^n Q} \qquad 3.3$$

with ω the angular frequency of the a.c. signal. It is important to mention that, for n = 1, the CPE behaves like a pure capacitor.

Unless otherwise stated, both Differential Capacitance measurements and EIS spectra were recorded in a 0.25 M Na_2HPO_4 solution (pH ~ 9) with a three-electrode configuration where the counter electrode was a Pt net with a very high surface area and the reference electrode was a silver/silver chloride electrode (0 V vs Ag/AgCl = 0.197 V vs SHE). The frequency range for EIS spectra was always 100 kHz – 100 mHz and the fitting procedure was performed with ZSimpWin software (Princeton Applied Research).

3.3.3 X-Ray Diffraction

X-Ray Diffraction, XRD, is a non-contact and non-destructive technique and it is the most widely used technique for crystalline materials characterization. Owing to the huge data bank available covering practically every phase of every known material (powder diffraction patterns), it is possible to identify phases in polycrystalline bulk material and to determine their relative amounts from diffraction peak intensities.[96]

X-rays are electromagnetic radiations with wavelengths of the order of 10^{-10} m. They are typically generated by bombarding a metal with high-energy electrons. The electrons decelerate as they fall into the metal and generate radiation with a continuous range of wavelengths called *Bremsstrahlung*. Superimposed on the continuum are a few high-intensity, sharp peaks. These peaks arise from collisions of the incoming electrons with the electrons in the inner shells of the atoms. A collision expels an electron from an inner shell, and an electron of higher energy drops into the vacancy, emitting the excess energy as an X-ray photon. If the electron falls into a K shell (a shell with $n = 1$), the X-rays are classified as K-radiation, and similarly for transitions into the L ($n = 2$) and M ($n = 3$) shells. Strong, distinct

lines are labelled Kα, Kβ, and so on.[97]

Crystals are composed of regularly spaced atoms which might act as scattering centers for X-rays and, being the X-rays electromagnetic waves of wavelength almost equal to the interatomic distance in crystals, it is possible to diffract X-rays by means of crystals. The condition for diffraction is:

$$n\lambda = 2d \sin\theta \qquad 3.4$$

being n an integer number, λ the wavelength of the incident X-ray, *d* is the distance between crystallographic planes and θ is the angle of incidence as shown in Figure 3.4.

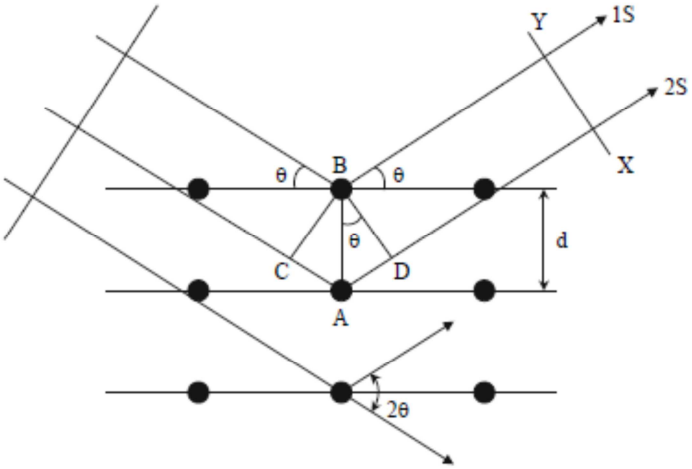

Figure 3.4 Diffraction of X-rays by a crystal.[98]

Equation 3.4 is called Bragg's law and states that the incident and diffracted beams are coplanar with the normal to the lattice planes and equally inclined at 90° – θ to it and that the angle θ (called the Bragg angle) is related to the X-ray wavelength and to the interplanar spacing.[98]

Therefore, X-ray diffraction principles are used to know if a material is crystalline or

amorphous and, if crystalline, which phases compose material. Practically, there are two main methods to characterize materials, Bragg-Brentano and Grazing Incidence, as shown in Figure 3.5.

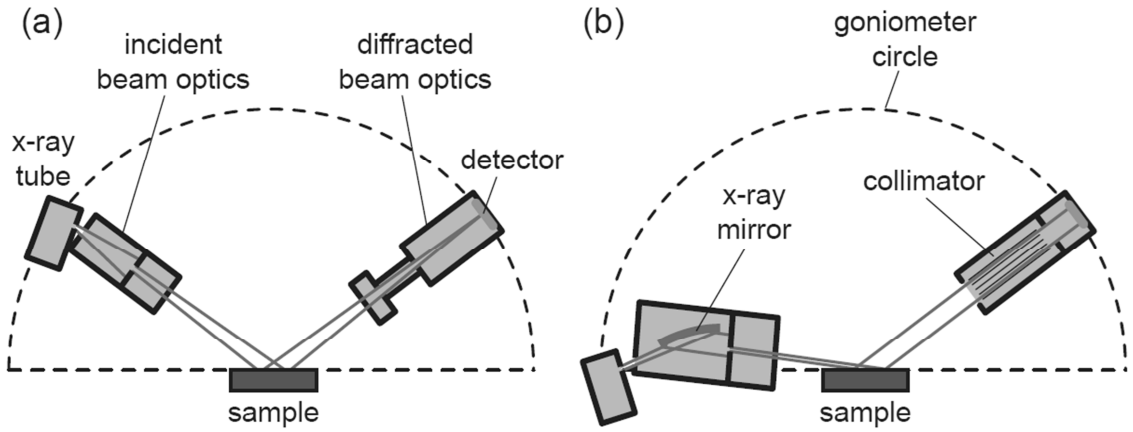

Figure 3.5 (a) Bragg-Brentano and (b) Grazing Incidence methods for X-Ray Diffraction.[99]

In the Bragg-Brentano (θ - 2θ) geometry (Figure 3.5(a)), tube and detector rotate with the same speed, maintaining symmetric scan conditions. In this way, only the crystallographic planes parallel to the surface sample can be detected, even though, most of the time, polycrystalline materials have a random crystals distribution. More important is that, when a thin film is characterized by the conventional θ - 2θ scan, diffraction signals from the film are much weaker than those from the substrate (e.g. metal layer in the case of anodic oxides) because the incident X-ray beam penetrates deeply into the substrate. Although the penetration depth varies with the symmetric sweep angle θ/2θ, it is generally much greater than the film thickness. Therefore, as in the case of thin anodic oxides, Grazing Incidence method (Figure 3.5(b)) is needed. With this geometry, only the detector rotates through the angular range, keeping the incident angle, the beam path length, and the irradiated area constant. The stationary incident beam makes a very small angle with the sample surface (typically 0.3° to 3°), which increases the path length of the X-ray beam through the film. This can enhance the diffraction intensity of an ultrathin film, while considerably reducing the

signal from the substrate at the same time. Since the path length is increased at Grazing Incidence, the diffracting volume of the film (i.e. its effective thickness) increases proportionally. As a result, there is a considerable improvement in the film's signal-to-background ratio. In this work, only GIXRD method was used, because of the low thickness (10 - 250 nm) of grown anodic oxides. These measurements have been carried out at Hokkaido University by using a Rigaku, RINT-2200 system: a Cu Kα radiation (λ = 0.15418 nm) was used with an incident angle of 1° at 40 kV and 20 mA over 20 - 90° as 2θ range with a step size of 0.02° and a scan rate of 2° min^{-1}.

3.3.4 Glow Discharge Optical Emission Spectroscopy

Glow Discharge Optical Emission Spectroscopy (GDOES) allows rapid depth profiling analysis of surface regions, from the first nanometers to depths of several tens of microns with excellent depth resolution and sensitivities for the detection of many elements. The specimen is sputtered through argon ions and is then excited in a low pressure plasma discharge and the resulting light emission is used to characterize and quantify the sample composition. The two mechanisms of sputtering and excitation are spatially separated. The sputtering phase is material dependent but the emission, taking place in the gas phase, is nearly independent from the material. Radiofrequency GDOES allows the analysis of both conducting and non-conducting specimens, whereas d.c. instruments are limited to the analysis of conducting samples.[100]

In this Ph.D. work, elemental depth profile analysis of the anodic layers was conducted by using a Jobin Yvon 5000 instrument in radiofrequency mode in the Laboratory of Interfacial Electrochemistry of Hokkaido University. A 4 mm diameter copper anode and high purity argon gas were used for the generation of plasma.

3.3.5 Transmission Electron Microscopy

Information about the structure of electrochemically prepared thin films were obtained by Transmission Electron Microscopy (TEM). Images obtained from electron microscopy, as

TEM, are due to the nature/degree of electron scattering from the constituent atoms of the sample. Electrons are easily absorbed by air, thus it is mandatory the use of ultrahigh vacuum (UHV) environments and they are scattered so much with the matter so that high sensitivity is got from the interaction of electrons with extremely small samples. Interaction between the electron source and atomic nuclei gives rise to elastic scattering, which results in a large-angle deflection of the electron beam with little or no energy loss, and gives information about the structure of the specimen. In contrast, electron-electron interactions between the source and electron clouds of individual atoms cause small-angle deflections with a significant loss of energy, known as inelastic scattering, giving information about the atomic species present in the specimen. In particular, by operating with a microscopy in transmission mode, the intensity from an electron source after it has passed through a transparent sample is measured. The relative degree of penetration through a particular sample is governed by the energy of the electron source. Higher energy electrons (e.g. 200 keV) will be more penetrating, allowing for the characterization of thicker and/or less transparent samples. Generally speaking, increasing the thickness of a sample, or decreasing the energy (i.e. accelerating voltage) of the electron beam, will induce more scattering events through more effective interactions between the electron beam and atoms of the sample. This effect will enhance image contrast, since there is a larger deviation between the path lengths of transmitted and scattered electrons that reach the viewing screen.[101] Since transparent samples are needed, specimen thickness has to be less than 200 nm in thickness,[102] but practically slices of < 40 nm in thickness are used. If the transmitted electrons do not come from a static beam but from a focused electron beam with a high current density and small diameter that is scanned across the sample, the microscope is called Scanning Transmission Electron Microscope (STEM). In this work, three different STEMs were used: a JEOL, JEM-ARM-1300 STEM operating at 1250 kV, a FEI, Titan3 G2 60-300 STEM operating at 300 kV and a HD-2000 Hitachi STEM operating at 200 kV. All the TEM observations were carried out at Hokkaido University with the collaboration of research group of Prof. Habazaki.

Most of the time, ultramicrotomy was used to prepare cross-sections of the different

investigated samples, with Al/alumina as substrate of the metal/anodic oxide junction. First of all, 0.2 × 1 cm samples were encapsulated in an epoxy resin, composed by four components: 1.5 ml of Epon 812 (a glycerol based aliphatic epoxy resin), 0.7 ml of DDSA (dodecyl succinic anhydride, hardener), 1.0 ml of MNA (methyl nadic anhydride, hardener) and 0.075 ml of DMP30 (2,4,6-tridimethyl amino methyl phenol, accelerator). The resin was then hardened in oven for at least 8 h at 60 °C. Afterwards, one side of the piece was cut into a V-shape along its long axis by mechanical polishing, leaving finally a small cross-sectional area, 100 μm wide and 2 mm long, at the top of V-shaped specimen. This was then rinsed with distillate water to remove residues of polishing materials and fixed to the sample holder of the ultramicrotome. The top of V-shaped specimen was trimmed initially with a glass knife as shown in Figure 3.6.

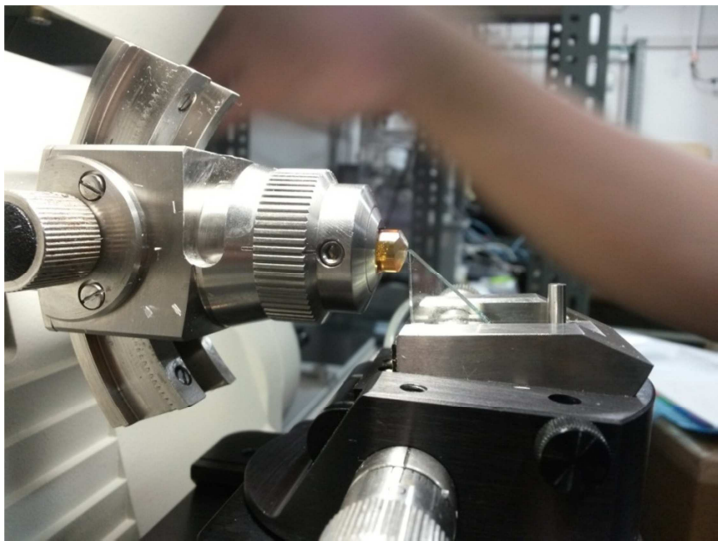

Figure 3.6 Trimming of the specimens with the ultramicrotome by using a glass knife.

In this phase it is essential that the sample should be oriented such that the cutting direction is approximately parallel to the oxide/metal interface to avoid detachment of the coating and substrate.[103] Finally, the cross sections of the samples were obtained by cutting the tips of trimmed specimens with a diamond knife. A RMC PT-X PowerTome Ultramicrotome was employed to prepare the sections in this study. The resulting specimen sections floated onto

the water meniscus above the diamond knife and were collected on copper grids. In the case of anodic oxides with glass/metal as substrate, a Hitachi FB-2100 FIB system employing a Ga^+ ion beam was used to prepare the cross sections. Prior to ion beam preparation, the surfaces were coated with a Pt layer to avoid any anodic oxides damage.

3.3.6 Electrical Measurements

Electrical Measurements were carried out at IWE 2, RWTH Aachen University, under the supervision of Dr. Ilia Valov. This characterization aimed to check, first of all, if metal/anodic oxide/Pt junction show resistive switching phenomena and, after that, determine the devices performances. As described in Section 3.1.3, top electrode was Pt for all the measurements and, unless otherwise mentioned, it was always grounded with the voltage applied on the bottom electrode (i.e. metal substrate that was previously anodized).

Typical electrical measurements comprise *I-V* sweeps, Cyclic Voltammetries (CV) and pulsed measurements such as the retention test, the endurance test and fast pulses measurements.

I-V sweeps are used to detect resistive switching phenomena and are performed usually by using a Keithley 2636 A System SourceMeter. Although the Keithley 2636 A can automatically adjust current and voltage ranges, it was recommended to preset these ranges to avoid switching between different ranges during the measurements. It was always chosen a current compliance (in the range between 20 μA and 10 mA) to avoid damage of the memory cells in the low resistance state.

Since ReRAM devices are based on redox reactions at both electrode/solid electrolyte interfaces (see Section 2.3), CVs were used to reveal redox reactions prior to any resistive switching in order to understand what species are involved in the switching phenomenon.[69,104,105] Cyclic Voltammetry is typically used in electrochemistry to understand what species are oxidizing and reducing by sweeping electrode potential with a forward and a reverse scan.[106] The use of a three-electrode configuration, i.e. using a reference electrode, is necessary. In the case of solid state devices, such as ReRAM devices, the use of a reference electrode is not simple as for liquid electrolyte so that the two-electrode configuration was

used, where the potential of the counter electrode (i.e. Pt) was used as a quasi-reference electrode. CVs were performed by using a Keithley 6430 Sub-FemtoAmp Remote SourceMeter because of its current resolution < 1 fA. These measurements were carried out in ambient atmosphere with different sweep rates (i.e. mV s^{-1}) in order to better resolve redox reactions peaks.

In order to investigate devices switching kinetics as well as durability and stress performances, pulsed measurements were carried out. Retention and endurance tests were performed by using a Keithley 2636 A System SourceMeter, in which the minimum pulse time was 2.5 ms whilst for switching kinetics (i.e. fast pulses measurements) a Keithley 4200-SCS Semiconductor Characterization System was employed to reach also 1 μs as pulse time.

How the voltage was applied in every single electrical measurement is sketched in Figure 3.7.

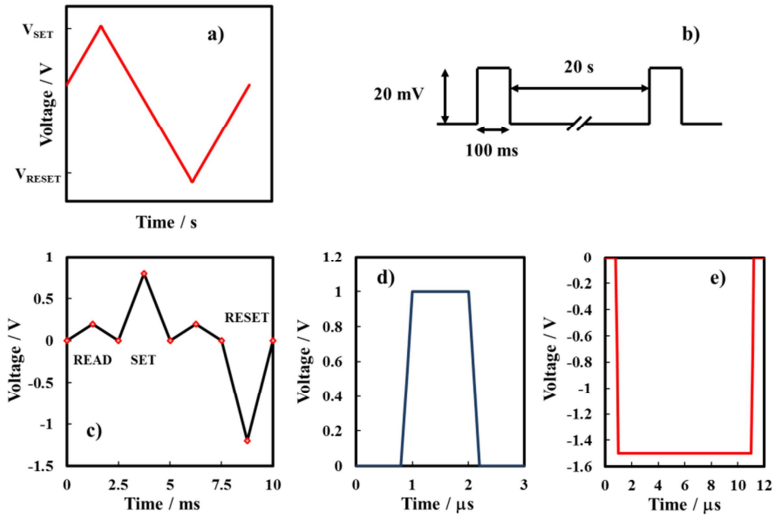

Figure 3.7 (a) *I-V* sweep; (b) retention test; (c) endurance test; (d) SET and (e) RESET pulses.

4 The Influence of the Anodizing Bath Composition on the Solid State Properties of the Anodic Oxides

As previously discussed in Section 2.1.2, the anodic oxides growth results to occur due to simultaneous migrations of metal cations M^{z+} outwards and oxygen anions O^{2-} inwards proceeding in a cooperative manner, developing film material both at the anodic film/electrolyte and metal/anodic film interfaces respectively. However, anodic layers structure and composition are strongly dependent upon the used electrolyte due to possible incorporation of foreign species from the anodizing bath.[107–109] This is a very important aspect because the presence of foreign species in anodic films could affect the electronic properties of the films with possible detrimental effects on dielectric properties of the oxides. Moreover, it was shown that during the anodizing process in ammonium-containing electrolytes of valve metals such as Nb, Ta and Ti, N incorporation occurs, with significant effects on the solid state properties of the corresponding oxides.[110–112] It is noteworthy to mention that, in the case of tantalum, such incorporation is reported to occur only when the anodizing electrolyte pH was higher than the pH of zero charge (pH_{pzc}) of Ta_2O_5, since negatively charged oxide surface allowed ammonium cations reaching the film and being de-protonated by the imposed electric field strength.

High-*k* anodic oxides grown on Al-Ta alloys in ammonium-containing anodizing bath were chosen as the suitable system to study if the incorporation of foreign species leads to a change in the solid state properties of the oxides. The choice is motivated from the fact that, the same anodic oxides but grown in borate buffer solution (i.e. ammonium-free bath) were already studied[113] so that it is possible to make a reliable comparison and to understand what is the effect of the anodizing bath composition on the solid state properties of the anodic layers.

Al-Ta alloys with various compositions (10, 18, 20, 30, 42, 62, 81, 91 at % of Ta) were prepared by magnetron sputtering on glass substrates as discussed in Section 3.1.2. Mixed Al-Ta oxides were grown potentiodynamically up to 20 V vs Hg/HgO (see Section 3.2) in two different solutions: a borate buffer (0.42 M H_3BO_3, 0.08 M $Na_2B_4O_7$) (pH = 8) and a 0.1 M ABE (pH ~ 9). Anodic layers were then characterized through X-Ray Reflectivity (XRR),

GDOES Spectroscopy (see Section 3.3.4), PCS (see Section 3.3.1) and Impedance measurements (see Section 3.3.2).

4.1 Anodic Oxides Growth

In Figure 4.1(a) the growth curve relating to the anodizing of Al-91at.%Ta alloy is reported. As typical of anodic oxides growth on valve metals, after an abrupt increase, the current density reaches an almost constant value, which is a function of the metallic substrate composition. The growth efficiency of the anodizing process for all the investigated alloys, as defined by Equation 2.6, is close to the unity since i_{diss} is expected to be negligible for all the oxides according to the Pourbaix diagrams relating to Al and Ta,[114] and i_{el} is negligible due the blocking character of the oxides, as confirmed by the very low current circulating during the reverse scan (see Figure 4.1(a)).

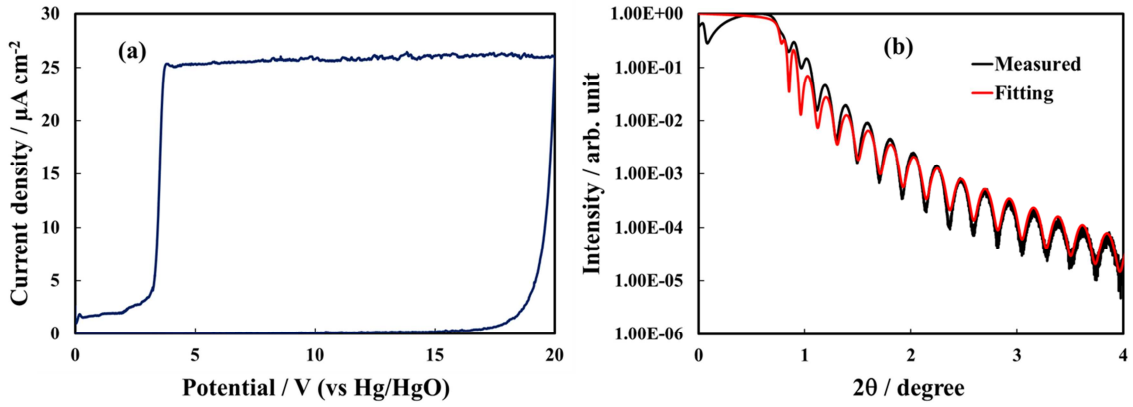

Figure 4.1 (a) Current density vs potential curve recorded during the growth of anodic film on Al-91at.%Ta alloy. (b) X-Ray Reflectivity spectrum relating to the same oxide. Fitting parameters: density = 8.5 g cm^{-3}, thickness = 37 nm, roughness = 0.33 nm.

In Figure 4.1(b) the XRR spectrum relating to Al-91at.%Ta anodic film is reported. The resulting angle-dependent curve, which is correlated to changes of the electron density in the sample, was fitted with a triple layer model (SiO_2/Alloy/Oxide). The fitting procedure allowed to estimate a film thickness very close to that estimated from the anodizing ratio (see Table 4.1), and a density which is very close to that reported for pure anodic Ta_2O_5[34] with

roughness in order of few Å. The roughness factor resulted between 0.3 and 0.5 nm for the investigated samples.

Table 4.1 Thickness of the anodic layers estimated according to the anodizing ratios reported in literature.[34,115]

Base alloy	Thickness / nm
Al	24
Al-10at.%Ta	24.5
Al-18at.%Ta	25
Al-20at.%Ta	25
Al-30at.%Ta	26
Al-42at.%Ta	27
Al-62at.%Ta	29
Al-81at.%Ta	30.5
Al-91at.%Ta	31
Ta	32

Oxide thickness increases due to chemical reaction between Ta^{5+}, Al^{3+} and O^{2-}. Mobile cationic species are produced at the metal/oxide interface and migrate outward toward the oxide/electrolyte interface. Mobile anionic species are produced at the oxide/electrolyte interface and migrate inward. In aqueous solution, where water molecules might be expected to adhere to the film with negatively charged oxygen atom adjacent to the oxide surface, mobile anionic species are mainly O^{2-} and OH^- ions derived from water de-protonation.[18,19] The OH^-, once incorporated, are converted to O^{2-} ions and protons, with H^+ migrating out of the film under the high electric field strength. If large oxyanions are present in the anodizing bath (e.g. biborate), hydrogen bonds can be formed between H of water molecules and O of such oxyanions (see Figure 4.2) with a consequent weakening of O-H covalent bonds in H_2O and, thus, easier de-protonation.

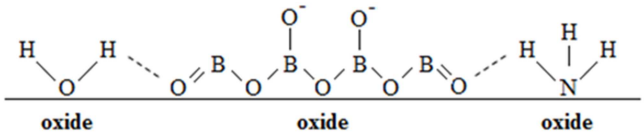

Figure 4.2 Absorption of water and biborate molecules at oxide surface.

However, it was proved that other anionic species, A^{y-}, of the anodizing bath can be also incorporated during the anodizing process, leading to the formation of oxides containing foreign species.[116] More specifically, incorporation of several inorganic[117] and organic[118] anions has been reported during the anodizing of Al, while incorporation of several ions has been proved during the anodizing of Ta.[119] Recently, it has been also demonstrated that N incorporation occurs during the anodizing of tantalum in ammonium biborate solutions, provided that the electrolyte pH is higher that the pH of zero charge (pH_{pzc}) of the oxide. In the latter case oxide surface is negatively charged, thus allowing NH_4^+ ions to approach the oxide/electrolyte interface and to be de-protonated generating NH_{3-x}^{x-} moieties that are incorporated into the anodic film with the consequent formation of a N-doped anodic oxide.[111] In Figure 4.3 GDOES elemental depth profiles relating to anodic films grown to 20 V in 0.1 M ABE on Al-10at.%Ta, Al-42at.%Ta and Al-81at.%Ta alloys are reported. N signal is weak but present across the whole film thickness, thus confirming that nitrogen incorporation occurs also during the anodizing of Al-Ta alloys. The pH of zero charge, pH_{pzc}, of aluminium and tantalum oxide are of ~ 9.5 and 2.9 respectively,[120,121] thus it is supposed that the higher is Al content into the oxide, the lower is the extent of the N incorporation phenomena.

Formation of NH_{3-x}^{x-} moieties is assisted by weakening of the N-H bond as depicted in Figure 4.2 since, due to the large electronegativity of nitrogen, formation of hydrogen bonds between H of ammonia and O of oxyanions (i.e. -NH···O) can also occur. As occurs for OH^-, NH_{3-x}^{x-} can lose protons and being finally incorporated into the anodic films as N^{3-} ions. N-H dissociation energy in ammonia (388 kJ mol^{-1}) is lower than O-H dissociation energy in water (463 kJ mol^{-1}). Moreover, ionic radii of NH_2^- and N^{3-} (0.173 nm and 0.171, respectively)[122,123] are close to that of O^{2-} and OH^- (0.140 nm and 0.153 nm, respectively) and even lower than

that of oxyanions, whose incorporation has been proved in literature (e.g. 0.238 nm for PO_4^{3-} and 0.230 nm for SO_4^{2-}).[119] Thus, it is likely that a oxynitride or N-doped oxide can be formed during anodizing process without significant structural problems, considering that the films are amorphous and that according to the literature the only effect of nitridation of crystalline tantalum oxide is an expansion of the lattice, due to the smaller ionic radius of O^{2-} (0.140 nm) with respect to N^{3-} (0.171 nm).[124] Such expansion is also reported to occur for N-doped Ta_2O_5 and in spite of this, a crystalline stable phase is formed.

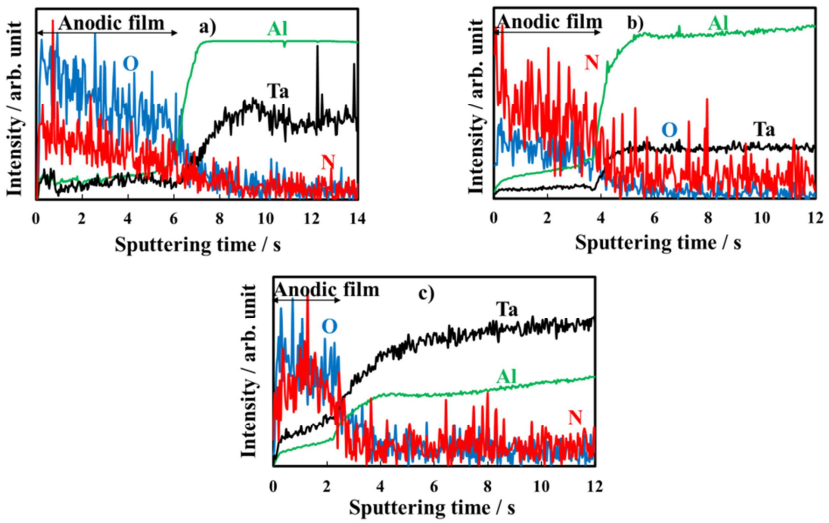

Figure 4.3 GDOES depth profiles of the anodic films grown to 20 V on (a) Al-10at.%Ta, (b) Al-42at.%Ta and (c) Al-81at.%Ta alloys in 0.1 M ABE.

4.2 Impedance Measurements

In order to get information on the dielectric properties of the investigated oxides, electrochemical impedance spectra and differential capacitance curves were recorded. In Figure 4.4 the EIS spectra, recorded at U_E = 5 V vs Hg/HgO (i.e. at potential more anodic than the corresponding flat band potential, see below), are shown in Modified Bode representation relating to the anodic films grown on Al-42at.%Ta, Al-62at.%Ta and Al-91at.%Ta alloys in 0.1 M ABE and borate buffer to 20 V.

It is important to note that no significant differences are found in EIS spectra due to the

anodizing bath composition. The high |*Z*| and a phase angle very close to -90°, confirm the formation of blocking oxides. Spectra can be simulated by the electrical circuit reported in Figure 4.4(d), where R_{el} is the electrolyte resistance (employed to get the Modified Bode representation), R_{ox} is the anodic film resistance and Q_{ox} is a Constant Phase Element (CPE) introduced to model the oxide capacitance.

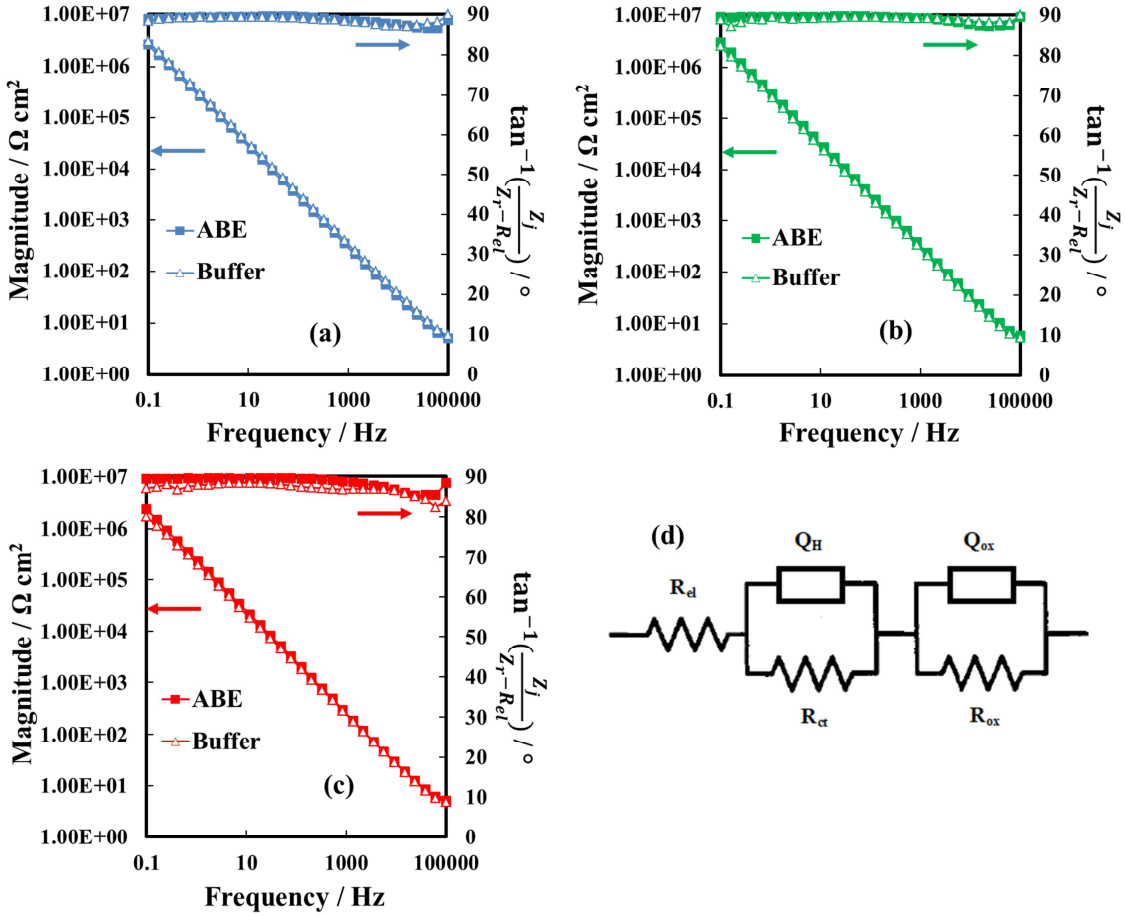

Figure 4.4 EIS spectra relating to anodic films grown on (a) Al-42at.%Ta, (b) Al-62at.%Ta and (c) Al-91at.%Ta alloys in ABE and borate buffer, recorded by polarizing the film at 5 V vs Hg/HgO. (d) Electrical equivalent circuit employed to model metal/oxide/electrolyte interfaces.

Another RQ parallel was inserted to model the electrochemical reaction, where R_{ct} is the charge-transfer resistance and Q_H the non ideal Helmholtz double layer capacitance. This

equivalent circuit very well fits the experimental data relating to all the investigated anodic layers grown in 0.1 M ABE, with the fitting parameters reported in Table 4.2. The very high R_{ox} values and n very close to 1 suggest that the oxides behave like ideal capacitors. It is interesting to mention that very high R_{ct} were estimated, as expected for blocking interface, and Q_H allowed to estimate double layer capacitance very close to 20 μF cm^{-2}, the value reported in the literature for aqueous solutions.[92]

Table 4.2 Fitting parameters relating to EIS spectra of the all investigated anodic films using equivalent electric circuit of Figure 4.4(d).

Base alloy	R_{el} / Ω cm^2	R_{ct} / Ω cm^2	Q_H / S s^n cm^{-2}	n	R_{ox} / Ω cm^2	Q_{ox} / S s^n cm^{-2}	n
Al	14	1×10^4	2.1×10^{-5}	0.82	1×10^5	4.3×10^{-7}	1
Al-10at.%Ta	15	1×10^6	2.3×10^{-5}	0.85	1×10^8	4.4×10^{-7}	0.99
Al-18at.%Ta	14	1×10^6	2.1×10^{-5}	0.80	1×10^8	5.4×10^{-7}	1
Al-20at.%Ta	39	1×10^6	2.4×10^{-5}	0.87	1×10^9	4.2×10^{-7}	0.99
Al-30at.%Ta	26	1×10^6	2.5×10^{-5}	0.88	9×10^9	4.4×10^{-7}	0.99
Al-42at.%Ta	20	1×10^6	2.2×10^{-5}	0.88	1×10^8	6.2×10^{-7}	0.99
Al-62at.%Ta	24	1×10^6	2.2×10^{-5}	0.85	1×10^8	5.4×10^{-7}	0.99
Al-81at.%Ta	23	1×10^6	2.0×10^{-5}	0.82	1×10^8	7.8×10^{-7}	1
Al-91at.%Ta	27	4×10^6	2.2×10^{-5}	0.95	1×10^9	6.9×10^{-7}	0.99
Ta	39	1×10^6	2.2×10^{-5}	0.88	1×10^8	8.5×10^{-7}	1

In Figure 4.5(a) the Differential Capacitance measurements, recorded at f = 1 kHz, for all the investigated anodic oxides are reported. It is evident that the measured capacitance, C_M, is almost potential independent and slightly dependent on frequency, as expected for amorphous insulating materials.[125] A comparison with the capacitance of 20 V anodic films on Al-Ta alloys grown in borate buffer solution shows that no appreciable differences are evident on the overall impedance (see Figure 4.5(b),(c),(d)). This suggests that the presence of N into the oxide causes the formation of deep localized states, thus at energy level so far from the conduction band mobility edge that they cannot contribute to the measured capacitance in the range of investigate frequencies. This is agreement with previous experimental findings on the

effect of nitrogen incorporation during the anodizing of Ta and Ti,[111,112] which is reported to induce formation of localized states close to the valence band mobility edge.

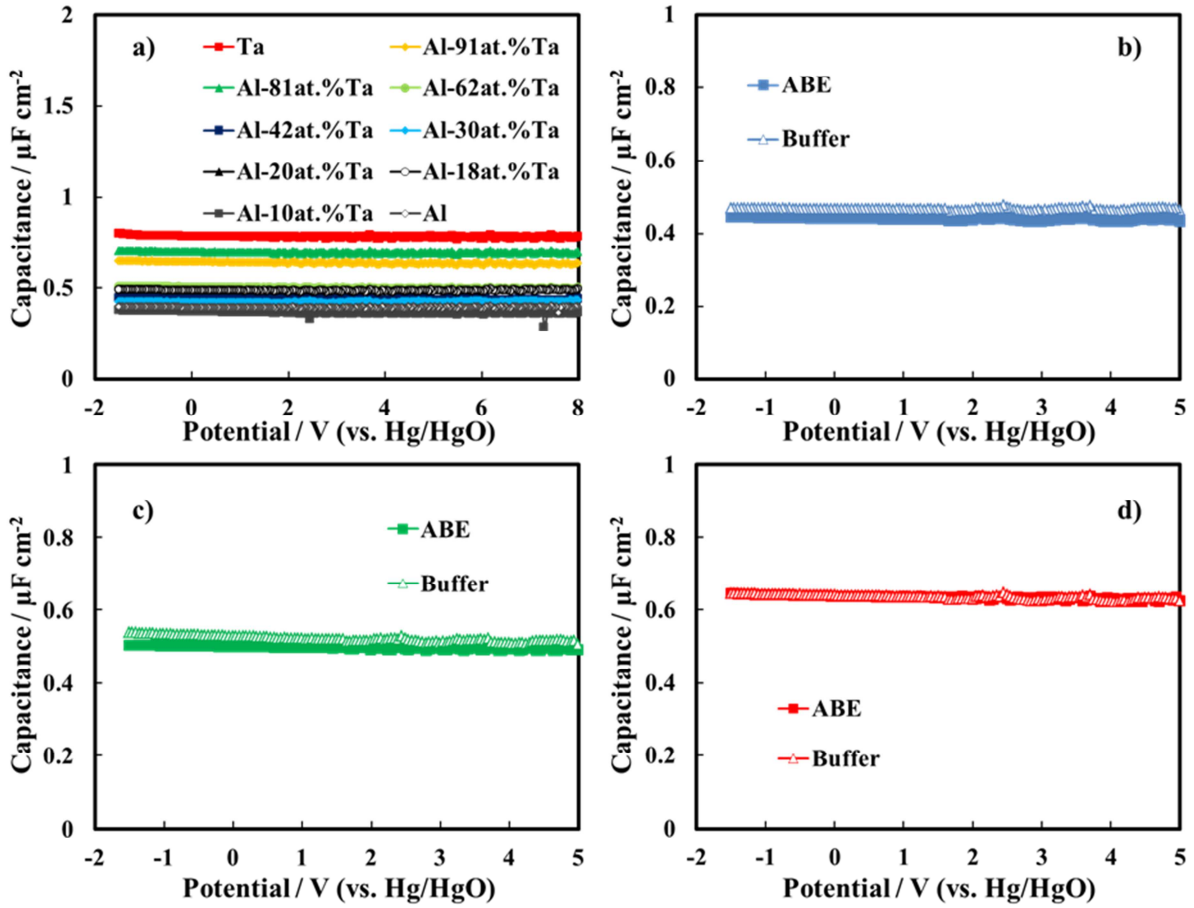

Figure 4.5 (a) Measured series capacitance relating to all the anodic oxides grown in ABE. Measured series capacitance relating to the anodic films grown on (b) Al-42at.%Ta, (c) Al-62at.%Ta and (d) Al-91at.%Ta alloys in ABE and borate buffer. a.c. signal frequency: 1 kHz.

Provided that the equivalent circuit of Figure 4.4(d) well simulates the impedance of the overall metal/oxide/electrolyte interface, it is easy to extract the oxide capacitance from C_M. Assuming that C_{ox} can be described by a parallel plate capacitor model:

$$C_{ox} = \frac{\varepsilon\varepsilon_0}{d_{ox}} \qquad 4.1$$

where ε_0 (8.85×10^{-14} F cm^{-1}) is the vacuum permittivity, ε the film relative permittivity and d_{ox} its thickness. Whereas there are no differences in anodic film growth with respect to anodizing solutions, oxides thicknesses reported in Table 4.1 can be considered in calculating ε for the oxides grown in 0.1 M ABE. Dielectric constants are reported in Table 4.3 and the values are in very good agreement with that reported for the oxides grown in borate buffer.[113]

Table 4.3 Anodic films dielectric constants estimated from Differential Capacitance measurements.

Base alloy	Dielectric constant
Al	9
Al-10at.%Ta	10
Al-18at.%Ta	14
Al-20at.%Ta	12
Al-30at.%Ta	13
Al-42at.%Ta	14
Al-62at.%Ta	16
Al-81at.%Ta	24
Al-91at.%Ta	23
Ta	29

4.3 Photoelectrochemical Measurements

In order to study the influence of N incorporation on the solid state properties of the oxides, photoelectrochemical measurements were also carried out. Anodic photocurrent spectra (normalized for the maximum value of I_{ph}) relating to the anodic film grown on Al-62at.%Ta alloy in both solutions, recorded by polarizing the electrodes at 5 V vs Hg/HgO, are reported in Figure 4.6(a).

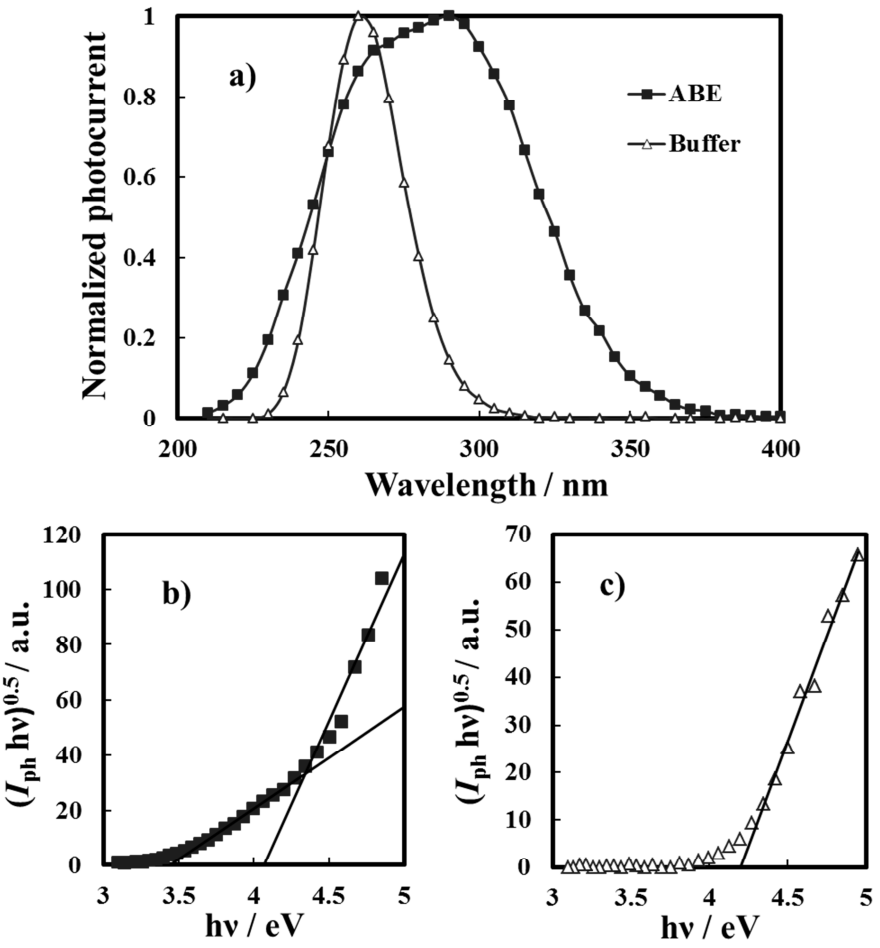

Figure 4.6 Anodic photocurrent spectra (a) relating to anodic films grown on Al-62at.%Ta alloy in ABE and borate buffer. Band gap estimate by assuming non direct optical transitions relating to the same anodic films grown in ABE (b) and borate buffer (c).

An evident redshift in the optical absorption threshold is present for the anodic film grown in 0.1 M ABE, while no photocurrent is detected for $\lambda \geq 310$ nm in the spectrum relating to the oxide grown in borate buffer. From photocurrent spectrum (see Section 2.2), it is possible to estimate the optical band gap value of the investigated anodic films according to Equation 2.16, assuming that I_{ph} is proportional to the light absorption coefficient and taking to account n value equal to 4 as for non direct optical transitions. As discussed in Section 2.2, due to the amorphous structure of the investigated oxides, presence of allowed localized states inside the gap is predicted according to several models of density of states distribution thus it is more

appropriate to call the optical band gap as the mobility gap of the anodic layers.

An E_g^m of 4.2 eV has been estimated for the anodic film grown in buffer, as shown in Figure 4.6(c), which is slightly lower than that estimated for thinner oxides (i.e. formation potential = 10 V).[113] For the oxide grown in the ammonium-containing solution (Figure 4.6(b)) by extrapolating to zero the $(I_{ph}h\nu)^{0.5}$ vs hν plot, it was possible to estimate an E_g^m of ~ 4.1 eV but a long photocurrent tail is also present ending at 3.4 eV. The latter is due to optical transitions involving allowed states in the mobility gap of the oxide, generated by N incorporation.

The same photoelectrochemical behaviour was shown by anodic films grown on Al-Ta alloys with a Ta content ≥ 42 at.%, (see Figure 4.7), while for oxide grown on Al-20at.%Ta there is no evidence of photocurrent at energy lower than E_g^m of the oxide. It is noteworthy to mention that no anodic photocurrent was measured for anodic films grown on Al-Ta alloys with a lower Ta content.

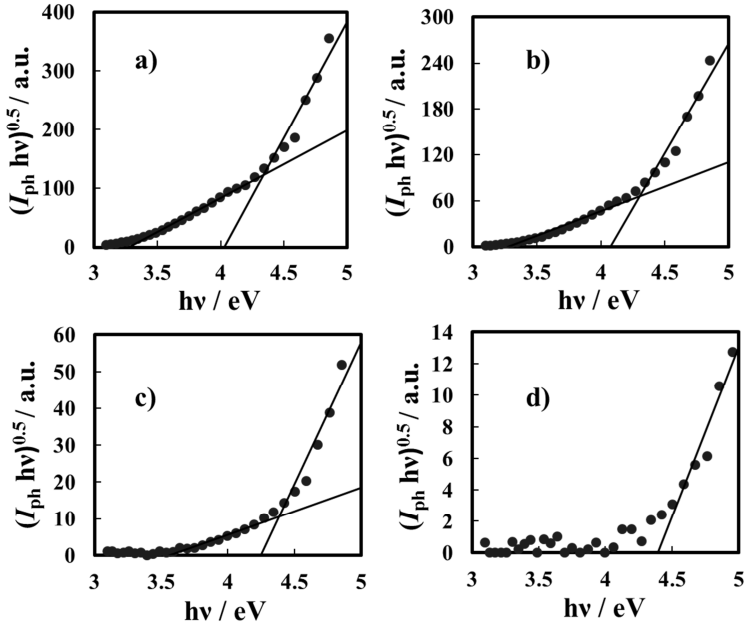

Figure 4.7 Band gap estimate by assuming non direct optical transitions relating to anodic films grown on (a) Al-91at.%Ta, (b) Al-81at.%Ta, (c) Al-42at.%Ta, and (d) Al-20at.%Ta alloys in ABE.

The dependence of the measured photocurrent on the applied potential, i.e. on the electric field strength across the films, has been also studied. In Figure 4.8(a) the I_{ph} vs U_E curves (photocharacteristics) for the anodic films grown on Al-62at.%Ta in both ABE and borate buffer, recorded at λ = 270 nm (hν = 4.58 eV), are shown. As it will be better discussed in the Section 4.4, the shape of I_{ph} vs U_E curves suggests the occurrence of recombination phenomena for both films grown in ABE and borate buffer. As expected for insulating films, by scanning the electrode potential toward the cathodic direction, a clear inversion of the photocurrent sign was revealed, as confirmed by a sharp change in the photocurrent phase angle (not shown). In the case of insulating materials both anodic and cathodic photocurrent can be measured when polarizing potential is more anodic and more cathodic than the flat band potential, U_{FB}, of the oxide, respectively.

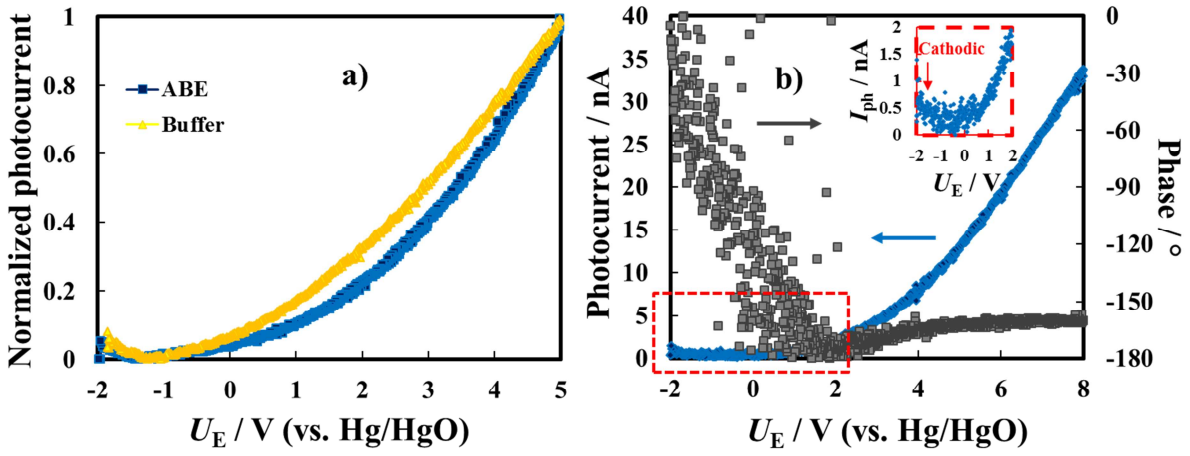

Figure 4.8 (a) Photocurrent vs potential curves relating to anodic films grown on Al-62at.%Ta alloy in ABE and borate buffer. (b) Photocharacteristic relating to the same oxide grown in ABE recorded at λ = 330 nm. Potential scan rate: 10 mV s^{-1}.

In order to estimate U_{FB} for the investigated layers, current vs time measurements were carried out under constant irradiating wavelength and manually chopping the irradiation. Figure 4.9 shows current transients relating to the anodic film grown on Al-91at.%Ta alloy in ABE at two different polarizing potentials. Under strong anodic polarization, i.e. at 8 V vs Hg/HgO (see Figure 4.9(a)), soon after irradiation the current reaches an almost stationary

value for all the investigated wavelengths (up to λ = 360 nm).

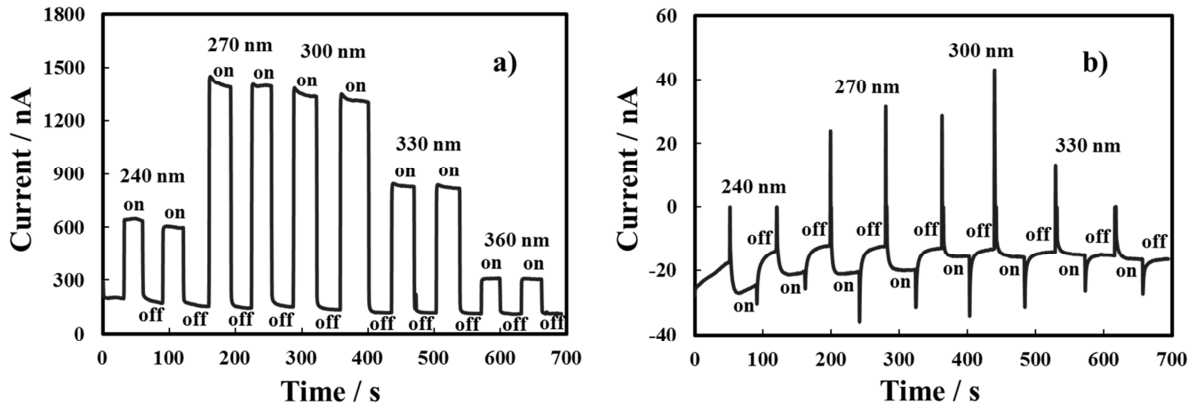

Figure 4.9 Total current circulating under irradiation (on) and in the dark (off) in the oxide grown on Al-91at.%Ta alloy in ABE, by polarizing the electrode at 8 V (a) and – 0.8 V (b) vs Hg/HgO at different wavelengths.

At U_E = - 0.8 V vs Hg/HgO (see Figure 4.9(b)), in spite of the presence of anodic photocurrent spikes soon after irradiation, stationary photocurrent is cathodic, thus suggesting that U_{FB} is more anodic than - 0.8 V vs Hg/HgO. At this electrode potential, the electric field is not high enough to avoid photocarriers recombination preventing cathodic photocurrent detection at λ = 360 nm, i.e. at photon energy lower than the oxide mobility gap.

U_{FB} values estimated from current vs time transients for anodic films grown on alloys with Ta content ≥ 62at.% are reported in Table 4.4. For anodic films grown in 0.1 M ABE with a Ta content ≥ 62at.%, it was possible to record photocharacteristics under illumination with photons corresponding to hν lower than their mobility gap. In Figure 4.8(b) the I_{ph} vs U_E curve recorded at λ = 330 nm (i.e. hν = 3.75 eV) for the anodic film grown on Al-62at.%Ta in ABE is shown. I_{ph} decreases during the potential scan toward cathodic direction and for U_E < U_{FB} cathodic photocurrent is measured, as evidenced in the magnified area of the plot. Thus, photocurrent spectra were recorded at potential lower than U_{FB} (i.e. at -1.5 V vs Hg/HgO), as shown in Figure 4.10(a) for oxides grown on Al-62at.%Ta alloy in both ABE and borate buffer solutions.

Table 4.4 Flat band potential values estimated by recording current transients under constant irradiating wavelength relating to the anodic oxides with a Ta content ≥ 62at.%.

Base alloy	U_{FB} / V vs Hg/HgO
Al-62at.%Ta	-0.70
Al-81at.%Ta	-0.75
Al-91at.%Ta	-0.70
Ta	-0.65

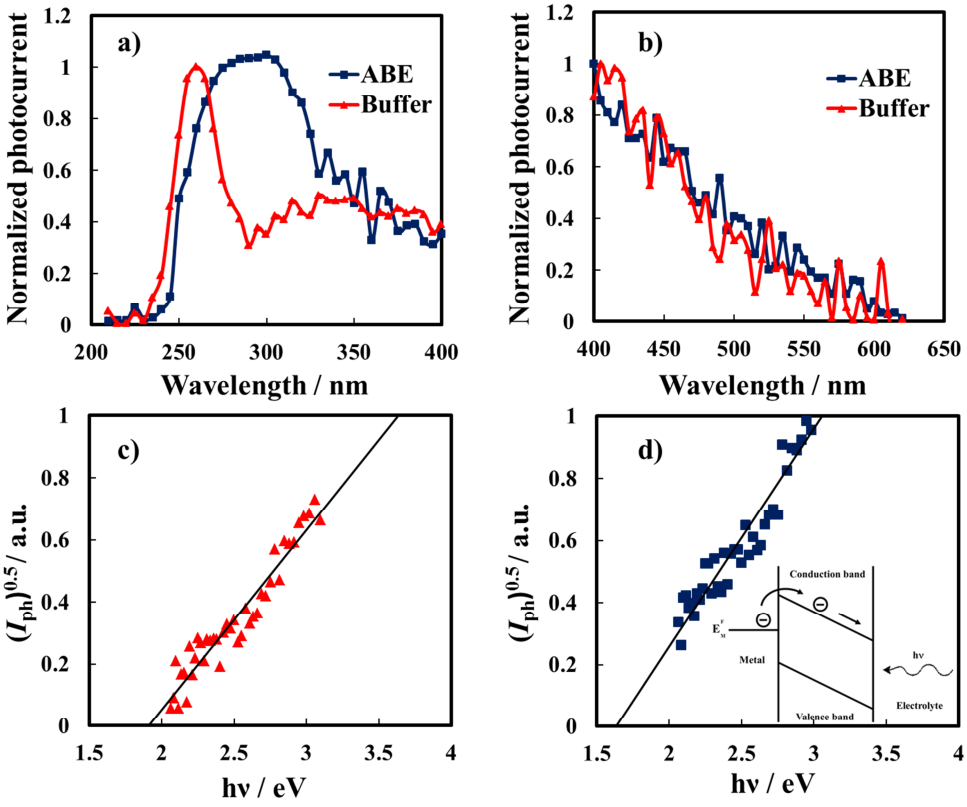

Figure 4.10 (a) Cathodic photocurrent spectra relating to the oxides grown on Al-62at.%Ta alloy in ABE and borate buffer recorded at – 1.5 V vs. Hg/HgO. (b) Long wavelength region of the photocurrent spectra, recorded by using a UV filter. Fowler plots relating the oxide grown in (c) buffer and in (d) ABE. Inset: electrons internal photoemission from metal Fermi level.

As already found for several insulating oxides[126–129] as well as for thinner films grown in ammonium-free electrolyte on Al-Ta alloys,[113] a long photocurrent tail appears that has been

explained by electrons injection processes from the alloy Fermi level to the oxide conduction band (see the inset of Figure 4.10(d)).

The threshold energy, E_{th}, associated to this process can be estimated according to Fowler's law (Equation 2.21) from the long wavelength region of the photocurrent spectra, corresponding to $\lambda \geq 400$ nm, which has been recorded using a 400 nm cut off filter to avoid doubling effect (see Figure 4.10(b)). The same internal photoemission process occurs for the anodic film grown in ABE with a Fowler threshold almost coincident with that estimated for N-free oxide. This experimental finding further supports that N incorporation induces formation of allowed states close to valence band mobility edge of the anodic films without significant effects on the DOS distribution close to the conduction band mobility edge.

4.4 Modelling of the Photocurrent vs Electrode Potential Curves

In the frame of Butler-Gärtner model, for crystalline insulating films, a linear dependence of the measured photocurrent on the applied potential is expected in absence of trapping phenomena, which can modify the electric field distribution across the layer (see Section 2.2 by substituting the width of the space charge region, x_{SC}, to the total oxide film thickness, d_{ox}). However, for both anodic films grown in ABE and buffer, such dependence is not linear supporting the presence of recombination phenomena. For amorphous materials the lack of long range order induces the formation of allowed localized states close to the mobility edge of the oxide, in agreement with the Mott and Davis model discussed in Section 2.2.[40] Thus, together with surface and bulk recombination phenomena expected for both crystalline and amorphous materials, it is needed to account for the occurrence of geminate recombination phenomena which reduce the efficiency of free carrier generation for amorphous anodic film on Al-Ta alloys.

Geminate recombination occurs generally in any material where the photogenerated carriers display very low mobility. The mobility of carriers in the localized states (below the conduction band and above the valence band edges) is much lower than in the extended states, so that the probability of initial recombination effects in amorphous materials is quite high. In

fact, during the thermalization time, the electron-hole pairs do not cover a distance long enough to prevent recombination due to their mutual coulombic attraction. Owing to this insufficient separation, a certain fraction of the photogenerated carriers recombine before the transport process can separate them permanently.[44,130]

To explain the dependence of photocurrent on both the applied potential and irradiating wavelength, it is useful to recall the Onsager's theory,[131,132] originally developed for weak electrolytes, and then applied by Pai and Enck to the initial recombination process (geminate recombination) of electron-hole pairs in amorphous selenium.[48] This was achieved deriving a mathematical expression for the efficiency of photogeneration, η_g, taking into account the tri-dimensional aspect of the generation and the effect of the electric field strength on the initial separation of the photocarriers:

$$\eta_g(r_0, E) = \frac{k_B T}{eEr_0} e^{-A} e^{-eEr_0/k_B T} \times \sum_{m=0}^{\infty} \frac{A^m}{m!} \sum_{n=0}^{\infty} \sum_{l=m+n+1}^{\infty} \left(\frac{eEr_0}{k_B T}\right)^l \frac{1}{l!} \qquad 4.2$$

where E is the electric field strength, k_B is the Boltzmann's constant, e is the electronic charge, $A=e^2/4\pi\varepsilon\varepsilon_0 k_B T r_0$ and by considering that every absorbed photon creates a pair of thermalized carriers bound by their mutual coulombic attraction. r_0 is the thermalization length, i.e. the distance travelled by the photocarriers before their effective separation by the electric field.

In Equation 4.2 the only parameter that changes with irradiating photon wavelength is r_0, which is a function of the excess energy $\Delta E = (h\nu - E_{trans})$, i.e. the extra energy with respect to that necessary for the optical transition. During the thermalization process, this excess energy is dissipated over the local potential by phonons emission.[48] According to Equation 4.2, higher generation efficiencies can be obtained with high electric field strengths and high thermalization lengths. Since r_0 directly depends on photon energy, high efficiency values are achieved at short irradiation wavelengths, while strong geminate recombination effects are characteristic of photogeneration at high irradiation wavelengths. η_g has been introduced in

Equation 2.18, i.e. the general expression of photocurrent on applied potential (applied electric field) and, by substituting d_{ox} to x_{SC}, it is possible to get:

$$I_{ph} = \eta_g e \Phi_0 (1 - R) \frac{\alpha L_d}{1 + \alpha L_d} \left[1 - exp\left(-d_{ox} \frac{1 + \alpha L_d}{L_d} \right) \right] \quad 4.3$$

where R is the reflection coefficient and L_D is the sum of drift lengths of injected photocarriers, expressed as:

$$L_D = (\mu_h \tau_h + \mu_e \tau_e) E \quad 4.4$$

with μ photocarriers mobility and τ photocarriers lifetime.[43] Equation 4.3 has been used to fit photocharacteristics relating to anodic films grown on Al-62at.%Ta, Al-81at.%Ta, Al-91at.%Ta alloys and on pure Ta in 0.1 M ABE.

In Figure 4.11 fitting curves are overlapped to the photocharacteristics relating to the anodic films grown on Al-62at.%Ta, Al-81at.%Ta and Al-91at.%Ta alloys, recorded at two different wavelengths, 240 nm and 330 nm, corresponding to irradiating photon energy higher and lower than oxides mobility gap.

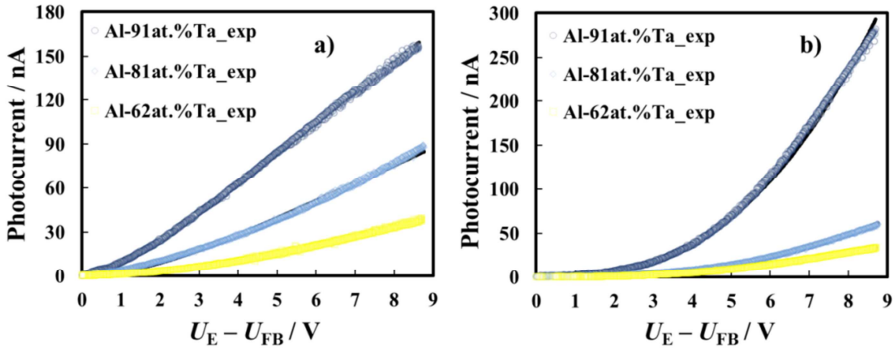

Figure 4.11 Photocurrent vs band bending curves relating to anodic films grown on Al-91at.%Ta, Al-81at.%Ta, and Al-62at.%Ta alloys in ABE, recorded at λ = 240 nm (a) and λ = 330 nm (b). Continuous lines are plotted according to Equation 4.3 with the fitting parameters of Table 4.5.

The reflection coefficient has been calculated by using a three layers model (i.e. solution/oxide/metal) under normal light incidence and by including the effects of multiple reflections,[133] with optical constants for solution, metal and oxide taken from the literature.[134–136] During fitting procedure the flat band potentials estimated from current time transients (see Table 4.4) have been used as well as the oxides thicknesses calculated from the anodizing ratio estimated by direct inspection of transmission electron micrographs of ultramicrotomed section (see Table 4.1). The best fitting parameters are summarized in Table 4.5.

Table 4.5 Fitting parameters relating to photocharacteristics, recorded at different wavelengths in 0.1 M ABE, for anodic film grown on Al-Ta alloys with Ta content ≥ 62at.%.

Base alloy	Wavelength / nm	$\mu\tau$ / cm^2 V^{-1}	r_0 / Å
Al-62at.%Ta	240	6.7×10^{-15}	10
	270	3.7×10^{-15}	7.5
	300	9.2×10^{-16}	7
	330	4.8×10^{-16}	6
Al-81at.%Ta	240	1.3×10^{-14}	10
	270	1.0×10^{-14}	6
	300	3.7×10^{-15}	4.5
	330	1.9×10^{-15}	4
Al-91at.%Ta	240	2.3×10^{-14}	14
	270	2.1×10^{-14}	7
	300	1.0×10^{-14}	5
	330	9.0×10^{-15}	4
Ta	240	2.4×10^{-14}	17.5
	270	1.9×10^{-14}	6
	300	9.0×10^{-15}	4
	330	7.7×10^{-15}	3

It is interesting to mention that r_0 is inversely proportional to wavelength and that very low $\mu\tau$ values were derived from the best fitting procedure. This suggests that for λ corresponding to both supra and sub band gap values, photocarriers are generated in localized states. Due to the

amorphous nature of the investigated anodic films, it is expected that close to conduction and valence band mobility edges, lattice disorder and/or presence of not stoichiometric oxides induce the formation of localized states, which can extend up to 0.2 eV below CB and above VB edges.[127] For $h\nu < E_g$ it is possible to state that allowed localized states are also present inside the mobility gap and $\mu\tau$ even lower than that estimated for higher irradiating wavelength suggest that they are strongly localized.

Recalling that Fowler threshold energies for films grown in borate buffer and films grown in ABE are almost coincident and that N incorporation does not contribute significantly to the measured impedance, it is suggested that anodizing in ABE leads to the formation of anodic films whose density of states can be described according to the sketch of Figure 4.12.

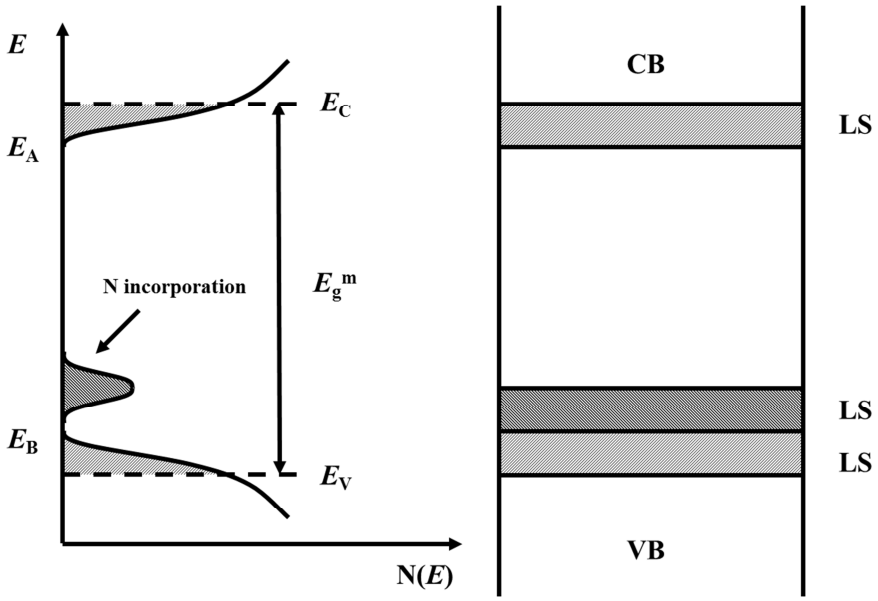

Figure 4.12 Electronic structure of an amorphous semiconducting oxides following the Mott-Davis model with allowed localized states in the mobility gap. LS: localized states.

N incorporation induces the formation of allowed localized states close to the valence band mobility edge of the oxides and the energy distance of such states from conduction band mobility edge is related to the redshift of the light absorption threshold of the anodic spectra.

4.5 Modelling of the Photoelectrochemical Behaviour of Layered Oxide Films

The occurrence of N incorporation into anodic oxides grown in suitable anodizing bath, e.g. ammonium biborate solution, allows to study the photoelectrochemical response of layered oxides, that are usual in e.g. corrosion studies. In fact, passive films and corrosion layers often consist of multiple layers with different composition and with a variable content of hydroxylate species.[137–139] Furthermore, it has been shown that by anodizing pure Ta in ammonium biborate solution, double-layered oxides are formed since N is incorporated into the oxide only in the outer 70 % of the total film.[111] Therefore, in order to correctly get information from PCS measurements, it is necessary to model the photoelectrochemical response of layered oxides. To this aim, it has been performed the growth of layered anodic films on Al-81at.%Ta alloy by a double formation procedure with a first anodizing step in ABE and second anodizing step in borate buffer solutions or vice versa up to 50 V in two-electrode configuration (see Section 3.2), exploiting the fact that N is incorporated into mixed Al-Ta oxides throughout the whole oxide thickness.

4.5.1 Theoretical Background

The photoelectrochemical response under irradiation of anodic films grown on valve metals and valve metals alloys with a double-layered structure, as that depicted in Figure 4.13, arises from the contribution coming from inner and outer phases, which are expected to have different optical gaps and photocarriers transport properties. The model used to describe the photoelectrochemical behaviour of double-layered films under particular simplifying conditions, was already employed to fit the dependence of photocurrent on photon energy for films having an inner anhydrous layer and an outer hydrated layer.[140]

The following assumptions are made in order to simplify the real systems:

i. the two photoactive layers are compact and connected in series;
ii. both layers are insulating (or semiconducting with a thickness lower than the width of

the space charge region).

The first hypothesis is fulfilled in the case of barrier anodic films grown on valve metals and valve metals alloys, as anodic oxides grown on Al-Ta alloys. Moreover, according to the second assumption, a drift transport of the photocarriers is postulated to occur in both layers (no diffusive contribution to the photocurrent), which is reasonable under high electric field strength.

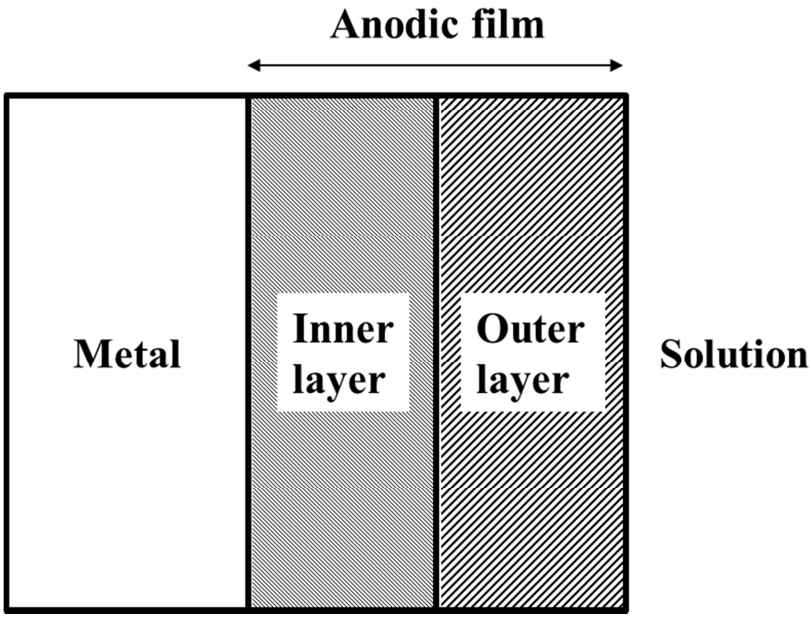

Figure 4.13 Schematic representation of a metal/double-layered anodic film/solution junction.

To model theoretically the behaviour of the present system, an expression must be derived of the collected photocurrent as a function of the wavelength of the incident light, the thickness of the layers and the electric field strength. In this case, Equation 2.18 was rearranged to get the following expression of the photocurrent yield:

$$Q = \frac{I_{ph}}{e\Phi_0(1-R)} = \eta_g[1-\exp(-\alpha d_{ox})]\frac{\mu\tau E}{d_{ox}}\left[1-exp\left(-\frac{d_{ox}}{\mu\tau E}\right)\right] \quad 4.5$$

In Equation 4.5 μ and τ are mobility and lifetime of the photogenerated carriers (holes, h, and electrons, e) expressed as in Equation 4.4 and η_g (λ, E) is the generation efficiency (almost unitary in low defective crystalline phases), much lower than 1 as result of geminate recombination effects in disordered materials at low electrode potentials as discussed in Section 4.4. Moreover, the incident flux ϕ_0 can be corrected for the reflection at the metal/oxide/electrolyte interface introducing R, the total reflectivity of the junction. Nevertheless, effects of multiple reflections at the metal/anodic film/electrolyte interfaces have been neglected taking into account the constancy of film thickness in the reported photocurrent measurements. Assuming $\alpha d_{ox} << 1$ (uniform light absorption throughout the whole film thickness), $\mu\tau E = L_D$ (the collection length of the carriers, see Equation 4.4), and a unitary efficiency of carriers generation, Equation 4.5 coincides with the Crandall expression[141] of the photocurrent for insulating layers in the absence of trapping effects on the electric field.[44] It follows that the photocurrent yield (or, equivalently, the collected photocurrent) is the product of a generation term:

$$G = \eta_g[1-\exp(-\alpha d_{ox})] \quad 4.6$$

times a transport term:

$$T = \frac{\mu\tau E}{d_{ox}}\left[1-exp\left(-\frac{d_{ox}}{\mu\tau E}\right)\right] \quad 4.7$$

The use of the Lambert-Beer law for the G term is correct in the present model because multiple reflection effects on the generation are assumed to be negligible.

For the double-layered structure of Figure 4.13, the collected photocurrent can be calculated

as the sum of the contributions coming from both layers, each contribution being the product of the generation term times the transport term:

$$I_{ph} = I_{ph,out} + I_{ph,inn} = e\Phi_0(1-R)[T_{out}G_{out} + \exp(-\alpha_{out}d_{ox,out}) \times T_{inn}G_{inn}] \quad 4.8$$

In this equation, indices "inn" and "out" refer to the inner and to the outer layers respectively; G and T refer to the generation and transport term in each layer, given by Equations 4.6 and 4.7; α_{out} refer to the absorption coefficient of the outer layer, given by Equation 2.15; $d_{ox,out}$ refer to the thickness of the external layer; and d_{ox} is the entire anodic film thickness. Photon flux impinging the inner layer surface is assumed to be $\phi_0\exp(-\alpha_{out}\, d_{ox,out})$.
For non direct optical transitions, as those occurring in amorphous materials, and after algebraic manipulation, Equation 4.5 becomes:

$$(Q \times h\nu)^{0.5} = [(T_{out}G_{out} + \exp(-\alpha_{out}d_{ox,out}) \times T_{inn}G_{inn}) \times h\nu]^{0.5} \quad 4.9$$

that will be used for interpolating the experimental data.

4.5.2 Fitting of Experimental Data

GDOES elemental depth profile relating to an anodic film grown on Al-81at.%Ta up to 50 V in 0.1 M ABE is reported in Figure 4.14(a). Nitrogen is incorporated into the oxide during anodizing in ammonium-containing electrolyte and it is present throughout the whole anodic film thickness (N signal is weak but present across the entire oxide), as discussed before. In contrast, in the case of pure Ta, anodizing in ABE induces N incorporation only in the outer part of the anodic films, i.e. in the region at the oxide/electrolyte interface corresponding roughly to the 70% of the whole oxide thickness.[111]

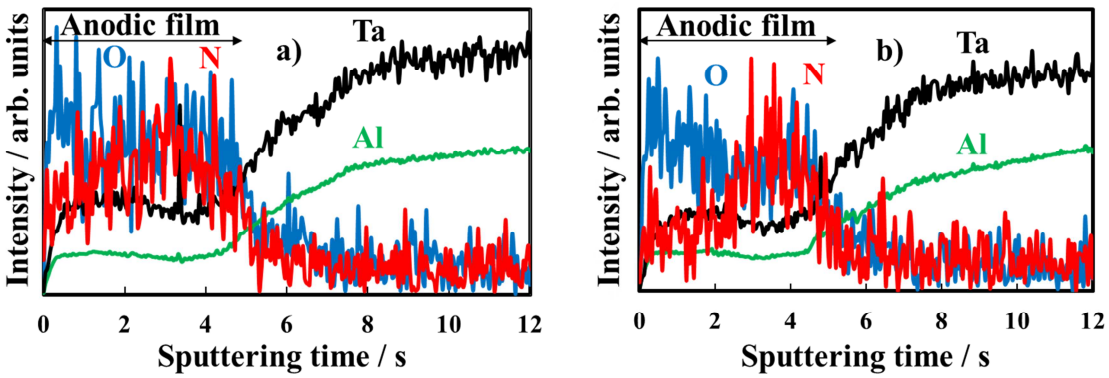

Figure 4.14 GDOES elemental depth profiles of (a) anodic film grown to 50 V on Al-81at.%Ta alloy in 0.1 M ABE; (b) double-layered anodic film grown to 50 V on the same alloy (first anodizing step to 20 V in 0.1 M ABE and second anodizing step to 50 V in borate buffer).

Moreover, in Figure 4.14(b) the GDOES elemental depth profile relating to film grown on the same alloy after a first anodizing step in 0.1 M ABE to 20 V and a second anodizing step in borate buffer to 50 V is shown. N signal shows that such anodic film is composed by two different layers in series: a nitrogen-containing inner layer and a nitrogen-free outer layer.

The photocurrent spectrum relating to anodic films grown on Al-81at.%Ta to 20 V in borate buffer (thickness ~ 30 nm, see Table 4.1) is reported in Figure 4.15(a). Through Equation 2.16, it is possible to estimate a mobility band gap of 4.12 eV by extrapolating to zero the $(Q\ h\nu)^{1/2}$ vs $h\nu$ plot, as shown in Figure 4.15(b). This value is slightly lower than that estimated for anodic films grown on the same alloy but at lower formation voltage (i.e. lower thickness, see Section 4.3). A reduction of E_g^m with increasing formation voltage has been explained by an increase in the short range order of the oxide,[127,128,130,142] due to the film thickening. A different photoelectrochemical behaviour is shown by the anodic film grown on the same alloy with a first anodizing step to 10 V in 0.1 M ABE and a second anodizing step to 20 V in borate buffer and vice versa (see Figure 4.15(a)). The different growth procedure induces a strong red shift in the light absorption threshold of the anodic film with the appearance a long photocurrent tail in the long wavelength region.

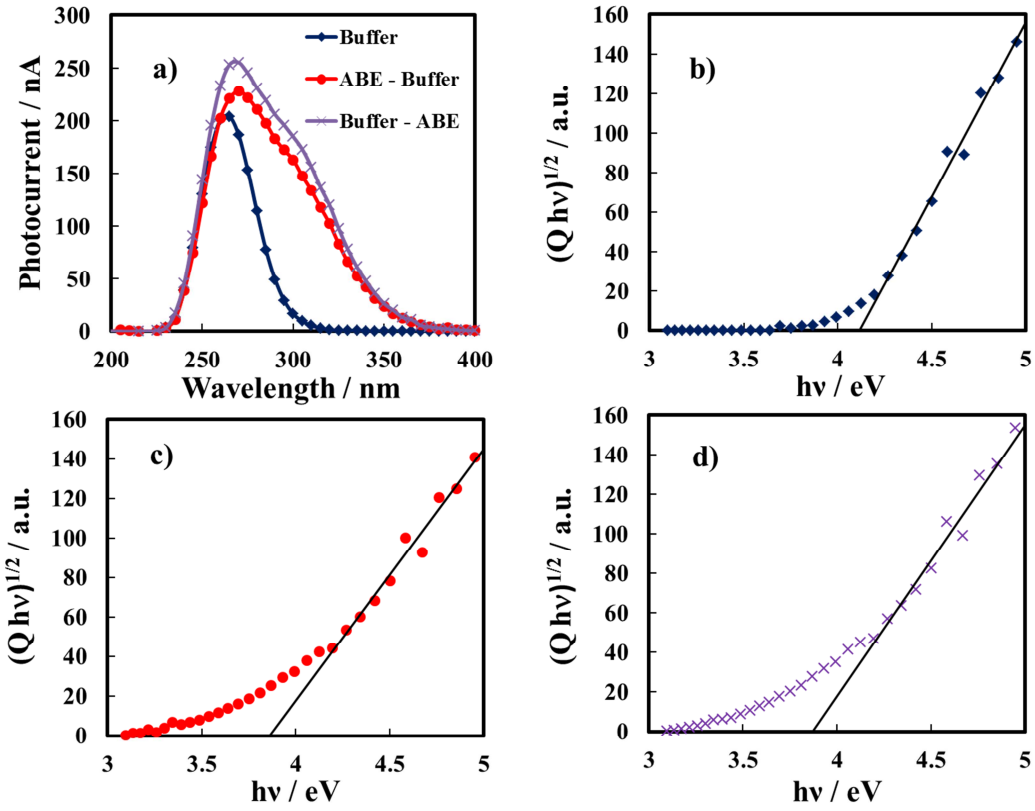

Figure 4.15 (a) Raw photocurrent spectra relating to anodic films grown to 20 V on Al-81at.%Ta alloy, recorded by polarizing the electrodes at 8 V vs Hg/HgO in 0.1 M ABE. Band gap estimate by assuming non direct optical transitions for anodic films grown in (b) borate buffer, (c) in 0.1 M ABE to 10 V (first anodizing step) and then in borate buffer to 20 V (second anodizing step) (ABE – Buffer), (d) in borate buffer to 10 V (first anodizing step) and then in 0.1 M ABE to 20 V (second anodizing step) (Buffer – ABE).

As confirmed by recording current vs time curves under constant potential and irradiating wavelength, the photocurrent is anodic at all the investigated wavelengths in agreement with the measured photocurrent phase angle, which does not change in the investigated photon energy interval (see Figure 4.16).

The presence of a photocurrent tail in the spectra is evident in the corresponding $(Q\ h\nu)^{1/2}$ vs $h\nu$ plot inducing uncertainty in the estimate of the optical/mobility band gap of the oxide. By extrapolating to zero the plot of Figure 4.15(c) and (d) in the high energy region, $E_g = 3.86$ eV can be estimated, which is far from the value estimated for N-free oxide.

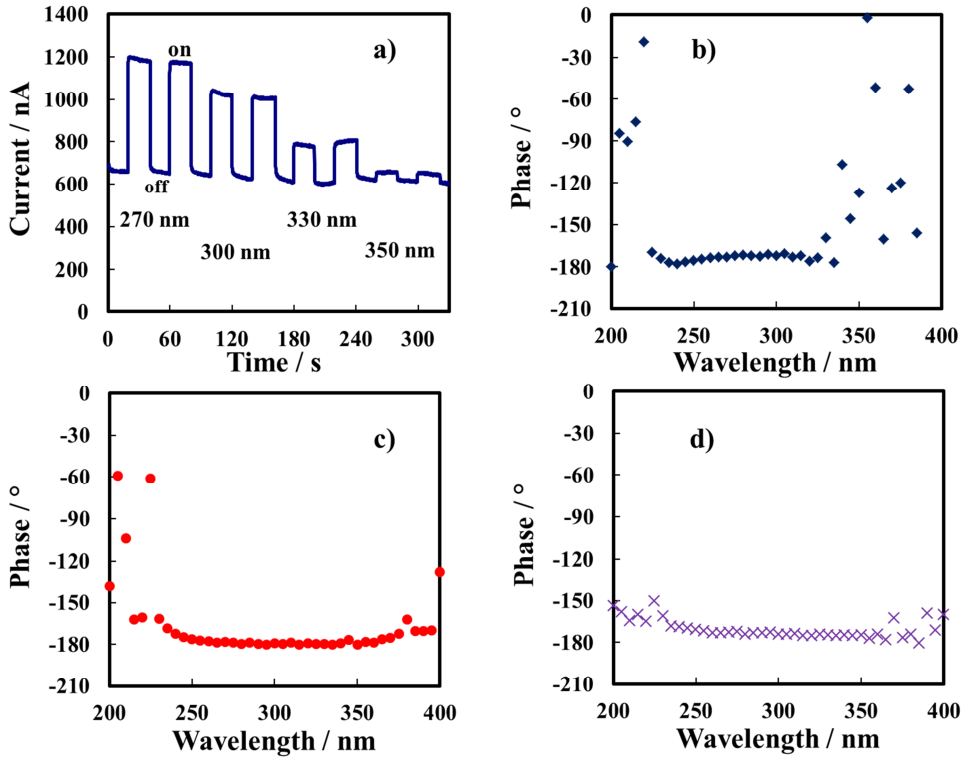

Figure 4.16 (a) Total current circulating under irradiation (on) and in the dark (off) in the oxide grown to 20 V with Buffer - ABE procedure. (b),(c),(d) Phase angle vs irradiating wavelength relating to photocurrent spectra shown in Figure 4.15(a).

In Figure 4.17 the photocharacteristics recorded under constant different irradiating wavelength (λ = 270, 330 nm, i.e. hν = 4.59, 3.75 eV) for the films of Figure 4.15, scanning the electrode potential toward the cathodic direction at 10 mV s^{-1}, are compared. As already evidenced for anodic films on Al-Ta alloys with a Ta content > 42at.%, an inversion of the photocurrent sign is present as expected for insulating oxides.[113] Sign inversion potential, U_{inv}, is a rough estimate of the flat band potential, U_{FB}, of the oxide in absence of significant trapping phenomena. U_{inv} is ~ - 1.2 V vs Hg/HgO for the anodic film grown in borate buffer, thus coincident with U_{FB} estimated in previous work.[113] Slightly more cathodic values recorded for double-layered films can be explained by holes trapping into localized states due to N incorporation.

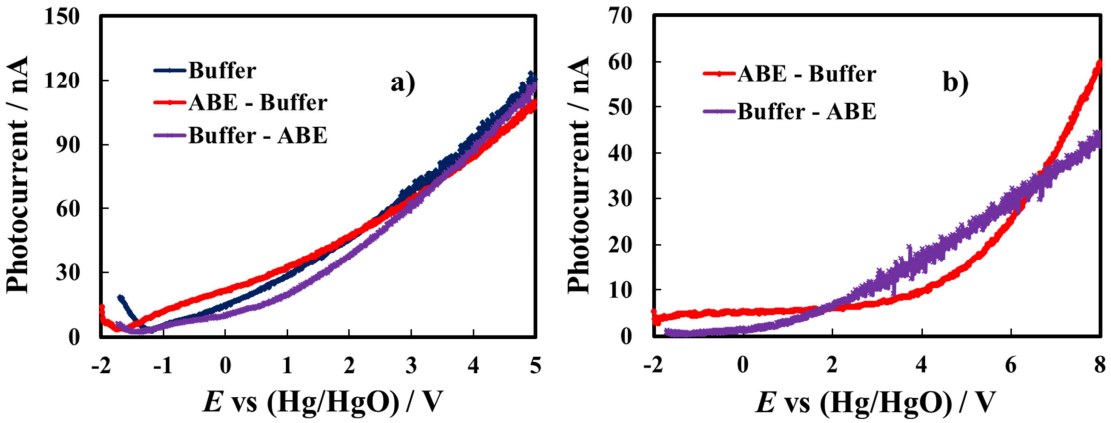

Figure 4.17 Photocurrent vs potential curves relating to 20 V anodic films of Figure 4.15. Irradiating wavelength: (a) 270 nm and (b) 330 nm.

Moreover, photocharacteristics were fitted according to the Pai-Enck model for the geminate recombination, as discussed in Section 4.4, and the fitting are shown in Figure 4.18.

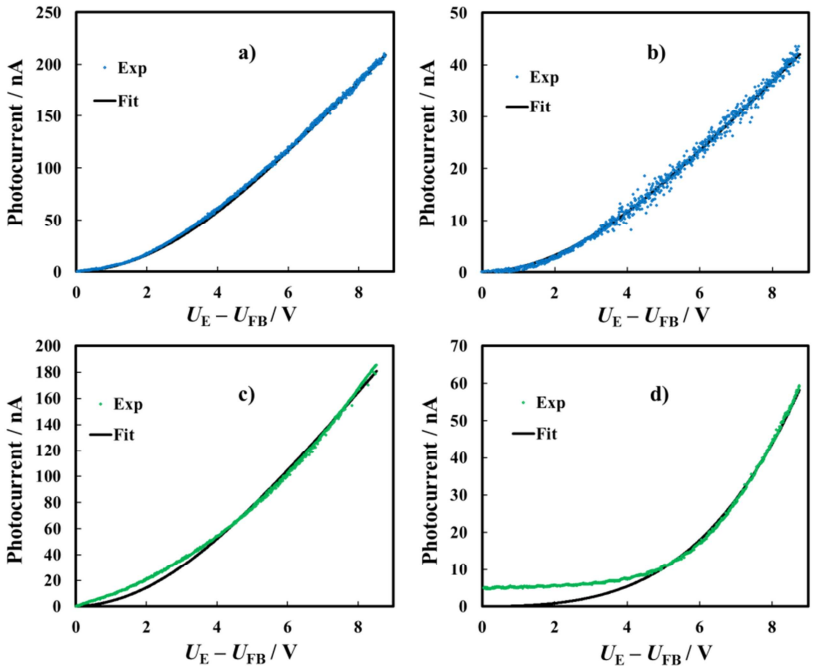

Figure 4.18 Photocurrent vs band bending relating to anodic films grown to 20 V with (a), (b) Buffer – ABE procedure (wavelength: 270 nm (a) and 330 nm (b)) and with (c), (d) ABE – Buffer procedure (wavelength: 270 nm (c) and 330 nm (d)). Solid lines: fitting curves.

There is a very good agreement between the experimental curves and those simulated according to Pai-Enck model with the exception of the low band bending region of the photocharacteristic relating to anodic film grown to 10 V in ABE and then to 20 V in buffer. In the latter case mismatch between the experimental and the simulated curves at low electrode potentials (U_E < 2.5 V vs Hg/HgO, see Figure 4.17(b)) can be attributed to the presence of anodic photocurrent spikes, as shown in Figure 4.19.

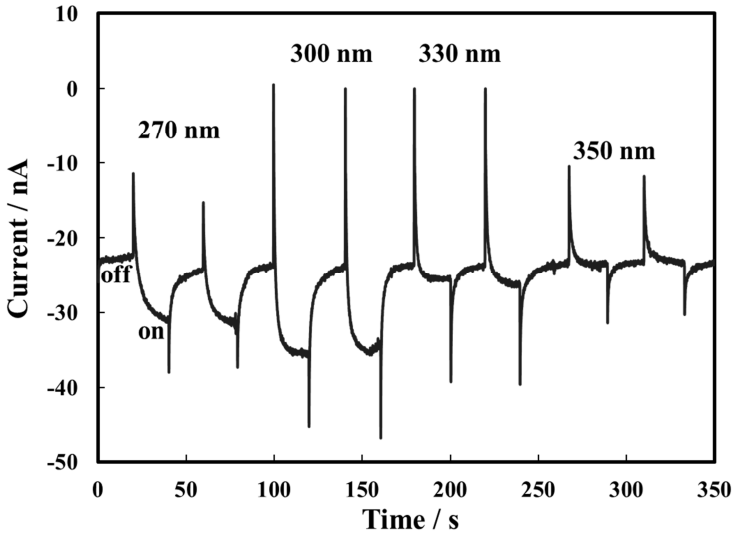

Figure 4.19 Total current circulating under irradiation (on) and in the dark (off) in the oxide grown on Al-81at% Ta alloy up to 20 V with Buffer – ABE procedure, by polarizing the electrode at -1 V vs Hg/HgO in 0.1 M ABE.

The different photoelectrochemical behaviour of the anodic oxides formed by double anodizing procedure with respect to those anodized in borate buffer, can be explained taking into account their double-layered structure, as sketched in Figure 4.20. The anodic films are both constituted by N-containing and N-free layers. When the first anodizing step is performed in ABE, the structure of Figure 4.20(a) is expected, whilst if the first anodizing step is performed in borate buffer the structure of Figure 4.20(b) is expected, which is also representative of anodic films grown on Ta in 0.1 M ABE, where N is concentrated in the outer part of the oxide.[111]

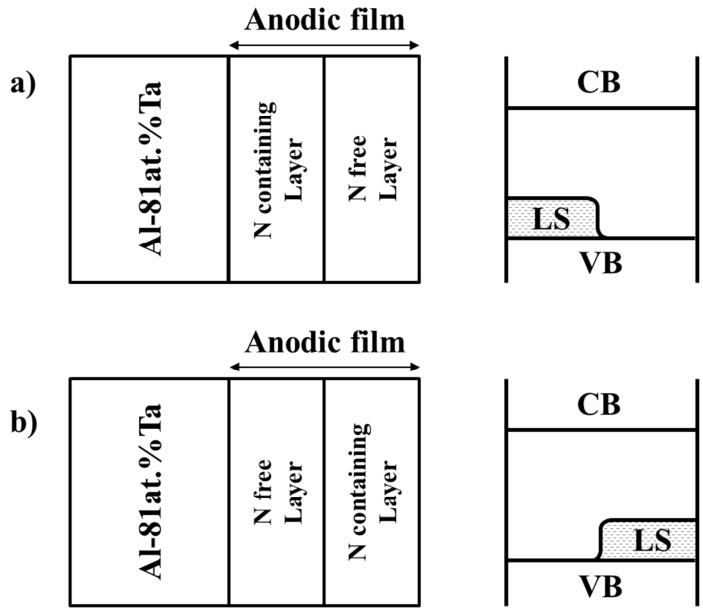

Figure 4.20 Schematic representations of double-layered anodic films grown on Al-81at.%Ta alloy with (a) "ABE – Buffer" anodizing procedure and (b) with "Buffer – ABE" anodizing procedure and corresponding energy band diagrams. LS: Localized States.

The overall films are considered as the series of two layers of different composition so that it is possible to use Equation 4.9 to simulate the dependence of Q on photon energy and, thus, get a reliable estimate of the optical band gaps of both layers. In Figure 4.21 the experimental $(Q\ h\nu)^{1/2}$ vs $h\nu$ plots relating to anodic films grown to 20 V on Al-81at.%Ta alloy by double anodizing procedures and on pure Ta by anodizing in 0.1 M ABE are reported. The plots, simulated according to Equation 4.9, almost overlap to the experimental points, suggesting that the proposed model is effective in simulating the dependence of Q on photon energy for the investigated double layered films. Fitting parameters are reported in Table 4.6. Since photocurrent spectra were recorded under high anodic potential (i.e. under very high electric field strength in the order of MV cm^{-1}), η_g has been kept constant and equal to 1 in the fitting procedure.

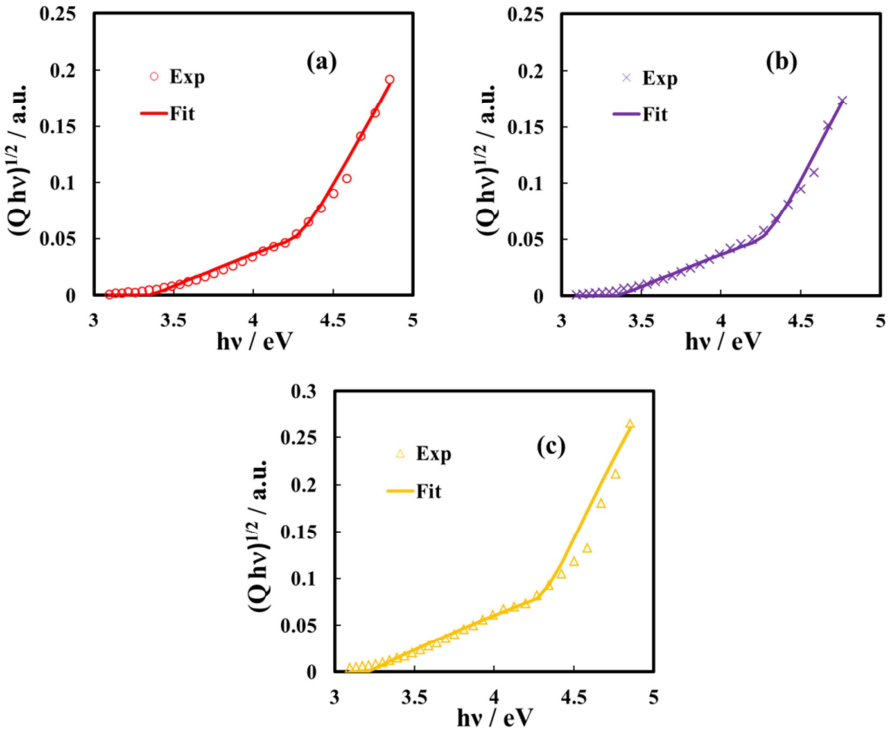

Figure 4.21 Theoretical fitting (continuous line), according to Equation 4.9, of the experimental $(Q\ h\nu)^{1/2}$ vs hν plots (symbol) relative to anodic films grown on Al-81at.%Ta alloy to 20 V with (a) "ABE – Buffer" anodizing procedure and with (b)"Buffer – ABE" anodizing procedure and (c) grown on pure Ta in 0.1 M ABE.

Table 4.6 Fitting parameters relating to photocurrent spectra, recorded at U_E = 8 V vs Hg/HgO for the anodic films grown on pure Ta and Al-81at.%Ta alloy.

Sample	Anodizing conditions	$(\mu\tau)_{N\text{-free}}$ / cm^2 V^{-1}	$E_{g\ N\text{-free}}$ / eV	$(\mu\tau)_{N\text{-cont}}$ / cm^2 V^{-1}	$E_{g\ N\text{-cont}}$ / eV
20 V pure Ta	Single step in ABE	9.0×10^{-13}	4.25	8.0×10^{-15}	3.20
20 V Al-81at.%Ta	1st step: ABE 2nd step: buffer	4.8×10^{-14}	4.22	3.5×10^{-15}	3.35
	1st step: buffer 2nd step: ABE	5.5×10^{-14}	4.22	3.5×10^{-15}	3.35
50 V Al-81at.%Ta	1st step: ABE 2nd step: buffer	4.8×10^{-13}	4.25	2.0×10^{-14}	3.45
	1st step: buffer 2nd step: ABE	1.3×10^{-13}	4.05	7.0×10^{-15}	3.52

It is important to stress that the optical band gap for the N-free layer is almost coincident with that estimated for the film grown to 20 V in borate buffer (i.e. without any N incorporation). Moreover, the thicknesses of the N-free and N-containing layer are assumed equal, in agreement with the increase in formation voltage for each anodizing step (10 V). The products $\mu\tau$ resulted to be strongly different for the N-containing and N-free layers. $\mu\tau$ in the order of $10^{-14} - 10^{-13}$ cm^2 V^{-1} are derived by the fitting procedures for N-free layers, in agreement with previous values derived also for other amorphous anodic oxides.[143] Moreover, for both the investigated structures (Figure 4.20), mobility of photogenerated carriers in energy states due to N incorporation is ~ one order of magnitude lower (10^{-15} - 10^{-14} cm^2 V^{-1}), thus suggesting a strong localization of such states.

The same fitting procedure was followed to fit the experimental data recorded for anodic films grown to 50 V by double anodizing procedure (20 V in 0.1 M ABE and up to 50 V in borate buffer and vice versa), as shown in Figure 4.22. Also for thicker layers there is a good agreement with the experimental points and the theoretical expectations according to Equation 4.9.

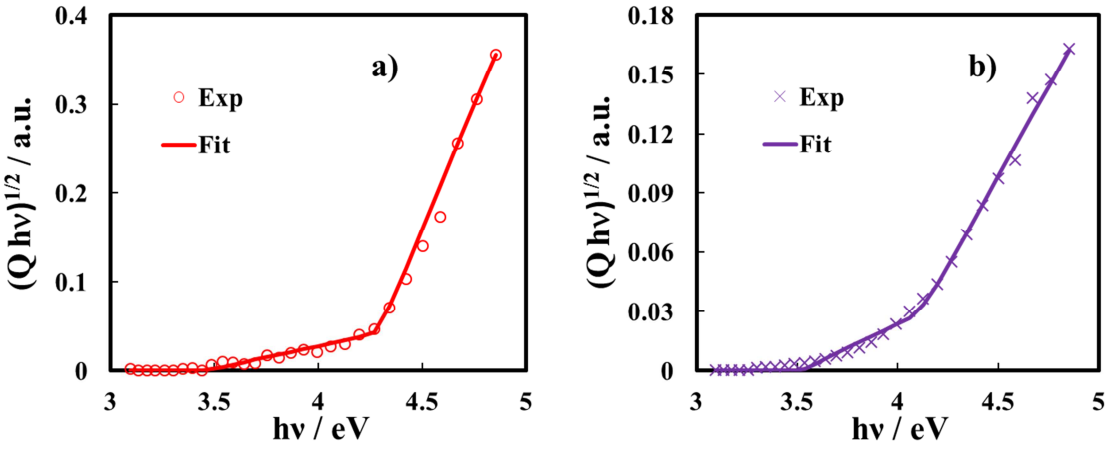

Figure 4.22 Theoretical fitting (continuous line), according to Equation 4.9, of the experimental $(Q\ h\nu)^{1/2}$ vs $h\nu$ plots (symbol) relative to anodic films grown on Al-81at.%Ta alloy to 50 V with (a) "ABE – Buffer" anodizing procedure and with b) "Buffer – ABE" anodizing procedure.

All the photoelectrochemical findings support the band energy diagrams of Figure 4.20 for the investigated layers. As discussed before, incorporation of N during anodizing of Al-Ta alloys induces the formation of localized states close to the valence band mobility edge of the anodic oxides. Such states are at the metal/oxide or oxide/electrolyte interfaces depending on the anodizing conditions. Under anodic polarization with the respect to the flat band potential of the oxides, bands are upward bended. For $h\nu > E_g$, holes are driven toward the oxide/electrolyte interface by the electric field across the oxide, while electrons are driven in the opposite direction (toward metal/oxide interface). If photon energy is lower than E_g but sufficiently high to induce excitation of electrons from localized states (due to N incorporation) to the conduction band, electrons can travel across allowed energy states for both the investigated double-layered films. In the case of anodic film with a N-containing outer layer (Figure 4.20(b)) (i.e. second anodizing step performed in ABE electrolyte), photogenerated holes can easily migrate toward the oxide/electrolyte interface allowing for the photo-oxidation processes (anodic photocurrent). In the case of N-containing inner layer (Figure 4.20(a)) the generation term (see Equation 4.6) is almost coincident with $\alpha_{inn} d_{ox,inn} \times \eta_g$, with η_g a function of the electric field existing in the inner layer as well as of the photon energy ($h\nu \geq 3.35$ eV). In this case, the photogenerated holes must cross the outer layer moving through localized states of the mobility gap before reaching the oxide/electrolyte interface, lying above the valence band mobility edge. Both a Poole-Frenkel field-assisted emission and/or tunnelling to extended states in the valence band of the external layer could cooperate in transferring of inner layer photogenerated holes toward the oxide/electrolyte interface. The almost constant photocurrent at low electrode potentials ($U_E <$ 2.5 V vs Hg/HgO, see Figure 4.17(b)) can be attributed to the dependence of the generation efficiency on electric field strength across the oxide thickness, in the frame of the Pai-Enck mechanism of geminate recombination as discussed before.

4.6 Concluding Remarks

The choice of the composition of anodizing bath is very important since it can strongly

influence the morphological and solid state properties of the anodic oxide layers. In the case of mixed high-*k* Al-Ta oxides, anodizing in ammonium biborate electrolyte, with a suitable bath pH, leads to the incorporation of N species into the oxides that change the optical response of the oxides and, thus, could lead to a detrimental effect in terms of leakage current and dielectric properties.

According to GDOES compositional depth profiles, N incorporation is extended throughout the whole Al-Ta oxides thicknesses nevertheless the presence of N does not change appreciably the impedance of the oxides, as suggested by the comparison between the impedance spectra and the differential capacitance curves related to anodic oxides grown in ammonium-free and ammonium-containing solutions. In contrast, N incorporation significantly changes the photoelectrochemical behaviour of the anodic films grown on Al–Ta alloys with the Ta content > 20 at%. A red-shift of the light absorption threshold of the investigated layers was evidenced, which is attributed to the optical transitions involving allowed states inside the mobility gap of the films.

The dependence of photocurrent on photon energy and the electric field strength in the framework of Pai–Enck model for geminate recombination suggested that incorporation of nitrogen induces the formation of allowed localized states. Such states are close to the valence band mobility edge, since they do not contribute to the measured impedance up to a very low frequency of the a.c. signal (0.1 Hz) and since they do not affect the Fowler threshold for the internal electron photoemission phenomena.

This N incorporation result was also exploit to grow anodic oxides by a two-step anodizing procedure in ammonium-free and ammonium-containing solutions in order to induce the formation of double layered films constituted by N-containing and N-free layers, as confirmed by GDOES compositional depth profiles. The photoelectrochemical behaviour of these films was compared to that of anodic oxides of uniform composition. The dependence of photocurrent yield on photon energy under constant electric field (i.e. constant electrode potential) was modelled considering their double-layered structure and the different optical band gap and transport properties of the two series layers.

The model allows for a precise estimate of the optical band gap of the N-free layers, which can be underestimated by neglecting the presence of a phase with a lower optical band gap, i.e. N-containing layer. The model was also successfully employed for N-containing anodic films grown on pure Ta and can be also used to model double-layered oxide films very common in passivity and corrosion studies.

5 Growth of Anodic Hf Oxide as a Function of the Anodizing Conditions

Among many high dielectric constant materials, Hf oxide is surely one the most studied in the last years being the material that replaced SiO_2 as gate dielectric in CMOS-based and logic devices,[5,144–147] to be used in MIM capacitors for DRAM memories,[148] and also as solid electrolyte in ReRAM devices.[57,76,149] For both technological applications, compact, uniform and flat oxides are necessary in order to reduce probability of oxide failure. Since Hafnium is a valve metal, anodizing can be an efficient technique to prepare HfO_2 layers of controlled thickness, as recently proposed by Hassel and co-workers.[150,151]

The anodic films growth mechanism has been extensively studied in the past starting from earlier seminal work of 1961 by Young,[24] where the high field conduction model was proposed to describe the anodizing process, as discussed in Section 2.1.1. Cations and anions carry ionic current in a percentage directly proportional to their transport number and it is well known that ionic current during anodizing of Zr and Hf is almost entirely sustained by anions migration, less than 5% being carried by metal cations.[28] A survey of the already published works on Hf anodizing revealed that only a few papers have addressed the study of the kinetic of growth of anodic oxides,[152,153] reporting kinetic parameters far from each other.

In order to study how the anodizing parameters can change the properties of the anodic oxides, Hf rod was anodized up to 5 V vs Ag/AgCl in ammonium biborate and sodium hydroxide aqueous solutions potentiodynamically at several constant potential scan rates (see Sections 3.1.1 and 3.2). This study was also useful to check if the dependence of the anodizing current density on the electric field strength across the growing oxide is well described by the *high field model*, discussed in Section 2.1.1.

Electrochemical impedance measurements were also performed in order to get information on the electrical properties of the anodic films and on the dielectric constant as a function of the growing conditions. The investigation is also supported by photoelectrochemical measurements allowing to get information on the energetic of the metal/oxide/electrolyte interface and the presence of defects on the oxides that can induce the presence of allowed

localized states inside the mobility gap of HfO_2, that can induce oxide instability and leakage current.

5.1 Anodizing Behaviour

Mechanical polished Hf was anodized in 0.1 M ABE and 0.1 M NaOH potentiodynamically at several constant scan rates (ranging from 2 mV s^{-1} to 1 V s^{-1}). In Figure 5.1 the potentiodynamic curves recorded at all the scan rates in both the electrolytes are reported.

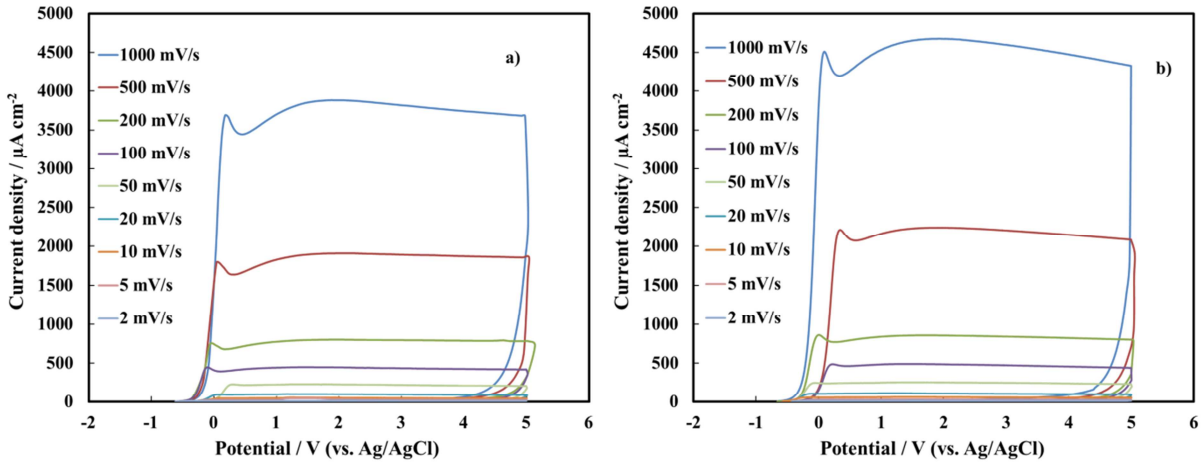

Figure 5.1 Current density vs electrode potential curves relating to Hf anodic film grown potentiodynamically in (a) 0.1 M ABE and (b) 0.1 M NaOH.

During the forward scan, current suddenly increases and reaches an almost constant plateaux value, while it decreases rapidly during the reverse scan as expected for valve metals.[154] However the current density during potentiodynamic anodizing in NaOH solution is higher than that measured in ABE.

Under high field regime, d_{ox} and circulated charge q are linked by the Faraday's law (Equation 2.7). The latter can be arranged to show the relationship between the electric field strength, E, across a growing anodic oxide, and growth rate, dV/dt, as follows:

$$\frac{dV}{dt} = \eta \frac{i\,E\,MW}{z\,F\,\rho}\frac{1}{r} \qquad 5.1$$

where i is the measured current density, MW is the molecular weight of the growing oxide (210.5 g mol^{-1}), z = 4 the number of electrons circulating per mole of formed oxide, F the Faraday's constant, ρ the oxide density (9.68 g cm^{-3}), r the roughness factor (expressed as the ratio between the real and the geometrical surfaces) and η the growth efficiency (expressed by Equation 2.6).

Equation 5.1 allows calculating for each scan rate the corresponding electric field strength, provided that r and η are known. A roughness factor of ∼ 1.2 was estimated comparing the growth curves relating to mechanical polished Hf and sputtering-deposited Hf, whose surface is flat at the nm scale.

Concerning the growth efficiency, HfO_2 is reported to be chemically stable for pH > 4,[114] even if some authors report that hafnium oxides dissolves in strongly alkaline solutions.[155] If a growth efficiency η equal to 1 is assumed, according to Equation 5.1, E = 4.7 MV cm^{-1} and E = 4.3 MV cm^{-1} for anodizing Hf at 20 mV s^{-1} in 0.1 M ABE and 0.1 M NaOH respectively. From the electric field strength it is possible to estimate the anodizing ratio, A, i.e. the reciprocal of the electric field strength, providing an estimate of film thickening per each applied volt. Therefore, a thicker layer is expected to grow in NaOH.

5.2 Photoelectrochemical Measurements

Anodic photocurrent spectra (U_E = 3 V vs Ag/AgCl), relating to 5 V anodic films grown in both 0.1 M ABE and 0.1 M NaOH electrolytes at 10 mV s^{-1}, are reported in Figure 5.2(a). The dependence of photocurrent on irradiating photon wavelength is not influenced by anodizing electrolyte.

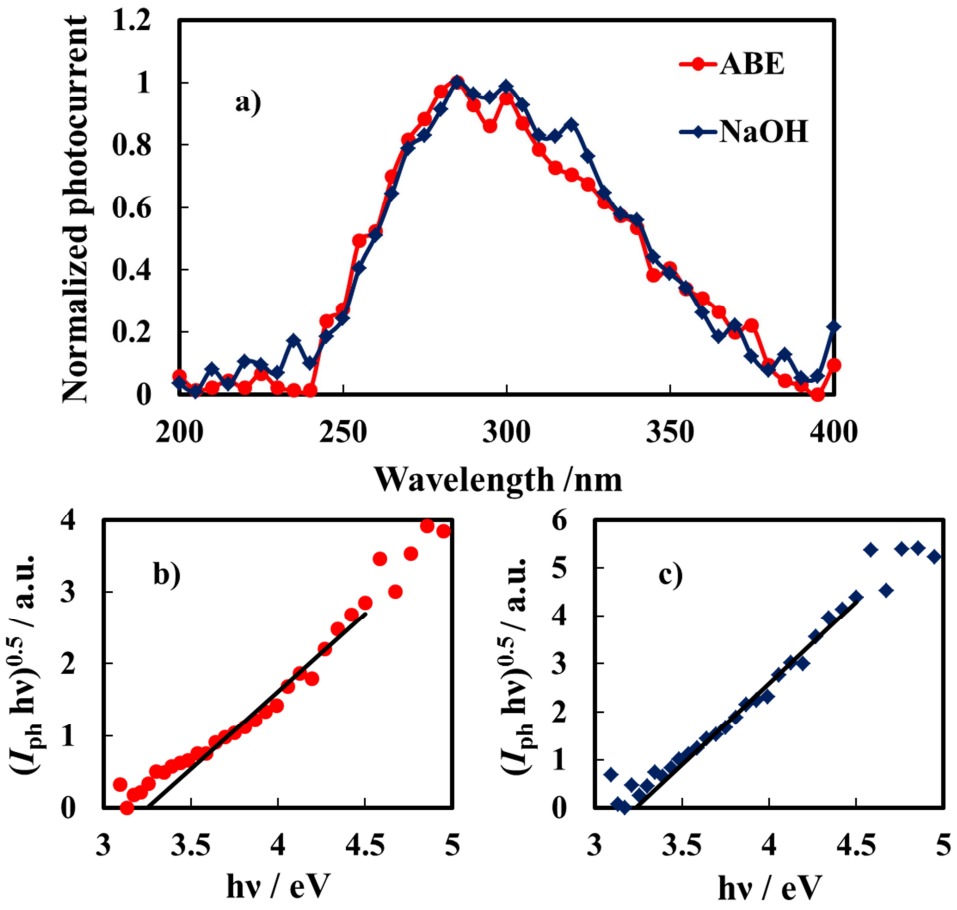

Figure 5.2 Anodic photocurrent spectra (a) relating to anodic films grown on Hf in ABE and NaOH, recorded by polarizing the electrodes at 3 V vs Ag/AgCl. Band gap estimate by assuming indirect optical transitions relating to the same anodic film grown in (b) ABE and (c) NaOH.

From photocurrent spectra (see Section 2.2), it is possible to estimate E_g^{opt} value of the investigated anodic films according to Equation 2.16, resulted to be 3.25 eV by extrapolating to zero the $(I_{ph}\ h\nu)^n$ vs hν plot with n = 0.5 (shown in Figure 5.2(b) and Figure 5.2(c)).

This value is significantly lower than the band gap reported in the literature for HfO_2 (5.1 - 6.1 eV)[156–161] thus suggesting that the measured photocurrent is due to optical transitions involving allowed localized states inside the mobility gap of the oxide. Their origin, concentration and energy distributions have been extensively studied, due to the large interest on the electronic properties of hafnia in view of its possible application in MOS-based

devices.[5,144–147] They can be present even in a perfect crystal as a consequence of the potential well created in a perfect crystal by lattice polarization induced by the carriers themselves.[144] According to theoretical studies based on static approach and density functional theory, hole and electron polarons create localized states close to the valence and conduction band edges.[144,159] Localized states can be also generated by structural defects that, in the case of HfO_2, are mainly oxygen vacancies in different charge states. Oxygen vacancies in hafnia can be double or single positively charged (V_O^{++}, V_O^{+}), neutral (V_O^{x}), and single or double negatively charged (V_O^{-}, V_O^{--}), depending on the number of trapped electrons.[159,160] On the basis of theoretical calculations of the formation energy of each defect, the dominant defect is expected to be V_O^{-}. The transition energy from the states generated by a significant concentration of single negatively charged oxygen vacancies to the conduction band is reported to be 3.2 eV by different authors.[159,160] This energy value is almost coincident with that estimated from Figure 5.2, thus suggesting the formation of an oxygen deficient hafnium oxide during the anodizing process in both solutions. It is noteworthy to mention that it is not possible to record photocurrent due to optical transitions involving electrons from the valence band to the conduction band, since the experimental setup employed has a very poor efficiency at short wavelengths (200 – 230 nm), thus being very difficult to reveal photocurrent at the corresponding photon energy.

Dependence of photocurrent on applied electrode potential, i.e. electric field strength across the anodic film, was also studied under constant irradiating energy. As shown in Figure 5.3 for irradiating wavelength equal to 280 nm, by scanning the electrode potential downward at 10 mV s^{-1}, photocurrent changes from anodic to cathodic, as suggested by the photocurrent phase angle (not reported) and as expected for an insulating oxide, where the photocurrent sign depends on the direction of the imposed electric field strength. i.e. on the potential with respect to the flat band potential, U_{FB}. Therefore, the zero photocurrent potential provides a rough estimate of the flat band potential of the oxide. In wide band gap oxides, as HfO_2, the inversion potential is usually more anodic than the flat band potential due to the occurrence of recombination phenomena involving photo-generated electron-hole pairs at low band

bending.[113,162]

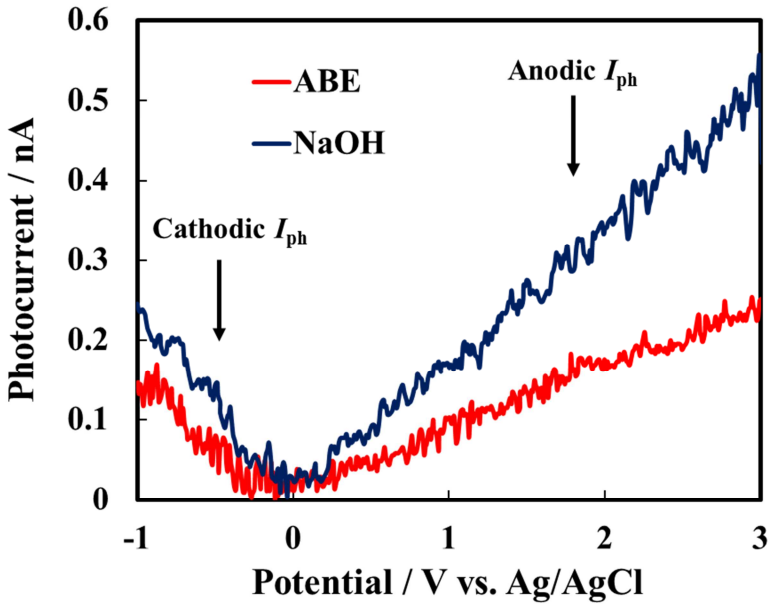

Figure 5.3 Photocharacteristics relating to the 5 V anodic oxides grown in ABE and NaOH, recorded at λ = 280 nm in 0.1 M ABE by scanning the electrode potential at 10 mV s^{-1}.

Photocurrent spectra at a potential below the U_{FB} (i.e. − 1 V vs Ag/AgCl) were also recorded, as shown from the I_{ph} vs. wavelength curves in Figure 5.4 for oxides grown in both 0.1 M ABE and 0.1 M NaOH. At this cathodic potential, a photocurrent tail appears in the long wavelength region of the spectra, as shown in Figure 5.4(b) (UV filter was used to avoid photocurrent doubling effects).

As already found for other valve metals oxides and also reported for anodic films on sputtering-deposited Hf, such photocurrent can be attributed to photoemission phenomena, involving electrons of the metallic Hafnium promoted to the conduction band of the oxide. In such a case, the dependence of I_{ph} on photon energy is described by the Fowler's law (Equation 2.21) and E_{th} resulted to be ~ 2.15 ± 0.1 eV, independently on anodizing electrolyte composition and on anodic growth scan rate, in agreement with previous experimental results.[126]

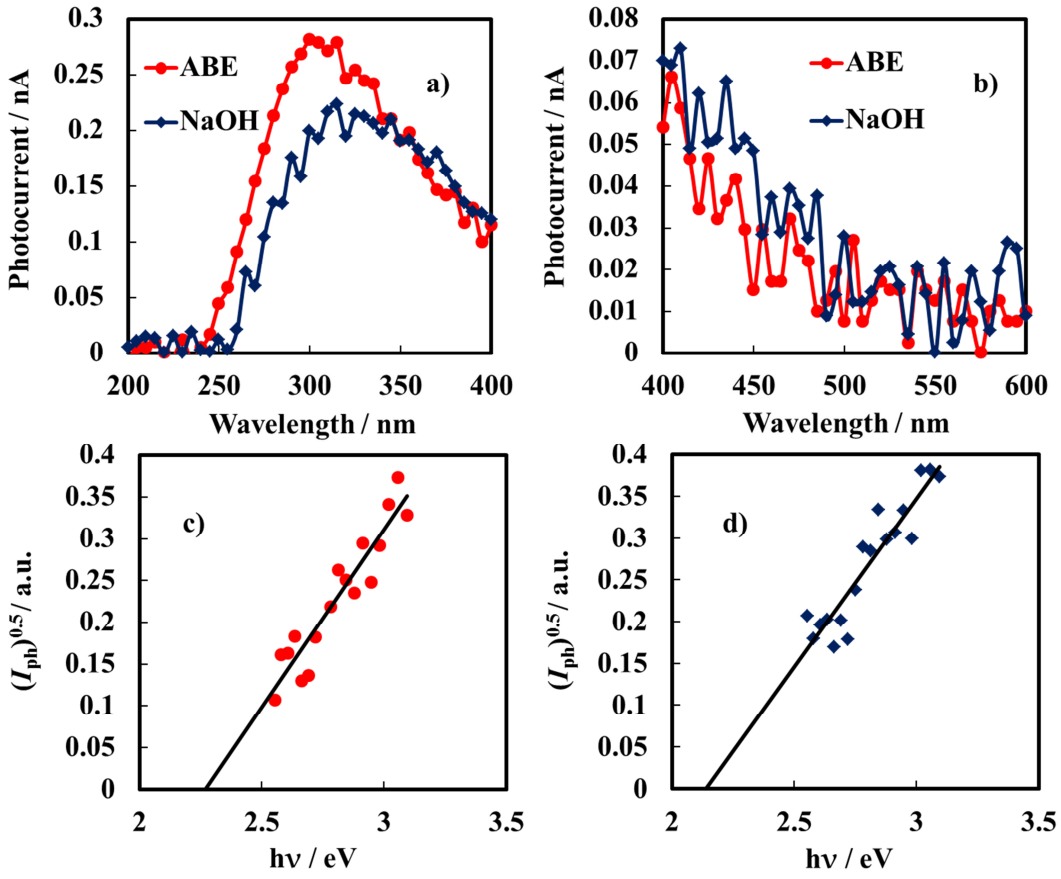

Figure 5.4 (a) Cathodic photocurrent spectra relating to the oxides grown on Hf in ABE and NaOH recorded at -1 V vs. Ag/AgCl. (b) Long wavelength region of the photocurrent spectra, recorded by using a UV filter. Fowler plots relating to the oxides grown in (c) ABE and (d) NaOH.

During the anodizing of other valve metals in ammonium-containing solutions, such as ABE, N incorporation occurs[111,112] provided that the pH of the anodizing bath is higher than the pH of zero charge of the oxides as discussed in Section 4 for mixed Al-Ta anodic oxides.

N incorporation induces the formation of allowed localized states close to the valence band edges of the anodic oxides. Even though the pH of zero charge of HfO_2 is lower than 9 (pH_{pzc} = 7.1),[121] the anodic films grown in ABE have the same photoelectrochemical behaviour of anodic films grown in 0.1 M NaOH. Therefore, it is possible to state that N incorporation does not occur appreciably in the case of Hf and/or the corresponding localized states are very

close to valence band edge and do not induce any change in the photoelectrochemical behaviour of the oxide.

The same photoelectrochemical characterization has been performed for anodic films grown on Hf at different scan rates. In Table 5.1 the results obtained for films formed in 0.1 M ABE are summarized, confirming that the photoelectrochemical behaviour is almost independent of the growth rate.

Table 5.1 Optical transition (E_g^{opt}) and threshold energy (E_{th}) for Hf anodic films grown at different scan rates in 0.1 M ABE.

Growth scan rate / mV s^{-1}	E_g^{opt} **/ eV**	E_{th} **/ eV**
2	3.21	2.10
10	3.25	2.25
50	3.26	2.13
1000	3.19	2.25

5.3 Impedance Measurements

In Figure 5.5 electrochemical impedance spectra are reported in the Bode representation (i.e. impedance modulus and -phase angle vs frequency), relating to anodic oxides grown on Hf in both 0.1 M ABE and 0.1 M NaOH electrolytes, recorded at U_E = 3 V vs Ag/AgCl, i.e. under potential higher than the oxides flat band potential.

The impedance spectra can be very well simulated by the electrical circuit shown in the inset of Figure 5.5(b), consisting of R_{el}, accounting for the electrolyte resistance, in series with a parallel between R_{ox}, representative of the oxides resistance, and Q_{ox} introduced to model oxide capacitance. Fitting parameters are reported in Table 5.2.

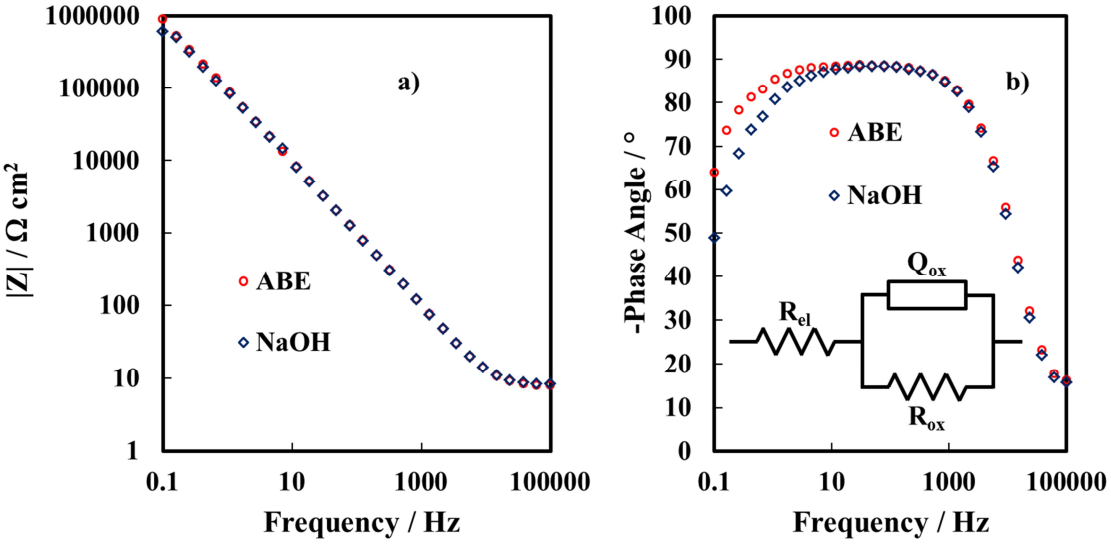

Figure 5.5 EIS spectra relating to Hf anodic films grown in ABE and NaOH electrolytes, recorded at 3 V vs Ag/AgCl in 0.25 M Na_2HPO_4. (a) Impedance modulus, (b) -phase angle. Inset: electrical equivalent circuit employed to model the metal/oxide/electrolyte interfaces.

Table 5.2 Fitting parameters relating to EIS spectra of 5 V Hf anodic oxides, grown in ABE and NaOH, using equivalent electric circuit of Figure 5.5(b).

Anodizing electrolyte	U_E / V vs Ag/AgCl	R_{el} / Ω cm^2	R_{ox} / Ω cm^2	Q_{ox} / S s^n cm^{-2}	n
0.1 M NaOH	3	8	9.61×10^5	1.78×10^{-6}	0.982
	-1	8	3.86×10^6	1.93×10^{-6}	0.974
0.1 M ABE	3	8	2.07×10^6	1.73×10^{-6}	0.985
	-1	8	1.13×10^7	1.85×10^{-6}	0.977

The very high R_{ox} values as well as the CPE exponent n close to 1 suggest that anodic oxides behave almost like pure capacitors, as already reported for anodic films grown on valve metals.[113,125] It is noteworthy to mention that R_{ox} for the film grown in ABE is slightly higher than that estimated for the anodic oxide grown in NaOH, thus suggesting the formation of a less defective oxide at pH = 9. EIS spectra at potential lower than U_{FB} (see Figure 5.6) were also recorded and, notably, they were very similar to the high potential EIS spectra, as also confirmed by the fitting parameters reported in Table 5.2.

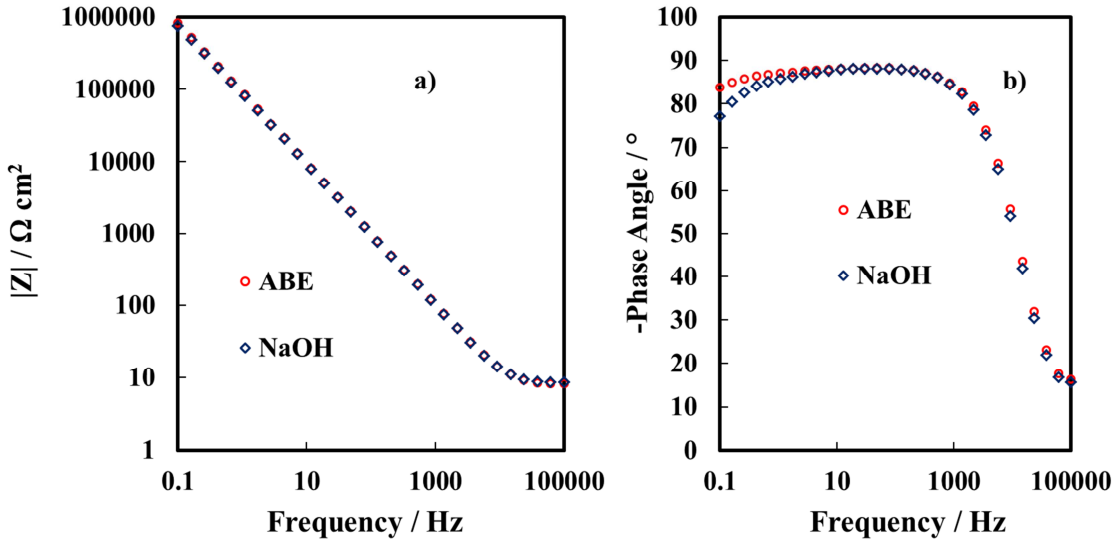

Figure 5.6 EIS spectra relating to Hf anodic films grown in ABE and NaOH electrolytes, recorded at - 1 V vs Ag/AgCl in 0.25 M Na_2HPO_4. (a) Impedance modulus and (b) -phase angle.

The EIS spectra recorded for anodic oxides grown at different scan rates are very similar to those reported in Figure 5.5 and Figure 5.6, thus suggesting that the impedance of the film is not significantly influenced by the growth rate in agreement with the photoelectrochemical findings. This is confirmed by the fitting parameters of the EIS spectra under anodic polarization (U_E = 3 V vs Ag/AgCl) and cathodic polarization (U_E = − 1 V vs Ag/AgCl) reported in Table 5.3 and Table 5.4.

In Figure 5.7 differential measured capacitance curves, recorded by sweeping electrode potential from 3 to − 0.8 V vs Ag/AgCl, are reported. For anodic oxides grown in both ABE and NaOH electrolytes at all constant a.c. signal frequencies (i.e. 10 kHz, 1 kHz and 100 Hz), capacitance is almost independent of electrode potential and slightly dependent on frequency, as expected for defective insulating oxides.[125] However, the measured capacitance was slightly different, with a higher value measured for the anodic oxide layer formed in alkaline solution.

Table 5.3 Fitting parameters relating to EIS spectra, recorded at 3 V vs Ag/AgCl, of 5 V Hf anodic oxides, grown in ABE at different scan rates, using equivalent electric circuit of Figure 5.5(b).

Growth scan rate / mV s^{-1}	R_{el} / Ω cm^2	R_{ox} / Ω cm^2	Q_{ox} / S s^n cm^{-2}	n
2	8	1.69×10^6	1.69×10^{-6}	0.986
5	8	1.01×10^6	1.77×10^{-6}	0.986
20	8	1.38×10^6	1.78×10^{-6}	0.984
50	8	1.36×10^6	1.85×10^{-6}	0.977
100	8	9.57×10^5	1.85×10^{-6}	0.984
200	8	1.37×10^6	2.20×10^{-6}	0.979
500	8	9.68×10^5	2.00×10^{-6}	0.983
1000	8	9.91×10^5	2.13×10^{-6}	0.980

Table 5.4 Fitting parameters relating to EIS spectra, recorded at - 1 V vs Ag/AgCl, of 5 V Hf anodic oxides, grown in ABE at different scan rates, using equivalent electric circuit of Figure 5.5(b).

Growth scan rate / mV s^{-1}	R_{el} / Ω cm^2	R_{ox} / Ω cm^2	Q_{ox} / S s^n cm^{-2}	n
2	8	1.99×10^6	1.83×10^{-6}	0.977
5	8	4.13×10^6	1.90×10^{-6}	0.978
20	8	1.75×10^6	1.90×10^{-6}	0.976
50	8	2.59×10^6	1.98×10^{-6}	0.970
100	8	6.63×10^5	1.92×10^{-6}	0.981
200	8	1.35×10^5	2.22×10^{-6}	0.980
500	8	6.63×10^6	2.14×10^{-6}	0.975
1000	8	1.28×10^6	2.38×10^{-6}	0.968

Assuming that the oxide can be modelled as a simple parallel plate capacitor, the oxide capacitance can expressed through Equation 4.1 that can be also written, by considering the roughness factor, as:

$$C_{ox} = \frac{\varepsilon \varepsilon_0 r}{d_{ox}} \qquad 5.2$$

Assuming that dielectric constant of HfO_2 is 19,[150] it is possible to estimate the oxide thickness from Equation 5.2 once the measured capacitance has been corrected for the Helmholtz double layer capacitance (i.e. 20 μF cm^{-2}).

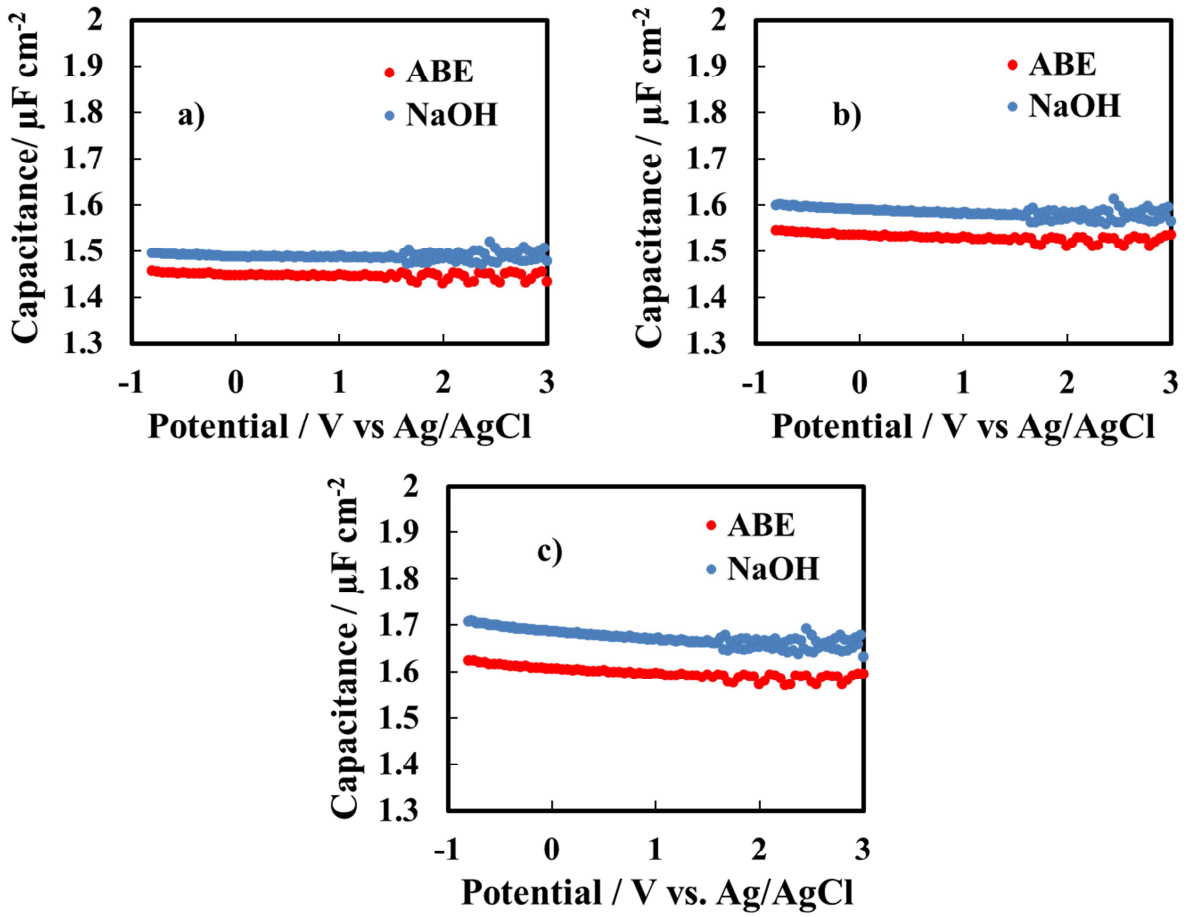

Figure 5.7 Measured series capacitance relating to 5 V Hf oxides grown in 0.1 M ABE and 0.1 M NaOH. A.c. signal frequencies: (a) 10 kHz, (b) 1 kHz and (c) 100 Hz.

To reduce the contribution to the capacitance arising from localized states inside the gap,[163] the capacitance measured at 10 kHz was used to estimate the oxides thicknesses that are reported in Table 5.5 and result do not differ significantly.

Table 5.5 Oxide thicknesses calculated according Equation 5.2 and 5.4.

Anodizing electrolyte	$d_{ox,Cap}$ / nm	$d_{ox,Sim}$ / nm
0.1 M NaOH	12.5	12.6
0.1 M ABE	12.9	12.4

5.4 Mechanism of Anodic Oxide Growth on Hafnium

The experimental results reported in Sections 5.1, 5.2 and 5.3 allowed insight into the mechanism of anodic oxide growth on Hafnium.

The growth of anodic films on valve metals (of which Hf is an example) is presented as a problem of ionic conduction at high electric field strength, complicated by the occurrence of transfer processes at the metal/oxide and oxide/electrolyte interfaces.[24] The main assumption of the *high field model* is that anodic oxide growth is sustained by hopping of mobile ions acquiring energy from thermal agitation plus the applied electric field sufficient to jump across the potential barrier and reach the next closest available site. Following Verwey, the movement of ions within the film is the rate determining step for the overall growth process, while Mott and Cabrera assumed as rate limiting step the entry of oxidized metal ions at the metal/film interface (see Section 2.1.1).

Regardless of the step controlling the overall growth process, according to the high field mechanism, an exponential dependence of the current density *i* on the electric field strength is expected, according to the Equation 2.4, that can be also expressed as:

$$i = i_0 \, exp \frac{q\alpha a(U_E - U_{FB})}{k_B T d_{ox}} \qquad 5.3$$

In Figure 5.8 the logarithm of the plateau current densities (averaged from at least 3 runs) as a function of electric field strength is reported, derived by anodizing Hf in 0.1 M ABE and 0.1 M NaOH, corresponding to different employed scan rates and derived according to Equation 5.1.

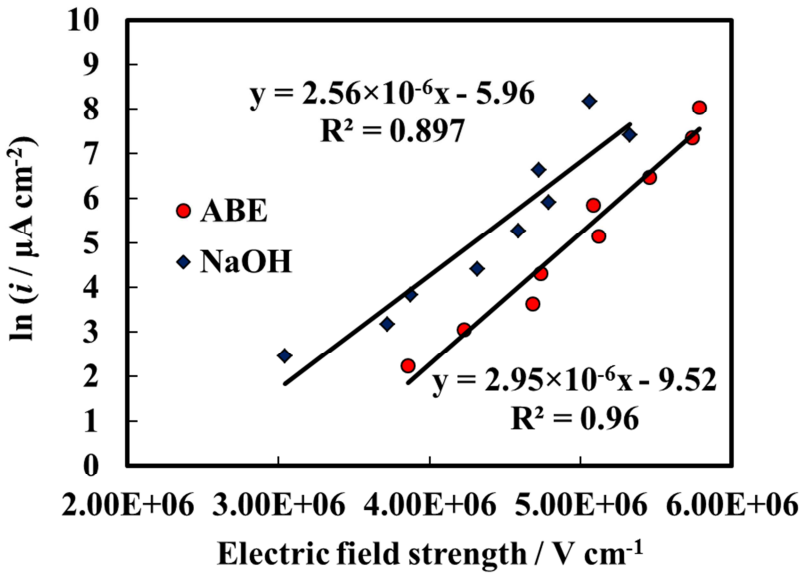

Figure 5.8 Tafel plot relating to Hf anodizing processes in 0.1 M ABE and 0.1 M NaOH.

A linear dependence of ln *i* on *E* supports the ability of the *high field model* in describing the anodizing of Hf. Electric field strength between ~ 3 and 5.8 MV cm^{-1} was estimated as a function of the growth rate, comparable with previous values reported in the literature.[24,129,164] From the linear fit of this plot, it is also possible to calculate the parameters describing the kinetic of growth of the anodic oxides, i_0 and αa. By assuming $q = 2\times1.6\times10^{-19}$ C, since according to previous results reported in the literature[28,36] anodic films growth for hafnium is almost entirely sustained by migration of O^{2-}, while Hf^{4+} ions are almost immobile with a transport number ≤ 0.05. From the slope of the best fitting line a half-jump distance of 3.8 Å was estimated, whilst an activation energy of 1.1 eV was estimated from the intercept for the anodizing process of Hf in 0.1 M ABE. A half-jump distance of 3.3 Å and an activation energy of 1.0 eV were estimated relating to Hf anodizing in 0.1 M NaOH. αa well compares to the activation distance reported by Young[24] and with hopping distances calculated theoretically,[165] while it is far from other values reported in literature (that are significantly lower than the value expected according to the lattice parameters of m-HfO_2, which is the

more stable hafnia polymorph at room temperature).[152,153]

The estimated barrier height was compared with other values reported in the literature and it was in very good agreement with the value reported by Young,[24] as well as with the value calculated theoretically by density functional theory.[165] Notably, in the latter work, the authors have also calculated the energy barrier for oxygen vacancy hopping, which is strongly dependent on the direction of motion, ranging from 90.47 meV along the <001> direction to 2814.79 meV along the <010> direction. The values estimated according to Figure 5.8 fall in this energy range.

The estimated kinetic parameters were used to simulate the potentiodynamic curves for the anodizing of Hf at 20 mV s^{-1} in 0.1 M ABE and in 0.1 M NaOH following the procedure described in literature.[166,167] The oxide thickness has been estimated according to the following equation:[167]

$$d_{ox} = d_0 + \frac{MW}{\rho zF}\int i_{form}dt = d_0 + \frac{MW}{\rho zF}\int \eta i_{tot}dt \qquad 5.4$$

with d_0 the thickness of the air-formed oxide film. If η is assumed to be constant, the film thickness can be computed by an iterative spreadsheet solution of Equations 5.3 and 5.4.

As shown in Figure 5.9(a), there is a very good agreement between the experimental and the simulated curves assuming d_0 = 15 Å, η ~ 1 and U_{FB} = − 0.8 V vs Ag/AgCl.

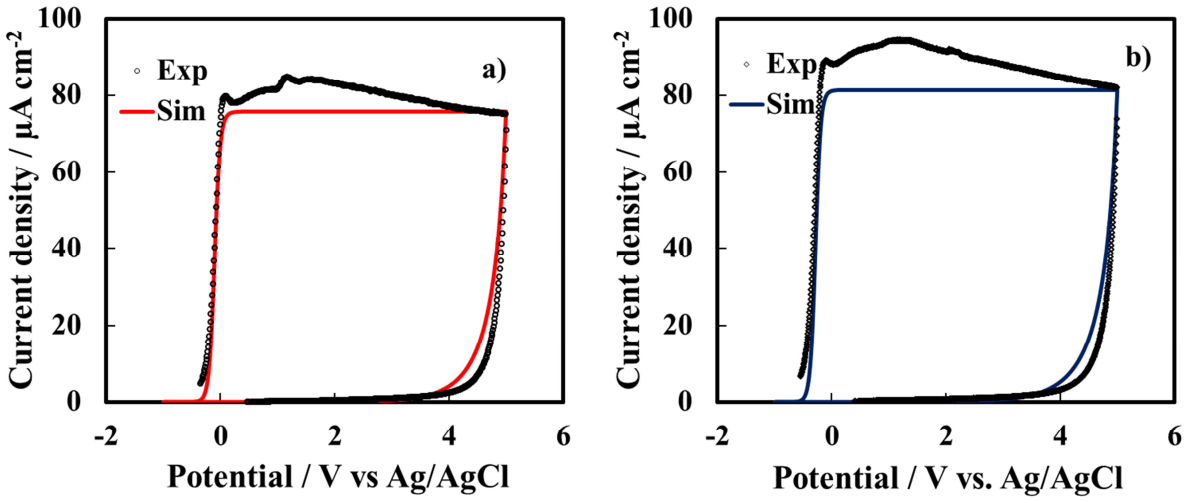

Figure 5.9 Experimental (symbols) and simulated (according to Equation 5.3, continuous lines) current density vs electrode potential curves relating to Hf anodic films growth in (a) 0.1 M ABE and in (b) 0.1 M NaOH. Growth scan rate: 20 mV s^{-1}.

Moreover, the oxide thickness estimated according to Equation 5.4 is almost coincident with that estimated from the capacitance. When the anodizing is performed in NaOH according to the kinetic parameters derived from Figure 5.8, assumption of $\eta \sim 1$ does not provide a good agreement between the thickness estimated from the capacitance and that estimated according to Equation 5.4. It is necessary to consider $\eta < 1$ and use αa and W derived from the growth curves recorded in ABE, where anodizing occurs at 100% efficiency. An efficiency of ~ 91% allows improvement of the fitting of the i-U_E curve, as shown in Figure 5.9(b). The thickness of the anodic oxide grown to 5 V vs Ag/AgCl in NaOH is very close to that estimated from the capacitance (see Table 5.5).

To get more insight into the phenomena responsible of an efficiency < 1, the oxide capacitance during potentiostatic polarization at 3 V vs Ag/AgCl in NaOH was measured. As shown in Figure 5.10, a current density of 0.3 µA cm^{-2} was measured during the 1st hour of polarization, but it became negligible for longer times. The capacitance (and consequently the oxide thickness) measured after each step of potentiostatic polarization (see Figure 5.10) remains almost constant, thus suggesting that the current is employed for oxide repairing and/or for oxygen evolution reaction.

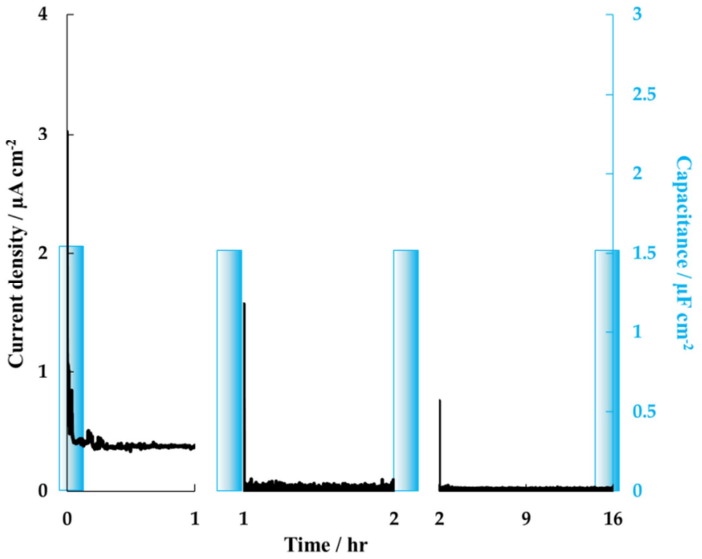

Figure 5.10 Capacitance (blue bars) and current density measurements vs time during potentiostatic polarization at U_E = 3 V vs Ag/AgCl relating to Hf anodic oxide grown in 0.1 M NaOH at 20 mV s^{-1}.

All the experimental findings can be used to sketch the energetic of the metal/oxide/electrolyte interface, as depicted in Figure 5.11. In order to position the energy levels of Hf anodic oxide, it is necessary to know Hf work function (3.9 eV)[134] and it is possible to set the oxide Fermi level, E_F^{ox}, according to the following equation:[162]

$$E_F^{ox} = -|e|U_{FB} + |e|U_{ref} \qquad 5.5$$

in which U_{ref} is the potential of the Ag/AgCl reference electrode with respect to the vacuum scale.[168]

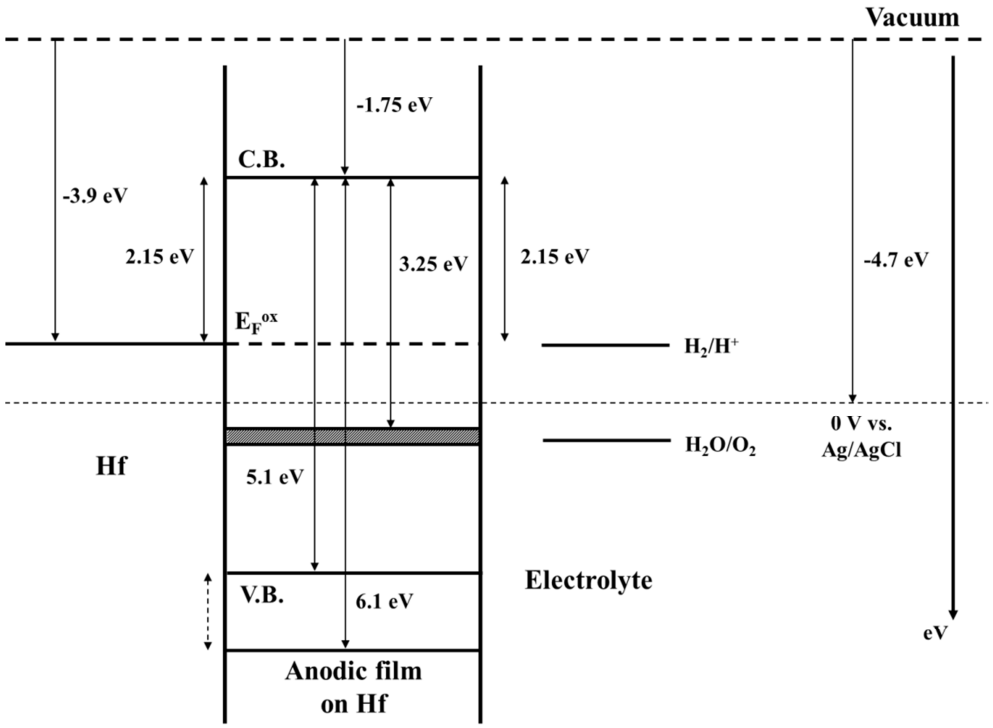

Figure 5.11 Approximate sketch of the energetic levels of metal/oxide/electrolyte interface for anodic films grown on Hf. Dotted arrow: energy interval in which valence band edge can be placed according to the literature.

The charge transfer for the oxygen evolution reaction at oxide films is usually explained in terms of electron tunnelling.[169] After the early stages of the anodizing process when oxide with thickness is > 2 nm, direct tunnelling is not probable, while it is likely that tunnelling occurs through localized states. The latter are transient states produced as a consequence of the mobile ions responsible of oxide growth and/or states generated by the presence of defects (for instance oxygen vacancies).

The more negative equilibrium potential for O_2 evolution reaction in alkaline solution (and, thus, the higher available overvoltage) can account for the presence of a larger electronic current dissipated during the oxide formation in NaOH with respect to ABE.

5.5 Concluding Remarks

Anodic films were grown to 5 V vs Ag/AgCl on mechanical polished Hf in 0.1 M ABE and 0.1 M NaOH potentiodynamically at different scan rates. The photoelectrochemical characterization revealed that band gap, flat band potential and Fowler threshold are not significantly influenced by the anodizing electrolyte as well as by the growth rate. Optical transitions from allowed localized states inside the band gap of the anodic oxides to the conduction band were indicated, and are associated with the presence of oxygen vacancies in the anodic oxide films. The conduction band edge was located at -1.75 eV with respect to the vacuum, according to the estimated Fowler threshold. The impedance measurements allowed the conclusion that the oxides behave as insulating materials and are high-*k* thin films, with dielectric constant of 19.

The dependence of the anodizing current on the growth rate was studied in the frame of the *high field model*. Anodizing in ABE proceeds at high efficiency with an activation energy of 1.1 eV and an activation distance of 3.8 Å, which are physically reasonable if compared with other results reported in the literature. The anodizing in alkaline solutions occurs at lower efficiency due to the presence of oxide dissolution phenomena and/or oxygen evolution reaction.

The experimental findings provided the energetic of the Hf/anodic HfO_2/electrolyte interface, which is crucial to evaluate any technological application of the oxide.

6 Growth of Anodic Oxides as a Function of the Metal Substrate Composition: Hf-Nb Mixed Oxides

High-*k* dielectrics play an essential role in DRAM memories and CMOS logic applications. With the further scaling of the dimensions of memory and logic devices, a suitable high-*k* material has to be chosen with a mandatory requirement: high dielectric constant for DRAM devices and high band gap CMOS logic applications.

HfO_2 is surely one of the most studied and employed dielectric material but several attempts can be found in the literature aimed to enhance its dielectric constant, e.g. by stabilizing at room temperature hafnia polymorphs (i.e. cubic and tetragonal) which have a higher ε with respect to monoclinic phase.[170] Mardare et al.[171] showed that anodizing of Hf-33at.%Nb alloy allows to grow thin oxides (14 nm thick) with a dielectric constant higher than that of pure HfO_2. Therefore, preparing mixed oxides can be a promising strategy to fabricate materials with enhanced properties with respect to anodic oxides grown on pure partner metals. For instance, anodizing Hf-Nb alloys can be a valuable and facile route to prepare high-*k* oxides since the very high dielectric constant value of pure Nb_2O_5.[154] However, in any electronic device, the leakage current must maintain very low values, in the order of 10^{-8} A cm^{-2} (in solid state devices) and the equivalent oxide (dielectric) thickness (EOT), estimated as:

$$EOT = d_{ox}\frac{\varepsilon_{SiO_2}}{\varepsilon_{ox}} \qquad 6.1$$

is required in the sub-nanometer range.

Anodizing of Hf proceeds differently with respect to Nb. For Hafnium the growth of the anodic oxide is mainly sustained by inward migration of O^{2-} ions from the oxide/electrolyte interface to the metal/oxide interface, since the transport number of Hf^{4+} is 0.05, and the corresponding anodic oxides are crystalline.[28,36] Moreover, for high formation voltage electronic current circulates across the oxide, leading to O_2 evolution, whose presence can be detrimental for a possible application of HfO_2 as dielectric. In contrast, Nb_2O_5 grows due to

the simultaneous migration of Nb^{5+} (whose transport number is 0.24-0.27)[28,32,172] and O^{2-} ions, and the corresponding anodic layers are amorphous[173,174] with no appreciable electronic current even at high formation voltages.

In the attempt to prepare high performances dielectrics of different thicknesses, the solid state properties of anodic films grown on sputtering deposited Hf-Nb alloys to several formation voltages (up to 100 V), i.e. thicknesses, were investigated. In particular, pure Hf, pure Nb and Hf-Nb alloys of several compositions (4, 19, 39, 57, 76 at.%Nb) were deposited by magnetron sputtering on glass and alumina substrates (see Section 3.1.2). The samples were then anodized to different voltages (5, 10, 20 and 100 V) potentiodynamically (thin films) and galvanostatically (thick films) in 0.1 M ammonium pentaborate and ammonium biborate electrolytes. Transmission electron microscopy and Grazing incidence X-ray diffraction were employed to study their structure as a function of Hf/Nb ratio and, thus, of the composition of metallic substrate to evidence the formation of crystalline or amorphous films. Photoelectrochemical measurements were performed to study the solid state properties of the oxides (band gap, flat band potential, conductivity type). Impedance measurements coupled with withstand voltage and leakage current estimates were carried out in order to have a comprehensive view of the dielectric properties of the layers.

6.1 Oxides Growth Kinetics

Voltage vs time curves recorded during anodizing in 0.1 M ammonium pentaborate at 5 mA cm^{-2} are shown in Figure 6.1(a) for Hf-rich oxides (≤ 39at.%Nb) and Figure 6.1(b) for Nb-rich oxides (≥ 57at.%Nb). Regarding pure Hf oxide growth, the initial slope of the curve is 1.57 V s^{-1}, close to that reported for the anodizing of hafnium in ABE electrolyte.[126] For voltage higher than 60 V, the d*V*/d*t* slope decreases due to the onset of oxygen evolution reaction with a consequence decrease in growth efficiency.

More abundant oxygen evolution is detected during the electrochemical oxidation of Hf-4at.%Nb alloy with a deviation of the curve from the linearity starting at ~ 35 V and with a slower voltage rise up to 100 V with respect to pure HfO_2 growth.

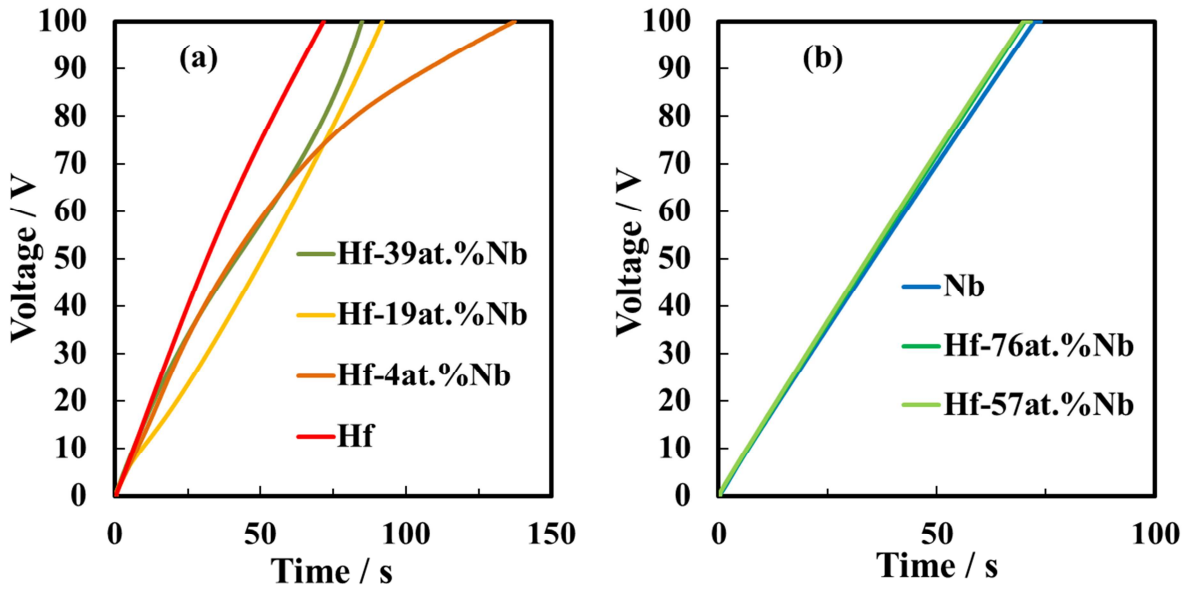

Figure 6.1 Voltage vs time curves of anodizing sputtering deposited (a) Hf and Hf-4at.%Nb, Hf-19at.%Nb, Hf-39at.%Nb alloys and (b) Hf-57at.%Nb, Hf-76at.%Nb alloys and pure Nb at 5 mA cm^{-2} in 0.1 M ammonium pentaborate.

This is an indication of a strong reduction of growth efficiency due to the occurrence of electrochemical processes other than film growth. A careful inspection of the growth curve of anodic film on Hf-4at.%Nb reveals a change in the slope from 1.34 V s^{-1} (up to 20 V) to 1.55 V s^{-1} (between 20 and 35 V) before the onset of oxygen evolution. This change is supposed to be related to the formation of an outer amorphous layer detected in the TEM image related to 50 V anodic film on this alloy (see below).

Curve slope markedly changes also during the growth of anodic films on Hf-19at.%Nb alloy in which the formation of an outer amorphous layer is also detected from TEM observations.

Regarding Nb-rich anodic oxides, Figure 6.1(b) shows that the curves are linear during the entire growth time regardless of alloy composition and the slope decreases from 1.43 V s^{-1} (Hf-57at.%Nb) to 1.38 V s^{-1} (pure Nb oxide), in agreement with growth curves slope already reported for the anodizing of pure Nb.[174] Growth efficiency associated to these Nb-rich oxides is close to 1 due to the absence of Faradaic process during the film thickening and to the

negligible dissolution rate of pure Hf and Nb oxides at electrolyte pH.

6.2 Grazing Incidence X-Ray Diffraction Characterization

Anodic oxides grown to 100 V on pure Hf and Hf-rich alloys (up to 39 at.%Nb) are crystalline as shown by XRD patterns reported in Figure 6.2 whilst anodic films formed on Nb-rich alloys (57 and 76at.%Nb) and pure Nb are amorphous. Regarding pure HfO_2, monoclinic crystalline phase but also tetragonal and cubic phases are present in the anodic film. The former phase is usually reported as thermodynamically stable at room temperature, whilst the latter are stable at high temperatures.[175]

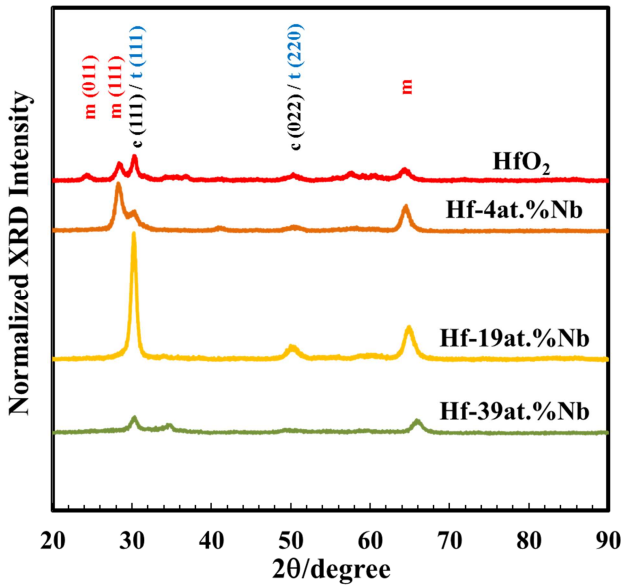

Figure 6.2 Grazing Incidence X-Ray Diffraction patterns of the oxides grown to 100 V on Hf and Hf-4at.%Nb, Hf-19at.%Nb, Hf-39at.%Nb alloys.

By adding 4at.%Nb to pure HfO_2, the three crystallographic phases are maintained with the monoclinic phase peak associated to (111) plane being the most intense. A further increase of Nb content in anodic oxides leads to the disappearance of the monoclinic phase peak with increasing in intensity of cubic (111) / tetragonal (111) peak[176,177] and to a small shift toward higher 2θ of monoclinic peak at 64.72°. The XRD patterns relating to Nb-rich and pure Nb

anodic oxides disclose peaks associated only to the cubic crystal structure of metallic substrates (not shown) without peaks relating to possible crystalline features of the oxides, therefore it is possible to conclude that Nb-rich oxides are amorphous.

6.3 Transmission Electron Microscopy Observations

Microstructure and thickness of anodically grown oxides were also studied by TEM observations. In Figure 6.3 ultramicrotomed sections of 100 V anodized pure Hf and Nb and Hf-Nb alloys (containing 4, 19 and 57 at.%Nb respectively) are shown.

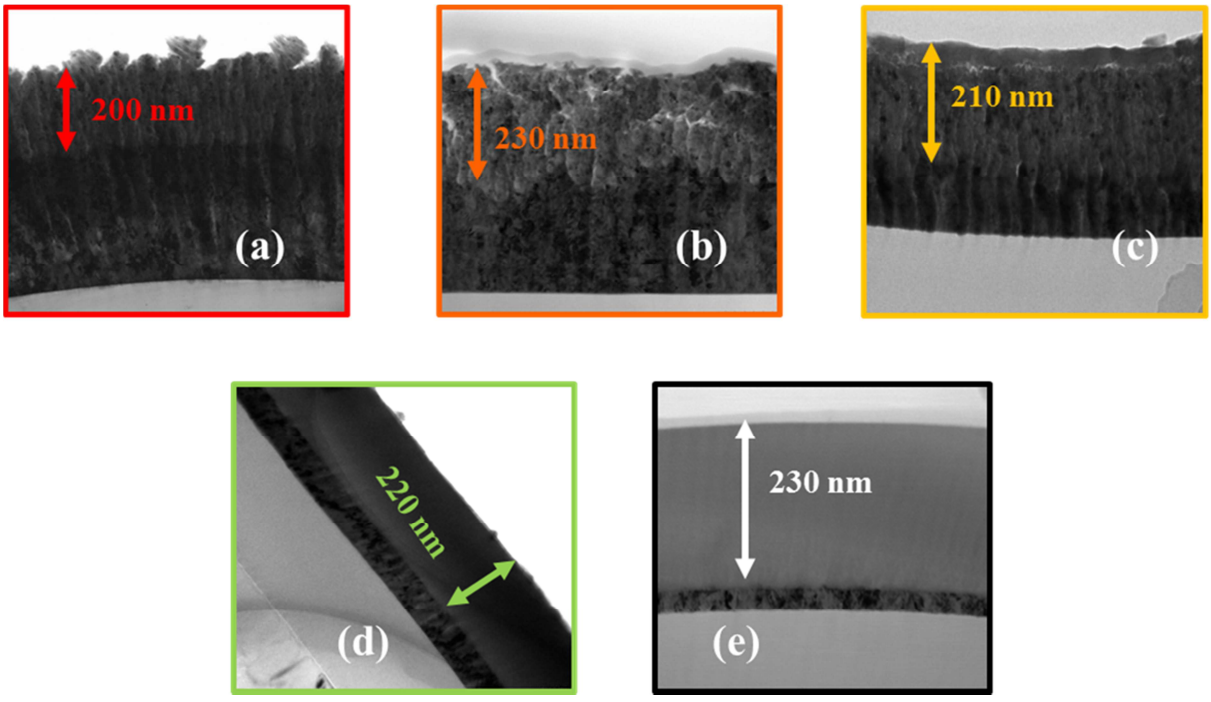

Figure 6.3 Transmission electron micrographs of ultramicrotomed sections of (a) pure Hf, (b) Hf-4at.%Nb, (c) Hf-19at.%Nb, (d) Hf-57at.%Nb and (e) pure Nb anodized at 5 mA cm^{-2} in 0.1 M ammonium pentaborate.

Nb-rich (≥ 57at.%Nb) oxide films and pure Nb oxide present completely featureless due to their amorphous nature and appear to be uniform in thickness. Anodic film thickness is almost constant in this range of composition varying from 220 nm for the oxide grown on Hf-57at.%Nb alloy to 230 nm for pure Nb_2O_5. The latter leads to an anodizing ratio of 2.3 nm V^{-}

[1], in agreement with previous results reported in literature.[174]

In contrast, pure Hf oxide appears nanocrystalline with a growth efficiency lower than 1 due to oxygen evolution during anodic film growth process from ~ 60 to 100 V (see above). This result is largely expected since it is already reported in literature that anodic films grown on Hf or on Zr are usually crystalline,[28,36] whilst anodic oxides grown on Nb are usually amorphous.[173,174] The structure of anodic film grown on Hf-4at.%Nb alloy up to 100 V is different with respect to pure Hf oxide since it is not uniform in thickness and it is rough at both metal/film and film/electrolyte interfaces. Furthermore, several cracks are evident in the middle part of the oxide due to a very abundant oxygen production during the growth starting from ~ 35 V.[178]

In order to better understand how the anodic film structure evolves during the growth, high-resolution transmission electron micrographs of FIB cross sections of the oxide grown on Hf-4at.%Nb up to 20 and 50 V were also performed (see Figure 6.4).

As shown, the 20 V anodic oxide is already nanocrystalline (the analysis of the fast Fourier transformation image shown in the inset of Figure 6.4(b) reveal the presence of a monoclinic phase) with a good uniformity in thickness without any crack inside it. The oxide thickness is 53 nm, i.e. the anodic film thickens of 2.65 nm V^{-1} up to 20 V. The structure of 50 V anodic film is slightly different (see Figure 6.4(c) and Figure 6.4(d)) with a thin amorphous outer layer with same composition with respect the inner nanocrystalline layer (as shown from EDXS elemental map of the specimen shown in Figure 6.5) and a thickness of 110 nm, i.e. an anodizing ratio of 2.2 nm V^{-1} lower than that associated to 20 V anodic film. This result confirms that, due to the onset of oxygen evolution reaction, the growth efficiency decreases during the film formation on Hf-4at.%Nb alloy.

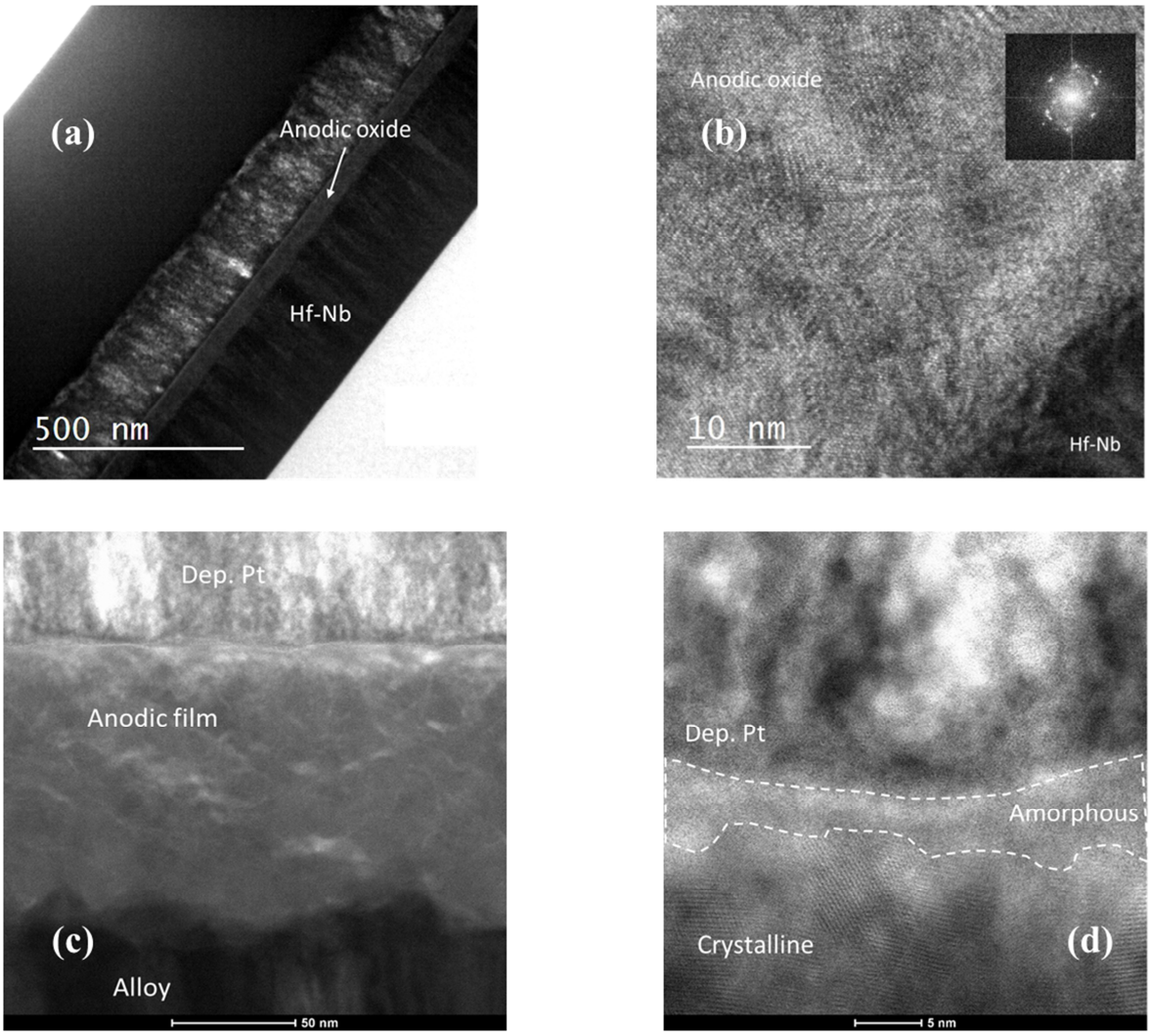

Figure 6.4 High-resolution transmission electron micrographs of cross sections of the oxide grown on Hf-4at.%Nb to (a),(b) 20 V and (c),(d) 50 V in 0.1 M ABE.

Similar structure is revealed by TEM micrograph of ultramicrotomed cross section of 100 V anodic film grown on Hf-19at.%Nb (see Figure 6.3(c)). An amorphous layer is present at the film/electrolyte interface but no cracks are visible inside the oxide since no oxygen evolution reaction occurs during the growth. From TEM inspections of anodic oxides, a crystalline-amorphous transition takes place by increasing Nb content in metallic substrate in agreement with GIXRD patterns.

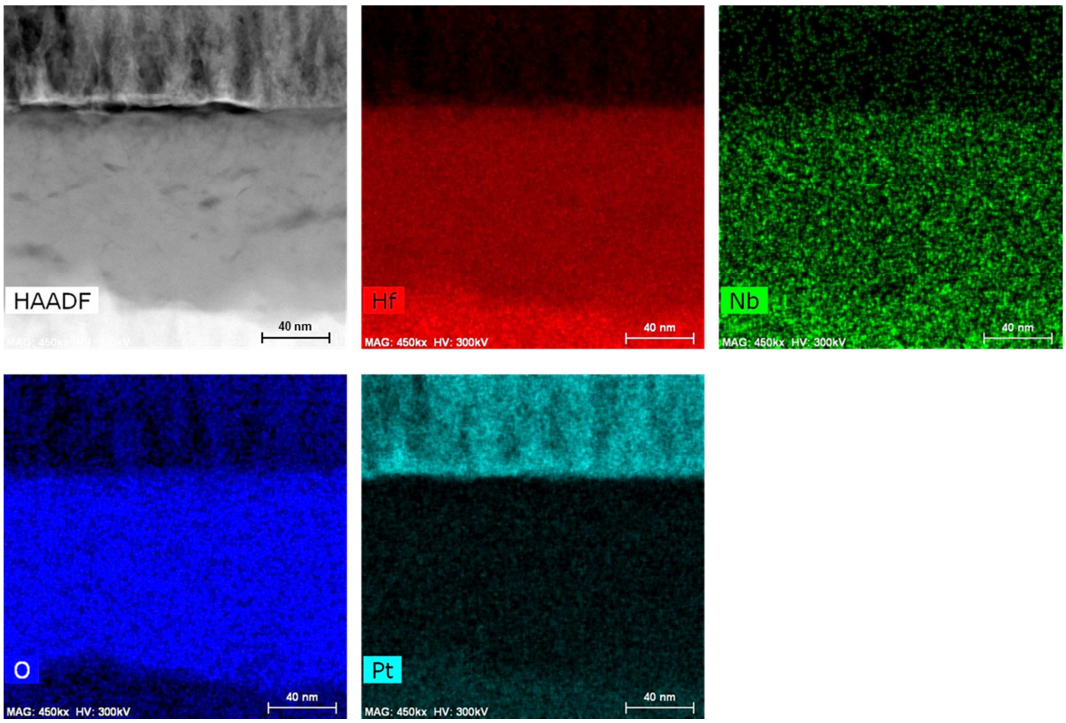

Figure 6.5 High angle annular dark field transmission electron micrograph and EDXS elemental map of a cross section of the anodic oxide grown on Hf-4at.%Nb alloy at 5 mA cm^{-2} in 0.1 M ABE up to 50 V.

6.4 Glow Discharge Optical Emission Spectroscopy

GDOES elemental depth profiles are shown in Figure 6.6 for anodic oxides grown on Hf-4at.%Nb, Hf-19at.%Nb, Hf-57at.%Nb and Hf-76at.%Nb alloys to 100 V. Hf and Nb are present throughout the whole film thicknesses with the presence of B species in the outer part of the oxide layer.

The oscillations in the signals of Hf and Nb are due to optical interference. No enrichment or layered structures are detected regardless oxide composition despite very different transport number of Hf^{4+} (0.05) in the growth of pure crystalline HfO_2[28,36] and Nb^{5+} (0.24 - 0.27) in the growth of pure amorphous Nb_2O_5.[28,32,172] This result is typically explained in the frame of M^{z+}-O^{2-} bond energies strength: the higher is the bond strength, the lower is the current carried by the specific cation during the anodic film growth.[36,174] Since the bond energies related to Nb^{5+}-O^{2-} and Hf^{4+}-O^{2-} are not so different (329 kJ mol^{-1} and 283 kJ mol^{-1}

respectively), it is quite reasonable that Nb and Hf are present throughout the whole films thickness without any layered structure, in agreement also with the results reported in literature for a similar system (i.e. anodic oxides grown on Hf-Al alloys).[36] The incorporation of B species only in an outer layer can be also rationalized taking into account a higher bond strength B^{3+}-O^{2-} (526 kJ mol^{-1}) with respect to that of the two M^{z+}-O^{2-} bonds, thus B is quite immobile during the growth.

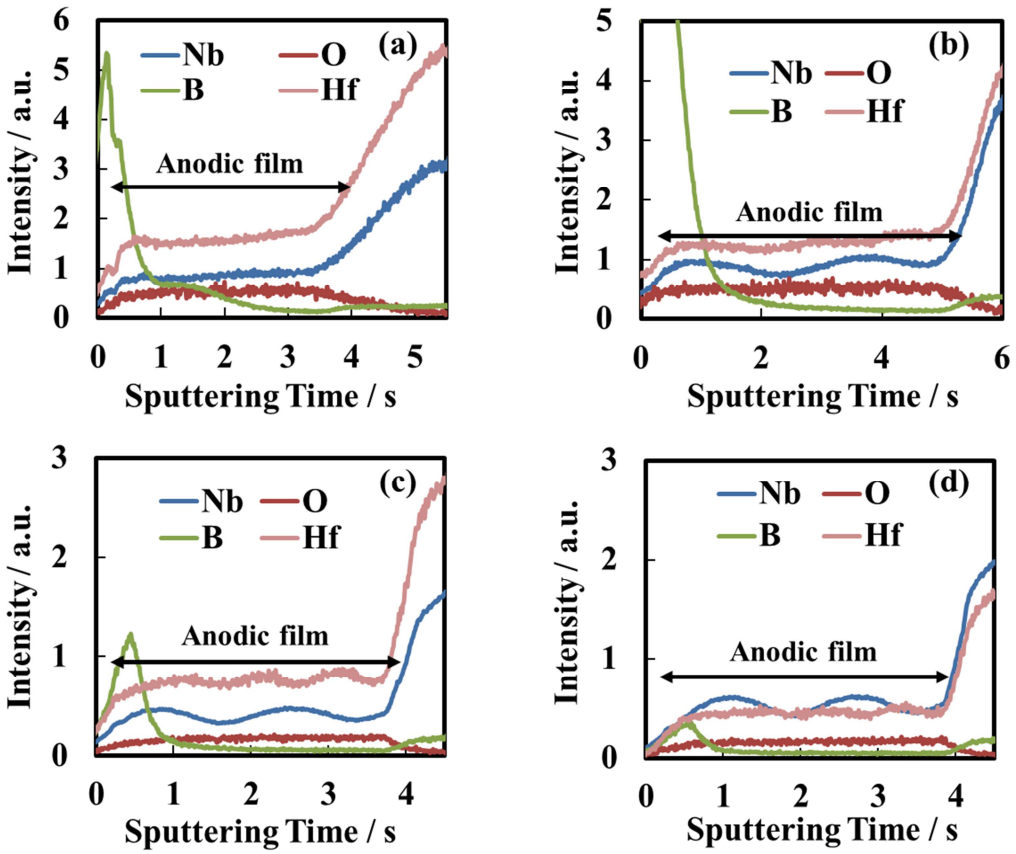

Figure 6.6 GDOES elemental depth profiles for (a) Hf-4at.%Nb, (b) Hf-19at.%Nb, (c) Hf-57at.%Nb and (d) Hf-76at.%Nb alloys anodized at 5 mA cm^{-2} to 100 V in 0.1 M ABE.

It is well known that the anodizing of pure Hf or pure Zr leads to the formation of crystalline oxides, and that the transport number of cations (i.e. Hf^{4+} or Zr^{4+}) is close to 0 so that the growth is predominantly carried out by oxygen anions coming from the electrolyte and

migrating toward the metal/oxide interface according to the direction imposed by the electric field. Thus, the anodic film thickening predominately occurs at this interface. On the contrary, for other valve metals like Nb, amorphous oxides are grown by anodizing and the transport number of cation is not negligible so that the anodic film thickens due to the simultaneous migration of both Nb^{5+} and O^{2-}. From these results, it is quite complicated to think the growth of an amorphous outer layer since cations should not migrate into the inner crystalline layer. For this reason, it is supposed that amorphous domains are present also into the crystalline matrix of the oxides grown on the alloys with Nb content up to 39at.% so that cations migrate through the inner layer to form the amorphous layer.

The formation of an amorphous outer layer is also supported from the presence of B species in the outer part of the oxide that can stabilize the growth of anodic film with no long range order, as reported in literature for other oxides grown on valve metals alloys.[179] According to these results and previous papers reported in literature,[180] it is possible to state that the outer amorphous layer is formed at the film/electrolyte interface by migration of cations and the inner layer develops at the alloy/film interface.

6.5 Photoelectrochemical Characterization

In Figure 6.7 photocurrent spectra (photocurrent vs irradiating wavelength curves) recorded at 5 V vs Ag/AgCl relating to anodic oxides grown to 10 V vs Ag/AgCl on the investigated Hf-Nb alloys are reported. All the oxide films result to be photoactive under anodic polarization, even Hf-rich anodic oxides, and the intensity of photocurrent signal increases by increasing the Nb content in the oxide.

In the case of anodic HfO_2 and Nb-doped HfO_2, E_g^{opt} was related to the optical transitions between localized states, due to the presence of negatively charged oxygen vacancies, and conduction band extended states.[159,160] Considering indirect optical transitions,[15] E_g^{opt} was calculated for all the investigated mixed anodic oxides (as shown in Figure 6.8) and the values are summarized in Table 6.1.

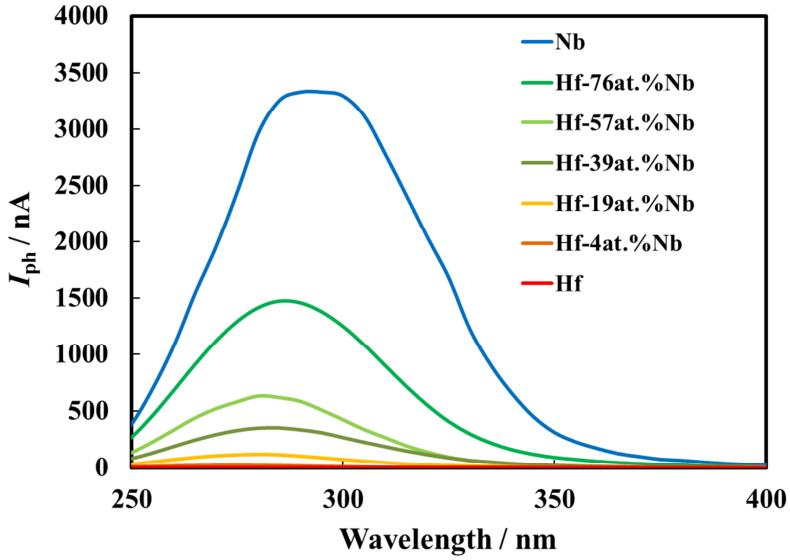

Figure 6.7 Raw photocurrent spectra relating to anodic oxides grown to 10 V vs Ag/AgCl on all the investigated samples, recorded at 5 V vs Ag/AgCl in 0.1 M ABE.

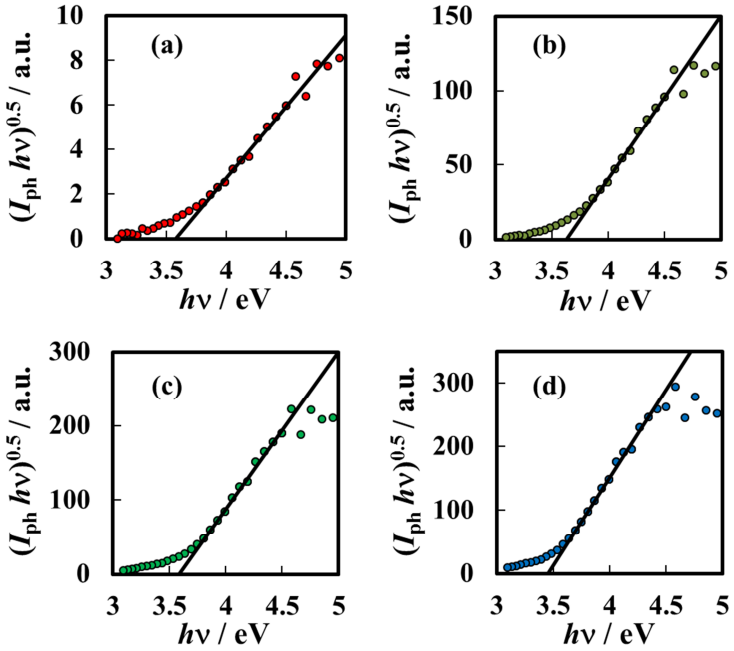

Figure 6.8 E_g^{opt} estimate by assuming non direct optical transitions relating to anodic oxides grown to 10 V vs Ag/AgCl on (a) pure Hf, (b) Hf-39at.%Nb, (c) Hf-57at.%Nb, and (d) pure Nb.

Table 6.1 E_g^{opt} estimated from $(I_{ph}\ h\nu)^{0.5}$ vs $h\nu$ plot for all the investigated anodic oxides.

Base alloy	E_g^{opt} / eV
Hf	3.58
Hf-4at.%Nb	3.85
Hf-19at.%Nb	3.75
Hf-39at.%Nb	3.63
Hf-57at.%Nb	3.75
Hf-76at.%Nb	3.58
Nb	3.45

The optical absorption threshold energy is almost independent on the films composition ranging between 3.8 ± 0.05 eV for Hf-rich oxides (Hf-4at.%Nb) and 3.45 ± 0.05 eV for pure Nb oxide.[14] Only for anodic oxide grown on Hf-4at.%Nb, a second optical absorption threshold was detected with a value of 2.75 ± 0.05 eV, regardless of anodic or cathodic polarization.

The detected anodic photocurrent for Hf-rich oxides is supposed to be related to optical transitions between localized and extended states. On the contrary, the much lower E_g of pure Nb_2O_5 allows us to detect photocurrent coming from optical transitions between O 2p-band (valence band) and Nb d-band (conduction band) states. This means that there is probably a threshold film composition for which, for higher Nb content, it is possible to estimate the oxide E_g (Nb_2O_5-like band structure) and, for lower Nb content, it is not possible to estimate the actual oxide E_g but only an optical threshold energy related to transitions between localized and extended states (HfO_2-like band structure).

Photocharacteristics were also recorded by scanning U_E toward cathodic direction at 10 mV s^{-1} under several irradiating wavelengths for all the investigated oxides in order to get information about the nature of anodic films (e.g. semiconducting or insulating) and the flat band potential value, U_{FB}, that is correlated to the Fermi level of the oxides, E_F^{ox}, through the Equation 5.5. I_{ph} vs U_E curves recorded at λ = 300 nm (i.e. $h\nu$ = 4.13 eV) are shown in Figure 6.9. For all the investigated specimens, recorded photocurrent is anodic (see phase angle in

Figure 6.9) and its intensity decreases by scanning U_E toward cathodic direction.

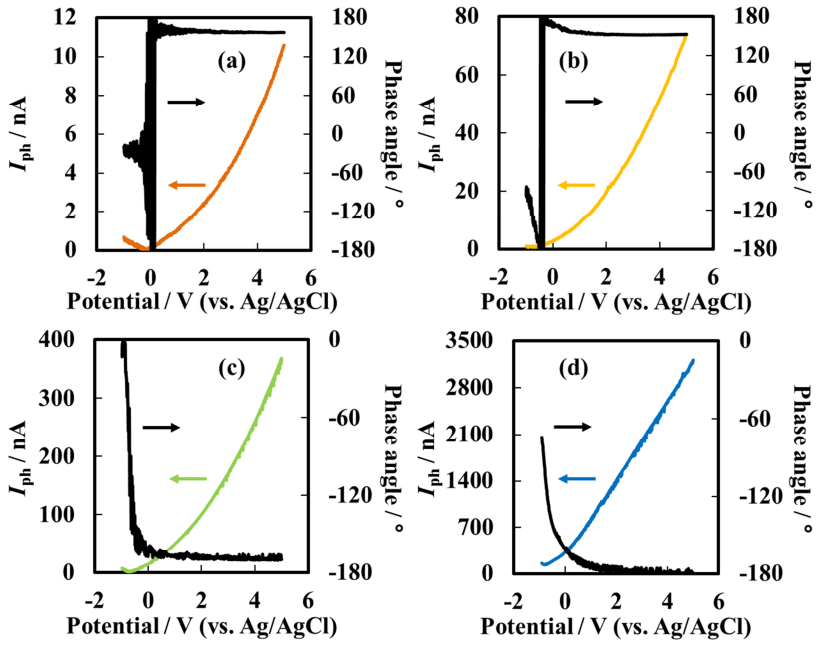

Figure 6.9 Photocurrent and phase angle vs potential curves relating to 10 V anodic oxides grown on (a) Hf-4at.%Nb, (b) Hf-19at.%Nb, (c) Hf-57at.%Nb, and (d) pure Nb. Irradiating wavelength: 300 nm. Potential scan rate: 10 mV s^{-1}.

In some cases, e.g. oxide grown on Hf-4at.%Nb alloy, a change in photocurrent sign is detected as typical of insulating materials for which both anodic and cathodic photocurrent can be generated depending on the direction of electric field across the layer, i.e. depending on applied potential with respect to the oxide flat band potential.[113] For this reason, photocurrent sign inversion potential, U_{inv}, is usually considered as a proxy of oxides U_{FB}.

The shape of the measured photocurrent vs applied potential curves can provide important information regarding possible recombination phenomena of photogenerated carriers. Thus the photocharacteristics can be fitted according the power law:

$$I_{ph}{}^{n} \propto U_E \qquad 6.2$$

The best fitting exponent n for all the investigated oxides is reported in Table 6.2.

Table 6.2 Parameters obtained by fitting the experimental photocharacteristics recorded for all the 10 V anodic oxides according to the power law $I_{ph}{}^{n} \propto U_E$.

Base alloy	Wavelength / nm	n
Hf	260	Not reliable
	300	
Hf-4at.%Nb	260	0.50
	300	0.50
Hf-19at.%Nb	260	0.55
	300	0.50
	340	0.50
Hf-39at.%Nb	260	0.65
	300	0.50
	340	0.55
Hf-57at.%Nb	260	0.60
	300	0.50
	340	0.40
Hf-76at.%Nb	260	0.75
	300	0.60
	340	0.55
Nb	260	1.40
	300	1.00
	340	0.90

A supralinear behaviour (n < 1) of the photocharacteristics is exhibited for almost all the specimens with the exception of pure Nb_2O_5. This behaviour is usually associated to the presence of bulk and surface recombination phenomena of the photogenerated carriers as well as geminate recombination effects (see Section 4.4). It is noteworthy to mention that n is quite independent on irradiating photon wavelength for anodic films grown on alloys with Nb content lower than 57at.% (i.e. crystalline oxides) whilst it decreases with increasing λ for the amorphous films (oxides with Nb content ≥ 57at.%Nb), as expected for that materials in

which the mobility of electrons and holes is usually very low and strongly depends on the irradiating photon energy.

6.6 Differential Capacitance Measurements and Electrochemical Impedance Spectra

In order to get information on dielectric properties of the investigated oxides, differential capacitance measurements were carried out. In Figure 6.10(a) the measured series capacitance for 10 V anodic oxides are reported as a function of Nb content, recorded from 5 V to - 1 V vs Ag/AgCl and a.c. frequency of 1 kHz.

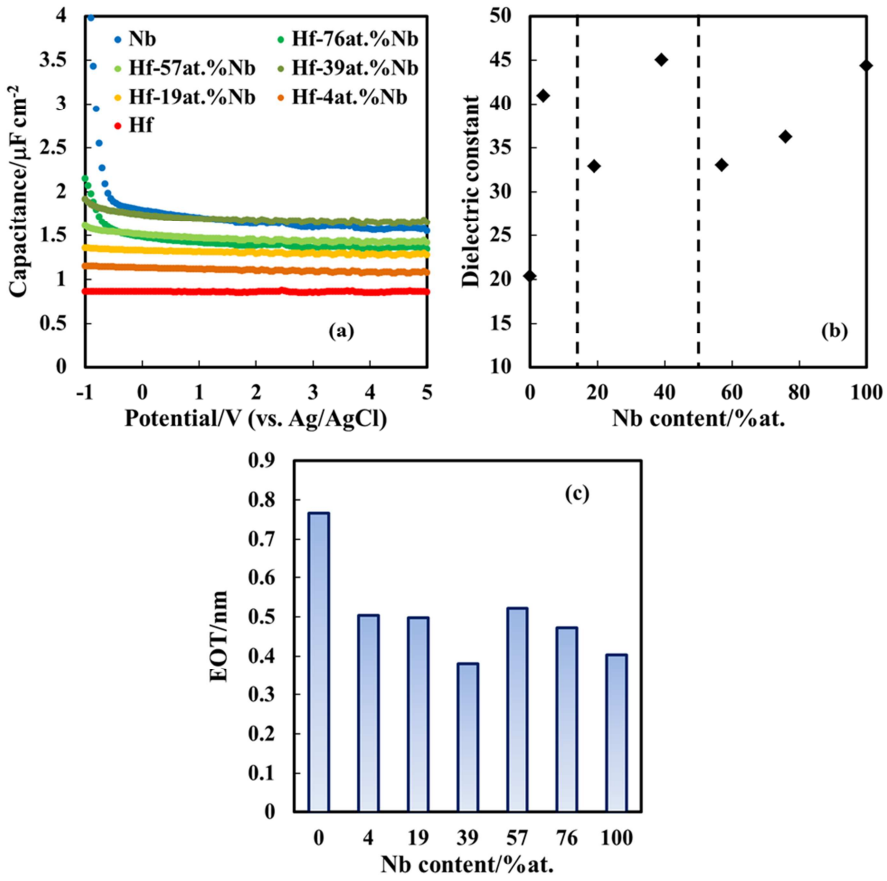

Figure 6.10 (a) Measured series capacitance relating to all the investigated anodic layers grown to 10 V vs Ag/AgCl.. Characterization solution: 0.25 M Na_2HPO_4. (b) Dielectric constant for all the investigated anodic oxides as a function of Nb content. (c) Equivalent oxide thickness for all the 2 V anodic oxides.

It is possible to note that for anodic films grown on Hf-Nb alloys with Nb content ≤ 19at.%, C_{series} is almost independent from electrode potential as typical of insulating materials, whilst C_{series} relating to oxides with Nb content ≥ 39at.% increases by sweeping U_E toward cathodic potentials as typical of n-type semiconductors.[143] This behaviour is more evident recording differential capacitance curves at lower a.c. frequencies, e.g. 100 Hz and 10 Hz. Capacitance dependence on base alloy composition is not linear with the maximum value recorded for the mixed oxide grown on Hf-39at.%Nb alloy. From these measurements, assuming that the oxide capacitance can be described by a parallel plate capacitor model, it is also possible to estimate the oxides dielectric constant from the Equation 4.1, where C_{ox} was calculated by considering the value of C_{series} at high band bending and high frequency and by subtracting to it the Helmholtz double layer capacitance contribution, $C_H \approx 20$ μF cm^{-2} in aqueous solution.[92,125] Oxides dielectric constants are reported in Figure 6.10(b) as a function of Nb content in the oxides. It is possible to distinguish three different composition ranges corresponding to three different anodic film structures: 1) pure anodic HfO_2 and anodic oxide on Hf-4at.%Nb (formation voltage < 50 V), that are entirely crystalline; 2) anodic mixed oxides composed by an inner crystalline layer and an outer thin amorphous layer (anodic film on Hf-19at.%Nb and Hf-39at.%Nb); 3) anodic mixed oxide with a Nb content ≥ 57at.%, that are completely amorphous. Notably, the oxide grown on Hf-4at.%Nb and Hf-39at.%Nb have a dielectric constant higher than those corresponding to pure oxides.

The addition of small amount of Nb (namely 4at.%) allowed to get an anodic oxide with a dielectric constant of 41, thus significantly higher than that estimated for Nb-free HfO_2. Moreover, as disclosed in Figure 6.10(b) the highest ε_{ox} is measured for the mixed oxide grown on Hf-39at.%Nb alloy (i.e. 45), which is roughly twice the dielectric constant of pure HfO_2 (19)[150] and comparable to the dielectric constant of Nb_2O_5 (40 - 50).[125,154] Therefore, anodizing valve metals alloys of tailored composition is a promising strategy to prepare hafnia-based dielectric with dielectric constant higher than that of HfO_2, as an alternative to typical strategies of electronic industry, e.g. to stabilize at room temperature HfO_2 in higher symmetry tetragonal and cubic phases by doping.[170]

Assuming that DRAM MIM_{cap} work under potential difference in the order of 1 V,[148] a formation voltage of 2 V can be selected to provide the oxides thickness according to the corresponding anodizing ratio. Knowing the oxide dielectric constant, it is possible to estimate the equivalent oxide thickness, EOT, defined by Equation 6.1, whose values are reported in Figure 6.10(c). Incorporation of Nb into HfO_2 allows to get EOT of ~ 0.5 nm for anodic films on Hf-4at.%Nb and Hf-19at.%Nb, while even lower (0.38 nm) with anodic oxide on Hf-39at.%Nb. This result is notable since anodic thin films grown on Hf-4at.%Nb have high band gap and low EOT, being suitable for the use in MIM_{cap} for DRAM memories.

In Figure 6.11 EIS spectra relating to all the investigated 20 V anodic oxides recorded at 8 V vs Ag/AgCl are reported. The electrochemical impedance spectra can be very well simulated by the electrical equivalent circuit shown in the inset of Figure 6.11(b), consisting of R_{el}, relating to the electrolyte resistance, in series with a parallel between R_{ox}, representative of the oxides resistance, and the Q_{ox} introduced to model the oxide capacitance.

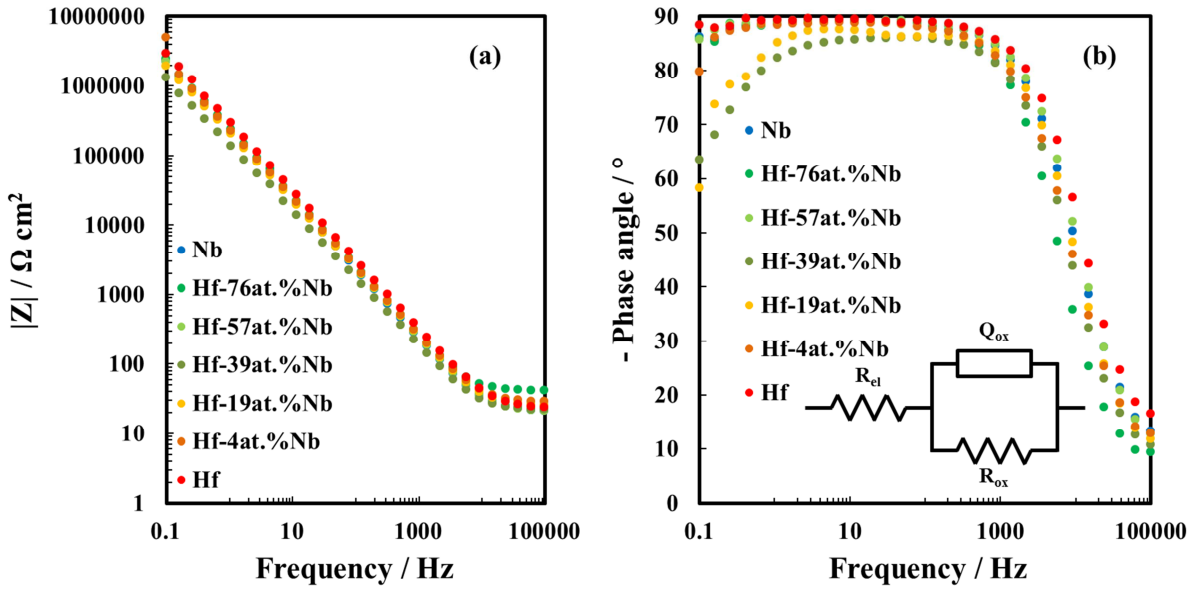

Figure 6.11 Bode representation of EIS spectra relating to all the investigated anodic oxides grown to 20 V vs Ag/AgCl, recorded at U_E = 8 V vs Ag/AgCl in 0.25 M Na_2HPO_4. Inset: Electrical equivalent circuit employed to model the metal/oxide/electrolyte interfaces.

The high |Z| and a phase angle very close to -90° for pure HfO_2 and amorphous mixed oxides (i.e. oxides with Nb content ≥ 57at.%) confirm the formation of blocking oxides. In Table 6.3 fitting parameters of 20 V anodic layers EIS spectra are reported. Very high values of the oxides resistance as well as the CPE exponent n close to 1 leading to the conclusion that anodic layers behave almost like pure capacitors.

Table 6.3 Fitting parameters relating to the EIS spectra shown in Figure 6.11.

Base Alloy	R_{el} / Ω cm^2	R_{ox} / Ω cm^2	Q_{ox} / S s^n cm^{-2}	n	χ^2
Hf	24	9.0×10^7	5.1×10^{-7}	0.99	0.0019
Hf-4at.%Nb	29	4.6×10^7	6.8×10^{-7}	0.98	0.0016
Hf-19at.%Nb	25	4.2×10^6	7.5×10^{-7}	0.97	0.0013
Hf-39at.%Nb	21	2.8×10^6	1.2×10^{-6}	0.96	0.0019
Hf-57at.%Nb	21	4.5×10^7	6.9×10^{-7}	0.99	0.0018
Hf-76at.%Nb	30	5.0×10^7	6.3×10^{-7}	0.99	0.0021
Nb	22	3.8×10^7	7.0×10^{-7}	0.99	0.0019

6.7 Withstand Voltage and Leakage Current Measurements

In order to fully evaluate the dielectric properties of the films, further measurements to estimate the withstand voltage and the leakage current of the investigated anodic layers have been carried out. Figure 6.12 shows the *V-t* curves relating to the galvanostatic re-anodizing step performed on all the investigated oxides at 0.5 mA cm^{-2} in the same electrolyte used for the first anodizing procedure.

In the case of amorphous anodic oxides (i.e. films with Nb content ≥ 57at.%), an initial voltage jump equal to the formation voltage is detected followed by a voltage increase with a slope lower than that relating to the first anodizing step. This is expected, according to the Faraday's law, since the current density relating to the re-anodizing step is 10 % of the current

density relating to the initial anodic oxide growth.

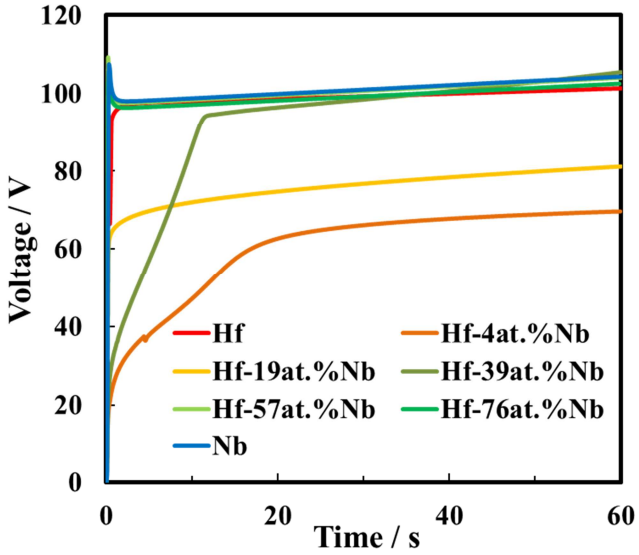

Figure 6.12 Voltage vs time curves related to re-anodizing procedure of all the investigated anodic oxides at 0.5 mA cm^{-2} in 0.1 M ABE for the evaluation of oxides withstand voltage.

For these oxides, the withstand voltage values are close to the formation voltages, thus confirming the reliability as dielectrics of these layers. Almost the same behaviour is reported for the anodic film grown on pure Hf with an estimated withstand voltage close to the values related to the amorphous oxides. A consistent delay (~ 30 s) in reaching the formation voltage value is reported for the anodic oxide grown on Hf-39at.%Nb whilst, in the case of the anodic layers grown on Hf-4at.%Nb and Hf-19at.%Nb alloys, the voltage recorded during the re-anodizing step does not reach the formation value, even after 1 min. The latter result leads to withstand voltages far from that estimated for amorphous oxides and pure HfO_2, whilst a higher withstand voltage (91.4 V) is estimated for the oxide grown on Hf-39at.%Nb alloy. These behaviours can be explained considering that, during the re-anodizing step, the defects present into the oxide structure are repaired so that, the more defective is the oxide, the longer is the delay in reaching the oxide formation voltage.[181]

Another important parameter in the evaluation of the dielectric properties of the anodic layers

is the leakage current, i_L, the latter being the current measured after 900 s by polarizing the oxides at 75 V (i.e. 75 % of the formation voltage).

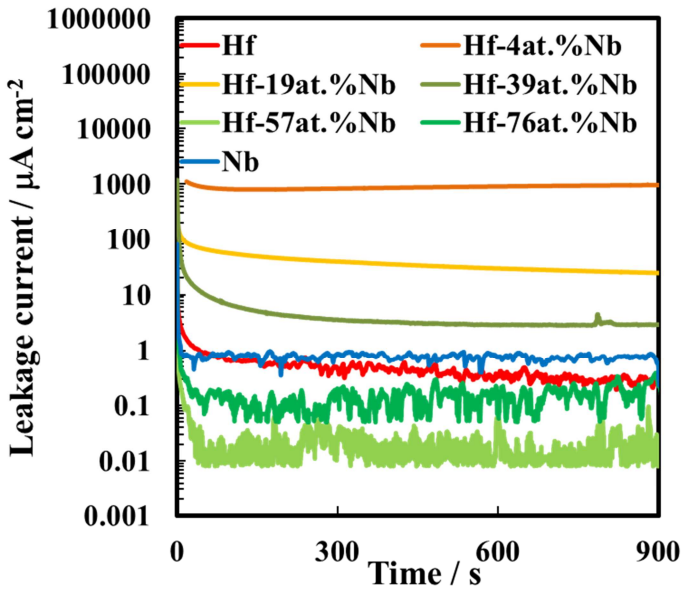

Figure 6.13 Leakage current measured for all the investigated 100 V anodic oxides by applying 75 V for 900 s.

Under potentiostatic polarization, current density decreases quickly during the first seconds and then reaches a plateau value for long times, as shown in Figure 6.13 in which all the leakage current measurements are shown. The highest leakage current is recorded for the anodic film grown on Hf-4at.%Nb, in the order of 1 mA cm^{-2}, due to the oxygen evolution during the measurement whilst the lowest leakage currents are detected for amorphous oxides and for pure HfO_2.

6.8 The Interplay between Structure and Dielectric Properties

In order to better evaluate the dielectric properties of the anodic layers, it is important to understand what is the relationship between structure (morphological and electronic properties) and performances (withstand voltage and leakage current). At this aim, all the results obtained from photoelectrochemical measurements were used to sketch the energetics

of the metal substrate/anodic oxide/electrolyte interfaces, as shown in Figure 6.14 for anodic oxides grown on Hf-4at.%Nb, Hf-19at.%Nb and Hf-57at.%Nb alloys.

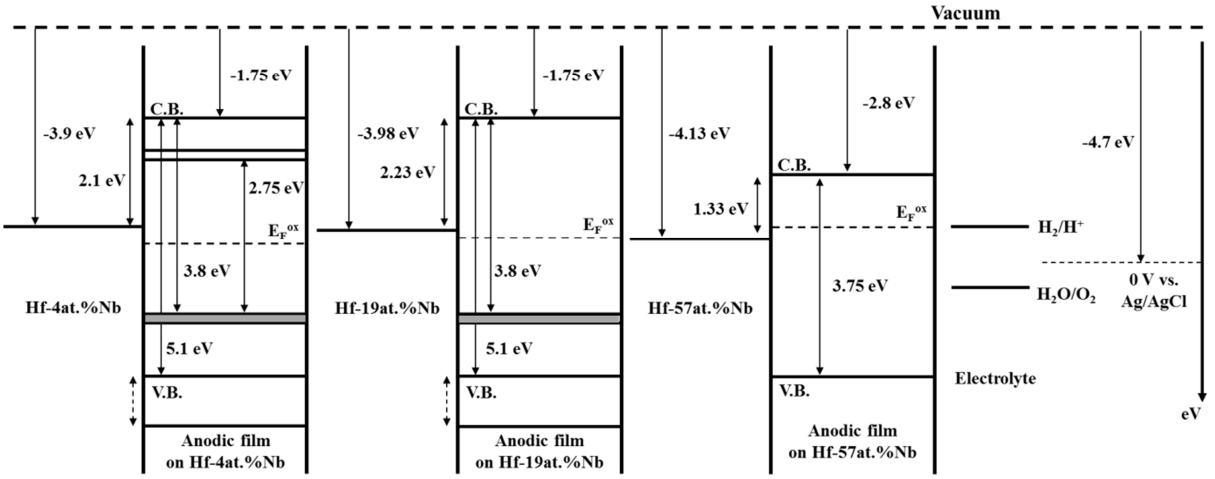

Figure 6.14 Sketch of the energetic levels of metal/oxide/electrolyte interface for anodic films grown on Hf-4at.%Nb, Hf-19at.%Nb and Hf-57at.%Nb alloys. Dotted arrow: energy interval in which valence band edge can be placed according to the literature. Grey localized states in the band gap: full electron states. White localized states in the band gap: empty electron states.

In order to set the position of energy levels of anodic layers, it is necessary to know the work function of metallic substrates, calculated as the arithmetic mean of pure Hf and pure Nb work functions (3.9 and 4.3 eV respectively),[182] and the band gap values and flat band potentials of the oxides that are estimated through the photoelectrochemical measurements (see above).

In Figure 6.14 the energy levels relating to the two main redox reactions, involving aqueous electrolyte, that sustain the carriers conduction were also added:

i. $H_2 \rightarrow 2H^+ + 2e^-$ $U_{eq} = - 0.2 – 0.059$ pH (V vs Ag/AgCl)

ii. $2H_2O \rightarrow O_2 + 4H^+ + 4e^-$ $U_{eq} = 1.03 – 0.059$ pH (V vs Ag/AgCl)

Leakage current that flows across the dielectrics is strictly related to the insulating or semiconducting properties of the films and it is mainly due to the electrons/holes conduction

across the oxide, so that if percolation paths are present throughout the anodic layers, the carriers conduction is easier and leakage current increases. The presence of localized electron states inside the band gap of the oxide can provide percolation paths inside the layers for electronic conduction. These states can be also involved in conduction mechanisms, such as Poole-Frenkel emission or tunnelling, that are made easier in presence of strong electric field strengths across the anodic layers, as sketched in Figure 6.15.

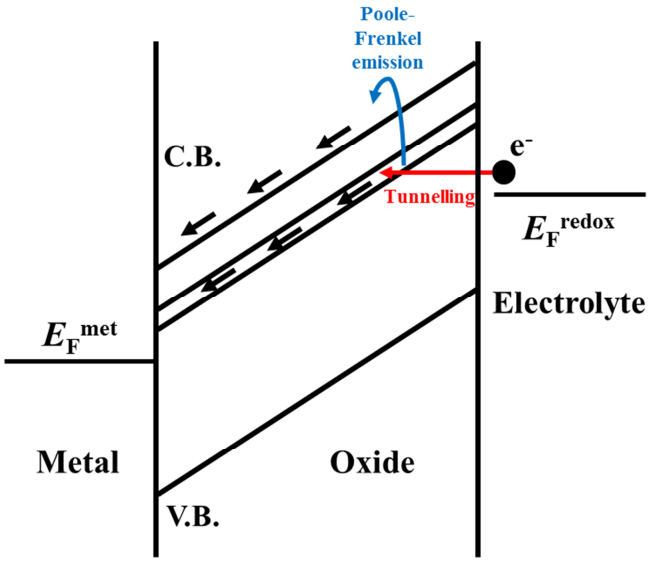

Figure 6.15 Sketch of the possible transport process across the oxide and at oxide/electrolyte interface. Blue: Poole-Frenkel emission. Red: Tunnelling.

Furthermore, in the case of anodic film growth where the involved electric field strengths are in the order of MV cm^{-1}, also the ionic migration is activated so that it is possible to have both ionic and electronic conduction with possible gas development within the growing oxide.[178] In fact, O^{2-} anions can be oxidized according to the reaction:

iii. $2O^{2-} \rightarrow O_2 + 4e^-$

leading to oxygen evolution reaction into the layer, therefore producing oxygen bubbles that

can be blocked in the oxide, as in the case of anodic film growth on Ti.[178]

During anodic film growth and leakage current measurements, an anodic polarization (with respect to the oxide flat band potential) is applied to the metal/oxide junction. Therefore, in evaluating the current flow across the layer, both oxidation reactions (i) and (ii) at oxide/electrolyte interface should be considered since they are thermodynamically possible but also oxygen anions oxidation can contribute to the current flow.

Generally speaking, crystalline oxides have higher ionic resistivity with respect to the amorphous counterpart, thus higher electric field strengths are present, for instance, during the anodic films growth.[178] Pure Hf oxide is the only investigated layer that is entirely crystalline. As discussed before, oxygen is produced during the anodic HfO_2 growth from ~ 60 V to the final formation voltage, with a consequent decrease in the growth efficiency. Since no cracks are present inside the anodic layer, it is supposed that whole produced oxygen comes from the water oxidation reaction (ii) at the oxide/electrolyte interface (since the absence of dissolved H_2 in the solution). Despite this experimental evidence, the leakage current for pure Hf oxide is very low (~ 300 nA cm^{-2}) due to the insulating nature of this anodic layer. The highest leakage current and the most abundant O_2 evolution were observed during anodizing of Hf-4at.%Nb alloy. This can be explained by looking at the band structure of the oxide: the presence of empty localized states close to the conduction band gives a way to the electrons, coming from water oxidation, to flow across the oxide and, then, to be emitted or to tunnel to the conduction band. Leakage current for the other oxides is markedly lower due to the absence of such states.

6.9 Concluding Remarks

Anodizing can be a facile and valuable route to fabricate high-*k* mixed oxides with tailored dielectric properties. In this case, mixed Hf-Nb oxides were fabricated by anodizing sputtering deposited Hf-Nb metallic alloys. Depending on Nb content in the metallic substrate, the anodic oxides can have different characteristics, from a morphological and structural point of view, as well as regarding electronic properties.

The structure and the composition of the anodic oxides were studied by TEM observations as well as by GIXRD and GDOES. The mixed oxides with a Nb content ≥ 57at.% resulted to be amorphous whilst mixed oxides with Nb content ≤ 39at.% resulted to be formed by an outer amorphous layer and an inner crystalline layer, thus a crystalline-amorphous transition is detected by increasing Nb content in the oxides.

Photoelectrochemical characterization was performed in order to estimate band gap and flat band potential of the anodic oxides. Detected anodic photocurrent was attributed to optical transitions between allowed localized electron states (near oxides valence band) in the band gap and oxides conduction band (Nb content ≤ 39at.%) or to band-to-band optical transitions (Nb content ≥ 57at.%). In the case of anodic oxide grown on Hf-4at.%Nb, the presence of a long photocurrent tail leads to the conclusion that empty localized electron states near the conduction band are present.

Impedance as well as withstand voltage and leakage current measurements have been carried out to study dielectric properties of the anodic layers. In particular, the highest value of capacitance was recorded for the anodic oxide grown on Hf-39at.%Nb but amorphous mixed oxides report the highest withstand voltages and the lowest leakage currents. It is noteworthy to mention that, when thin films are required (e.g. MIM_{cap} in DRAM memories), the anodic oxide grown on Hf-4at.%Nb seems to be the most suitable, because of its high dielectric constant (with respect pure HfO_2) and high band gap.

Therefore, the experimental results reported suggest that by properly selecting the alloy composition (and also the formation voltage) it is possible tailoring both the oxides band gap and dielectric constant as well as crystallinity or amorphosity of mixed oxides, which are key parameters in determining the performances of high-*k* materials.

7 Anodic Oxides as Solid Electrolytes of Resistive Switching Devices

As discussed in Section 2.3, ReRAMs are typically composed by metal/solid electrolyte/metal junctions in which the solid electrolyte is often a metal oxide or multilayer oxides structures. In last decade ReRAMs have been intensively investigated in order to understand in details the switching kinetics and the microscopic ionic/electronic mechanisms in order to improve retention and endurance and to optimize devices performances.[56] Most attractive are the filament type switching systems based on a change in electrolyte resistance due to the formation/dissolution of electronically conducting filaments that short circuit the metal electrodes leading the device from a high resistance state (HRS) to a low resistance state (LRS). Filament formation and dissolution are the consequence of electrodes redox reactions at the metal/electrolyte interfaces and of the movement of the ions, generated by these reactions.[61]

In the case of VCM cells, resistive switching is described with the formation of an oxygen-deficient filament for the SET process that can be reoxidized leading to its partial dissolution (RESET). Oxygen anions movement is supposed to be responsible for the resistive switching in these cells although recently also cations movement was demonstrated by several authors.[76,183–185]

Solid oxide electrolytes for ReRAMs, are usually prepared by means of atomic layer deposition, chemical vapor deposition, pulsed laser deposition or RF sputtering.[56,75,186,187] Despite these techniques are largely used for producing high quality thin films for nanoelectronics, these methods require high/ultrahigh vacuum conditions and in many cases the high energy particles penetrate into the underlying matrix inducing interface mixing of materials.

An alternative way to produce high-quality metal oxides is the anodizing process that allows to grow oxides with well-defined characteristics such as thickness, composition, structure, and morphology by easily controlling operating parameters such as formation potential, growth rate, electrolyte, and metal substrate compositions, as discussed in the previous sections. To

date, there are several papers in which porous anodic aluminum oxide is used as a matrix for the fabrication of ReRAMs[188–191] or anodic nanostructured oxides are used as solid electrolytes,[192–196] but only few papers discuss on ReRAMs devices with barrier-type anodic oxides.[197–200]

In this Ph.D. work, anodizing process was used also to fabricate solid electrolytes for ReRAM devices with controlled properties such as morphology, thickness and structure. All the investigated devices are composed as follows: Me/anodic MeO_x/Pt in which Me = Ta, Hf, Nb and also metallic alloys such as Hf-4at.%Nb, Al-91at.%Ta, Al-62at.%Ta, Al-42at.%Ta and Al-20at.%Ta. Anodizing electrolyte was carefully chosen in order to avoid incorporation of foreign species from the bath that could change electronic properties of the oxide films, i.e. a borate buffer solution (pH = 8) was used for all the anodic oxides growths. Pt top electrode has been chosen as the most common inert electrode used in ReRAM devices and the fabrication of Pt pads is described in Section 3.1.3. The part of Pt top electrode fabrication and electrical characterization of the devices was entirely carried out at the Institut für Werkstoffe der Elektrotechnik 2 at RWTH Aachen University with the collaboration of Prof. Rainer Waser's research group under the supervision of Dr. Ilia Valov.

7.1 Ta/Anodic Ta Oxide/Pt devices

Several Ta/anodic Ta_2O_5/Pt junctions have been fabricated. In particular, the anodic oxide was grown on Ta substrate/bottom electrode up to three different formation potentials: 5, 10 and 20 V vs Ag/AgCl potentiodynamically at 10 mV s^{-1} and also galvanostatically at 5 mA cm^{-2} up to 10 V. From XRR measurements conducted at IWE 2, the thickness of the 10 V Ta_2O_5 is 20 nm, over 270 nm of metallic Ta substrate.

Before investigating in details the resistive switching properties of this system, cyclic voltammetry (CV) measurements were carried out in order to understand which redox processes are directly involved and responsible in the switching of Ta/anodic Ta_2O_5/Pt VCM cells. At this aim, the redox processes have been studied in a voltage range restricted to values for which there are no complete switching processes (i.e. filament formation due to FORM

and/or SET processes) by using the thickest Ta oxide, i.e. 20 V anodic Ta_2O_5. In this way, the electronic contribution to the total conductivity is very low allowing the possible detection of the redox peaks.[184]

CV measurements shown in Figure 7.1 reveal at least three different processes. In the first cycle only one redox peak is well-resolved, related to an oxidation reaction, recorded at positive voltage of V_1 = 2.1 V. This peak merges and is further not clearly distinguishable during subsequent cycles. Within the sweep in the negative voltage range, reduction processes (or process) are observed appearing within the range of + 1 V and – 1 V. However, no distinguished peak(s) can be resolved and, for this reason, this region is marked in Figure 7.1 by V_{red}, without indexing.

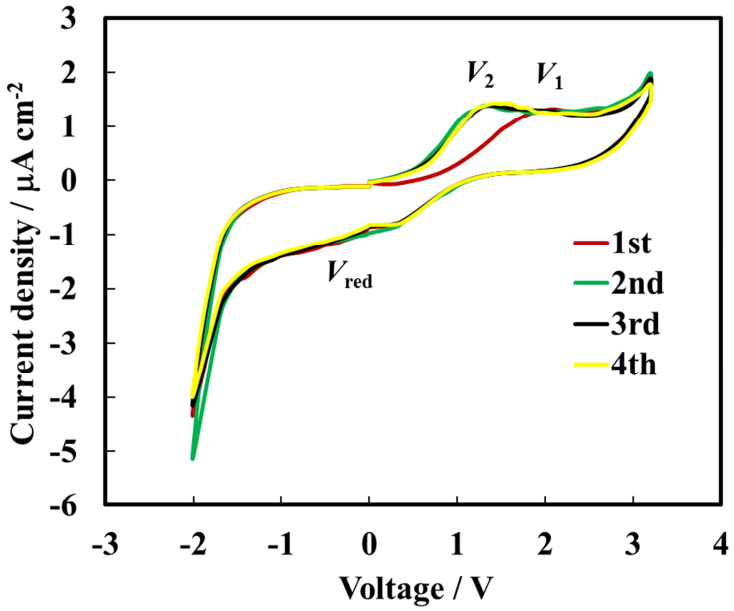

Figure 7.1 Cyclic voltammogram of Ta/20 V Ta_2O_5/Pt cell recorded with a sweep rate of 900 mV s^{-1}. The measurements were performed in a proper voltage range (between -2 V and 3.2 V) in order to avoid the first SET process in the device.

During the reduction process(es) obviously new species are formed because, on the second positive sweep scan, a new oxidation peak at V_2 = 1.3 V is detected. It merges with V_1 and forms a plateaux in the range 1.3 V to 2.5 V. Increasing the voltage over + 3 V leads to a

formation of filament i.e. resistive switching. In order to more clearly distinguish the individual redox peaks, it was necessary to use a sweep rate of 900 mV s^{-1}, higher with respect to that used in literature for same measurements with same materials.[184]

Several electrode reactions are possible, including the Ta/Ta^{x+} and O/O^{2-} half-cell reactions but also those related to moisture, as follows:[184]

$$Ta \rightleftharpoons Ta^{x+} + xe^- \quad (7.1)$$

$$2O^{2-} \rightleftharpoons O_2 + 4e^- \quad (7.2)$$

$$2OH^- \rightleftharpoons \frac{1}{2}O_2 + H_2O + 2e^- \quad (7.3)$$

$$2OH^- + H_2 \rightleftharpoons 2H_2O + 2e^- \quad (7.4)$$

$$2H_2O \rightleftharpoons O_2 + 4H^+ + 4e^- \quad (7.5)$$

CVs are classically recorded in a three-electrode configuration to exactly identify redox potential of any peaks with respect to the reference electrode potential. In this case, a reference electrode is not available and it is difficult to identify the exact electrochemical reaction related to every redox peak. For positive voltages, oxidation of Ta is the most probable from a thermodynamic point of view with a possible further chemical reaction of the metal cations with O^{2-} and/or OH^- to form Ta oxide or hydroxide.[184] Nevertheless, since all the measurements have been performed in ambient atmosphere, the influence of water molecules bonded on TaO_x matrix cannot be excluded, with particular reference to oxygen reduction reaction to form OH^- ions and water decomposition to form molecular oxygen.[68,184] It is noteworthy to mention that the anodic Ta oxide used for the experiments is much denser (8.5 g cm^{-3} from XRR measurements) compared to same oxides (and composition) prepared by physical deposition techniques, that resulted in nanoporous structures which can easily host water molecules.[69] For this reason, it has been assumed that the redox peaks are related to reactions 7.1 and 7.2 rather than to reactions 7.3, 7.4 and 7.5.

Basic functionalities of ReRAMs devices can be studied with *I-V* characteristics usually applying a current compliance, I_{CC}, during the SET process and/or during the RESET process (see Section 3.3.6).

In Figure 7.2 a typical *I-V* sweep for anodic Ta_2O_5-based devices is reported, regardless of solid electrolyte thickness and Pt top electrode pad dimensions.

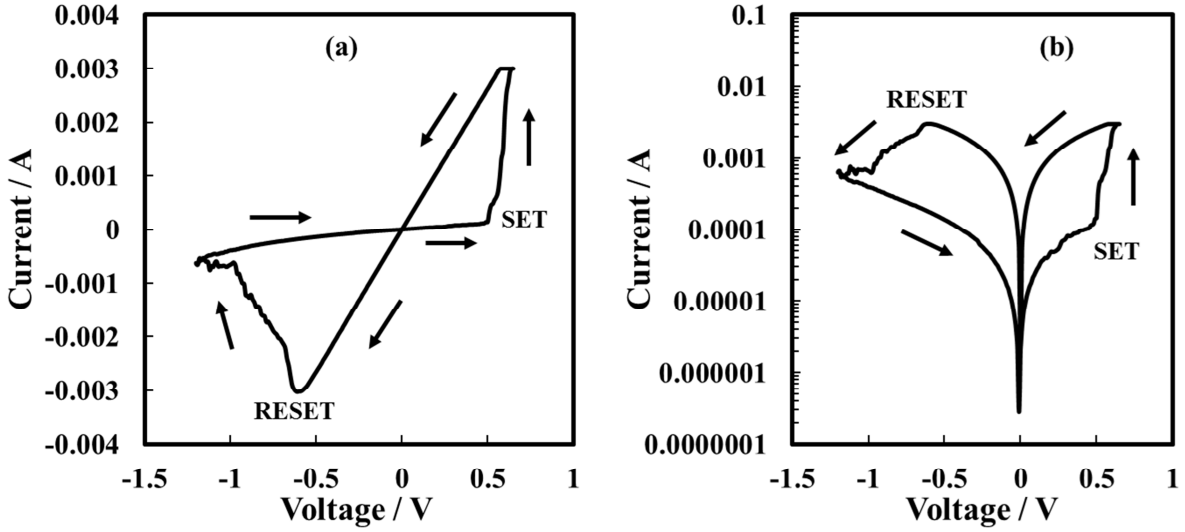

Figure 7.2 Typical *I-V* sweep of Ta/Anodic Ta_2O_5/Pt devices with the measured current in (a) linear scale and (b) log scale. Current compliance = 3 mA. Oxide thickness = 20 nm, pad area = 100×100 μm^2.

This eight-wise and bipolar characteristic is usually reported in VCM cells, i.e. almost symmetric SET and RESET voltages as well as RESET current comparable with the current compliance applied for positive voltages.[76]

Despite Ta oxide is one of the most used solid electrolyte for ReRAM devices, this is the first time in which electrochemically prepared Ta_2O_5 with anodizing process is used in resistive switching memories. The reliability of these anodic layers as solid electrolytes is shown in Figure 7.3 and Figure 7.4, in which multilevel switching is reported for 5 V Ta_2O_5 (d_{ox} = 10 nm) and 20 V Ta_2O_5 (d_{ox} = 40 nm) respectively. These *I-V* characteristics are reached by simply adjusting the current compliance during the SET processes for positive polarities. In this way, the destructive breakdown on the anodic layer is avoided and it is also possible to

control the size of the formed conducting filament (CF) leading to different values of the ON state resistance.

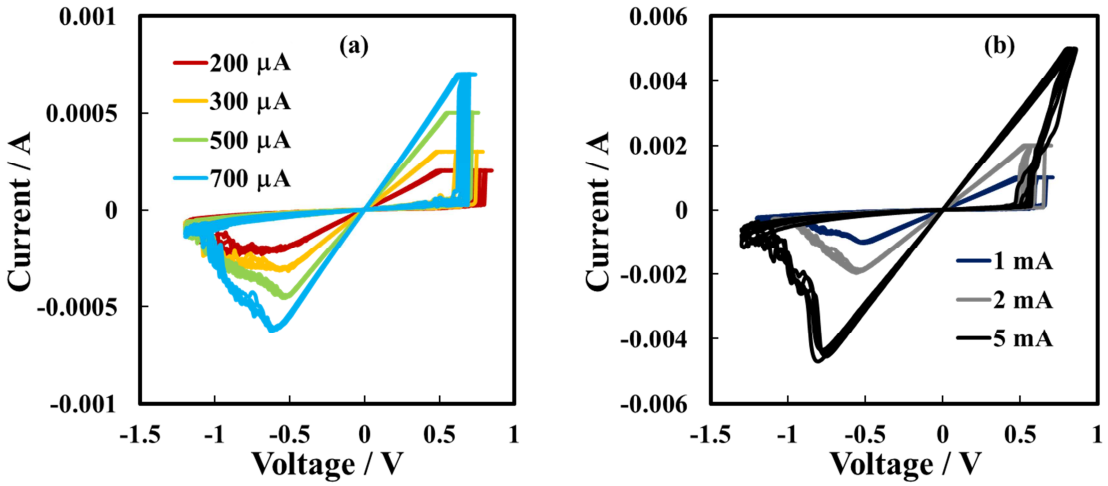

Figure 7.3 *I–V* sweeps recorded with different applied current compliances relating to the Ta/5 V anodic Ta_2O_5/Pt device. Oxide thickness = 10 nm.

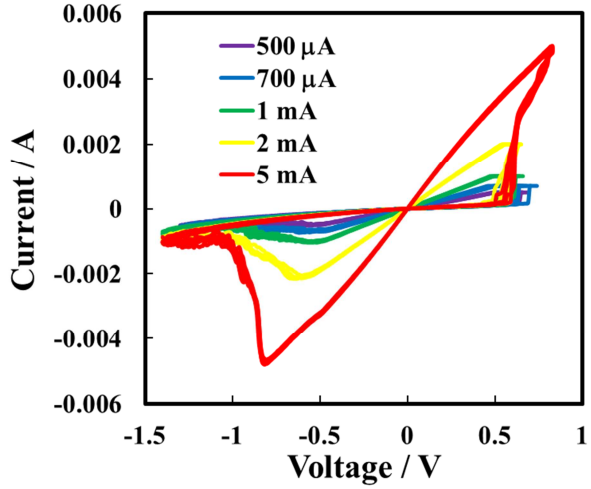

Figure 7.4 *I–V* sweeps recorded with different applied current compliances relating to the Ta/20 V anodic Ta_2O_5/Pt device. Oxide thickness = 40 nm.

Before any switching experiments, the cells were formed into the LRS (FORMING process)

by applying a positive voltage to the Ta bottom electrode, always employing a current compliance. It is important to say that there was no good repeatability in forming voltage values, ranging between ~ 0.5 V and the formation potential of the anodic oxide. This property is common to all the Ta_2O_5-based devices, probably due to a contact resistance originating from the air-formed oxide layer on bare Ta bottom electrode, being the latter a not noble metal and thus easily oxidizes in ambient atmosphere. Moreover, when the devices are formed and not broken during the first SET cycle, they reliably switch from the LRS to the HRS and vice versa for many cycles without huge signs of degradation leading to a very high yield for these cells (almost 90 %), crucial parameter to use the cells in "real" memory devices.

Among the three studied devices, that one composed by Ta/10 V anodic Ta_2O_5/Pt (d_{ox} = 20 nm) resulted to be the most stable and reliable, as shown in Figure 7.5(a) from the selected number of 10^3 consecutive *I–V* sweeps on a single device.

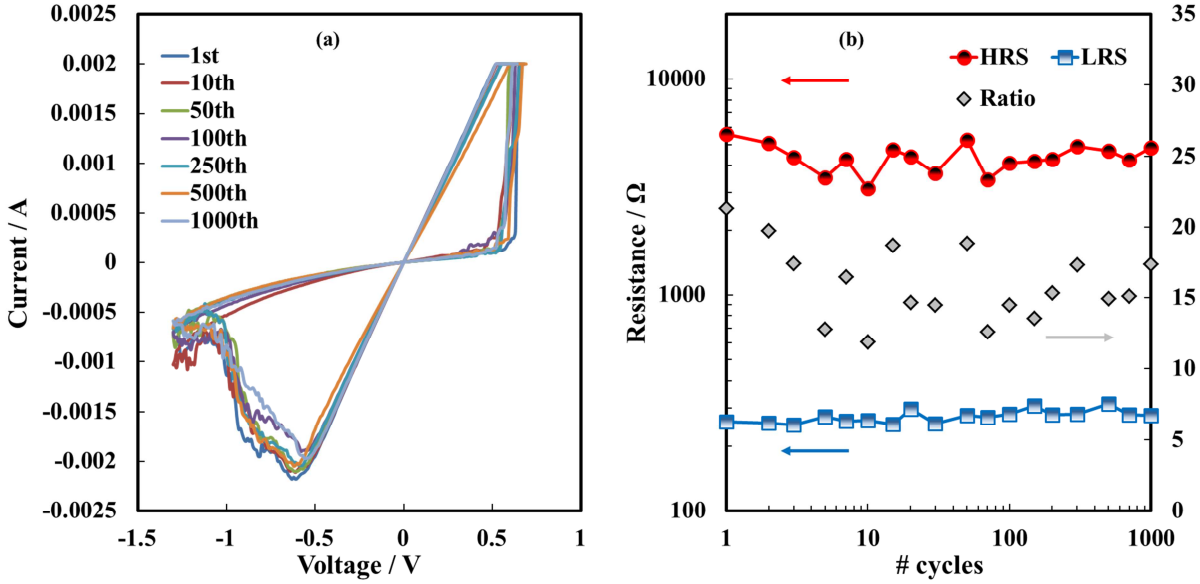

Figure 7.5 (a) 10^3 *I–V* cycles related to Ta/10 V Ta_2O_5/Pt cell and (b) resistance window during cycling the device. A current compliance of 2 mA was used during this measurement.

The device shows bipolar, eight-wise switching with low-switching voltages, V_{SET} ranging

between 0.45 and 0.65 V and V_{RESET} ranging between − 0.55 and − 0.65 V. The low voltage variability proves that the memory device exhibits high uniformity in SET and RESET processes with narrow distribution. Resistances were calculated by Ohm's law at 0.1 V as READ voltage for both HRS and LRS that vary between 6350 and 3100 Ω and between 250 and 320 Ω respectively as shown in Figure 7.5(b). R_{OFF} and R_{ON} are almost constant with the number of cycles, maintaining a R_{OFF}/R_{ON} ratio >10, standard requirement to use these devices for memory applications.[201]

As done for 5 V and 20 V Ta oxides, by varying the current compliance during the SET cycle, it was possible to demonstrate multilevel switching with at least nine adjustable resistance levels as shown in Figure 7.6.

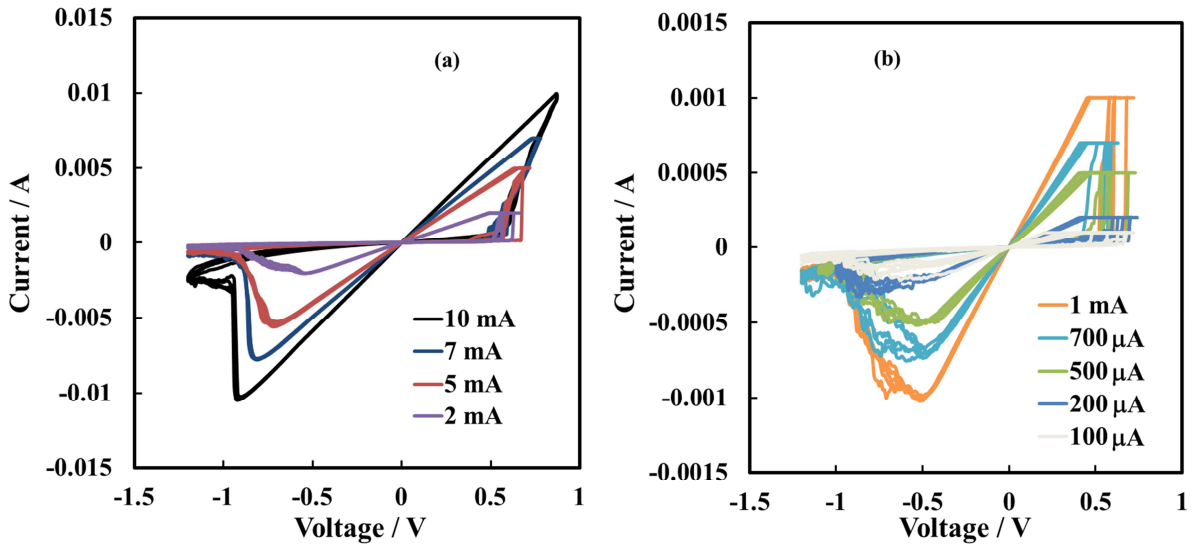

Figure 7.6 *I–V* sweeps recorded with different applied current compliances.

By increasing I_{CC}, R_{ON} decreases from 3870 (I_{CC} = 100 µA) to 85 Ω (I_{CC} = 10 mA) (see Figure 7.7). The different resistance values are determined by changes in the thickness of the filament and/or by the change of the composition (oxidation state) of both filament and disc. These resistances were shown to be stable and do not vary within the time of the observation (Figure 7.6).

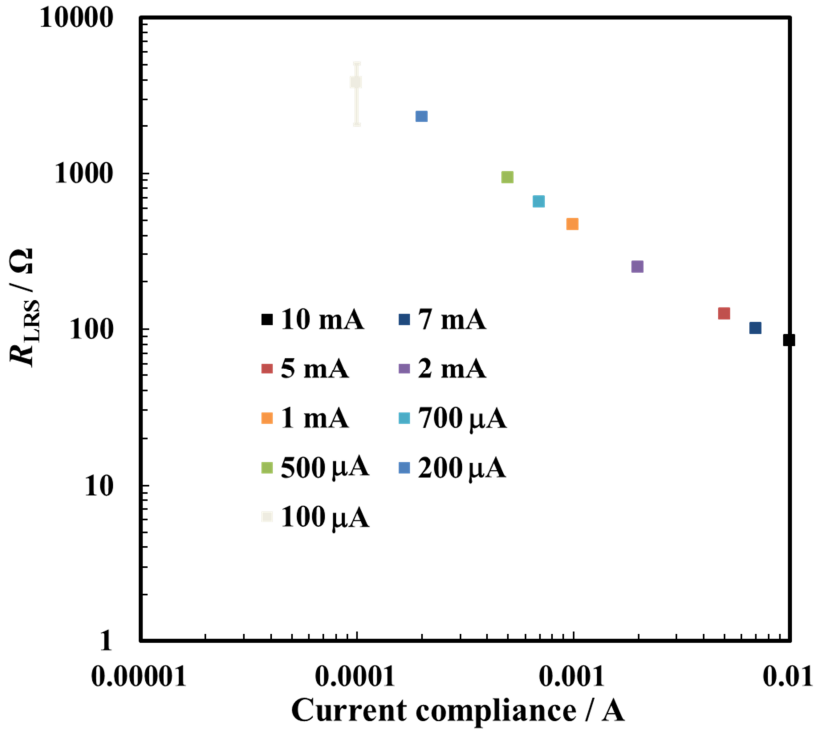

Figure 7.7 LRS resistance vs current compliance related to *I–V* sweeps shown in Figure 7.6(a) and (b).

It is noteworthy to mention that the increase in the current compliance leads to higher V_{RESET} values (~ - 1 V for I_{CC} = 10 mA) as well as to more sharp RESET processes with respect to the cycles with lower I_{CC}.

The kinetics of the switching process are directly connected to the sweep rate of the triangular voltage signal during the *I-V* sweeps. In Figure 7.8 different *I-V* sweeps of 10 V Ta_2O_5-based resistive memory device are shown by changing the voltage sweep rate, from 70 mV s^{-1} to 3400 mV s^{-1}. As it is possible to see from the magnifications of ON and OFF switching, V_{SET} and V_{RESET} increase by increasing the sweep rate. The latter condition gives less time to the system for the switching process so that the resistive cell needs a higher voltage to switch. For a ECM device such as Cu/SiO_2/Ir memory, an exponential relationship between the switching voltage and the sweep rate was observed for medium to high sweep rates, whilst for low sweep rates (< 10 mV s^{-1}), a critical SET voltage seemed to be approached.[202]

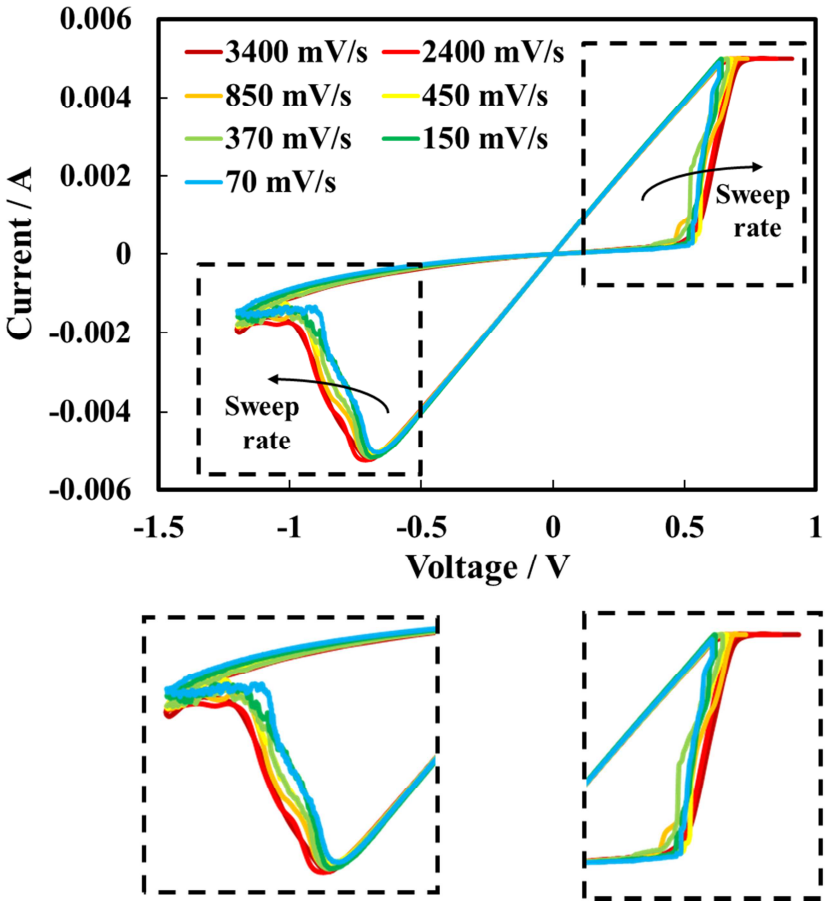

Figure 7.8 *I-V* characteristics of Ta/10 V anodic Ta oxide/Pt cells by changing the voltage sweep rate. Oxide thickness = 20 nm.

The pronounced exponential relationship and, in particular, a critical threshold voltage for the SET process explain how the voltage-time dilemma (i.e. the combination between fast switching and immunity to long-lasting read-disturb)[203] is overcome for the SET process in resistive switching memory cells.

It has been recently demonstrated by STM studies that samples history (e.g. thermal treatments) plays a key role in defining the dominant resistive switching mechanism for TaO_x solid electrolytes.[204] Furthermore, moisture present inside the oxide can play a significant role in switching processes, being involved e.g. in the oxygen evolution reaction or in the OH^- ions

generation.[68,69,184] Strictly related to the moisture is the density of the solid electrolytes.[69] Density is closely related to the transport properties of thin films. In general, lower density (higher porosity) lowers the ion diffusion as the path of an ion to pass same effective distance becomes longer and/or related to overcoming additional energetic barriers. Moreover, lower density supports a higher water/moisture uptake, and higher density supports a lower uptake of moisture.

In order to understand which is the effect of the moisture on the switching properties of anodic Ta_2O_5-based devices, 200 *I-V* cycles have been carried out at room temperature under vacuum conditions ($P = 4 \cdot 10^{-5}$ mbar), as shown in Figure 7.9.

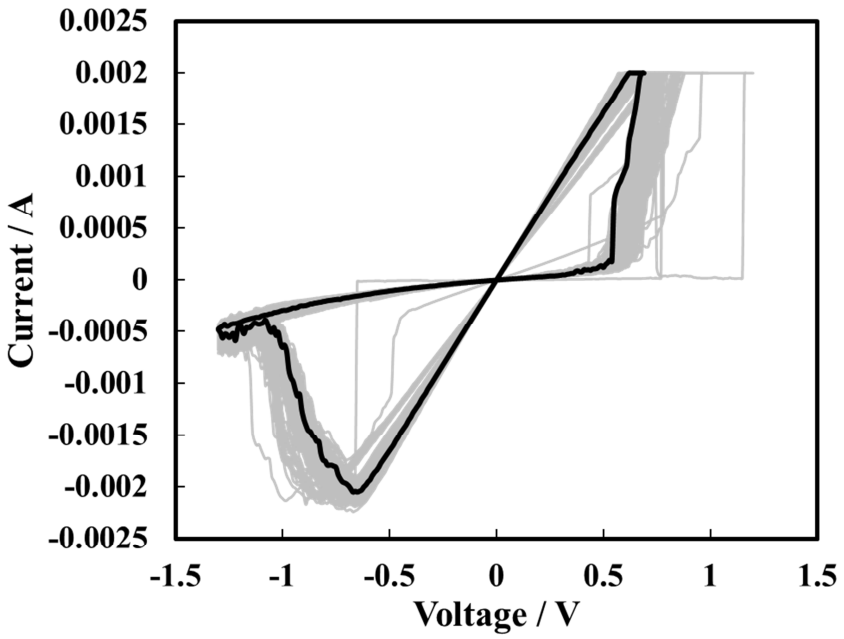

Figure 7.9 200 cycles of Ta/10 V anodic Ta oxide/Pt cell under vacuum condition ($P = 4 \cdot 10^{-5}$ mbar).

As shown, the switching is quite stable with narrow distributions of V_{SET} and V_{RESET}. However, it is important to say that the device was previously formed in ambient atmosphere and that it was not possible to form the sample under vacuum conditions, leading to the breakdown of the anodic oxide during the first SET cycle. This result confirm what it is

already reported in literature, that the moisture is essential, at least, for the FORMING step.[68,69] No unequivocal answer is given on the question whether moisture is also so essential for the following SET/RESET operations. On the other hand, since Ta is less noble than water,[114] moisture can promote Ta oxidation (according to Equation 7.1) i.e. should decrease the stability.[78] The oxidation of Ta is additionally enhanced by applying a positive voltage to the Ta electrode during cycling. Thus, density appears a factor in ReRAMs influencing the transport and stability directly (diffusion), and indirectly (uptake of moisture). In the ideal case, Ta_2O_5 should contain some moisture (to enable forming and possibly support faster switching) but not too much as it will affect the stability. Thus, the good performances of this anodic Ta_2O_5-based device could be a direct consequence of the high density of the solid electrolyte, i.e. contain enough moisture to allow forming but also less enough to avoid metal oxidation and support high stability and fine dispersed multilevel switching.

Further measurements on the device performances and stability were performed using voltage pulses, as described in Section 3.3.6.

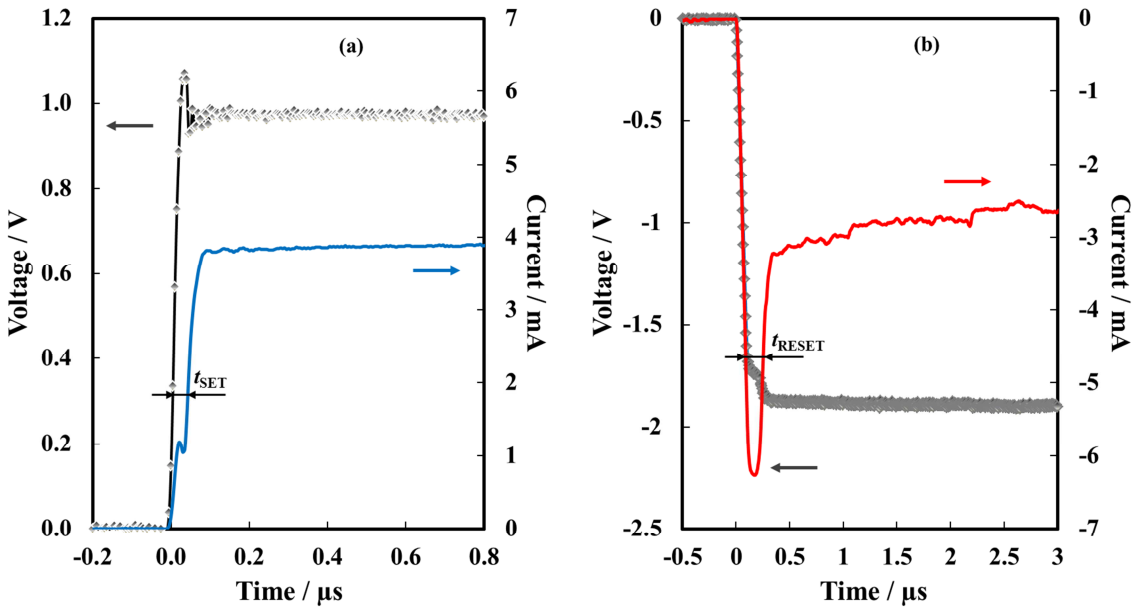

Figure 7.10 (a) SET pulse at 0.98 V and (b) RESET pulse at − 1.9 V: switching time was evaluated as the time between the voltage rise and the half height of current rise after the peak related to the charging current of the cell capacitance.

In order to study the switching kinetics and how fast is the resistance switching, fast pulses (minimum t_{pulse} = 1 µs) were applied to the device with a Keithley 4200-SCS connecting the smallest Pt top electrode pads. This is necessary to reduce as much as possible the current peak related to the charging process of the cell capacitance. The switching time was evaluated as the time between the voltage rise and the half height of current rise after the peak related to the charging current of the cell capacitance,[205–207] as shown in Figure 7.10. The samples could be switched to the LRS as fast as 20 ns at 1.25 V and also very short RESET times were achieved of 165 ns at − 1.9 V. These results are excellent considering the quite low pulse voltages for both SET and RESET operations.

The endurance of the 10 V (i.e. d_{ox} = 20 nm) anodic Ta_2O_5 devices was tested with SET pulses of 0.8 V (t_{SET} ≈ 75 ns) and RESET pulses of − 1.2 V (t_{RESET} < 200 ns). The READ operation was performed at 200 mV with 2.5 ms pulse length. The sequence of the cycles were: READ, SET, READ, RESET. Test results are shown in Figure 7.11(a).

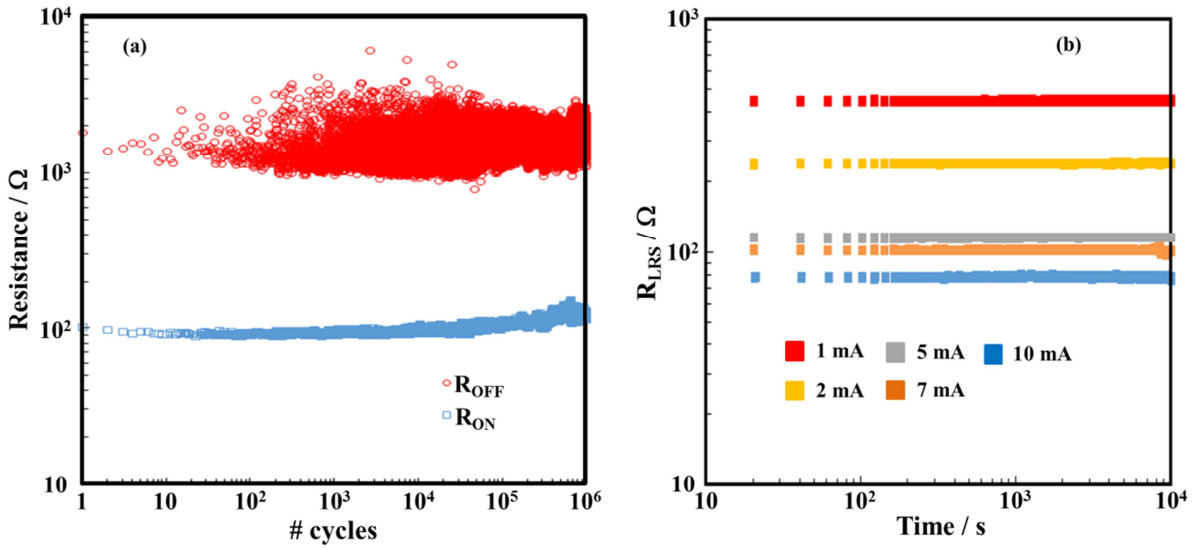

Figure 7.11 (a) Endurance test was performed by applying 2.5 ms pulses. Switching was carried out with V_{SET} = 0.8 V and V_{RESET} = − 1.2 V and 0.2 V as READ voltage. (b) Retention test for five different current compliances applied during the SET cycle preceding the test. A 20 mV pulse was applied every 20 s.

Endurance, at least, of 10^6 cycles without degeneration of the ON and OFF states was

demonstrated for the 10 V anodic Ta_2O_5-based device.

The retention of the LRS has also been confirmed to be at least 10^4 s without any sign of degeneration as shown in Figure 7.11(b). It has been performed at 20 mV every 20 s with a 100 ms READ pulse. RESET process was successfully performed after every retention test without any change in the value for the V_{RESET}. These performances are comparable to that obtained by devices prepared through sputtering deposition process or even better.[208] The excellent stability of the current during retention tests indicate that much longer retention times and endurance can be easily reached by the devices.

To test whether the growth of the anodic oxide could lead to change in resistive switching properties of the devices, *I-V* sweeps and retention test were also carried out for a device with Ta oxide grown galvanostatically at 5 mA cm^{-2} up to 10 V. The results are shown in Figure 7.12.

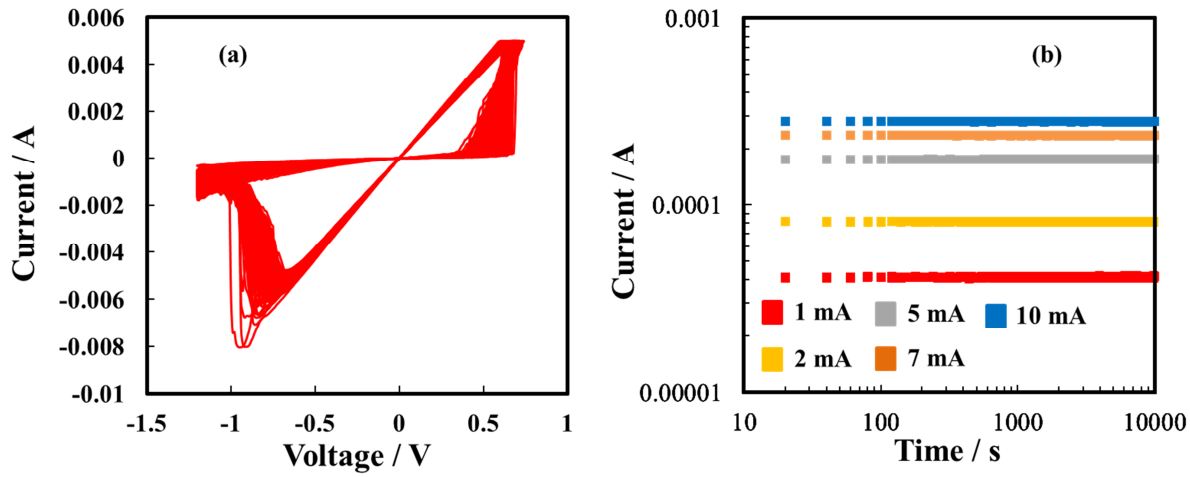

Figure 7.12 (a) 10^3 consecutive cycles and (b) retention test for different applied current compliances related to the galvanostatically grown 10 V Ta_2O_5-based device.

Excellent performances of anodic Ta oxide-based devices seem to be independent on the growth mode of the solid electrolyte, confirming the reliability of the anodizing process to prepare materials to be used in ReRAM devices.

7.2 Hf/Anodic Hf Oxide/Pt devices

As done for the anodic Ta oxide-based devices, three different systems regarding anodic Hf oxide have been tested. In particular, the same formation potentials (i.e. 5, 10, 20 V vs Ag/AgCl) have been chosen for HfO_2 solid electrolytes. As discussed in Sections 5 and 6, the growth mechanism of anodic Hf oxide is quite different from the typical one associated to the anodic film formation on valve metals. In fact, anodic Hf oxide results to be crystalline regardless of formation potential/voltage (i.e. thickness) and, during the growth, Hf^{4+} cation is quite immobile. However, depending on the oxide matrix, Hf cations move during the growth, as in Hf-Al and Hf-Nb mixed oxides systems.

In Figure 7.13 typical *I-V* sweeps for anodic HfO_2-based devices are reported.

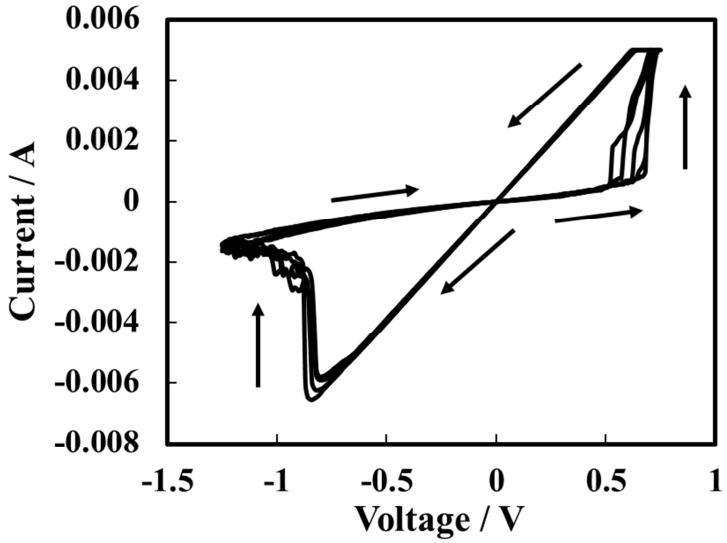

Figure 7.13 Typical *I-V* sweeps of Hf/Anodic HfO_2/Pt devices. Current compliance = 5 mA. Oxide thickness = 20 nm, pad area = 100×100 μm^2.

As for Ta oxide devices, Hf/Hf oxide junction is usually associated to VCM memories and *I-V* characteristic depicted in Figure 7.13 is in agreement with this conclusion.[76] In fact, I_{RESET} is almost equal to the current compliance applied for positive polarity and V_{RESET} value is not so low as in ECM memories.

Also in the case of anodic HfO_2, it was possible to determine different LRS states by changing the current compliance during the SET cycles, as shown in Figure 7.14(a) and (b) for 5 V and 20 V anodic Hf oxide-based devices respectively.

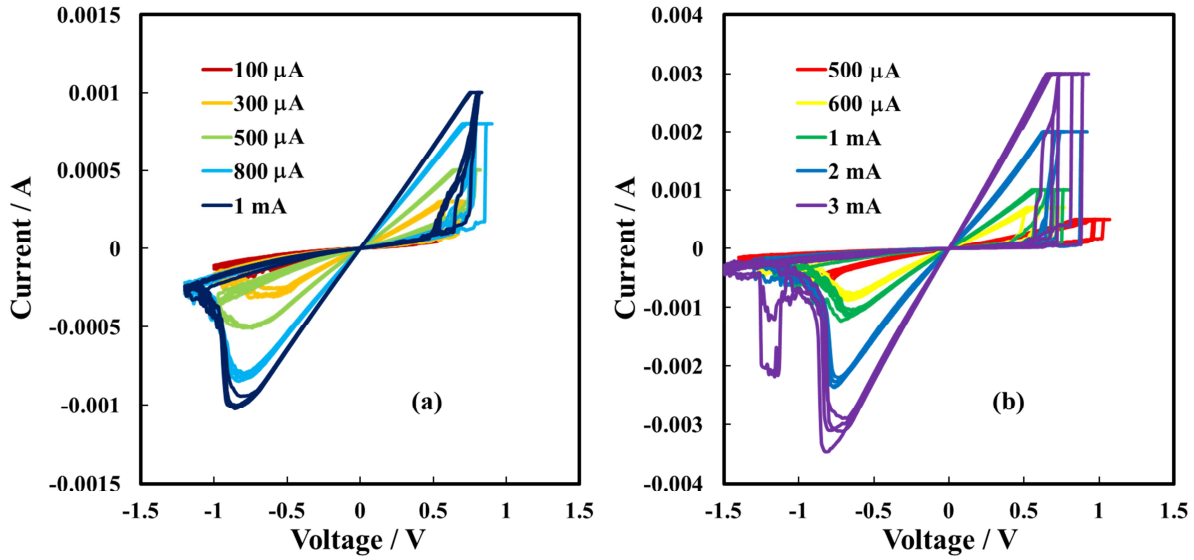

Figure 7.14 *I–V* sweeps recorded with different applied current compliances relating to (a) Hf/5 V anodic HfO_2/Pt and (b) Hf/20 V anodic HfO_2/Pt devices. 5 V oxide thickness = 10 nm. 20 V oxide thickness = 40 nm.

Good control of the LRS is necessary in order to achieve reproducible devices with high-bit density. This property was reached in literature by local doping HfO_2 solid electrolyte with Al.[209]

It is noteworthy to mention that it was possible to reach 10^3 consecutive *I-V* cycles on a single Hf/10 V anodic Hf oxide/Pt device, as depicted in Figure 7.15 where a selected number of cycles and the corresponding distribution of R_{ON} and R_{OFF} are reported. V_{SET} and V_{RESET} maintain in 0.48 V - 0.62 V range and in – 0.59 V and – 0.72 V range respectively, showing a low-voltage variability (i.e. high uniformity in SET and RESET processes) with a narrow resistances distribution through the 10^3 cycles estimated at a READ voltage of 0.1 V. It is important to say that the measurement was stopped after 10^3 cycles, thus the devices could easily reach a higher number of *I-V* sweeps without any sign of performances degradation.

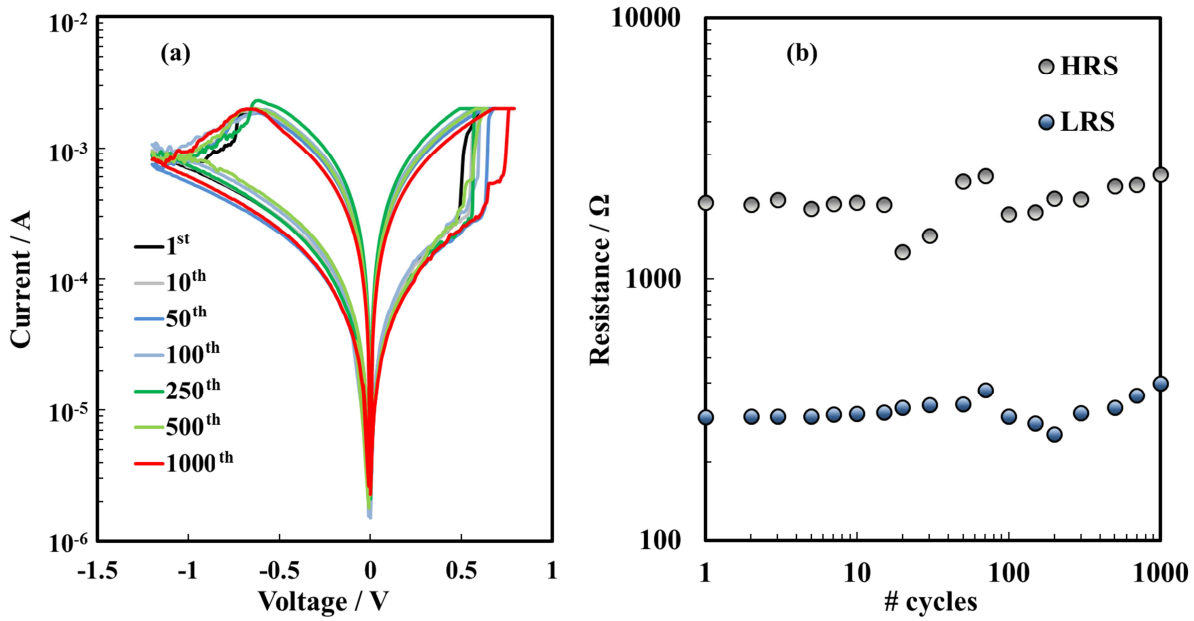

Figure 7.15 (a) 10^3 *I–V* cycles related to Hf/10 V HfO_2/Pt cell and (b) resistance window during cycling the device. A current compliance of 2 mA, only for positive polarity, was applied during this measurement. Oxide thickness = 20 nm.

As for the devices comprising 5 V and 20 V anodic oxides, also for 10 V anodic Hf oxide-based device was possible to reliably change R_{ON}, displaying an analog behaviour that can be used for multilevel storage, i.e. to store more than 1 bit per cell, as depicted in Figure 7.16(a). In fact, it was demonstrated that at least 5 different values of LRS resistance could be reached, from 565 Ω (cc = 1 mA) to 155 Ω (cc = 5 mA), with a variability < 10 % within the time of the observation. The difference in R_{ON} values is supposed to be ascribed to changes in the thickness of the CF and/or by the change of the composition (oxidation state) of both filament and disc. In fact, the filament can be considered as divided in two parts called plug and disc. The plug describes the conducting region that consists of a reduced oxide with a high concentration of oxygen vacancies whilst the disc is the region between the front of the plug and (usually in VCM cells) the Pt electrode in the HRS state.[210,211]

It is noteworthy to mention that SET and RESET processes (through V_{SET}, V_{RESET} and R_{ON} values) resulted to be independent on the anodic oxide thickness that ranges between ~ 10 and

40 nm. This is supposed to be due to a RESET process that corresponds to an incomplete dissolution of CF at the Pt electrode/electrolyte interface, thus the subsequent SET process needs just to connect plug region to the electrode instead of rebuilding the entire conductive path.

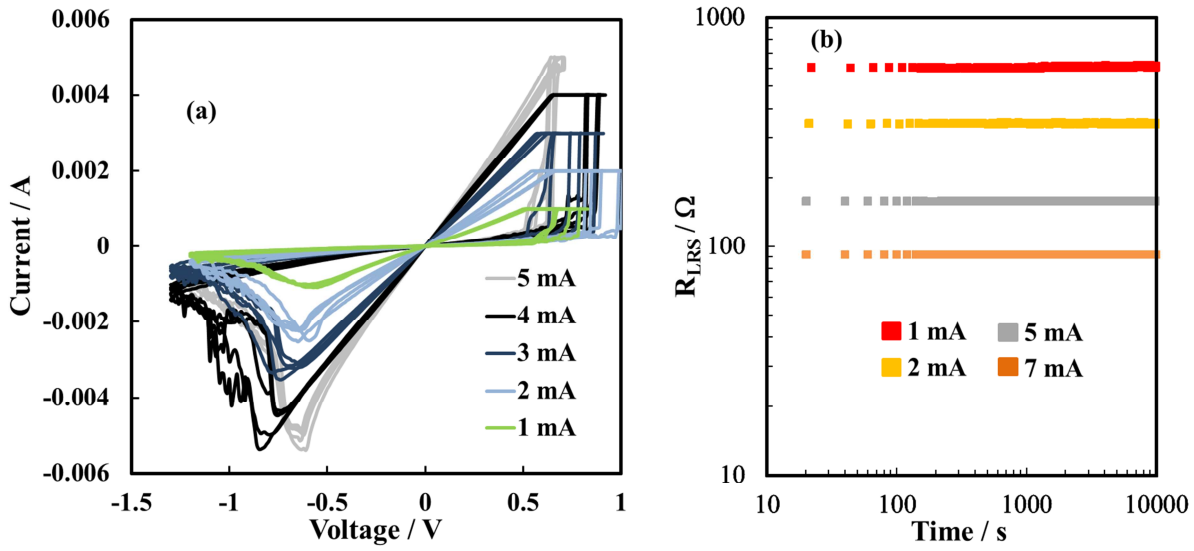

Figure 7.16 (a) *I–V* sweeps, related to Hf/10 V HfO_2/Pt device, recorded with different applied current compliances (between 5 mA and 1 mA). (b) Retention test for four different current compliances applied during the SET cycle preceding the test.

Retention test, reported in Figure 7.16(b), was also performed to verify if the data is steadily memorized during longer times. As shown, LRS is stable for at least 10^4 s without any sign of degeneration, also by changing current compliance during the SET sweep before every test. RESET process was successfully performed after every retention test without changes in the V_{RESET} value.

Performances of anodic HfO_2-based devices seem very similar to that of anodic Ta_2O_5-based devices. Indeed, Hf is a not noble metal and the Gibbs free energy of the oxide formation, ΔG^0_{form}, is highly negative, i.e. it oxidizes easily in ambient atmosphere, so that Hf/HfO_2 and Ta/Ta_2O_5 systems expect to behave in a similar manner. Thus, despite it was not possible to perform reliable cyclic voltammetries for anodic HfO_2-based system, it is expected that, by

polarizing positively the Hf bottom electrode, Hf^{4+} can be generated leading to the reaction of HfO_x formation at the Hf/HfO_2 interface.[76] Investigation on Hf/HfO_2 interface using X-ray Absorption Spectroscopy agree with the latter statement leading to the conclusion that a new intermediate oxide forms with a tetragonal/orthorhombic short-range order, different from the monoclinic structure of the bulk Hf oxide, that is reminiscent of a rutile-like local structure of intermediate TaO_x out of the matrix in the Ta_2O_5/Ta system.[78] This intermediate layer is also called Oxygen Exchange Layer (OEL) that is believed to induce a distributed reservoir of defects at the metal−insulator interface, thus providing an unlimited availability of defects which are the building blocks for the conductive filament (CF).[80]

Regarding the filament formation, Scalpel-Scanning Probe Microscopy (SPM) was used in a similar system, $Hf/HfO_2/TiN$, to observe the different studies of the formation of CF, as depicted in Figure 7.17.[212]

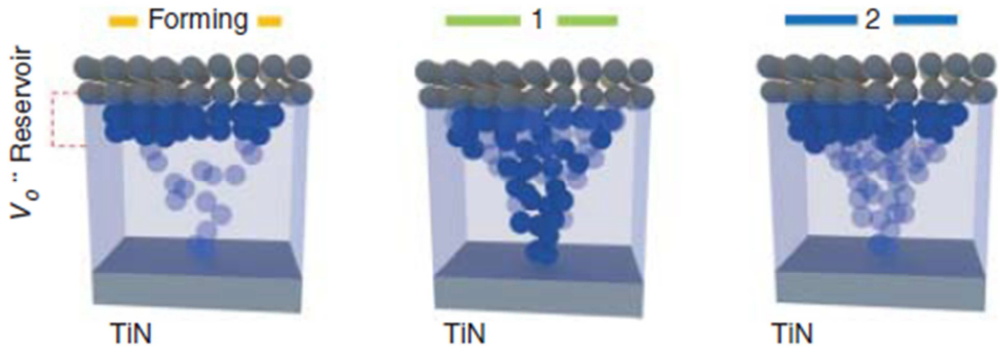

Figure 7.17 CF formation in a VCM-type $Hf/HfO_2/TiN$ cell. 1: ON state, 2: OFF state.[212]

In this case, the CF is thought to be formed by the creation/dissolution of a chain of oxygen vacancies ($V_O^{\cdot\cdot}$). Indeed, through the creation of the high electric field strength inside the oxide during the FORMING process (~ 10^7 V cm^{-1}), oxygen atoms start to leave their lattice position and drift toward the anode, leaving behind an oxygen vacancy. The accumulation of $V_O^{\cdot\cdot}$ into a chain of oxygen vacancies leads to the formation of a conductive path shorting the TiN (or Pt) with the Hf/HfO_2 interface. The formed OEL acts as a $V_O^{\cdot\cdot}$ reservoir and locally provides an exchange layer to sustain the successive CF rearrangements.

7.3 Nb/Anodic Nb Oxide/Pt devices

Nb is a valve metal as Ta, Hf etc. and the corresponding oxide Nb_2O_5, grown by anodizing, is amorphous even though could crystallize at high formation voltages and/or high electrolyte temperatures.[174] Nb_2O_5 is a high-*k* n-type semiconducting material, unlike pure Ta and Hf oxides that are more insulating. The Nb/anodic Nb_2O_5 system has been already studied as bottom electrode/solid electrolyte junction for ReRAM devices coupled with Au top electrodes.[197,198] In that case unipolar resistive switching of the system was shown, with a resistance ratio of 10^3 demonstrated with both dc and pulses measurements, and good retention properties. Generally speaking, Nb_2O_5 has been extensively studied as electrolyte for ReRAM and various results have been reported: bipolar switching,[213,214] threshold switching,[215–217] and analog switching[218] depending on oxide thickness, stoichiometry and electrodes materials.

As for anodic Ta_2O_5 and anodic HfO_2-based devices, anodic Nb oxide was grown to three different formation potentials (5, 10 and 20 V vs Ag/AgCl), thus devices with three different oxide thicknesses have been tested.

Very low yield has been found for anodic Nb_2O_5-based devices, regardless of oxide thickness, so that a low number of devices has been tested since the easy irreversible breakdown of the electrolytes during the FORMING step. For 5 V anodic Nb oxide device no reliable resistive switching has been found, whilst for 10 V and 20 V anodic oxides-based devices resistive switching has been proved. Two examples of *I-V* characteristics of Nb/10 V anodic Nb oxide/Pt ($d_{ox} \approx 23$ nm) cells are shown in Figure 7.18. In Figure 7.18(a) a current compliance of 5 mA was applied during SET cycles; SET and RESET processes are quite stable with V_{SET} equal to 1.2 V and V_{RESET} equal to - 0.82 V, thus higher switching voltages with respect pure Ta and pure Hf oxides-based devices. These *I-V* sweeps are probably the best cycles recorded for this system; in fact, very unstable LRS and HRS states were usually found, with high switching voltages and not reproducible cycles. Moreover, LRS is quite ohmic between 0.5 and - 0.5 V with the current that sharply increases approaching V_{RESET}. This kind of behaviour was also reported using Ti or Al electrode instead of Nb,[214] i.e. materials that, as well as Nb,

are not noble metals and thus probably lead to the formation of a OEL at the metal/electrolyte interface.

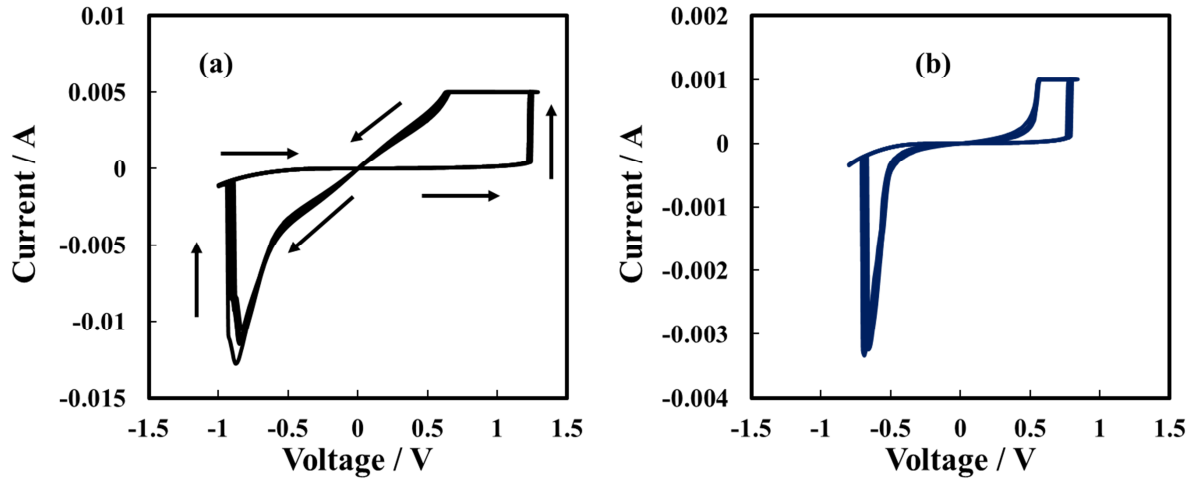

Figure 7.18 Resistive switching behaviours found for Nb/10 V anodic Nb_2O_5/Pt cells.

Nevertheless, a good resistance ratio R_{OFF}/R_{ON} of ~ 200 was estimated at READ voltage of 0.1 V during the *I-V* sweeps and thus higher than those estimated for anodic Ta and Hf oxides-based cells. In Figure 7.18(b) a different behaviour of this system is reported. The LRS is not ohmic, it is highly semiconducting and seems to tend to a threshold switching behaviour, at least for positive polarity.

The same electrical characterization has been carried out for the system with the thickest solid electrolyte, 20 V anodic Nb oxide ($d_{ox} \approx 45$ nm), and the standard *I-V* sweeps recorded are reported in Figure 7.19. As it is possible to see, the cycles characteristics seem to be independent on the solid electrolyte thickness, as reported in the previous sections for the other systems. The 20 V anodic Nb oxide-based cells resulted to be the most stable among those studied with a quite narrow distribution in V_{SET}, V_{RESET} as well as in R_{ON} and R_{OFF} resistance values. Also for this device, a drift toward a threshold switching behaviour was found and, in this case, it seems more pronounced when the current compliance applied during the SET cycle increases (see Figure 7.19(b)), despite a huge variability in V_{SET} value.

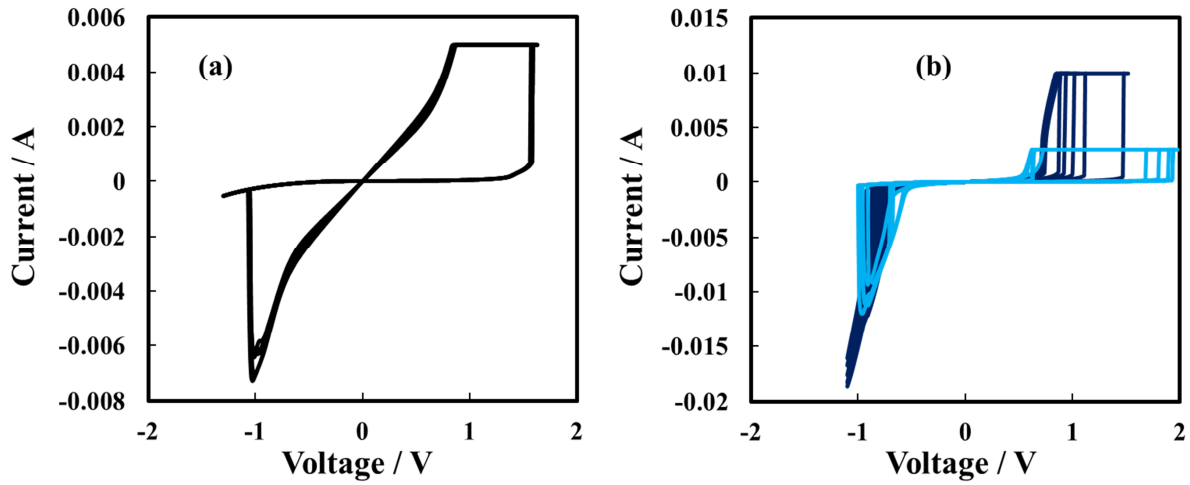

Figure 7.19 Resistive switching behaviour of Nb/20 V anodic Nb_2O_5/Pt cells.

Moreover, this drift was not controllable in any way so that Nb oxide-based devices resulted the less stable, reproducible and reliable among the studied cells.

7.4 Metallic Alloy/Anodic Mixed Oxide/Pt devices

In the case of metallic alloys, anodizing process leads to the growth of a mixed oxide whose composition strongly depends on the transport properties of the involved cations and anions (see Section 2.1.2). Therefore, anodizing metal alloys can be a valuable route to obtain oxides with tailored properties, such as band gap, dielectric constant and so on, exploiting and mixing the good properties of the pure "partner" oxides. Moreover, if the ions involved in the growth of the mixed oxides have strong differences in transport numbers, layered oxides could be obtained in a reliable and controlled way. This is one of the advantages of the anodizing process relating to metallic alloys. In this Ph.D. work, different metal alloy/anodic mixed oxide/Pt systems were studied; in particular, Hf-4at.%Nb was anodized to 5, 10 and 20 V vs Ag/AgCl whilst Al-91at.%Ta, Al-62at.%Ta, Al-42at.%Ta and Al-20at.%Ta were anodized to 5 and 10 V vs Hg/HgO with all the systems took in contact with top electrode Pt pads to study the resistive switching properties of the grown mixed oxides.

Starting from Hf-4at.%Nb system, in Figure 7.20 *I-V* sweeps, recorded by changing the current compliance during the SET cycles, for 5 V and 20 V mixed oxide-based devices are reported.

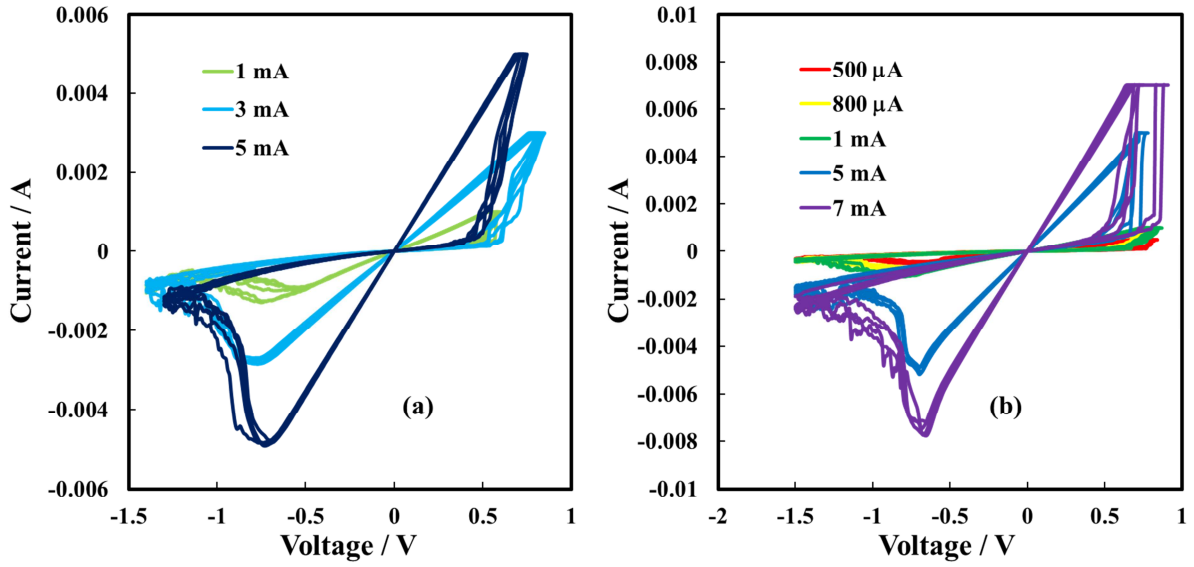

Figure 7.20 *I–V* sweeps recorded with different applied current compliances relating to (a) Hf-4at.%Nb/5 V anodic mixed oxide/Pt and (b) Hf-4at.%Nb /20 V anodic mixed oxide/Pt devices.

It is important to say that the composition of the mixed oxide, in this case, is the same of the metallic alloy, without any enrichment or layered structure (see Section 6). Despite a not so high yield of these samples, it was possible to obtain reproducible and reliable bipolar resistive switching, demonstrating also the possibility of multilevel switching changing I_{CC}. Furthermore, the presence of a small amount of Nb in the oxide matrix does not seem to influence *I-V* sweeps, in term of V_{SET}, V_{RESET} and resistances values, with respect to that obtained for pure Hf oxide, reported in Section 7.2. The most stable sample remain, as in the other cases, that one with an intermediate oxide thickness, i.e. 10 V anodic mixed oxide-based cells. For these samples, it was possible also to test the devices with long-lasting measurements, e.g. 10^3 *I-V* cycles and retention test, shown in Figure 7.21 and Figure 7.22 respectively.

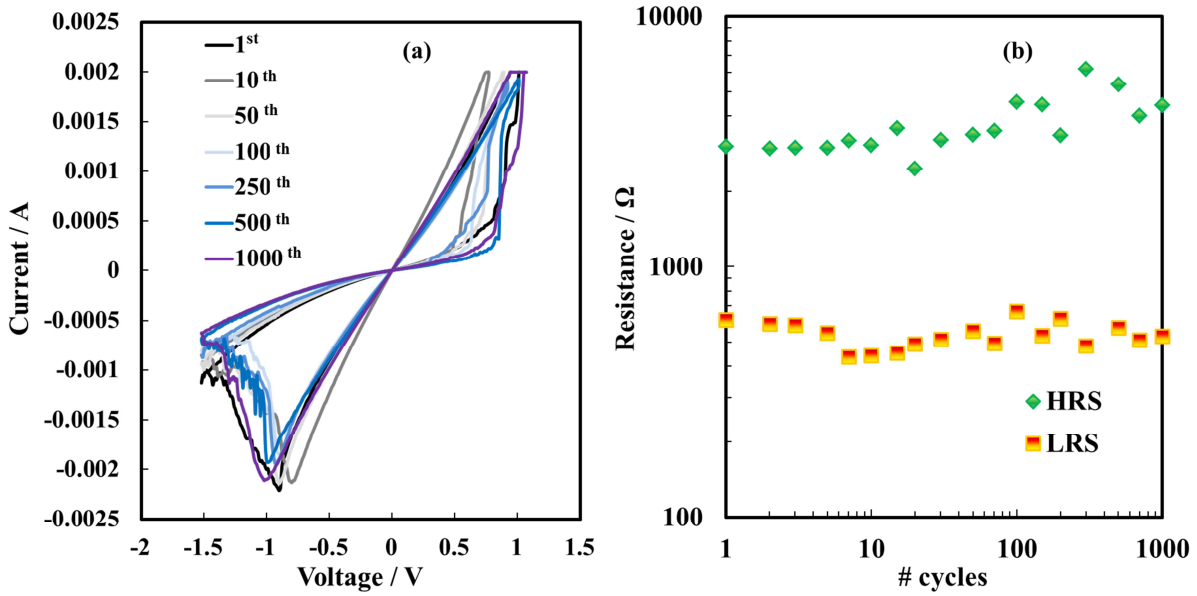

Figure 7.21 (a) 10^3 *I–V* cycles related to Hf-4at.%Nb/10 V anodic mixed oxide/Pt cell and (b) resistance window during cycling the device. A current compliance of 2 mA, only for positive polarity, was applied during this measurement.

R_{ON} and R_{OFF} keep a large enough window during the 10^3 consecutive cycles, with a ratio > 5 as average, with peaks of 10 - 12 at the end of the measurement when HRS resistance increases whilst LRS resistance is very stable all over the time. Having a look to the *I-V* characteristics, V_{SET} has a larger distribution of values with respect to that of pure anodic Hf oxide-based cells and, as said, R_{OFF} increases during the measurement time. Thus, the presence of Nb into the oxide has some influence on long-lasting behaviour of the cells, leading to a minimum degradation of the performances (see the huge difference in *I-V* cycle between the 1st and the 1000th). Nevertheless, retention test shows that, at least for 10^4 s, LRS is very stable without any sign of degradation (see Figure 7.22). As for every retention test, I_{CC} was changed during the SET cycle preceding the measurement and, after the test, RESET process was verified to be successful and reliable.

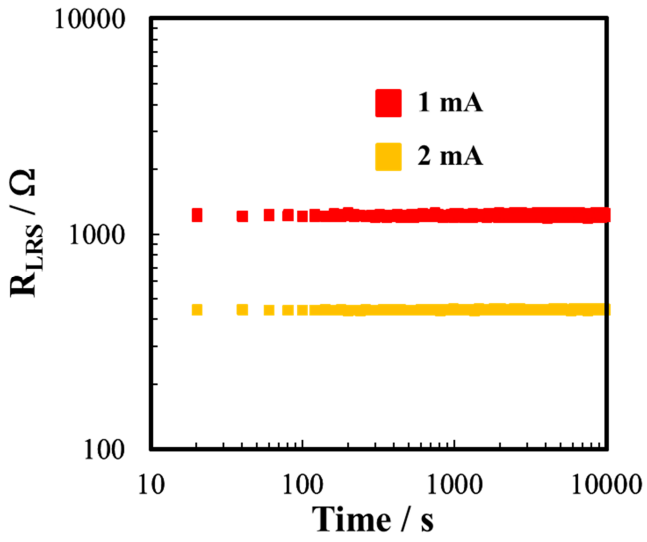

Figure 7.22 Retention test for two different current compliances applied during the SET cycle preceding the test.

The other systems involving mixed oxides are based on Ta oxide and an increasing content of Al, from 9at.% to 80at%. As deeply discussed in literature and in Section 4, the composition of the mixed oxide is equal to that of metallic alloy and the presence of Al into the anodic layer increases the insulating character and leads to the reduction of the dielectric constant.[113] In Figure 7.23 CV measurements and 10^3 consecutive *I-V* sweeps, relating to the Al-91at.%Ta/10 V anodic mixed oxide/Pt cells, are reported. Regarding cyclic voltammetries recorded before any resistive switching phenomena (see Figure 7.23(a)), the curves are more noisy with respect to those shown for pure anodic Ta oxide system but the shape, and the peaks position, is very similar. Moreover, the sweep rate used to obtain these curves is as high as for pure Ta oxide system, i.e. 900 mV s^{-1}, because lower sweep rates led to much more noisy measurements. Regarding the *I-V* sweeps (Figure 7.23(b)), the system look very stable all over the measurement time with a narrow distribution of V_{SET} (0.5 – 0.75 V) and a very narrow distribution in V_{RESET}. Also LRS and HRS keep almost constant values during the measurement ranging between 260 - 320 Ω and 4700 - 9000 Ω respectively. The latter result leads to higher R_{OFF}/R_{ON} values with respect to anodic Ta oxide-based devices.

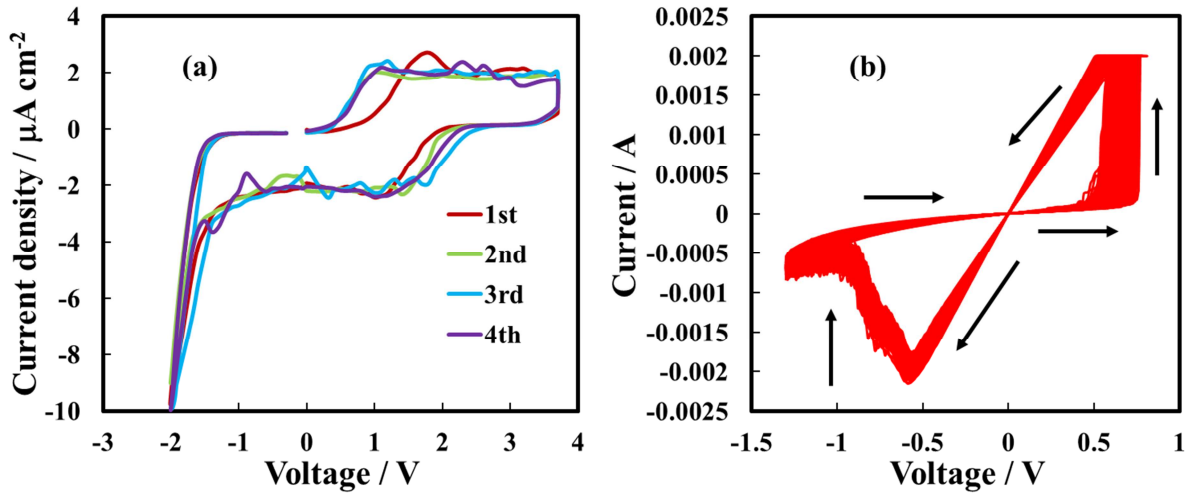

Figure 7.23 (a) Cyclic voltammogram of Al-91at.%Ta/10 V anodic mixed oxide/Pt cell recorded with a sweep rate of 900 mV s^{-1}. The measurements were performed in a proper voltage range (between -2 V and 3.6 V) in order to avoid the first SET process in the device. (b) 10^3 consecutive *I-V* sweeps with I_{CC} = 2 mA.

For this system, it was also possible to obtain different LRS values by changing I_{CC} during the SET cycle, demonstrating at least six different low resistance states, as shown in Figure 7.24.

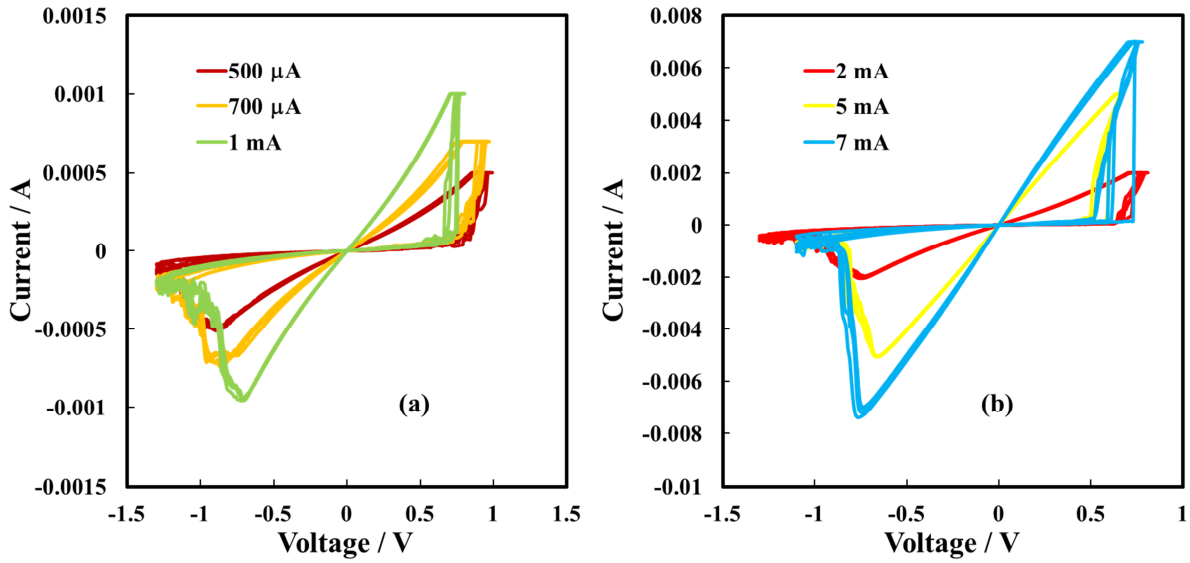

Figure 7.24 *I–V* sweeps recorded with different applied current compliances for Al-91at.%Ta/10 V anodic mixed oxide/Pt cells.

The weakness of the system is surely the too low yield; in fact, only 10% of the tried cells were correctly formed showing reliable bipolar resistive switching and were not irreversibly broken. Therefore, from performances point of view, the presence of small amount of Al seems does not influence too much the excellent characteristics of pure anodic Ta oxide-based devices but strongly influences the cells yield. The latter consideration needs further investigation.

Similar results have been obtained for the characterization carried out of the Al-62at.%Ta/anodic mixed oxide/Pt cells, as shown in Figure 7.25, in which 10^3 consecutive *I-V* sweeps and multilevel switching are reported.

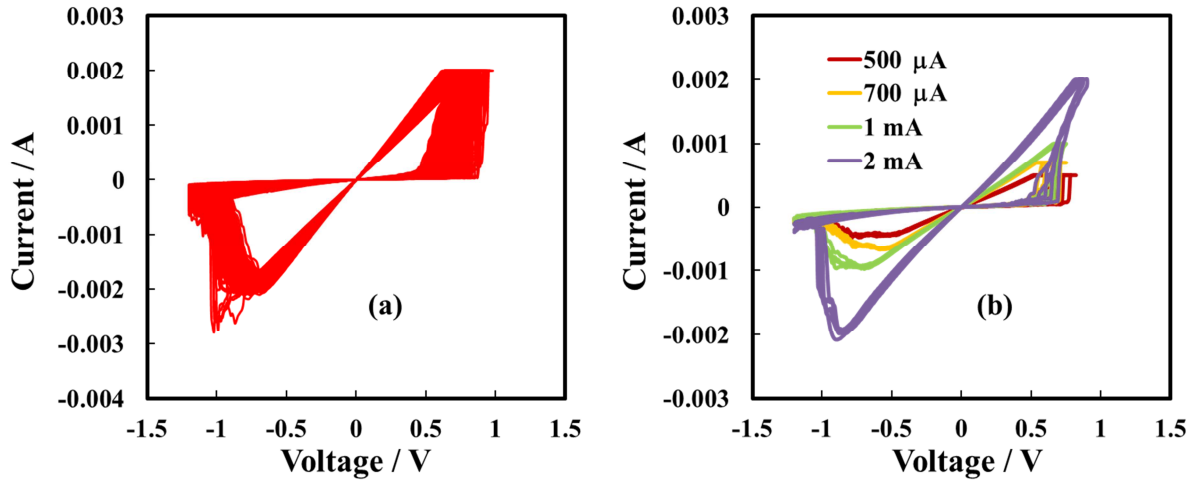

Figure 7.25 (a) 10^3 consecutive *I-V* sweeps with I_{CC} = 2 mA and (b) *I–V* sweeps recorded with different applied current compliances for Al-62at.%Ta/5 V anodic mixed oxide/Pt cell.

In this case, the R_{OFF} value is averagely higher during the 10^3 *I-V* sweeps with respect to the systems comprising oxides with higher Ta content; in fact, it ranges between 4300 and 26000 Ω confirming that the higher Al content increases the insulating character of the resulting anodic layer, whilst almost same values for R_{ON} are found, between 300 and 430 Ω. Regarding V_{SET} and V_{RESET}, the former has almost the same values distribution whilst the latter has a larger distribution with respect higher Ta content oxides-based devices. The cells yield is slightly higher with respect to the system with Al-91at.%Ta anodic layer (i.e. 33 %)

but not high enough to carry also long-lasting measurements.

Regarding Al-42at.%Ta/anodic mixed oxide/Pt cells, no resistive switching has been detected, since the FORMING process led, every time, to the irreversible breakdown of the solid electrolyte.

Something more and better has been detected in the case of Al-20at.%Ta/anodic mixed oxide/Pt system. In particular, for the 10 V anodic layer-based devices, bipolar resistive switching has been detected as shown in Figure 7.26(a).

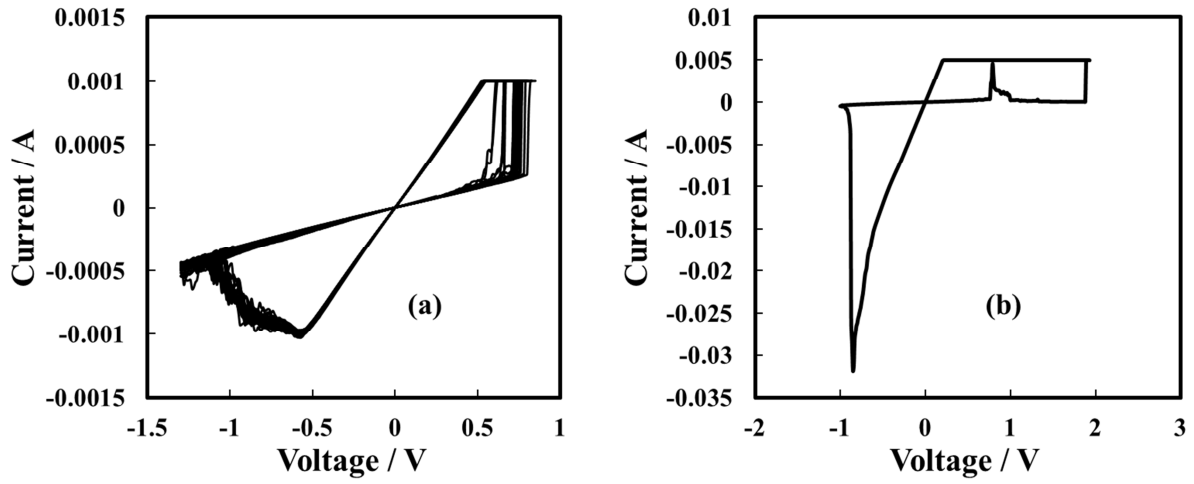

Figure 7.26 (a) 20 consecutive *I-V* sweeps with I_{CC} = 1 mA and (b) typical behaviour of the Al-20at.%Ta/anodic mixed oxide/Pt cells.

The resistance ratio is lower with respect to the other systems studied in this work but the reproducibility is good. Unfortunately, this is not the typical behaviour of the cells comprising the mixed Al-20at.%Ta oxide. In fact, during the polarization for positive values, the current usually does not reach the current compliance (i.e. a complete SET process) so that V_{SET} strongly increases and, consequently, R_{ON} decreases (see Figure 7.26(b)). The measured current for negative polarities is higher than I_{CC} and V_{RESET} does not reach a stable value during consecutive cycles leading to an unstable resistive switching of the junction. This behaviour seems to be random so that it is not possible to control and, thus, have a stable and reproducible resistive switching.

7.5 Concluding Remarks

The potentialities of metal/anodic oxide as bottom electrode/solid electrolyte for ReRAM devices have been shown.

For $Ta/Ta_2O_5/Pt$ system based on electrochemically prepared Ta oxide, *I–V* cycling and pulse endurances have been demonstrated for at least 10^3 and 10^6 cycles respectively, with high stability and low dispersion of SET and RESET voltages and excellent data retention. Stable resistance window and capability for at least nine distinguished LRS levels have been achieved. Switching times in the ~ 20 ns range were demonstrated. Moreover, the influence of sweep rate and of electrochemical fabrication technique has been shown, leading in any case to reliable and reproducible resistive switching. The presence of moisture inside the oxide matrix has been demonstrated as one of the crucial characteristic in order to have reliable FORMING processes and not irreversible anodic layers breakdown.

The reliability of $Hf/HfO_2/Pt$ system based on electrochemically prepared Hf oxide has been also demonstrated, showing reproducible 10^3 *I-V* cycles and good data retention for at least 10^4 seconds. The possibility to have different R_{ON} states has been investigated demonstrating the capability for several distinguished levels. In contrast, the $Nb/Nb_2O_5/Pt$ system has poorly reproducible resistive switching characteristics, regardless of the anodic layer/solid electrolyte thickness, with a not clear possible drift to threshold switching behaviour, as typically reported in literature for Nb oxide in ReRAM devices.

The possibility to tailor solid state properties of the anodic oxides through anodizing metallic alloys has been applied also to the ReRAM devices, so that different metal alloy/anodic mixed oxide/Pt systems have been investigated. In the case of Hf-4at.%Nb-based cells, the performances are very similar to that reported for pure Hf oxide-based devices with a possible degradation for long-lasting measurements. Al-Ta mixed anodic oxides have been tested as solid electrolytes and the performances confirm the excellent behaviour of Ta oxide, at least for Ta-rich layers, by increasing the resistance ratio due to the more insulating character of the Al-containing oxides. In contrast, for Ta-poor anodic layers, the performances are not so good despite in some case reproducible resistive switching has been detected.

A comparison between the resistive switching parameters of the different investigated materials is reported in Table 7.1.

Table 7.1 Resistive switching parameters of the materials investigated in this Ph.D. work. These values are related to consecutive *I-V* sweeps with I_{CC} = 2 mA except for the measurements related to the anodic oxides grown on Nb and on Al-20at.%Ta in which I_{CC} = 5 mA and 1 mA respectively.

Anodic Oxide	V_{SET} / V	V_{RESET} / V	R_{OFF} / Ω	R_{ON} / Ω	# cycles (max.)
Ta	0.45 – 0.65	-0.55 – -0.65	6350 – 3100	250 – 320	1000
Hf	0.48 – 0.62	-0.59 – -0.72	2760 – 1450	260 – 400	1000
Nb	1.2	-0.82	30000	150	5
Hf-4at.%Nb	0.45 – 0.81	-0.75 – -1	7400 – 1820	430 – 870	1000
Al-20at.%Ta	0.50 – 0.80	-0.55	3150 – 2900	560	20
Al-42at.%Ta	n.d.	n.d.	n.d.	n.d.	n.d.
Al-62at.%Ta	0.50 – 0.85	-0.65 – -0.75	26000 – 4300	300 – 430	1000
Al-91at.%Ta	0.50 – 0.75	-0.55	9000 – 4700	260 – 320	1000

The low yield of some devices needs further studies and investigation to produce more reliable cells and possible techniques, such as scanning droplet cell, needed to be studied to fabricate patterned anodic oxides to be integrated in CMOS technology.

8 Conclusions and Perspectives

This Ph.D. work was focused on the preparation by electrochemical oxidation, namely anodizing, of high-*k* thin oxide films, suitable to be used in several electronic devices such as electrolytic capacitors and, in particular, resistive switching devices.

The first part of the research activity was devoted in understanding how the anodizing process parameters, such as electrolyte composition, growth rate and formation voltage, and the metallic substrate composition can influence the structural and the electronic properties of the anodic oxides. For this purpose, pure valve metals and valve metals alloys with several compositions, deposited by magnetron sputtering on glass substrate, were anodized in different anodizing conditions.

Electrochemically prepared Hf oxide, Al-Ta and Hf-Nb mixed oxides were then characterized by both *in-situ* techniques, such as Photocurrent Spectroscopy and Electrochemical Impedance Spectroscopy, and *ex-situ* techniques, such as Glow Discharge Optical Emission Spectroscopy, X-Ray Diffraction and Transmission Electron Microscopy, in order to get information on how growth parameters are correlated with the structural (thickness, crystallinity, composition) and solid state (band gap, flat band potential, dielectric constant) properties of the anodic layers. These characterization allowed to understand that, anodizing in ammonium biborate solution could lead, in certain conditions, to incorporate N into Al-Ta mixed anodic oxides or that anodizing a Hf-Nb alloy with a small amount of Nb leads to prepare a crystalline oxide with a higher dielectric constant with respect to pure Hf oxide.

The second part of the research activity was devoted to demonstrate that metal/anodic oxide interfaces can be suitable bottom electrode/solid electrolyte junctions for resistive switching devices, as ReRAMs, and therefore anodizing can be a reliable route to prepare oxide thin films for electronic devices. In order to test the metal/anodic oxide junctions performances, Pt top electrode was deposited on the surface of anodic layers, being Pt one of the most common electrode used in ReRAM devices. Electrical characterization was carried out by *I-V* cycling and pulsed measurements, in order to study stability (in terms of SET, RESET voltages, R_{ON} and R_{OFF} values) as well as endurance and data retention of the devices. Among the

investigated systems, Ta/anodic Ta_2O_5-based cells demonstrated to be the most suitable for ReRAMs showing high stability, low dispersion of SET and RESET voltages, excellent data retention, capability for at least nine distinguished R_{ON} levels and switching times down to 20 ns.

Research activity conducted during the Ph.D. three years showed that anodizing process is a valuable way to prepare high-*k* oxide thin films starting from valve metals substrate and that it is possible to obtain precise and controlled characteristics of the oxide layers by changing the process parameters. Furthermore, it was demonstrated that metal/anodic oxide systems are suitable and reliable bottom electrode/solid electrolyte junctions for ReRAM devices. Nevertheless, further studies and investigation are necessary in order, first of all, to better understand the causes of the low yield of some anodic oxides-based cells. Moreover, it will be necessary to design a fabrication process to have anodic oxide-based cells at nanometre scale involving special techniques to grow anodic oxides (e.g. the use of a droplet cell) that could lead also to crossbar structures. Finally, more characterizations on anodic oxides, before and during the operation, are needed to better understand what are the physical processes underlying the excellent performances of the anodic oxides-based devices.

List of Figures

Bibliography

(1) Moore, G. E. Cramming More Components onto Integrated Circuits. *Electronics* **1965**, *38* (8), 114–117.

(2) Manchanda, L.; Morris, M. .; Green, M. .; van Dover, R. .; Klemens, F.; Sorsch, T. .; Silverman, P. .; Wilk, G.; Busch, B.; Aravamudhan, S. Multi-Component High-K Gate Dielectrics for the Silicon Industry. *Microelectron. Eng.* **2001**, *59* (1–4), 351–359.

(3) Pétry, J.; Richard, O.; Vandervorst, W.; Conard, T.; Chen, J.; Cosnier, V. Effect of N_2 Annealing on AlZrO Oxide. *J. Vac. Sci. Technol. A Vacuum, Surfaces, Film.* **2003**, *21* (4), 1482–1487.

(4) Paskaleva, A.; Bauer, A. J.; Lemberger, M.; Zürcher, S. Different Current Conduction Mechanisms through Thin High-K $Hf_xTi_ySi_zO$ Films due to the Varying Hf to Ti Ratio. *J. Appl. Phys.* **2004**, *95* (10), 5583–5590.

(5) Robertson, J.; Wallace, R. M. High-K Materials and Metal Gates for CMOS Applications. *Mater. Sci. Eng. R Reports* **2015**, *88*, 1–41.

(6) Masuda, H.; Fukuda, K. Ordered Metal Nanohole Arrays Made by a Two-Step Replication of Honeycomb Structures of Anodic Alumina. *Science (80-.).* **1995**, *268* (5216), 1466–1468.

(7) Thompson, G. E. Porous Anodic Alumina: Fabrication, Characterization and Applications. *Thin Solid Films* **1997**, *297* (1–2), 192–201.

(8) Garcia-Vergara, S. J.; Skeldon, P.; Thompson, G. E.; Habazaki, H. A Flow Model of Porous Anodic Film Growth on Aluminium. *Electrochim. Acta* **2006**, *52* (2), 681–687.

(9) Houser, J. E.; Hebert, K. R. The Role of Viscous Flow of Oxide in the Growth of Self-Ordered Porous Anodic Alumina Films. *Nat. Mater.* **2009**, *8* (5), 415–420.

(10) Roy, P.; Berger, S.; Schmuki, P. TiO_2 Nanotubes: Synthesis and Applications. *Angew. Chemie Int. Ed.* **2011**, *50* (13), 2904–2939.

(11) Habazaki, H. Growth of Passive Films on Valve Metals and Their Alloys. In *Reference Module in Chemistry, Molecular Sciences and Chemical Engineering*; Elsevier, 2017.

(12) Thompson, G. E.; Habazaki, H.; Shimizu, K.; Sakairi, M.; Skeldon, P.; Zhou, X.;

Wood, G. C. Anodizing of Aluminium Alloys. *Aircr. Eng. Aerosp. Technol.* **1999**, *71* (3), 228–238.

(13) Scaduto, G.; Santamaria, M.; Bocchetta, P.; Di Quarto, F. The Effect of Hydration Layers on the Anodic Growth and on the Dielectric Properties of Al_2O_3 for Electrolytic Capacitors. *Thin Solid Films* **2014**, *550*, 128–134.

(14) Di Franco, F.; Bocchetta, P.; Santamaria, M.; Di Quarto, F. Light Induced Electropolymerization of poly(3,4-Ethylenedioxythiophene) on Niobium Oxide. *Electrochim. Acta* **2010**, *56* (2), 737–744.

(15) Di Franco, F.; Bocchetta, P.; Cali', C.; Mosca, M.; Santamaria, M.; Di Quarto, F. Electrochemical Fabrication of Metal/Oxide/Conducting Polymer Junction. *J. Electrochem. Soc.* **2011**, *158* (1), H50–H54.

(16) Mosca, M.; Macaluso, R.; Randazzo, G.; Di Bella, M.; Caruso, F.; Calì, C.; Di Franco, F.; Santamaria, M.; Di Quarto, F. Anodized Ti-Si Alloy as Gate Oxide of Electrochemically-Fabricated Organic Field-Effect Transistors. *ECS Solid State Lett.* **2013**, *3* (1), P7–P9.

(17) Di Franco, F.; Santamaria, M.; Di Quarto, F.; Macaluso, R.; Mosca, M.; Calì, C. Electrochemical Fabrication and Physicochemical Characterization of Metal/High-K Insulating Oxide/Polymer/Electrolyte Junctions. *J. Phys. Chem. C* **2014**, *118* (51), 29973–29980.

(18) *Oxides and Oxide Films, Vol. 1*; Diggle, J. W., Ed.; Marcel Dekker: New York, 1972.

(19) Brock, A. J.; Wood, G. C. Hydroxyl Ion and Proton Mobility during Anodic Oxidation of Aluminium. *Electrochim. Acta* **1967**, *12* (4), 395–412.

(20) Di Franco, F.; Zaffora, A.; Santamaria, M.; Di Quarto, F. Anodization and Anodic Oxides. In *Reference Module in Chemistry, Molecular Sciences and Chemical Engineering*; Elsevier: Waltham, MA, 2016.

(21) Lohrengel, M. M. Thin Anodic Oxide Layers on Aluminium and Other Valve Metals: High Field Regime. *Mater. Sci. Eng. R Reports* **1993**, *11* (6), 243–294.

(22) Young, L. Anomalies in the Growth of Anodic Oxide Films on Rough Surfaces. *Acta*

Metall. **1957**, *5* (12), 711–716.

(23) Güntherschulze, A.; Betz, H. Die Elektronenströmung in Isolatoren Bei Extremen Feldstärken. *Zeitschrift fur Phys. A* **1934**, *70*, 70–96.

(24) Young, L. *Anodic Oxide Films*; Academic Press: London, 1961.

(25) Mott, N. F. The Theory of the Formation of Protective Oxide Films on Metals. - III. *Trans. Faraday Soc.* **1947**, *43*, 429–434.

(26) Cabrera, N.; Mott, N. F. Theory of the Oxidation of Metals. *Reports Prog. Phys.* **1949**, *12* (1), 163–184.

(27) Verwey, E. J. W. Electrolytic Conduction of a Solid Insulator at High Fields The Formation of the Anodic Oxide Film on Aluminium. *Physica* **1935**, *2* (1–12), 1059–1063.

(28) Davies, J. A.; Domeij, B.; Pringle, J. P. S.; Brown, F. The Migration of Metal and Oxygen during Anodic Film Formation. *J. Electrochem. Soc.* **1965**, *112* (7), 675–680.

(29) Pringle, J. P. S. Transport Number of Metal and Oxygen during the Anodic Oxidation of Tantalum. *J. Electrochem. Soc.* **1973**, *120* (3), 398–407.

(30) Pringle, J. P. S. Migration of Oxygen during the Anodic Oxidation of Tantalum. *Journal of the Electrochemical Society*. 1973, pp 1391–1400.

(31) Pringle, J. P. S. The Anodic Oxidation of Superimposed Niobium and Tantalum Layers: Theory. *Electrochim. Acta* **1980**, *25* (11), 1403–1421.

(32) Pringle, J. P. S. The Anodic Oxidation of Superimposed Metallic Layers: Theory. *Electrochim. Acta* **1980**, *25* (11), 1423–1437.

(33) Palagonia, M. S.; Nemcova, A.; Kubena, I.; Smid, M.; Gao, S.; Liu, H.; Zhong, X. L.; Haigh, S. J.; Santamaria, M.; Quarto, F. D.; Habazaki, H.; Skeldon, P.; Thompson, G. E. Behavior of Alloying Elements during Anodizing of Mg-Cu and Mg-W Alloys in a Fluoride/Glycerol Electrolyte. *J. Electrochem. Soc.* **2015**, *162* (9), C487–C494.

(34) Habazaki, H.; Shimizu, K.; Skeldon, P.; Thompson, G. E.; Wood, G. C. Inter-Relationships between Ionic Transport and Composition in Amorphous Anodic Oxides. *Proc. R. Soc. A Math. Phys. Eng. Sci.* **1997**, *453* (1963), 1593–1609.

(35) de Sá, A. I.; Rangel, C. M.; Lu, Q.; Skeldon, P.; Thompson, G. E. Anodic Oxidation and Dielectric Behaviour of Aluminium–niobium Alloys. *Corros. Sci.* **2006**, *48* (8), 2203–2211.

(36) Fogazza, M.; Santamaria, M.; Di Quarto, F.; Garcia-Vergara, S. J.; Molchan, I.; Skeldon, P.; Thompson, G. E.; Habazaki, H. Formation of Anodic Films on Sputtering-Deposited Al–Hf Alloys. *Electrochim. Acta* **2009**, *54* (3), 1070–1075.

(37) Cohen, M. H.; Fritzsche, H.; Ovshinsky, S. R. Simple Band Model for Amorphous Semiconducting Alloys. *Phys. Rev. Lett.* **1969**, *22* (20), 1065–1068.

(38) Adler, D. *Amorphous Semiconductors*; CRS Press, 1971.

(39) Tauc, J. *Amorphous and Liquid Semiconductors*; Plenum Press: London, 1974.

(40) Mott, N. F.; Davis, E. A. *Electronic Processes In Non-Crystalline Materials*, 2nd ed.; Clarendon Press: Oxford, U.K., 1979.

(41) Gärtner, W. W. Depletion-Layer Photoeffects in Semiconductors. *Phys. Rev.* **1959**, *116* (1), 84–87.

(42) Butler, M. A. Photoelectrolysis and Physical Properties of the Semiconducting Electrode WO_2. *J. Appl. Phys.* **1977**, *48* (5), 1914–1920.

(43) Di Quarto, F.; La Mantia, F.; Santamaria, M. Physicochemical Characterization of Passive Films and Corrosion Layers by Differential Admittance and Photocurrent Spectroscopy. In *Modern Aspects of Electrochemistry, No. 46: Progress in Corrosion Science and Engineering I*; Pyun, S.-I., Lee, J.-W., Eds.; Springer: New York, 2009; pp 231–316.

(44) Di Quarto, F.; Piazza, S.; Santamaria, M.; Sunseri, C. Photocurrent Spectroscopy of Thin Passive Films. In *Handbook of Thin Films*; Nalwa, H. S., Ed.; Academic Press: San Diego, CA, 2002; pp 373–414.

(45) Di Quarto, F.; Di Franco, F.; Zaffora, A.; Santamaria, M. Photocurrent Spectroscopy in Passivity Studies. In *Reference Module in Chemistry, Molecular Sciences and Chemical Engineering*; Elsevier, 2017.

(46) Pleskov, Y. V.; Gurevich, Y. Y. *Semiconductor Photoelectrochemistry*; Consultants

Bureau: New York, 1986.

(47) Di Quarto, F.; Santamaria, M.; Sunseri, C. Photoelectrochemical Techniques in Corrosion Studies. In *Analytical Methods in Corrosion Science and Technology*; Marcus, P., Mansfeld, F., Eds.; Taylor & Francis Group: Boca Raton, 2005; pp 697–732.

(48) Pai, D. M.; Enck, R. C. Onsager Mechanism of Photogeneration in Amorphous Selenium. *Phys. Rev. B* **1975**, *11* (12), 5163–5174.

(49) Di Quarto, F.; Piazza, S.; Sunseri, C. Photoelectrochemistry in Corrosion Studies: Achievements and Perspectives. *Mater. Sci. Forum* **1995**, *192–194*, 633–648.

(50) Di Quarto, F.; Piazza, S.; Sunseri, C.; Yang, M.; Cai, S. M. Photoelectrochemical Characterization of Thin Anodic Oxide Films on Zirconium Metal. *Electrochim. Acta* **1996**, *41* (16), 2511–2522.

(51) Gurevich, Y. Y.; Pleskov, Y. V.; Rotenberg, Z. A. *Photoelectrochemistry*; Plenum Press: New York, 1980.

(52) Waser, R. Introduction and Survey. In *Memristive Phenomena - From Fundamental Physics to Neuromorphic Computing*; Forschungszentrum Jülich GmbH: Jülich, 2016.

(53) Kahng, D.; Sze, S. M. A Floating Gate and Its Application to Memory Devices. *Bell Syst. Tech. J.* **1967**, *46* (6), 1288–1295.

(54) Waser, R.; Aono, M. Nanoionics-Based Resistive Switching Memories. *Nat. Mater.* **2007**, *6* (11), 833–840.

(55) Waser, R.; Dittmann, R.; Staikov, G.; Szot, K. Redox-Based Resistive Switching Memories - Nanoionic Mechanisms, Prospects, and Challenges. *Adv. Mater.* **2009**, *21* (25–26), 2632–2663.

(56) *Resistive Switching: From Fundamentals of Nanoionic Redox Processes to Memristive Device Applications*; Ielmini, D., Waser, R., Eds.; Wiley-VCH Verlag GmbH & Co. KGaA: Weinheim, Germany, 2016.

(57) Ielmini, D. Resistive Switching Memories Based on Metal Oxides: Mechanisms, Reliability and Scaling. *Semicond. Sci. Technol.* **2016**, *31* (6), 63002.

(58) Valov, I. Interfacial Interactions and Their Impact on Redox-Based Resistive Switching Memories (ReRAMs). *Semicond. Sci. Technol.* **2017**, *32* (9), 93006.

(59) Valov, I.; Waser, R.; Jameson, J. R.; Kozicki, M. N. Electrochemical Metallization Memories—fundamentals, Applications, Prospects. *Nanotechnology* **2011**, *22* (25), 254003.

(60) Valov, I. Oxide Thin Films for Memristive Devices. In *Reference Module in Chemistry, Molecular Sciences and Chemical Engineering*; Elsevier, 2017.

(61) Valov, I. Redox-Based Resistive Switching Memories (ReRAMs): Electrochemical Systems at the Atomic Scale. *ChemElectroChem* **2014**, *1* (1), 26–36.

(62) Yang, Y.; Gao, P.; Li, L.; Pan, X.; Tappertzhofen, S.; Choi, S.; Waser, R.; Valov, I.; Lu, W. D. Electrochemical Dynamics of Nanoscale Metallic Inclusions in Dielectrics. *Nat. Commun.* **2014**, *5*, 4232/1.

(63) Lv, H.; Xu, X.; Sun, P.; Liu, H.; Luo, Q.; Liu, Q.; Banerjee, W.; Sun, H.; Long, S.; Li, L.; Liu, M. Atomic View of Filament Growth in Electrochemical Memristive Elements. *Sci. Rep.* **2015**, *5* (1), 13311.

(64) Yang, Y.; Lu, W. D. Progress in the Characterizations and Understanding of Conducting Filaments in Resistive Switching Devices. *IEEE Trans. Nanotechnol.* **2016**, *15* (3), 465–472.

(65) Wang, Z.; Jiang, H.; Hyung Jang, M.; Lin, P.; Ribbe, A.; Xia, Q.; Yang, J. J. Electrochemical Metallization Switching with a Platinum Group Metal in Different Oxides. *Nanoscale* **2016**, *8* (29), 14023–14030.

(66) Tappertzhofen, S.; Valov, I.; Tsuruoka, T.; Hasegawa, T.; Waser, R.; Aono, M. Generic Relevance of Counter Charges for Cation-Based Nanoscale Resistive Switching Memories. *ACS Nano* **2013**, *7* (7), 6396–6402.

(67) Tappertzhofen, S.; Waser, R.; Valov, I. Impact of the Counter-Electrode Material on Redox Processes in Resistive Switching Memories. *ChemElectroChem* **2014**, *1* (8), 1287–1292.

(68) Tsuruoka, T.; Terabe, K.; Hasegawa, T.; Valov, I.; Waser, R.; Aono, M. Effects of

Moisture on the Switching Characteristics of Oxide-Based, Gapless-Type Atomic Switches. *Adv. Funct. Mater.* **2012**, *22* (1), 70–77.

(69) Tsuruoka, T.; Valov, I.; Tappertzhofen, S.; van den Hurk, J.; Hasegawa, T.; Waser, R.; Aono, M. Redox Reactions at Cu,Ag/Ta_2O_5 Interfaces and the Effects of Ta_2O_5 Film Density on the Forming Process in Atomic Switch Structures. *Adv. Funct. Mater.* **2015**, *25* (40), 6374–6381.

(70) Valov, I.; Linn, E.; Tappertzhofen, S.; Schmelzer, S.; van den Hurk, J.; Lentz, F.; Waser, R. Nanobatteries in Redox-Based Resistive Switches Require Extension of Memristor Theory. *Nat. Commun.* **2013**, *4*, 1771.

(71) Cho, D.-Y.; Valov, I.; van den Hurk, J.; Tappertzhofen, S.; Waser, R. Direct Observation of Charge Transfer in Solid Electrolyte for Electrochemical Metallization Memory. *Adv. Mater.* **2012**, *24* (33), 4552–4556.

(72) Valov, I.; Kozicki, M. N. Cation-Based Resistance Change Memory. *J. Phys. D. Appl. Phys.* **2013**, *46* (7), 74005.

(73) Goux, L.; Valov, I. Electrochemical Processes and Device Improvement in Conductive Bridge RAM Cells. *Phys. Status Solidi* **2016**, *213* (2), 274–288.

(74) Kim, W.; Menzel, S.; Wouters, D. J.; Guo, Y.; Robertson, J.; Roesgen, B.; Waser, R.; Rana, V. Impact of Oxygen Exchange Reaction at the Ohmic Interface in Ta_2O_5-Based ReRAM Device. *Nanoscale* **2016**, *8* (41), 17774–17781.

(75) Lee, M.-J.; Lee, C. B.; Lee, D.; Lee, S. R.; Chang, M.; Hur, J. H.; Kim, Y.-B.; Kim, C.-J.; Seo, D. H.; Seo, S.; Chung, U.-I.; Yoo, I.-K.; Kim, K. A Fast, High-Endurance and Scalable Non-Volatile Memory Device Made from Asymmetric Ta_2O_{5-x}/TaO_{2-x} Bilayer Structures. *Nat. Mater.* **2011**, *10* (8), 625–630.

(76) Wedig, A.; Luebben, M.; Cho, D.-Y.; Moors, M.; Skaja, K.; Rana, V.; Hasegawa, T.; Adepalli, K. K.; Yildiz, B.; Waser, R.; Valov, I. Nanoscale Cation Motion in TaO_x, HfO_x and TiO_x Memristive Systems. *Nat. Nanotechnol.* **2016**, *11* (1), 67–74.

(77) Zhong, X.; Rungger, I.; Zapol, P.; Nakamura, H.; Asai, Y.; Heinonen, O. The Effect of a Ta Oxygen Scavenger Layer on HfO_2-Based Resistive Switching Behavior:

Thermodynamic Stability, Electronic Structure, and Low-Bias Transport. *Phys. Chem. Chem. Phys.* **2016**, *18* (10), 7502–7510.

(78) Cho, D.-Y.; Luebben, M.; Wiefels, S.; Lee, K.-S.; Valov, I. Interfacial Metal–Oxide Interactions in Resistive Switching Memories. *ACS Appl. Mater. Interfaces* **2017**, *9* (22), 19287–19295.

(79) Clima, S.; Chen, Y. Y.; Chen, C. Y.; Goux, L.; Govoreanu, B.; Degraeve, R.; Fantini, A.; Jurczak, M.; Pourtois, G. First-Principles Thermodynamics and Defect Kinetics Guidelines for Engineering a Tailored RRAM Device. *J. Appl. Phys.* **2016**, *119* (22), 225107.

(80) Celano, U.; Op de Beeck, J.; Clima, S.; Luebben, M.; Koenraad, P. M.; Goux, L.; Valov, I.; Vandervorst, W. Direct Probing of the Dielectric Scavenging-Layer Interface in Oxide Filamentary-Based Valence Change Memory. *ACS Appl. Mater. Interfaces* **2017**, *9* (12), 10820–10824.

(81) McTegart, W. J. *The Electrolytic and Chemical Polishing of Metals*; Pergamon Press: London, 1956.

(82) Foley, R. T. Localized Corrosion of Aluminum Alloys—A Review. *CORROSION* **1986**, *42* (5), 277–288.

(83) Peter, L. Photocurrent Spectroscopy. In *Comprehensive Chemical Kinetics, Vol. 29*; Compton, R. G., Ed.; Elsevier Science: Oxford, 1989; p 382.

(84) Afanas'ev, V. V.; Stesmans, A. Internal Photoemission at Interfaces of High-κ Insulators with Semiconductors and Metals. *J. Appl. Phys.* **2007**, *102* (8), 81301.

(85) Di Quarto, F.; Sunseri, C.; Piazza, S.; Romano, M. C. Semiempirical Correlation between Optical Band Gap Values of Oxides and the Difference of Electronegativity of the Elements. Its Importance for a Quantitative Use of Photocurrent Spectroscopy in Corrosion Studies. *J. Phys. Chem. B* **1997**, *2* (97), 2519–2525.

(86) Di Quarto, F.; Zaffora, A.; Di Franco, F.; Santamaria, M. Review — Photocurrent Spectroscopy in Corrosion and Passivity Studies: A Critical Assessment of the Use of Band Gap Value to Estimate the Oxide Film Composition. *J. Electrochem. Soc.* **2017**,

164 (12), C671–C681.

(87) Schottky, W. Zur Halbleitertheorie Der Sperrschicht Und Spitzengleichrichter. *Zeitschrift für Phys.* **1939**, *113* (5–6), 367–414.

(88) Dewald, J. F. The Charge Distribution at the Zinc Oxide-Electrolyte Interface. *J. Phys. Chem. Solids* **1960**, *14*, 155–161.

(89) Dewald, J. F. The Charge and Potential Distributions at the Zinc Oxide Electrode. *Bell Syst. Tech. J.* **1960**, *39* (3), 615–639.

(90) Stimming, U. Photoelectrochemical Studies of Passive Films. *Electrochim. Acta* **1986**, *31* (4), 415–429.

(91) Di Quarto, F.; La Mantia, F.; Santamaria, M. Physicochemical Characterization of Passive Films on Niobium by Admittance and Electrochemical Impedance Spectroscopy Studies. *Electrochim. Acta* **2005**, *50*, 5090–5102.

(92) La Mantia, F.; Habazaki, H.; Santamaria, M.; Di Quarto, F. A Critical Assessment of the Mott-Schottky Analysis for the Characterisation of Passive Film-Electrolyte Junctions. *Russ. J. Electrochem.* **2010**, *46* (11), 1306–1322.

(93) Orazem, M. E.; Tribollet, B. *Electrochemical Impedance Spectroscopy*; John Wiley & Sons: Hoboken, NJ, 2008.

(94) La Mantia, F.; Fan, M.; Stojadinović, J.; Santamaria, M.; Miraghaei, S.; Di Quarto, F. Assessment on the Use of the Amorphous Semiconductor Theory for the Analysis of Oxide Films. *Electrochim. Acta* **2015**, *179*, 460–468.

(95) Di Quarto, F.; Di Franco, F.; Miraghaei, S.; Santamaria, M.; La Mantia, F. The Amorphous Semiconductor Schottky Barrier Approach to Study the Electronic Properties of Anodic Films on Ti. *J. Electrochem. Soc.* **2017**, *164* (9), C516–C525.

(96) Toney, M. F. X-Ray Diffraction. In *Encyclopedia of Materials Characterization*; Brundle, R. C., Evans, C. A. J., Wilson, S., Eds.; Butterworth-Heinemann: Stoneham, MA, 1992.

(97) Atkins, P.; De Paula, J. *Physical Chemistry*, 10th ed.; Oxford University Press, 2010.

(98) Lee, M. *X-Ray Diffraction for Materials Research*; Apple Academic Press: Oakville,

Canada, 2016.

(99) Schmelzer, S. Ultra Thin Oxide Films for Dielectric and Resistive Memory Applications, RWTH Aachen University, 2013.

(100) Shimizu, K.; Habazaki, H.; Skeldon, P.; Thompson, G. E. Radiofrequency GDOES: A Powerful Technique for Depth Profiling Analysis of Thin Films. *Surf. Interface Anal.* **2003**, *35* (7), 564–574.

(101) Fahlman, B. D. *Materials Chemistry*; Springer Netherlands, 2007.

(102) Egerton, R. F. *Physical Principles of Electron Microscopy*, 2nd ed.; Springer Switzerland, 2016.

(103) Shimizu, K.; Mitani, T. *A New World of Scanning Electron Microscopy*.

(104) Tappertzhofen, S.; Menzel, S.; Valov, I.; Waser, R. Redox Processes in Silicon Dioxide Thin Films Using Copper Microelectrodes. *Appl. Phys. Lett.* **2011**, *99* (20), 203103.

(105) Tappertzhofen, S.; Mündelein, H.; Valov, I.; Waser, R. Nanoionic Transport and Electrochemical Reactions in Resistively Switching Silicon Dioxide. *Nanoscale* **2012**, *4* (10), 3040–3043.

(106) Bard, A. J.; Faulkner, L. R. *Electrochemical Methods. Fundamentals and Applications*, 2nd ed.; John Wiley & Sons, 2001.

(107) Habazaki, H.; Shimizu, K.; Nagata, S.; Skeldon, P.; Thompson, G. E.; Wood, G. C. Ionic Transport in Amorphous Anodic Titania Stabilised by Incorporation of Silicon Species. *Corros. Sci.* **2002**, *44* (5), 1047–1055.

(108) Zhou, F.; LeClere, D. J.; Garcia-Vergara, S. J.; Hashimoto, T.; Molchan, I. S.; Habazaki, H.; Skeldon, P.; Thompson, G. E. Incorporation and Migration of Phosphorus Species in Anodic Alumina Films Containing Tungsten Tracer Layers. *J. Electrochem. Soc.* **2010**, *157* (12), C437–C443.

(109) Garcia-Vergara, S. J.; Molchan, I. S.; Zhou, F.; Habazaki, H.; Kowalski, D.; Skeldon, P.; Thompson, G. E. Incorporation and Migration of Phosphorus Species within Anodic Films on an Al-W Alloy. *Surf. Interface Anal.* **2011**, *43* (5), 893–902.

(110) Ono, S.; Kuramochi, K.; Asoh, H. Effects of Electrolyte pH and Temperature on

Dielectric Properties of Anodic Oxide Films Formed on Niobium. *Corros. Sci.* **2009**, *51* (7), 1513–1518.

(111) Di Franco, F.; Santamaria, M.; Di Quarto, F.; Tsuji, E.; Habazaki, H. The Influence of Nitrogen Incorporation on the Optical Properties of Anodic Ta_2O_5. *Electrochim. Acta* **2012**, *59*, 382–386.

(112) Miraghaei, S.; Santamaria, M.; Di Quarto, F. Red Shift in the Light Absorption Threshold of Anodic TiO_2 Films Induced by Nitrogen Incorporation. *Electrochim. Acta* **2014**, *134*, 150–158.

(113) Zaffora, A.; Di Franco, F.; Santamaria, M.; Habazaki, H.; Di Quarto, F. The Influence of Composition on Band Gap and Dielectric Constant of Anodic Al-Ta Mixed Oxides. *Electrochim. Acta* **2015**, *180*, 666–678.

(114) Pourbaix, M. *Atlas of Electrochemical Equilibria in Aqueous Solutions*; Pergamon Press: Oxford, UK, 1966.

(115) Alcalá, G.; Mato, S.; Skeldon, P.; Thompson, G. E.; Bailey, P.; Noakes, T. C. Q.; Habazaki, H.; Shimizu, K. Anodic Film Growth in the Al–Ta Alloy System. *Corros. Sci.* **2003**, *45* (8), 1803–1813.

(116) Habazaki, H.; Fushimi, K.; Shimizu, K.; Skeldon, P.; Thompson, G. E. Fast Migration of Fluoride Ions in Growing Anodic Titanium Oxide. *Electrochem. commun.* **2007**, *9* (5), 1222–1227.

(117) Wood, G. C.; Skeldon, P.; Thompson, G. E.; Shimizu, K. A Model for the Incorporation of Electrolyte Species into Anodic Alumina. *J. Electrochem. Soc.* **1996**, *143* (1), 74–83.

(118) Shimizu, K.; Habazaki, H.; Skeldon, P.; Thompson, G. E.; Wood, G. C. Migration of Oxalate Ions in Anodic Alumina. *Electrochim. Acta* **2001**, *46* (28), 4379–4382.

(119) Shimizu, K.; Kobayashi, K.; Thompson, G. E.; Skeldon, P.; Wood, G. C. Anodic Oxide Films on Tantalum: Incorporation and Mobilities of Electrolyte-Derived Species. *Philos. Mag. Part B* **1996**, *73* (3), 461–485.

(120) McCafferty, E. A Surface Charge Model of Corrosion Pit Initiation and of Protection by Surface Alloying. *J. Electrochem. Soc.* **1999**, *146* (8), 2863–2869.

(121) McCafferty, E. Relationship between the Isoelectric Point (pH_{pzc}) and the Potential of Zero Charge (E_{pzc}) for Passive Metals. *Electrochim. Acta* **2010**, *55* (5), 1630–1637.

(122) Wells, A. F. *Structural Inorganic Chemistry*; Clarendon Press: Oxford, UK, 1975.

(123) Atkins, P. W. *The Elements of Physical Chemistry*; Oxford University Press: Oxford, UK, 1996.

(124) Dabirian, A.; van de Krol, R. High-Temperature Ammonolysis of Thin Film Ta_2O_5 Photoanodes: Evolution of Structural, Optical, and Photoelectrochemical Properties. *Chem. Mater.* **2015**, *27* (3), 708–715.

(125) Di Franco, F.; Santamaria, M.; Di Quarto, F.; La Mantia, F.; de Sá, A. I.; Rangel, C. M. Dielectric Properties of Al-Nb Amorphous Mixed Oxides. *ECS J. Solid State Sci. Technol.* **2013**, *2* (11), N205–N210.

(126) Di Quarto, F.; Santamaria, M.; Skeldon, P.; Thompson, G. E. Photocurrent Spectroscopy Study of Passive Films on Hafnium and Hafnium–Tungsten Sputtered Alloys. *Electrochim. Acta* **2003**, *48* (9), 1143–1156.

(127) Santamaria, M.; Di Quarto, F.; Skeldon, P.; Thompson, G. E. Effect of Composition on the Photoelectrochemical Behavior of Anodic Oxides on Binary Aluminum Alloys. *J. Electrochem. Soc.* **2006**, *153* (12), B518–B526.

(128) Santamaria, M.; Di Quarto, F.; Habazaki, H. Influences of Structure and Composition on the Photoelectrochemical Behaviour of Anodic Films on Zr and Zr–20at.%Ti. *Electrochim. Acta* **2008**, *53* (5), 2272–2280.

(129) Santamaria, M.; Di Quarto, F.; Zanna, S.; Marcus, P. The Influence of Surface Treatment on the Anodizing of Magnesium in Alkaline Solution. *Electrochim. Acta* **2011**, *56* (28), 10533–10542.

(130) Santamaria, M.; Di Quarto, F.; Habazaki, H. Photocurrent Spectroscopy Applied to the Characterization of Passive Films on Sputter-Deposited Ti–Zr Alloys. *Corros. Sci.* **2008**, *50* (7), 2012–2020.

(131) Onsager, L. Deviations from Ohm's Law in Weak Electrolytes. *J. Chem. Phys.* **1934**, *2* (9), 599–615.

(132) Onsager, L. Initial Recombination of Ions. *Phys. Rev.* **1938**, *54* (8), 554–557.

(133) Heavens, O. S. *Optical Properties of Thin Solid Films*; Dover Publications: New York, 1965.

(134) *CRC Handbook of Chemistry and Physics, 90th Edition*; Lide, D. R., Ed.; CRC Press/Taylor and Francis: Boca Raton, 2010.

(135) Adachi, S. *The Handbook on Optical Constants of Metals*; World Scientific, 2012.

(136) Azim, O. A.; Abdel-Aziz, M. M.; Yahia, I. S. Structure and Optical Analysis of Ta_2O_5 Deposited on Infrasil Substrate. *Appl. Surf. Sci.* **2009**, *255* (9), 4829–4835.

(137) Sunseri, C.; Piazza, S.; Di Quarto, F. Photocurrent Spectroscopic Investigations of Passive Films on Chromium. *J. Electrochem. Soc.* **1990**, *137* (8), 2411–2417.

(138) Hamadou, L.; Kadri, A.; Benbrahim, N. Impedance Investigation of Thermally Formed Oxide Films on AISI 304L Stainless Steel. *Corros. Sci.* **2010**, *52* (3), 859–864.

(139) Hakiki, N. E. Comparative Study of Structural and Semiconducting Properties of Passive Films and Thermally Grown Oxides on AISI 304 Stainless Steel. *Corros. Sci.* **2011**, *53* (9), 2688–2699.

(140) Piazza, S.; Sunseri, C.; Di Quarto, F. A Simple Model for the Photoelectrochemical Behavior of Corrosion Layers with Variable Hydration Degree. *Corrosion*. 2002, pp 436–447.

(141) Crandall, R. S. Modeling of Thin Film Solar Cells: Uniform Field Approximation. *J. Appl. Phys.* **1983**, *54* (12), 7176–7186.

(142) Santamaria, M.; Huerta, D.; Piazza, S.; Sunseri, C.; Di Quarto, F. The Influence of the Electronic Properties of Passive Films on the Corrosion Resistance of Mo-Ta Alloys. A Photoelectrochemical Study. *J. Electrochem. Soc.* **2000**, *147* (4), 1366–1375.

(143) Di Quarto, F.; Di Franco, F.; Monarca, C.; Santamaria, M.; Habazaki, H. Photoelectrochemical Characterization of Amorphous Anodic Films on Ti–6at.%Si. *Electrochim. Acta* **2013**, *110*, 517–525.

(144) Muñoz Ramo, D.; Shluger, A. L.; Gavartin, J. L.; Bersuker, G. Theoretical Prediction of Intrinsic Self-Trapping of Electrons and Holes in Monoclinic HfO_2. *Phys. Rev. Lett.*

2007, *99* (15), 155504.

(145) Khairnar, A. G.; Patil, L. S.; Salunke, R. S.; Mahajan, A. M. Electrical Properties of HfO_2 High-K Thin-Film MOS Capacitors for Advanced CMOS Technology. *Indian J. Phys.* **2015**, *89* (11), 1177–1181.

(146) Paskaleva, A.; Rommel, M.; Hutzler, A.; Spassov, D.; Bauer, A. J. Tailoring the Electrical Properties of HfO_2 MOS-Devices by Aluminum Doping. *ACS Appl. Mater. Interfaces* **2015**, *7* (31), 17032–17043.

(147) Salomone, L. S.; Lipovetzky, J.; Carbonetto, S. H.; García Inza, M. A.; Redin, E. G.; Campabadal, F.; Faigón, A. Deep Electron Traps in HfO_2-Based Metal-Oxide-Semiconductor Capacitors. *Thin Solid Films* **2016**, *600*, 36–42.

(148) Kittl, J. A.; Opsomer, K.; Popovici, M.; Menou, N.; Kaczer, B.; Wang, X. P.; Adelmann, C.; Pawlak, M. A.; Tomida, K.; Rothschild, A.; Govoreanu, B.; Degraeve, R.; Schaekers, M.; Zahid, M.; Delabie, A.; Meersschaut, J.; Polspoel, W.; Clima, S.; Pourtois, G.; Knaepen, W.; Detavernier, C.; Afanas'ev, V. V.; Blomberg, T.; Pierreux, D.; Swerts, J.; Fischer, P.; Maes, J. W.; Manger, D.; Vandervorst, W.; Conard, T.; Franquet, A.; Favia, P.; Bender, H.; Brijs, B.; Van Elshocht, S.; Jurczak, M.; Van Houdt, J.; Wouters, D. J. High-K Dielectrics for Future Generation Memory Devices. *Microelectron. Eng.* **2009**, *86* (7–9), 1789–1795.

(149) Wang, M.; Bi, C.; Li, L.; Long, S.; Liu, Q.; Lv, H.; Lu, N.; Sun, P.; Liu, M. Thermoelectric Seebeck Effect in Oxide-Based Resistive Switching Memory. *Nat. Commun.* **2014**, *5*, 4598.

(150) Mardare, A. I.; Siket, C. M.; Gavrilovic-Wohlmuther, A.; Kleber, C.; Bauer, S.; Hassel, A. W. Anodization Behavior of Glassy Metallic Hafnium Thin Films. *J. Electrochem. Soc.* **2015**, *162* (4), E30–E36.

(151) Siket, C. M.; Bendova, M.; Mardare, C. C.; Hubalek, J.; Bauer, S.; Hassel, A. W.; Mardare, A. I. Interfacial Oxide Formation during Anodization of Hafnium/Aluminium Superimposed Layers. *Electrochim. Acta* **2015**, *178*, 344–352.

(152) Abd El-Rahman, H. A.; Abou-Romia, M. M. Anodization of Hafnium in Phosphoric

Acid Solutions. *J. Appl. Electrochem.* **1990**, *20* (1), 39–44.

(153) Salih, S. A.; Abdel Khalek, A. A.; El Mahdy, G. A. Macroscopic Kinetic Studies of Anodic Oxide-Film Growth on Hafnium. *Bull. Soc. Chim. Fr.* **1991**, *128* (5), 665–670.

(154) Di Franco, F.; Zampardi, G.; Santamaria, M.; Di Quarto, F.; Habazaki, H. Characterization of the Solid State Properties of Anodic Oxides on Magnetron Sputtered Ta, Nb and Ta-Nb Alloys. *J. Electrochem. Soc.* **2012**, *159* (1), C33–C39.

(155) Gad-Allah, A. G.; Abd El-Rahman, H. A.; Abou-Romia, M. M. Influence of Oxide Bond Energies on the Kinetics of Chemical Dissolution of Anodic Oxides on Valve Metals. *J. Appl. Electrochem.* **1988**, *18* (4), 532–537.

(156) Bartels, C.; Schultze, J. W.; Stimming, U.; Habib, M. A. The Electrochemical Behaviour of Hafnium. *Electrochim. Acta* **1982**, *27* (1), 129–140.

(157) Afanas'ev, V. V.; Stesmans, A.; Chen, F.; Shi, X.; Campbell, S. A. Internal Photoemission of Electrons and Holes from (100) Si into HfO_2. *Appl. Phys. Lett.* **2002**, *81* (6), 1053–1055.

(158) Newmark, A. R.; Stimming, U. Photoelectrochemical Properties of Ion-Implanted Hafnium Dioxide Films. *Electrochim. Acta* **1989**, *34* (1), 47–55.

(159) Muñoz Ramo, D.; Gavartin, J. L.; Shluger, A. L.; Bersuker, G. Spectroscopic Properties of Oxygen Vacancies in Monoclinic HfO_2 Calculated with Periodic and Embedded Cluster Density Functional Theory. *Phys. Rev. B* **2007**, *75* (20), 205336.

(160) Hildebrandt, E.; Kurian, J.; Alff, L. Physical Properties and Band Structure of Reactive Molecular Beam Epitaxy Grown Oxygen Engineered $HfO_{2\pm x}$. *J. Appl. Phys.* **2012**, *112* (11), 114112.

(161) Gritsenko, V. A.; Perevalov, T. V.; Islamov, D. R. Electronic Properties of Hafnium Oxide: A Contribution from Defects and Traps. *Phys. Rep.* **2016**, *613*, 1–20.

(162) Santamaria, M.; Di Franco, F.; Di Quarto, F.; Skeldon, P.; Thompson, G. E. Tailoring of the Solid State Properties of Al–Nb Mixed Oxides: A Photoelectrochemical Study. *J. Phys. Chem. C* **2013**, *117* (8), 4201–4210.

(163) La Mantia, F.; Santamaria, M.; Di Quarto, F.; Habazaki, H. Physicochemical

Characterization of Thermally Aged Anodic Films on Magnetron-Sputtered Niobium. *J. Electrochem. Soc.* **2010**, *157* (7), C258–C267.

(164) Johansen, H. A.; Adams, G. B.; Van Rysselberghe, P. Anodic Oxidation of Aluminum, Chromium, Hafnium, Niobium, Tantalum, Titanium, Vanadium, and Zirconium at Very Low Current Densities. *J. Electrochem. Soc.* **1957**, *104* (6), 339–346.

(165) Wang, Z.; Yu, H.; Su, H. The Transport Properties of Oxygen Vacancy-Related Polaron-like Bound State in HfO_x. *Sci. Rep.* **2013**, *3*, 3246.

(166) Lee, H.; Xu, F.; Jeffcoate, C. S.; Isaacs, H. S. Cyclic Polarization Behavior of Aluminum Oxide Films in Near Neutral Solutions. *Electrochem. Solid-State Lett.* **2001**, *4* (10), B31–B34.

(167) Boxley, C. J.; Watkins, J. J.; White, H. S. Al_2O_3 Film Dissolution in Aqueous Chloride Solutions. *Electrochem. Solid-State Lett.* **2003**, *6* (10), B38–B41.

(168) Memming, R. *Semiconductor Electrochemistry*; J. Wiley-VCH: Weinheim, 2001.

(169) Hammer, C.; Walther, B.; Karabulut, H.; Lohrengel, M. M. Oscillating Oxygen Evolution at Ta Anodes. *J. Solid State Electrochem.* **2011**, *15* (9), 1885–1891.

(170) Ho Lee, J.; Yu, I.-H.; Young Lee, S.; Seong Hwang, C. Phase Control of HfO_2-Based Dielectric Films for Higher-K Materials. *J. Vac. Sci. Technol. B, Nanotechnol. Microelectron. Mater. Process. Meas. Phenom.* **2014**, *32* (3), 03D109.

(171) Mardare, A. I.; Ludwig, A.; Savan, A.; Hassel, A. W. Scanning Droplet Cell Microscopy on a Wide Range Hafnium – Niobium Thin Film Combinatorial Library. *Electrochim. Acta* **2013**, *110*, 539–549.

(172) Habazaki, H.; Matsuo, T.; Konno, H.; Shimizu, K.; Nagata, S.; Matsumoto, K.; Takayama, K.; Oda, Y.; Skeldon, P.; Thompson, G. E. Influence of Silicon Species on the Electric Properties of Anodic Niobia. *Electrochim. Acta* **2003**, *48* (23), 3519–3526.

(173) Habazaki, H.; Ogasawara, T.; Konno, H.; Shimizu, K.; Asami, K.; Saito, K.; Nagata, S.; Skeldon, P.; Thompson, G. E. Growth of Anodic Oxide Films on Oxygen-Containing Niobium. *Electrochim. Acta* **2005**, *50* (27), 5334–5339.

(174) Komiyama, S.; Tsuji, E.; Aoki, Y.; Habazaki, H.; Santamaria, M.; Di Quarto, F.;

Skeldon, P.; Thompson, G. E. Growth and Field Crystallization of Anodic Films on Ta–Nb Alloys. *J. Solid State Electrochem.* **2012**, *16* (4), 1595–1604.

(175) Matovic, B.; Pantic, J.; Lukovic, J.; Cebela, M.; Dmitrovic, S.; Mirkovic, M.; Prekajski, M. A Novel Reduction–oxidation Synthetic Route for Hafnia. *Ceram. Int.* **2016**, *42* (1), 615–620.

(176) Lauria, A.; Villa, I.; Fasoli, M.; Niederberger, M.; Vedda, A. Multifunctional Role of Rare Earth Doping in Optical Materials: Nonaqueous Sol–Gel Synthesis of Stabilized Cubic HfO_2 Luminescent Nanoparticles. *ACS Nano* **2013**, *7* (8), 7041–7052.

(177) Kumar, N.; George, B. P. A.; Abrahamse, H.; Parashar, V.; Ray, S. S.; Ngila, J. C. A Novel Approach to Low-Temperature Synthesis of Cubic HfO_2 Nanostructures and Their Cytotoxicity. *Sci. Rep.* **2017**, *7* (1), 9351.

(178) Habazaki, H.; Uozumi, M.; Konno, H.; Shimizu, K.; Skeldon, P.; Thompson, G. E. Crystallization of Anodic Titania on Titanium and Its Alloys. *Corros. Sci.* **2003**, *45* (9), 2063–2073.

(179) Koyama, S.; Aoki, Y.; Nagata, S.; Habazaki, H. Formation and Dielectric Properties of Anodic Oxide Films on Zr–Al Alloys. *J. Solid State Electrochem.* **2011**, *15* (10), 2221–2229.

(180) Habazaki, H.; Uozumi, M.; Konno, H.; Shimizu, K.; Nagata, S.; Asami, K.; Matsumoto, K.; Takayama, K.; Oda, Y.; Skeldon, P.; Thompson, G. E. Influences of Structure and Composition on Growth of Anodic Oxide Films on Ti-Zr Alloys. *Electrochim. Acta* **2003**, *48* (20), 3257–3266.

(181) Sato, Y.; Asoh, H.; Ono, S. Effects of Electrolyte Species and Their Combination on Film Structures and Dielectric Properties of Crystalline Anodic Alumina Films Formed by Two-Step Anodization. *Mater. Trans.* **2013**, *54* (10), 1993–1999.

(182) Eastman, D. E. Photoelectric Work Functions of Transition, Rare-Earth, and Noble Metals. *Phys. Rev. B* **1970**, *2* (1), 1–2.

(183) Privitera, S.; Bersuker, G.; Butcher, B.; Kalantarian, A.; Lombardo, S.; Bongiorno, C.; Geer, R.; Gilmer, D. C.; Kirsch, P. D. Microscopy Study of the Conductive Filament in

HfO_2 Resistive Switching Memory Devices. *Microelectron. Eng.* **2013**, *109*, 75–78.

(184) Lübben, M.; Karakolis, P.; Ioannou-Sougleridis, V.; Normand, P.; Dimitrakis, P.; Valov, I. Graphene-Modified Interface Controls Transition from VCM to ECM Switching Modes in Ta/TaO_x Based Memristive Devices. *Adv. Mater.* **2015**, *27* (40), 6202–6207.

(185) Carta, D.; Salaoru, I.; Khiat, A.; Regoutz, A.; Mitterbauer, C.; Harrison, N. M.; Prodromakis, T. Investigation of the Switching Mechanism in TiO_2-Based RRAM: A Two-Dimensional EDX Approach. *ACS Appl. Mater. Interfaces* **2016**, *8* (30), 19605–19611.

(186) Aslam, N.; Longo, V.; Rodenbücher, C.; Roozeboom, F.; Kessels, W. M. M.; Szot, K.; Waser, R.; Hoffmann-Eifert, S. Impact of Composition and Crystallization Behavior of Atomic Layer Deposited Strontium Titanate Films on the Resistive Switching of Pt/STO/TiN Devices. *J. Appl. Phys.* **2014**, *116* (6), 64503.

(187) Macaluso, R.; Mosca, M.; Costanza, V.; D'Angelo, A.; Lullo, G.; Caruso, F.; Calì, C.; Di Franco, F.; Santamaria, M.; Di Quarto, F. Resistive Switching Behaviour in ZnO and VO_2 Memristors Grown by Pulsed Laser Deposition. *Electron. Lett.* **2014**, *50* (4), 262–263.

(188) Han, U.-B.; Lee, J.-S. Bottom-up Synthesis of Ordered Metal/oxide/metal Nanodots on Substrates for Nanoscale Resistive Switching Memory. *Sci. Rep.* **2016**, *6*, 25537.

(189) Al-Haddad, A.; Wang, C.; Qi, H.; Grote, F.; Wen, L.; Bernhard, J.; Vellacheri, R.; Tarish, S.; Nabi, G.; Kaiser, U.; Lei, Y. Highly-Ordered 3D Vertical Resistive Switching Memory Arrays with Ultralow Power Consumption and Ultrahigh Density. *ACS Appl. Mater. Interfaces* **2016**, *8* (35), 23348–23355.

(190) Qi, L.-Q.; Pan, D.-Y.; Li, J.-Q.; Liu, L.-H.; Sun, H.-Y. HfO_2/porous Anodic Alumina Composite Films for Multifunctional Data Storage Media Materials under Electric Field Control. *Nanotechnology* **2017**, *28* (11), 115702.

(191) Morishita, Y.; Hosono, T.; Ogawa, H. Fabrication of Resistive Switching Memory Structure Using Double-Sided-Anodized Porous Alumina. *Solid. State. Electron.* **2017**, *131*, 30–33.

(192) Liu, N.; Lee, K.; Schmuki, P. Reliable Metal Deposition into TiO_2 Nanotubes for Leakage-Free Interdigitated Electrode Structures and Use as a Memristive Electrode. *Angew. Chemie Int. Ed.* **2013**, *52* (47), 12381–12384.

(193) Otsuka, S.; Shimizu, T.; Shingubara, S.; Makihara, K.; Miyazaki, S.; Yamasaki, A.; Tanimoto, Y.; Takase, K. Effect of Electric Field Concentration Using Nanopeak Structures on the Current–voltage Characteristics of Resistive Switching Memory. *AIP Adv.* **2014**, *4* (8), 87110.

(194) Bendova, M.; Hubalek, J.; Mozalev, A. Exploring Electron Transport and Memristive Switching in Nanoscale Au/WO_x/W Multijunctions Based on Anodically Oxidized Al/W Metal Layers. *Adv. Mater. Interfaces* **2016**, *3* (19), 1600512.

(195) Ji, Y.; Yang, Y.; Lee, S.-K.; Ruan, G.; Kim, T.-W.; Fei, H.; Lee, S.-H.; Kim, D.-Y.; Yoon, J.; Tour, J. M. Flexible Nanoporous WO_{3-x} Nonvolatile Memory Device. *ACS Nano* **2016**, *10* (8), 7598–7603.

(196) Marik, M.; Mozalev, A.; Hubalek, J.; Bendova, M. Resistive Switching in TiO_2 Nanocolumn Arrays Electrochemically Grown. *J. Phys. Conf. Ser.* **2017**, *829* (1), 12001.

(197) Kundozerova, T. V.; Grishin, A. M.; Stefanovich, G. B.; Velichko, A. A. Anodic Nb_2O_5 Nonvolatile RRAM. *IEEE Trans. Electron Devices* **2012**, *59* (4), 1144–1148.

(198) Kundozerova, T. V.; Stefanovich, G. B.; Grishin, A. M. Binary Anodic Oxides for Memristor-Type Nonvolatile Memory. *Phys. Status Solidi* **2012**, *9* (7), 1699–1701.

(199) Zhu, W.; Chen, T. P.; Liu, Y.; Fung, S. Conduction Mechanisms at Low- and High-Resistance States in Aluminum/anodic Aluminum Oxide/aluminum Thin Film Structure. *J. Appl. Phys.* **2012**, *112*, 63706.

(200) Yin, X.; Tian, K.; Tan, Z.; Yang, R.; Guo, X. Polarity Reversal in the Bipolar Switching of Anodic TiO_2 Film. *J. Electrochem. Soc.* **2015**, *162* (10), 271–275.

(201) Wouters, D. J.; Waser, R.; Wuttig, M. Phase-Change and Redox-Based Resistive Switching Memories. *Proc. IEEE* **2015**, *103* (8), 1274–1288.

(202) Schindler, C.; Staikov, G.; Waser, R. Electrode Kinetics of Cu–SiO_2-Based Resistive

Switching Cells: Overcoming the Voltage-Time Dilemma of Electrochemical Metallization Memories. *Appl. Phys. Lett.* **2009**, *94* (7), 72109.

(203) Menzel, S.; Böttger, U.; Wimmer, M.; Salinga, M. Physics of the Switching Kinetics in Resistive Memories. *Adv. Funct. Mater.* **2015**, *25* (40), 6306–6325.

(204) Moors, M.; Adepalli, K. K.; Lu, Q.; Wedig, A.; Bäumer, C.; Skaja, K.; Arndt, B.; Tuller, H. L.; Dittmann, R.; Waser, R.; Yildiz, B.; Valov, I. Resistive Switching Mechanisms on TaO_x and $SrRuO_3$ Thin-Film Surfaces Probed by Scanning Tunneling Microscopy. *ACS Nano* **2016**, *10* (1), 1481–1492.

(205) Nishi, Y.; Menzel, S.; Fleck, K.; Bottger, U.; Waser, R. Origin of the SET Kinetics of the Resistive Switching in Tantalum Oxide Thin Films. *IEEE Electron Device Lett.* **2014**, *35* (2), 259–261.

(206) Nishi, Y.; Fleck, K.; Bottger, U.; Waser, R.; Menzel, S. Effect of RESET Voltage on Distribution of SET Switching Time of Bipolar Resistive Switching in a Tantalum Oxide Thin Film. *IEEE Trans. Electron Devices* **2015**, *62* (5), 1561–1567.

(207) Havel, V.; Fleck, K.; Rosgen, B.; Rana, V.; Menzel, S.; Bottger, U.; Waser, R. Ultrafast Switching in Ta_2O_5-Based Resistive Memories. In *2016 IEEE Silicon Nanoelectronics Workshop (SNW)*; IEEE, 2016; pp 82–83.

(208) Prakash, A.; Jana, D.; Maikap, S. TaOx-Based Resistive Switching Memories: Prospective and Challenges. *Nanoscale Res. Lett.* **2013**, *8* (1), 418.

(209) Chen, Y. S.; Chen, B.; Gao, B.; Liu, L. F.; Liu, X. Y.; Kang, J. F. Well Controlled Multiple Resistive Switching States in the Al Local Doped HfO_2 Resistive Random Access Memory Device. *J. Appl. Phys.* **2013**, *113* (16), 164507.

(210) Marchewka, A.; Waser, R.; Menzel, S. Physical Simulation of Dynamic Resistive Switching in Metal Oxides Using a Schottky Contact Barrier Model. In *2015 International Conference on Simulation of Semiconductor Processes and Devices (SISPAD)*; IEEE, 2015; pp 297–300.

(211) Fleck, K.; La Torre, C.; Aslam, N.; Hoffmann-Eifert, S.; Böttger, U.; Menzel, S. Uniting Gradual and Abrupt Set Processes in Resistive Switching Oxides. *Phys. Rev.*

Appl. **2016**, *6* (6), 64015.

(212) Celano, U.; Vandervorst, W. Nanoscale Three-Dimensional Characterization with Scalpel SPM. In *Conductive Atomic Force Microscopy: Applications in Nanomaterials*; Lanza, M., Ed.; Wiley-VCH Verlag GmbH & Co. KGaA, 2017; pp 187–210.

(213) Mähne, H.; Berger, L.; Martin, D.; Klemm, V.; Slesazeck, S.; Jakschik, S.; Rafaja, D.; Mikolajick, T. Filamentary Resistive Switching in Amorphous and Polycrystalline Nb_2O_5 Thin Films. *Solid. State. Electron.* **2012**, *72*, 73–77.

(214) Mikolajick, T.; Wylezich, H.; Maehne, H.; Slesazeck, S.; Mikolajick, T. Versatile Resistive Switching in Niobium Oxide. In *2016 IEEE International Symposium on Circuits and Systems (ISCAS)*; IEEE, 2016; pp 381–384.

(215) Liu, X.; Md. Sadaf, S.; Son, M.; Park, J.; Shin, J.; Lee, W.; Seo, K.; Lee, D.; Hwang, H. Co-Occurrence of Threshold Switching and Memory Switching in Pt/NbO_x/Pt Cells for Crosspoint Memory Applications. *IEEE Electron Device Lett.* **2012**, *33* (2), 236–238.

(216) Mahne, H.; Wylezich, H.; Slesazeck, S.; Mikolajick, T.; Vesely, J.; Klemm, V.; Rafaja, D. Room Temperature Fabricated NbO_x/Nb_2O_5 Memory Switching Device with Threshold Switching Effect. In *2013 5th IEEE International Memory Workshop*; IEEE, 2013; pp 174–177.

(217) Funck, C.; Menzel, S.; Aslam, N.; Zhang, H.; Hardtdegen, A.; Waser, R.; Hoffmann-Eifert, S. Multidimensional Simulation of Threshold Switching in NbO_2 Based on an Electric Field Triggered Thermal Runaway Model. *Adv. Electron. Mater.* **2016**, *2* (7), 1600169.

(218) Mähne, H.; Wylezich, H.; Hanzig, F.; Slesazeck, S.; Rafaja, D.; Mikolajick, T. Analog Resistive Switching Behavior of Al/Nb_2O_5/Al Device. *Semicond. Sci. Technol.* **2014**, *29* (10), 104002.

Scientific Output

Publications in International Journals

1) A. Zaffora, F. Di Franco, M. Santamaria, H. Habazaki, F. Di Quarto
The influence of composition on band gap and dielectric constant of anodic Al-Ta mixed oxides
Electrochimica Acta 180 (2015) 666-678.

2) A. Zaffora, M. Santamaria, F. Di Franco, H. Habazaki, F. Di Quarto
Photoelectrochemical evidence of nitrogen incorporation during anodizing sputtering – deposited Al–Ta alloys
Physical Chemistry Chemical Physics 18 (2016) 351-360.

3) A. Zaffora, M. Santamaria, F. Di Franco, H. Habazaki, F. Di Quarto
Photoelectrochemical evidence of inhomogeneous composition at nm length scale of anodic films on valve metals alloys
Electrochimica Acta 201 (2016) 333-339.

4) A. Zaffora, G. Tranchida, F. Di Franco, F. Di Quarto, M. Santamaria
Physico-Chemical Characterization of Anodic Oxides on Hf as a Function of the Anodizing Conditions
Journal of The Electrochemical Society 163 (9) (2016) C563-C570.

5) M. Santamaria, A. Zaffora, F. Di Franco, G. Tranchida, H. Habazaki, F. Di Quarto
Synergistic Use of Electrochemical Impedance Spectroscopy and Photoelectrochemical Measurements for Studying Solid State Properties of Anodic HfO_2
ECS Transactions 75 (38) (2017) 1-15.

6) A. Zaffora, F. Di Franco, F. Di Quarto, R. Macaluso, M. Mosca, H. Habazaki, M. Santamaria
The Effect of Nb Incorporation on the Electronic Properties of Anodic HfO_2
ECS Journal of Solid State Science and Technology 6 (4) (2017) N25-N31.

7) F. Di Quarto, F. Di Franco, A. Zaffora, M. Santamaria
Photocurrent Spectroscopy in Corrosion and Passivity Studies. A Critical Assessment
ECS Transactions 75 (27) (2017) 33-48.

8) F. Di Quarto, A. Zaffora, F. Di Franco, M. Santamaria
Review - Photocurrent Spectroscopy in Corrosion and Passivity Studies: A Critical Assessment of the Use of Band Gap Value to Estimate the Oxide Film Composition
Journal of The Electrochemical Society 164 (12) (2017) C671-C681.

9) A. Zaffora, D.-Y. Cho, K.-S. Lee, F. Di Quarto, R. Waser, M. Santamaria, I. Valov
Electrochemical Tantalum Oxide for Resistive Switching Memories
Advanced Materials 29 (43) (2017) 1703357.

10) A. Zaffora, R. Macaluso, H. Habazaki, I. Valov, M. Santamaria
Electrochemically Prepared Oxides for Resistive Switching Devices
Submitted to Electrochimica Acta.

Books Chapters

1) Di Franco F., Zaffora A., Santamaria M. and Di Quarto F. (2016) *Anodization and Anodic Oxides*. In: Reedijk, J. (Ed.) Elsevier Reference Module in Chemistry, Molecular Sciences and Chemical Engineering. Waltham, MA: Elsevier.

2) Di Quarto F., Di Franco F., Zaffora A. and Santamaria M. (2017) *Photocurrent Spectroscopy in Passivity Studies*. In: Wandelt, K. (Ed.) Elsevier Reference Module in Chemistry, Molecular Sciences and Chemical Engineering. Waltham, MA: Elsevier.

National Conference Contributions

1) F. Di Franco, A. Zaffora, M. Santamaria, F. Di Quarto, E. Tsuji, H. Habazaki, *Electrochemical fabrication of high-k Al-Ta mixed oxides*, XXV Congresso Nazionale della Società Chimica Italiana – SCI 2014, 7 – 12 Settembre, 2014, Rende. (Oral Communication).

2) R. Macaluso, G. Lullo, M. Mosca, V. Costanza, A. D'Angelo, D. Russotto, V. Aglieri, A. Zaffora, A. Genovese, F. Caruso, C. Calì, F. Di Franco, M. Santamaria, F. Di Quarto, *Fabrication and Characterization of micrometer-scale ZnO memristors*, The 47th annual meeting of the Associazione Gruppo Italiano di Elettronica GE 2015, 22 – 24 Giugno, 2015, Siena. (Poster Communication).

3) (**Presenting Author**) Andrea Zaffora, M. Santamaria, F. Di Franco, F. Di Quarto, H. Habazaki, *Photoelectrochemical evidence of Nitrogen Incorporation during Anodizing of valve metal alloys*, Giornate dell'Elettrochimica Italiana GEI 2015, 20 – 24 Settembre, 2015, Bertinoro. (Oral Communication).

4) M. Santamaria, A. Zaffora, F. Di Franco, H. Habazaki, F. Di Quarto, *Solid state properties of anodic Hf-Nb mixed oxides*, Giornate dell'Elettrochimica Italiana GEI 2016, 11 – 14 Settembre, 2016, Gargnano. (Oral Communication).

5) (**Presenting Author**) Andrea Zaffora, F. Di Franco, V. Aglieri, R. Macaluso, H. Habazaki, F. Di Quarto, M. Santamaria, *Anodic TiO_2 in ReRAM: influence of Si-doping on the resistive switching properties of titanium oxide*, Giornate dell'Elettrochimica Italiana GEI 2016, 11 – 14 Settembre, 2016, Gargnano. (Oral Communication).

6) R. Macaluso, S. Barcellona, A. Zaffora, U. Lo Cicero, G. Lullo, M. Mosca, C. Calì, F. Di Franco, M. Santamaria, *Fabrication and Characterization of microscale HfO_2-based memristors*, The 49th annual meeting of the Associazione Società Italiana di Elettronica SIE 2017, 21 – 23 Giugno, 2017, Palermo. (Poster Communication).

7) (**Presenting Author**) Andrea Zaffora, F. Di Franco, F. Di Quarto, I. Valov, H. Habazaki, M. Santamaria, *Fabrication of Hf-Nb Anodic Oxides and Their Use in Resistive Switching Devices*, XXVI Congresso Nazionale della Società Chimica Italiana – SCI 2017, 10 – 14 Settembre, 2017, Paestum. (Oral Communication).

International Conference Contributions

1) F. Di Franco, A. Zaffora, M. Santamaria, F. Di Quarto, E. Tsuji, H. Habazaki, *Tuning of solid state properties of Al-Ta mixed oxides*, The 65th Annual Meeting of the International Society of Electrochemistry, August 31st – September 5th, 2014, Lausanne (Switzerland). (Oral Communication).

2) F. Di Franco, A. Zaffora, M. Santamaria, F. Di Quarto, E. Tsuji, H. Habazaki, *The influence of composition on the solid state properties of anodic films on Al-Ta alloys*, ASST 2015 VII Aluminium Surface Science & Technology, May 17th – 21st, 2015, Madeira (Portugal). (Oral Communication).

3) M. Santamaria, F. Di Franco, F. Di Quarto, H. Habazaki, A. Zaffora, *Photoelectrochemical evidence of inhomogeneous composition at nm length scale of anodic films on valve metals alloys*, The 17th Topical Meeting of the International Society of Electrochemistry, Multiscale Analysis of Electrochemical Systems, May 31st – June 3rd, 2015, Saint-Malo (France). (Oral Communication).

4) (**Presenting Author**) Andrea Zaffora, M. Santamaria, F. Di Franco, F. Di Quarto, H. Habazaki, *Photoelectrochemical evidence of Nitrogen Incorporation during Anodizing of Sputtering-Deposited Al-Ta alloys*, Hokkaido University - University of California, Berkeley, Joint Symposium on Chemical Sciences and Engineering, January 7th, 2016, Sapporo, (Japan). (Poster Communication).

5) F. Di Quarto, F. Di Franco, A. Zaffora, M. Santamaria, *Photocurrent Spectroscopy in Corrosion and Passivity Studies: A Critical Assessment*, PRiME 2016, October 2nd – 7th, 2016, Honolulu (USA). (Oral Communication).

6) M. Santamaria, G. Tranchida, A. Zaffora, F. Di Franco, H. Habazaki, F. Di Quarto, *Synergistic Use of Electrochemical Impedance Spectroscopy and Photoelectrochemical Measurements for Studying Solid State Properties of Anodic HfO_2*, PRiME 2016, October 2nd – 7th, 2016, Honolulu (USA). (Oral Communication).

7) (**Presenting Author**) Andrea Zaffora, H. Habazaki, F. Di Franco, F. Di Quarto, M. Santamaria, *Growth kinetics and physicochemical characterization of Hf-Nb anodic mixed oxides*, The 68th Annual Meeting of the International Society of Electrochemistry, August 27th – September 1st, 2017, Providence (USA). (Poster Communication).

8) (**Presenting Author**) Andrea Zaffora, F. Di Quarto, I. Valov, M. Santamaria, *Electrochemically prepared Oxides for Resistive Switching Devices*, The 68th Annual Meeting of the International Society of Electrochemistry, August 27th – September 1st, 2017, Providence (USA). (Oral Communication).

Ph.D. School

1) 47th IFF Spring School, "Memristive Phenomena – From Fundamental Physics to Neuromorphic Computing", Feb 22nd – Mar 04th, 2016, (50 hrs), Jülich, Germany.

Prizes and Awards

1) Best Poster Prize for Symposium 11 at the 68th Annual Meeting of the International Society of Electrochemistry, Aug 27th – Sep 1st, 2017, Providence (USA).

Abroad Research Periods

1) Visiting Ph.D. Student at "Laboratory of Interfacial Electrochemistry", Hokkaido University, Sapporo, Japan, 3rd Nov 2015 – 29th Jan 2016.

2) Visiting Ph.D. Student at "Institut für Werkstoffe der Elektrotechnik 2", RWTH Aachen University, Aachen, Germany, 1st Nov 2016 – 30th Apr 2017.